Advanced Signal Processing Tools for Ballistic Missile Defence and Space Situational Awareness

Adriano Rosario Persico

Centre for Signal and Image Processing
Department of Electronic and Electrical Engineering
University of Strathclyde
Glasgow

This dissertation is submitted for the degree of
Doctor of Philosophy

2018

To my Rosy,
love of my life

Declaration

This thesis is the result of the author's original research. It has been composed by the author and has not been previously submitted for examination which has led to the award of a degree.

Adriano Rosario Persico
2018

Acknowledgements

This work, fruit of my entire experience at University of Strathclyde in Glasgow, would has not been possible without the support of many people.

Firstly, I would like to thank my supervisors prof. John Soraghan and Dr Carmine Clemente, who gave me the opportunity to deal with a wide range of exciting and interesting topics. I am really grateful for the endless support they provided me in any my step, always with useful comments and suggestions, and encouraging me to give and get the best. I wish since I was a child to spend part of my life in Glasgow. Thank you very much for making this dream come true. It has been a wonderful experience for me.

A special thank goes to Domenico and Christos. When I arrived in Glasgow, we needed just a couples of days to become "the tripod", supporting and helping each other in almost all the projects conducted at university, and not only in those.
I really thank Alessio, colleague at the university, trainer at the gym, and the worst and best flatmate I could have, but even the one so brave to accept sharing the flat with me.
Many thanks to all the others from the Sensor Signal Processing for Defence (SSPD) laboratories, Pasquale, Hilias, William and Jianlin, for all the fun and the nice moments that made the working days more pleasant.
Thanks also to all the people from the Centre for Signal and Image Processing (CeSIP). I am so glad to work not with just colleagues, but with nice friends.

I want to manifest with the deepest love my unlimited gratitude to all my big family, my Dad and Mum, my brothers and sisters-in-law, my wonderful nephews and niece. And with same love, thanks to my other half family, my mother-in-low, my grandmother, my little sister and all the other loved ones, nobody except. They never stop to encourage me, making me felt loved and important even if so far away one from each other.

A big thank you is also for my closest friends. We are always the same people, we know each other from ever and I know surely that we will never stop to celebrate our successes together.

Finally, my greatest thank you goes to the love of my life, Rosy. The choice to move in Glasgow for so long time it has been one of the hardest decision in my life, because it has meant living a physical distance between us. The distance hurt very much, in each instant. However, it never broke us, and it could never do it. I knew at first sight that I have found my soul mate in you. A nothing, even thousands of kilometres, could separate our hearts any more. Thank you for your love, that covers any distances. Thank you for your unconditional support. Thank you for believing me, always. Thank you for being such an amazing person, choosing me every day. Thank you, because if *love is the answer*, you are and will be my answer. *I just can't stop loving you.*

Sharing the happiness make it double. Many thanks to whom is sharing mine.

Abstract

The research presented in this Thesis deals with signal processing algorithms for the classification of sensitive targets for defence applications and with novel solutions for the detection of space objects. These novel tools include classification algorithms for Ballistic Targets (BTs) from both micro-Doppler (mD) and High Resolution Range Profiles (HRRPs) of a target, and a space-borne Passive Bistatic Radar (PBR) designed for exploiting the advantages guaranteed by the Forward Scattering (FS) configuration for the detection and identification of targets orbiting around the Earth.
Nowadays the challenge of the identification of Ballistic Missile (BM) warheads in a cloud of decoys and debris is essential in order to optimize the use of ammunition resources. In this Thesis, two different and efficient robust frameworks are presented. Both the frameworks exploit in different fashions the effect in the radar return of micro-motions exhibited by the target during its flight.
The first algorithm analyses the radar echo from the target in the time-frequency domain, with the aim to extract the mD information. Specifically, the Cadence Velocity Diagram (CVD) from the received signal is evaluated as mD profile of the target, where the mD components composing the radar echo and their repetition rates are shown. Different feature extraction approaches are proposed based on the estimation of statistical indices from the 1-Dimensional (1D) Averaged CVD (ACVD), on the evaluation of pseudo-Zerike (pZ) and Krawtchouk (Kr) image moments and on the use of 2-Dimensional (2D) Gabor filter, considering the CVD as 2D image. The reliability of the proposed feature extraction approaches is tested on both simulated and real data, demonstrating the adaptivity of the framework to different radar scenarios and to different amount of available resources. The real data are realized in laboratory, conducting an experiment for simulating the mD signature of a BT by using scaled replicas of the targets, a robotic manipulator for the micro-motions simulation and a Continuous Waveform (CW) radar for the radar measurements.
The second algorithm is based on the computation of the Inverse Radon Transform

(IRT) of the target signature, represented by a HRRP frame acquired within an entire period of the main rotating motion of the target, which are precession for warheads and tumbling for decoys. Following, pZ moments of the resulting transformation are evaluated as final feature vector for the classifier. The features guarantee robustness against the target dimensions and the initial phase and the angular velocity of its motion. The classification results on simulated data are shown for different polarization of the ElectroMagnetic (EM) radar waveform and for various operational conditions, confirming the the validity of the algorithm.
The knowledge of space debris population is of fundamental importance for the safety of both the existing and new space missions. In this Thesis, a low budget solution to detect and possibly track space debris and satellites in Low Earth Orbit (LEO) is proposed. The concept consists in a space-borne PBR installed on a CubeSaT flying at low altitude and detecting the occultations of radio signals coming from existing satellites flying at higher altitudes. The feasibility of such a PBR system is conducted, with key performance such as metrics the minimum size of detectable objects, taking into account visibility and frequency constraints on existing radio sources, the receiver size and the compatibility with current CubeSaT's technology. Different illuminator types and receiver altitudes are considered under the assumption that all illuminators and receivers are on circular orbits. Finally, the designed system can represent a possible solution to the the demand for Ballistic Missile Defence (BMD) systems able to provide early warning and classification and its potential has been assessed also for this purpose.

Table of contents

List of figures

List of tables

Nomenclature

Roman Symbols

${}_2F_1(\cdot, \cdot; \cdot; \cdot)$	Gauss hypergeometric function
A	Target's silhouette area
a	Amplitude of received signal
A_{eff}	Effective antenna area
$\boldsymbol{N}_0(\cdot)$	Additive White Gaussian Noise sample
$\angle$Az	Radar azimuth angle
B	Pulse bandwidth
b	Arbitrary scale factor
$\bar{A}$	Minimum target silhouette's area
B_r	Receiver Bandwidth
c	Speed of light in vacuum $c \approx 3 \times 10^8$ m/s
d	Greater dimension of target
$\hat{\boldsymbol{E}}(\cdot)$	Skew symmetric matrix
e	Mathematical constant $e \simeq 2.71\ldots$
$\angle$El	Radar elevation angle
$\boldsymbol{F}$	Generic feature vector
F	Noise Figure
f_0	Carrier frequency

f_n	Sub-pulse carrier frequency
$\boldsymbol{F}^{\mathrm{avg}}$	Averaged cadence velocity diagram based Feature vector
f_{cs}	Central spatial frequency of 2-dimensional Gabor filter
f_D	Doppler frequency
f_{bD}	Doppler frequency shift due to target bulk motion
f_{D_i}	Doppler frequency of the i-th target scattering point
f_{mD_i}	Doppler frequency shift due to the i-th target scattering point motion
$\boldsymbol{F}^{\mathrm{GF}}$	Gabor Filter based Feature vector
$\boldsymbol{F}^{\mathrm{Kr}}$	Krawtchouk moment based Feature vector
f_p	Pulse repetition frequency
$\boldsymbol{F}^{\mathrm{pZ}}$	Pseudo-Zernike moment based Feature vector
F_r	Fraunhofer diffraction coefficient with respect to the receiver
F_t	Fraunhofer diffraction coefficient with respect to the transmitter
$f(\cdot,\cdot)$	Generic 2-dimensional function
$\mathcal{G}(\cdot,\cdot)$	Harmonic response of 2-dimensional Gabor filter
G_{FS}	Antenna gain of a uniformly illuminated aperture
G_r	Receiver antenna gain
G_t	Transmitter antenna gain
$\mathcal{H}(\cdot)$	High Resolution Range Profile
H	Target height
h_{MF}	Matched filter impulse response
H_{fin}	Target fin height
$\hat{\boldsymbol{I}}$	Identity matrix

$I(\cdot,\cdot)$	Real-valued Image
k	Boltzmann's constant $k \approx 1.38064852 \times 10^{-23}$ m^2 kg s^{-2} K^{-13}
$K_{n,m}$	Krawtchouk moments of order (n, m)
$\mathcal{N}$	Length of Krawtchouk polynomial
$K_r(\cdot, p, \mathcal{N})$	Krawtchouk polynomial of order r, length $\mathcal{N}$ and shift parameter p
$\overline{K}_r(\cdot, p, \mathcal{N})$	Weighted Krawtchouk polynomial of order r, length $\mathcal{N}$ and shift parameter p
$\mathcal{L}$	Generic line
$\boldsymbol{L}_n(\cdot)$	Log-normal random variable sample for RCS fluctuation
L_s	Loss factor
M	Dimension of High Resolution Range Profiles frame
N	Number of sub-pulses
N_{bin}	Number of spectrogram frequency bins
N_c	Number of velocity cadence bins
N_{fin}	Number of target fins
N_p	Number of principal scattering point of the target
n_p	Number of integrated pulses
N_s	Number of signal samples
$\mathcal{P}_C$	Probability of correct Classification
$\mathcal{P}_M$	Probability of correct Motion identification
P_n	Noise power
$\mathcal{P}_R$	Probability of correct Recognition
P_r	Received power
$\boldsymbol{p}_{rx}$	Receiver position with respect to $(\tilde{U}, \tilde{V}, \tilde{W})$ system

$\mathcal{P}_S$	Probability of Shape identification
$p_s(\cdot)$	Sub-pulse
$\boldsymbol{p}_{st}$	Space Target position with respect to $(\tilde{U}, \tilde{V}, \tilde{W})$ system
P_t	Peek Transmitted power
$\boldsymbol{p}_{tx}$	Transmitter position with respect to $(\tilde{U}, \tilde{V}, \tilde{W})$ system
$\mathcal{P}_U$	Probability of Unknown
$\zeta_{r,l}$	Pseudo-Zernike moments of order r and repetition l of image $I(\cdot, \cdot)$
$W_{l,r}$	Pseudo-Zernike polynomial of order r and repetition lF
Q_i	Incident power density
R_t	Distance from radar to target
R_b	Target base radius
$\boldsymbol{R}_c$	Conical rotation motion matrix
r_i	Distance between radar and the i-th target scattering point
$\boldsymbol{r}_i^{local}$	Position vector of the i-th target scattering point with respect to the local coordinate system
$\boldsymbol{r}_i^{radar}$	Position vector of the i-th target scattering point with respect to the radar coordinate system
$\boldsymbol{r}_i$	Position vector of the i-th target scattering point with respect to the reference coordinate system
$\boldsymbol{r}_{\mathrm{MC}}$	Position vector of target mass centre with respect to the radar coordinate system
$\boldsymbol{r}_{\mathrm{MC}}^{local}$	Position vector of target mass centre with respect to the local coordinate system
$\boldsymbol{R}_n$	Nutation motion matrix
R_r	Distance from radar receiver to target
$\boldsymbol{R}_s$	Spinning motion matrix

$\mathcal{R}_f(\cdot,\cdot)$	Radon Transform of function $f(\cdot,\cdot)$
R_t	Distance from radar transmitter to target
$S_{\mathrm{CEP}}(\cdot,\cdot)$	Cepstrogram
$S_{\mathrm{CVD}}(\cdot,\cdot)$	Cadence Velocity Diagram
$\mathcal{F}$	Space distribution function of target principal scatterers
SNR_c	Signal to noise ratio after the pulses coherent integration
SNR_{nc}	Signal to noise ratio after the pulses incoherent integration
SNR_{out}	Signal to noise ratio out from matched filter
$S_{\mathrm{PWD}}(\cdot,\cdot)$	Pseudo Wigner Distribution
$s_{rx}(\cdot)$	Received time signal
$S_{\mathrm{SM}}(\cdot,\cdot)$	S-Method Distribution
$S_{\mathrm{STFT}}(\cdot,\cdot)$	Short-Time Fourier Transform
$s(\cdot)$	Generic non-stationary signal
$s_{tx}(\cdot)$	Transmitted time signal
$S_{\mathrm{WVD}}(\cdot,\cdot)$	Wigner-Ville Distribution
t	Time variable
$\mathtt{T_0}$	Reference temperature ($T_0 = 290K$)
t_0	Round trip time of a signal to propagate from the radar to the target
$\mathtt{T_a}$	Antenna noise temperature
$\mathtt{T_{comp}}$	Composite noise temperature of receiver components
$\boldsymbol{T}_m$	Micor-motion matrix
$\mathtt{T_n}$	Effective noise temperature
T_p	Pulse repetition interval

$(\hat{U},\, \hat{V},\, \hat{W})$	Radar coordinates system
$(\tilde{U}, \tilde{V}, \tilde{W})$	Earth reference coordinates system
$\boldsymbol{v}$	Velocity vector of target bulk motion
v_r	Target relative velocity component along the line of sight
$(\hat{X},\, \hat{Y},\, \hat{Z})$	Reference coordinates system centred in the mass centre of the target
$(\hat{x},\, \hat{y},\, \hat{z})$	Local coordinates system

Greek Symbols

α	Aspect angle between the line of sight and the axis which defines the target orientation
α_{st}	Space target orbit squint angle with respect receiver orbit
α_{tx}	Transmitter orbit squint angle with respect receiver orbit
β	Bistatic angle between transmitter, receiver and target positions
$\boldsymbol{\chi}$	Threshold for target fin occlusion function
R_Δ	Range resolution
Δ_f	Frequency step
$\delta(\cdot)$	Delta function
$\Delta\Theta$	Variation of conical rotation angle
ε_1	Bistatic radar baseline elevation angle
ε_2	Bistatic radar baseline azimuth angle
η_x	Spatial width of 2-dimensional Gabor filter along the plane wave
η_y	Spatial width of 2-dimensional Gabor filter perpendicular to the plane wave
$g(\cdot,\cdot)$	Impulsive response of 2-dimensional Gabor filter
γ	Cone semi-angle

γ_{fin}	Semi-angle of Cone with fin
$\widehat{\boldsymbol{w}_c}$	Conical angular velocity direction
$\widehat{\boldsymbol{w}_r}$	Rotation angular velocity direction
$\widehat{\boldsymbol{w}_s}$	Spinning angular velocity direction
λ	Wavelength of carrier signal
Ω_c	Conical angular velocity
Ω_n	Nutation pulsation
Ω_{n_0}	Nutation initial phase
Ω_{s_0}	Spinning initial phase
Ω_r	Rotation angular velocity
Ω_s	Spinning angular velocity
ω_{rx}	Orbit angular velocity of receiver
ω_{st}	Orbit angular velocity of space target
ω_{tx}	Orbit angular velocity of transmitter
ϕ	Phase rotation of received signal
ϕ_{bD}	Signal phase rotation due to target bulk motion
ϕ	Phase of the complex coefficient of the i-th target scattering point
ϕ_{MC}	Signal phase rotation due initial range of target mass centre
π	Mathematical constant $\pi \simeq 3.14\ldots$
ρ_{rx}	Receiver's altitude
ρ_{st}	Space target's altitude
ρ_{tx}	Transmitter's altitude
σ	Radar cross section
σ_{avg}	Average radar cross section

$\sqrt{\sigma_{fin_i}}$	Magnitude of the complex coefficient of the i-th target fin
σ_{FS}	Forward scattering radar cross section
$\sqrt{\sigma_i}$	Magnitude of the complex coefficient of the i-th target scattering point
τ	Pulse width
Θ	Conical Rotation angle
Θ_n	Maximum oscillation angle of nutation
φ	Orientation angle between the perpendicular to the bistatic radar baseline and the symmetric axis of the target
ϖ_i	position angle of i-th target fin
$\varsigma_{\boldsymbol{F}}$	Statistical mean of vector $\boldsymbol{F}$
ϑ	Orientation angle of 2-dimensional Gabor filter
$\boldsymbol{w}_c$	Conical angular velocity vector
$\boldsymbol{w}_s$	Spinning angular velocity vector
$\Xi(\cdot,\cdot,f_{cs},\vartheta)$	Output of Gabor filter with a central spatial frequency f_{cs} and orientation angle ϑ.
$\zeta_{\boldsymbol{F}}$	Standard deviation of vector $\boldsymbol{F}$
ζ_v	Standard deviation of vector $\boldsymbol{F}$

Superscripts

$(\cdot)^*$	Complex conjugate operator
$(\cdot)^T$	Transpose operator

Subscripts

$(\cdot)_k$	Pochhammer operator

Other Symbols

$\int$	Integration operator

$\lvert \cdot \rvert$	Magnitude
$\lVert \cdot \rVert$	Norm
$\sum$	Summation operator

Acronyms / Abbreviations

1D	1-Dimensional
$(2D)^2$	2-Directional 2-Dimensional
2D	2-Dimensional
ATR	Automatic Target Recognition
BM	Ballistic Missile
BMD	Ballistic Missile Defence
BT	Ballistic Target
CVD	Cadence Velocity Diagram
CW	Continuous Waveform
EIRP	Effective Isotropic Radiated Power
EM	Electromagnetic
ESA	European Space Agency
ESSAS	European Space Situational Awareness System
FFT	Fast Fourier Transform
FMCW	Frequency Modulated Continuous Wave
FM	Frequency Modulation
FS	Forward Scattering
FSRCS	Forward-Scattering Radar Cross-Section
FT	Fourier Transform
GNSS	Global Navigation Satellite System

GS	Global Star
HRR	High Resolution Range
HRRP	High Resolution Range Profile
HY2A	Haiyang-2A
IFT	Inverse Fourier Transform
IRT	Inverse Radon Transform
ISAR	Inverse Synthetic Aperture Radar
ISR	Intelligence, Surveillance, and Reconnaissance
Kr	Krawtchouk
LEO	Low Earth Orbit
LFM	Linear Frequency Modulation
LNA	Low Noise Amplifier
LOS	Line Of Sight
MC	Mass Centre of the target
mD	micro-Doppler
MTI	Moving Target Indication
MW	Missile Warning
PBR	Passive Bistitic Radar
PCA	Principal Component Analysis
PRF	Pulse Repetition Frequency
PRI	Pulse Repetition Interval
PWD	Pseudo Wigner Distribution
pZ	pseudo-Zernike
RADAR	RAdio Detecting And Raging

RCS	Radar Cross-Section
RF	Radio Frequencies
RI	Radar Imaging
RRE	Radar Range Equation
RT	Radon Transform
RVP	Residual Video Phase
RV	Re-entry Vehicle
SAR	Synthetic Aperture Radar
SCR	Signal-to-Clutter Ratio
SDR	Software Defined Radio
SFW	Stepped Frequency Waveform
SNR	Signal-to-Noise Ratio
SSA	Space Situational Awareness
STFT	Short Time Fourier Transform
TFD	Time-Frequency Distribution
T/R	Transmitter/Receiver
WMD	Weapon of Mass Destruction
WVD	Wigner-Ville Distribution

Chapter 1

Introduction

1.1 Preface

After World War II, the progress in Ballistic Missile (BM) technology has led to the development of efficient Weapons of Mass Destruction (WMD) and of space technologies, with a relevant number of space mission held in the last decades. Therefore, a particular class of radar systems has been designed in order to perform satisfactorily the main functions of detection, tracking and recognition for Ballistic Missile Defence (BMD), ballistic Missile Warning (MW), and Space Situational Awareness (SSA). Both BMD and MW require the detection of incoming BM near the radar maximum range, the target characterization into major associated components e.g. boosters and Re-entry Vehicle (RV), in order to support target identification, and individual targets tracking with sufficient accuracy to predict their trajectories. The main aim of SSA is the monitoring of the space object population, in order to provide warning of potential collisions and to identify between operating objects and potential threats (Melvin and Scheer, 2014).

Ballistic Missile Classification Challenge

Since the early stages of the development of InterContinental-range Ballistic Missiles (ICBMs) and Submarine-Launched Ballistic Missiles (SLBMs), many countries invest annually a significant budget into research and production of countermeasures in order to minimize the effectiveness of BMD systems (Sessler et al., 2000). One of the most common practices is the use of a large number of decoys, or false targets, with the aim to confuse the defence systems. Nowadays different decoy strategies are available e.g. replica decoys, decoys using signature diversity and decoys using anti-simulation (Weiner and Rocklin, 1994). The

lightweight decoys are a very attractive strategy against exo-atmospheric defences. Long-range Ballistic Missiles (BM) move on sub-orbital trajectories and their ranges typically depend on the altitude achieved by using one ore more boosters. On the other hand, the missile warhead sizes and range depends on the weight of carried payload. Hence, missiles can be equipped with a large number of lightweight decoys without affecting the maximum warhead range (Sessler et al., 2000). The longer part of a BM flight takes place in the exo-atmosphere and it is commonly known as the mid-course phase. The lightweight decoys are released during the mid-course phase, so both the decoys and the much heavier warhead travel on similar trajectories due to the absence of atmospheric drag in the vacuum of space (Bankman et al., 2001). In addition to intentional decoys, missiles release also incidental debris and deployment hardware e.g. boosters for missile launch, which can pose an additional source of interference on radar returns. In absence of reliable target identification, the defence system has to intercept all the detected targets, including decoys, in order to prevent the warhead from reaching its aim. Therefore, the challenge of Ballistic Targets (BTs) classification, identifying the warhead into a cloud of decoys and debris is of fundamental importance to increase the safety level. Defence system efficiency can be critically affected by decoys in two related ways. In fact in the case in which a decoy is classified as a warhead (*false alarm*), the defence may run out its limited ammunition of interceptors prematurely. In contrast, the misclassification of a warhead (*leakage*) may lead to catastrophic consequences (Weiner and Rocklin, 1994).
The BM flight is generally divided into three phases, as shown in Figure 1.1: boost phase, which comprises the powered flight portion; mid-course phase, above mentioned, during which the warhead separates from the rest of missile; and the re-entry phase wherein the warhead re-enters the Earth's atmosphere to approach the target. The missile interception in the boost phase would be free from the issue represented by decoys. However, the boost phase does not offer much opportunity to track accurately for intercepting a BM since the launch point will normally be a significant distance from the defence radar system. Moreover, during this phase the missile separates from several boosters, which would result in significant interference. For these reason, BMD infra-red seekers are largely confined to exo-atmospheric operation due to sensitivity needs and atmospheric friction effects (Melvin and Scheer, 2014). A chance to discriminate between warheads and lightweight decoys occurs during the re-entry phase, since decoys would slow down more rapidly due to the atmospheric drag than the warhead. Nevertheless, the warhead interception in this phase may be not useful due its

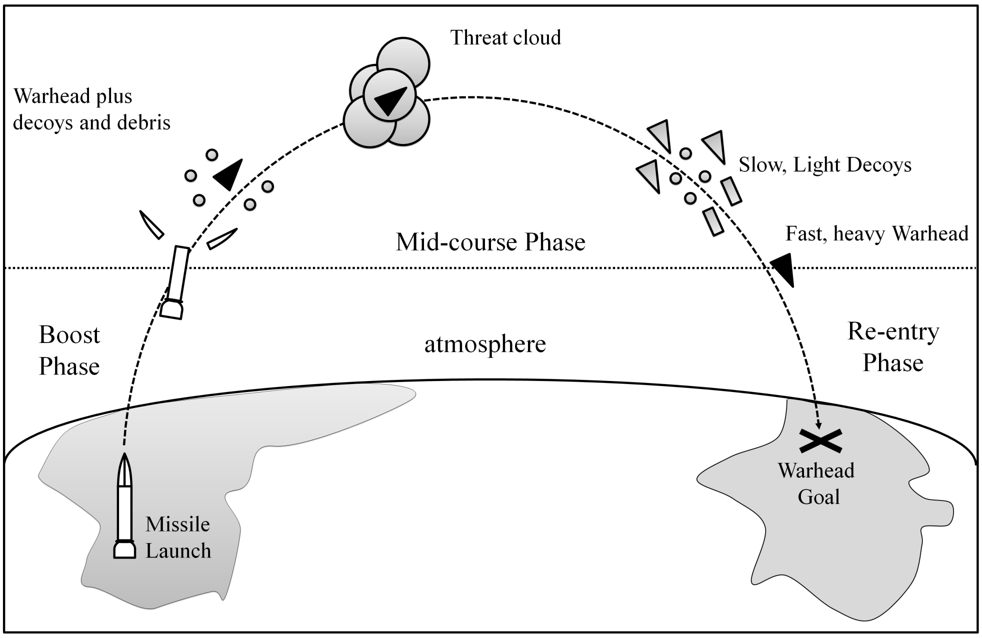

Fig. 1.1 Ballistic Missile flight phases.

short duration (few seconds), and because the warhead could have already passed the minimum intercept altitude for an above-the-atmosphere interceptor (Weiner and Rocklin, 1994). Additionally, the RVs could be armed with a nuclear or chemical bomb such that the warhead has to be intercepted at a safety altitude to avoid that a nuclear detonation has effects on the Earth's surface, or chemical and biological payloads disperse through the troposphere (Melvin and Scheer, 2014). Hence, the mid-course phase usually represents the most useful flight part for intercepting missiles, due to its relatively long duration and for the absence of tactical manoeuvring of targets since they are in free-flight motion.
The development of classification algorithms with high level of efficiency, low computational cost and short time decision is very attractive for both the ground-based defence station and the interceptor On-Board Computer. The main reason is that the defence may need to launch its interceptors before the lightweight decoys could be discriminated in order to intercept threats very far from the interceptor deployment site (Sessler et al., 2000). Moreover, once the warhead has been identified, it is essential for the seeker on the interceptor to determine the aim point on the RV for terminal guidance and effective impact during engagement (Bankman et al., 2001).

Space Debris Monitoring

In the past 60 years, since the launch of Sputnik 1, the number of objects in orbit around the Earth has increased considerably. A good part of these objects are classified as space debris and represent a significant hazard for all current and future missions. The growing traffic is increasing the probability of collisions also among functioning satellites as the Iridium-Cosmos collision in 2009 demonstrated (Pelton, 2013). Even collisions with very small objects (few cm in size) at orbital speed can cause catastrophic consequences. Each explosion or collision with space junk produces additional debris, which can lead to a cascade of more collisions. This chain reaction is known as *Kessler syndrome*, and some argue it has already started. Very large objects, such as defunct satellites, rocket bodies and large fragments, can represent a threat even for people on the ground since they may hit the ground at unpredictable locations after re-entry. In addition to trackable space debris, millions of non trackable small fragments, with the size of a grain of salt, exist that can penetrate the spacesuit of an astronauts or a window on a space vehicle with tragic consequences.

Fig. 1.2 from (Deb, 2017) shows the timeline of the growth in the number of tracked space objects in orbit around the Earth. However, the actual numbers is estimated being 2 to 3 times larger, since the available systems cannot track objects in orbit smaller than 10 cm (Deb, 2017). Information about space debris comes from a combination of ground-based and space-based measurements. One of the entities that identifies, tracks and categorizes space objects is the United States Space Command (Smirnov and Institute, 2002), which consists of a Space Based Space Surveillance (SBSS) satellite and a network of radars and optical telescopes (Ender et al., 2011). Optical sensors guarantee greater ranges with respect the radars. However, since its operating principle requires solar illumination conditions, their capability are limited against the low-altitude regime where space objects are often in Earth's shadow. On the other hand, ground-based radars generally control the space population in the Low Earth Orbit (LEO) regime (Melvin and Scheer, 2014).

In 2009 the European Space Agency (ESA) started a program for a European Space Situational Awareness System (ESSAS) which required the design of a radar system able to detect small targets with a size in the order of one decimetre in LEO (Ender et al., 2011). Moreover, in Europe, a number of radar systems are used to monitor space debris. An example is the BR system Grand Rséau Adapté la Veille Spatiale (GRAVES) that has been operating in France since

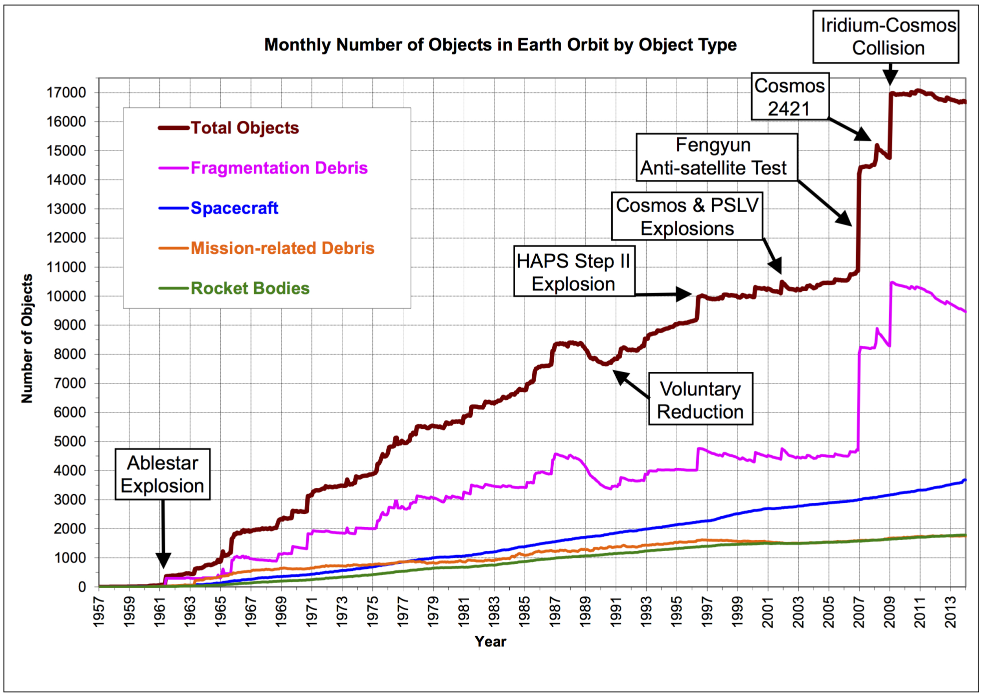

Fig. 1.2 Timeline of the growth in the number of tracked space objects in orbit around the Earth from (Deb, 2017).

2005. In Russia 20 radars and telescopes are positioned in eight different sites. In Germany the Tracking and Imaging Radar (TIRA) system of Fraunhofer FHR allows for the estimation of target's characteristics as orbital elements, intrinsic motion parameters, target shape and size and ballistic coefficient thanks to new signal processing techniques based on radar observations (Ender et al., 2011). Among all sensors deployed to detect and track space debris, radar systems represent an important contribution for their ability to provide high detection probabilities at very large ranges in addition to capabilities of estimation of target's characteristics. The feasibility study of tracking space debris by using a PBR was investigated in (Benson, 2014). Specifically, the author in (Benson, 2014) proposes a system which comprises a ground-based receiver for space object tracking with low-power scattering observations of any objects above the horizon. The underlying principle is to employ the occlusion phenomenons which occur in receiving the illuminator signal when an object passes through the Line Of Sight (LOS) between transmitter and receiver. The paper proposes several solutions to achieve a suitable SNR at the receiver, such as the use of multiple receiving elements and the integration of the received signal over time. The authors in (Jayasimha and Jyothendar, 2013) show the capability to detect small space debris by using a large-antenna earth-station communicating with geo-stationary satellite, exploiting self-interference cancellation. Specifically, when a space debris is at near-LOS, the output of self-interference cancellation may contain the return from one or two debris, which can be used for detection. However, the presented method is dependent on whether conditions, since the debris signature can be affected by inadequate cancellation of direct-path caused by the clutter from weather.

1.2 Motivation

Nowadays, the classification of BM and the space surveillance represent important open challenges, with a significant impact on the military and civilian safety of a Country, for the first, and on the safety of space missions, for the second. Specifically, the identification of a BM warhead within a cloud of interference factors is of fundamental importance for increasing the efficiency of BMD systems, optimizing the use of allocated resources in terms of interceptors. The information about target micro-motions represents a strong feature for target identification, especially when other characteristics such as target shape, dimensions or reflectivity are hardly estimable or they are not discriminant features between different targets. Moreover, despite the use of many different sensors deployed to detect and track space debris, from optic to radar systems, the minimum dimensions of detectable targets is limited due to several factors, such as the target velocities, the significant distance between targets and sensors, and the relative short observation times.
Based on the recent developments in the signal processing for the extraction of micro-Doppler (mD) information and for the extraction of the High Resolution Range Profile (HRRP) of a target, the scope of the Thesis is to propose novel advanced radar systems and signal processing tools for the sensitive challenge of missile warheads identification by employing the information on target motion observed in both time-frequency and range-time analysis, guaranteeing satisfactory performance in different radar scenarios, and for monitoring the population of space debris in LEO, improving the capability to detect very small target.

1.3 Original Contributions

The original contributions contained in this Thesis are in the fields of radar classification of BTs and space debris population monitoring. The novel contributions are as follows:

- Design of a mathematical model for simulating mD components within the radar return from BTs, considering the specific cases of precession and nutation for warheads, and tumbling for decoys. Two shapes for warheads are taken into account, namely cone and cone with fins, and three for decoys, which are cone, cylinder and sphere.

- Experimental validation of mathematical model of the radar return from BTs with micro-motions, by using scaled replica of targets of interest, a robotic manipulator for motions simulation and a Continuous Waveform (CW) radar.

- Design and testing different feature extraction approaches for discriminating between missile warheads, decoys and missile debris. Four approaches presented in (Persico et al., 2015, 2016a) are implemented into a classification framework based on the computation of the Cadence Velocity Diagram (CVD) from the acquired signals. The proposed approaches require different computational complexity and allow to discriminate efficiently between different BT motions and shapes, even in presence of high level of noise in radar measurements. The classification performance is assessed on both simulated data and in-home laboratory real data.

- Development of a novel framework designed for radar classification of BTs from a sequence of HRRPs within a single period of the main target rotational movement presented in (Persico et al., 2017b). The framework is based on the evaluation in sequence of the Inverse Radon Transform (IRT) and pseudo-Zernike (pZ) image moments, starting from the acquired HRRP frame. The extracted features provide efficient classification performance in different scenarios, being robust against radar measurement noise level, target motion initial phases and velocities. The classification performance is assessed on simulated data for wideband radar, considering a Stepped Frequency Waveform (SFW) radar, and a signal model for the radar return which takes into account two polarization, namely the vertical and the horizontal polarization.

- The precursory study of a novel space-borne PBR system orbiting in LEO for space debris population monitoring and early missile detection presented in (Kirkland et al., 2016; Persico et al., 2016b). The system configuration guarantees all the advantages provided by PBR, and allows to employ the enhancement for target detection given by Forward Scattering (FS). The performance of the proposed system is examined based on Radar Range Equation (RRE), considering the possible observation time of the target, according to transmitter, receiver and space object orbits.

1.4 Publications

Journal Papers

- Persico, A. R., Clemente, C., Gaglione, D., Ilioudis, C. V., Cao, J., Pallotta, L., Maio, A. D., Proudler, I., and Soraghan, J. J. (2017a). On Model, Algorithms, and Experiment for Micro-Doppler-Based Recognition of Ballistic Targets. *IEEE Transactions on Aerospace and Electronic Systems*, 53(3):1088–1108

Submitted Journal Papers

- Persico, A. R., Kirkland, P., Clemente, C., Vasile, M., and Soraghan, J. J. (2018b). Cubesat-based Passive Bistatic Radar for Space Situational Awareness: a Feasibility Study. *IEEE Transactions on Aerospace and Electronic Systems*. (accepted for being published)

- Persico, A. R., Ilioudis, C. V., Clemente, C., and Soraghan, J. J. (2018a). Novel Classification Algorithm for Ballistic Targets based on High Resolution Range Profile frame. *IEEE Transactions on Aerospace and Electronic Systems*. (under review)

- Gaglione, D., Clemente, C., Ilioudis, C. V., Persico, A. R., Proudler, I., Soraghan, J. J., and Farina, A. (2018). Waveform Design for Communicating Radar Systems Using Fractional Fourier Transform. *Digital Signal Processing*. (under review)

Conference Papers

- Persico, A. R., Clemente, C., Ilioudis, C., Gaglione, D., Cao, J., and Soraghan, J. (2015). Micro-Doppler Based Recognition of Ballistic Targets Using 2D Gabor Filters. In *2015 Sensor Signal Processing for Defence (SSPD)*, pages 1–5

- Özcan, M. B., Gürbüz, S. Z., Persico, A. R., Clemente, C., and Soraghan, J. (2016). Performance analysis of co-located and distributed MIMO radar for micro-Doppler classification. In *2016 European Radar Conference (EuRAD)*, pages 85–88

- Gaglione, D., Clemente, C., Ilioudis, C. V., Persico, A. R., Proudler, I. K., and Soraghan, J. J. (2016). Fractional Fourier Transform Based Co-Radar Waveform: Experimental Validation. In *2016 Sensor Signal Processing for Defence (SSPD)*, pages 1–5
- Persico, A. R., Clemente, C., Pallotta, L., Maio, A. D., and Soraghan, J. (2016a). Micro-Doppler classification of ballistic threats using Krawtchouk moments. In *2016 IEEE Radar Conference (RadarConf)*, pages 1–6
- Kirkland, P., Clemente, C., Persico, A. R., Vasile, M., and Soraghan, J. (2016). CubeSAT based passive bistatic radar for space debris detection and tracking. In *Stardust Final Conference on Asteroids and Space Debris*
- Persico, A. R., Ilioudis, C., Clemente, C., Brueggenwirth, S., Bieker, T., and Soraghan, J. (2016b). Ballistic Targets Discrimination based on High Resolution Range Profiles. In *11th IMA International Conference on Mathematics in Signal Processing*
- Persico, A. R., Ilioudis, C., Clemente, C., and Soraghan, J. (2017b). Novel Approach for Ballistic Targets Classification from HRRP Frame. In *2017 Sensor Signal Processing for Defence Conference (SSPD)*, pages 1–5

1.5 Thesis Organization

The remainder of the Thesis is divided into six chapters organised as follows:

Chapter 2 introduces the key concepts of radar systems, describing basic and advanced operational modes. In the second part of the chapter, the principal steps of target classification processing are discussed, introducing some of the most common approaches used for the extraction of information for target recognition. Specifically, the concept of mD effect in radar context is described in details. Following, the basic principles of radar processing for obtaining High Resolution Range Profiles (HRRPs) of a target are introduced, explaining the main issues in the presence of moving targets.

Chapter 3 provides an overview of the recent tools for the signature and features extraction used in radar target classification processing. Firstly, the concept of time-frequency analysis is introduced, with a detailed description of the commonly used time-frequency signal representations for Automatic Target Recognition (ATR). Then, the use of Radon transform (RT) and and its inverse function in radar image processing of a target is discussed. Following, an overview of recent techniques for image classification in radar context is presented, with particular focus on the challenge of BM classification from mD profile of the target.

Chapter 4 demonstrates the capability to distinguish efficiently between missile warheads and decoys by using information from different micro-motions exhibited during the mid-course phase. Specifically, evaluating the CVD from the radar measurement as mD based target signature, four different approaches for features extraction are presented. The reliability of the proposed features are tested on both simulated and in-home laboratory data, providing a detailed description of both the mathematical model for the radar return and the experiment set up.

Chapter 5 presents a novel framework for the classification of BTs from a sequence of HRRPs from the target. The framework is based on the computation of the IRT in combination with pZ moments, in order to extract reliable features from the pseudo-periodic range migrations of the principal scattering points observed within a HRRP frame due to micro-motions. The efficiency of the proposed framework is tested on simulated data by considering a mathematical model for the complex coefficient of principal scatterers which takes into consideration two possible polarizations for the radar waveform, namely vertical and horizontal polarization.

Chapter 6 presents a novel space-borne PBR system for BMD and SSA. The system configuration is discussed, focusing on the particular advantages guaranteed by PBRs in the FS configuration. The performance of the proposed system in terms of minimum size of detectable target is provided, with an analysis of the possible target observation time depending on transmitter, receiver and target specific orbits.

Chapter 7 presents a summary and conclusions of the Thesis, providing an overview of possible future directions of this research work.

The appendix provides the mathematical expressions from (Ross and DIV., 1969) of the complex coefficients of the principal scattering points for the several target shapes used in this Thesis as target of interest in Chapter 5.

Chapter 2

Radar Systems

2.1 Introduction

The word *RADAR* was coined in 1940 by the United States Navy as an acronym for RAdio Detection And Ranging for indicating a system able to detect a target and determine its range. The development of modern technology has lead to expansion of radar system capabilities, from the estimation of more information on the target, such as its shape, size, and trajectory, to the more complex target imaging (such as Synthetic Aperture Radar (SAR) image) and recognition. Modern systems apply these radar functions in a wide range of applications, from the traditional military surveillance and target identification to collision avoidance, Earth resources monitoring, and many others, expanding the application of radars even in civilian and commercial sectors (Levanon and Mozeson, 2004).
In this Chapter, the basic concepts of radar systems and their different configurations and functional modes are described, highlighting those particularly relevant to the scope of this thesis. A short discussion on the principal parameters and aspects that affect radar capabilities and performance are presented in Section 2.3, in order to identify the trade-offs and the assets, with particular focus on the target Radar Cross Section (RCS). Section 2.4 provides a brief description of the main steps of target classification process. Moreover, the effect of micro-Doppler (mD) in radar return is discussed in Section 2.5, representing a useful information which can be extracted for target classification. Finally, in Section 2.6 one of the most advanced radar techniques for achieving a target High Resolution Range Profile (HRRP) is discussed, analysing how target movements affect this specific signature for target classification.

2.2 Basic Concepts

A radar is an electrical system that generates and transmits Electromagnetic (EM) signals toward a particular region of interest in order to detect objects in that region. Although a radar system may be significantly simple or more complex, the major subsystems must include a transmitter (dedicated or transmitter of opportunity), one or more antennas, a receiver, and a signal processor. The basic operational process can be summarized in four steps: transmission of a EM radar signal; signal propagation through the free space; reflection of the signal from the target, and reception of the target echo. Finally, the received signal may be processed, in order to generate the desired information (Richards et al., 2010). The measurement of the round-trip propagation time, t_0, for the signal to travel from the radar to the target and back, allows to estimate the distance of the target from the radar (range). Specifically, the target range, R, can be evaluated as

$$R = \frac{c\,t_0}{2} \tag{2.1}$$

where c is the EM wave propagation speed in vacuum, which is almost the same in air as in a vacuum and is constant with the wavelength of the signal.

2.2.1 Monostatic And Bistatic Configurations

Radar systems can be characterized by two basic configurations: monostatic and bistatic.

In the monostatic configuration, the radar uses the same antenna (or co-located antennas) to perform the transmit and receive radar functions. When one antenna is used, a transmit/receive (T/R) device which connects transmitter and receiver to the antenna must be used in order to provide isolation between the transmitter and receiver to protect the sensitive receiver components from the high-powered transmit signal (Richards et al., 2010). Fig. 2.1 shows a representation of the radar process in the monostatic configuration.

In a bistatic configuration, different antennas are dedicated to the transmitter and receiver. However, this condition is not enough to distinguish between monostatic or bistatic radars, because the configuration definition depends on the transmitter and the receiver locations. An unequivocal specific for the distance between the transmitter and receiver sites of a bistatic system is not presented in literature. Attempts have been made to quantify this separation. Specifically, in cite (Def, 2008) the system is considered to be bistatic if there is sufficient separation between

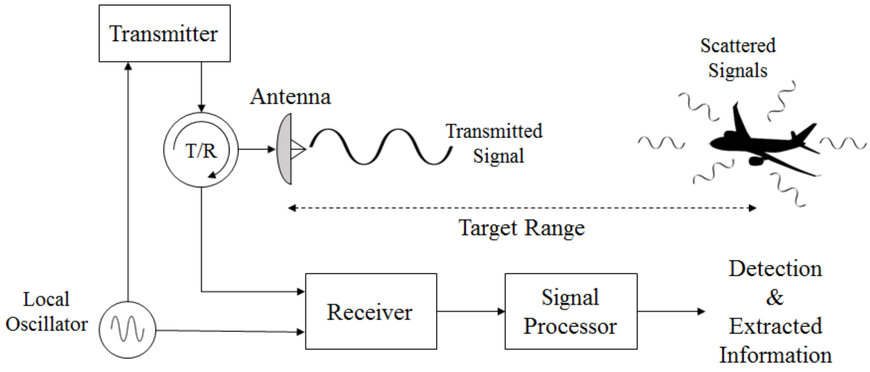

Fig. 2.1 The basic operational process of a radar system.

the transmitter and receiver antennas (comparable to the expected target distance) such that the angles or ranges to the target are sufficiently different. If the two antennas are very close, then the system is considered to be quasi-monostatic. Bistatic Radars (BRs) are further divided into two categories: the *hitchhiker*, when the transmitter is a radar, and the *Passive Bistatic Radar* (PBR) which exploits RF energy transmitted by other non-cooperative systems (broadcast, communications, or radio-navigation signal) to perform radar tasks (Melvin and Scheer, 2014). The angle defined by the transmitter-target and receiver-target Line Of Sight (LOS) is known as bistatic angle, β (see Figure 2.2). When β is in

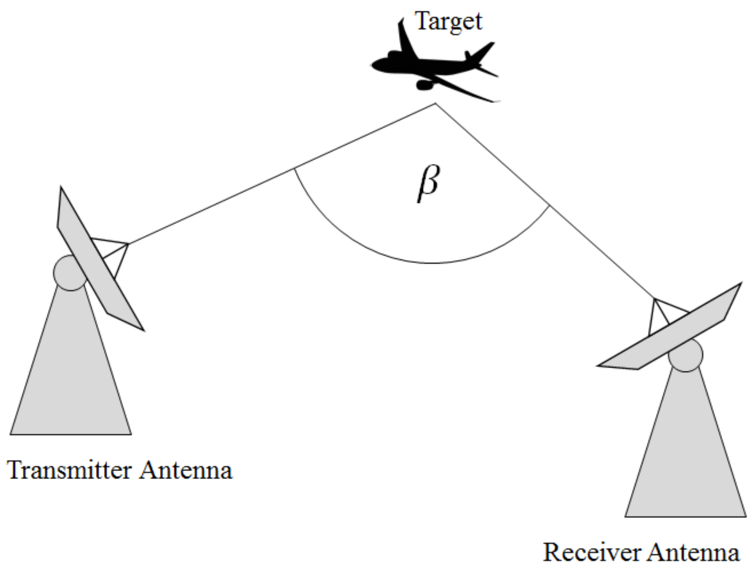

Fig. 2.2 Radar system in bistatic configuration.

a neighbourhood of 180°, the principal scattering phenomenon from the target is in the forward direction. In this specific case, the bistatic configuration is called Forward Scattering (FS) configuration (Willis, 2005).

2.2.2 Continuous Wave and Pulsed Wave Radars

Radar systems can transmit two different classes of EM waveform: Continuous Wave (CW) and Pulsed Wave.
For CW Radar, both the transmitter and the receiver are continually operating, usually without interruption. This class of waveform is often used in the bistatic configuration, taking advantages of the T/R isolation. As monostatic radars, the CW systems generally works in relative low power for short-range applications, since the isolation between the transmitter and receiver is not perfectly guaranteed. Generally, CW radars cannot measure the delays of the echoes from the target since they are continuously transmitting. However, it is possible to estimate the target range by changing some characteristics of the transmitted CW over the time. In this way a timing mark is defined on the EM waves (Richards et al., 2010). One of the most used technique consist of changing the waveform carrier frequency over the time, known as Frequency Modulated (FM) CW.
Pulsed radars transmit a sequence of pulses with a finite duration and separated by time intervals. The receiver is switched off during the transmission of the single pulse, while during the interval in between the transmission of two sequential pulses the transmitter is switched off and the receiver is on in order to acquire the target return. The time difference between two consequent transmission instants is known as Pulse Repetition Interval (PRI). When a target is located at a distance from the radar such that the round-trip propagation time is greater than the PRI, the target echo will not return before of the next pulse transmission, leading to an ambiguity in the range estimation. Hence, the maximum unambiguous range is

$$R_u = \frac{c\,T_p}{2} \tag{2.2}$$

where T_p is the PRI. A graphical representation of radar range ambiguity is shown in Fig. 2.3.
The range resolution represents the radar capability to distinguish two (or more) different targets of the same dimension, which are closely located. It is expressed in terms of minimum relative distance between two targets with respect to the radar such that the returns from different targets are acquired separated in time. Considering the transmission of a simple unmodulated pulse, the range resolution

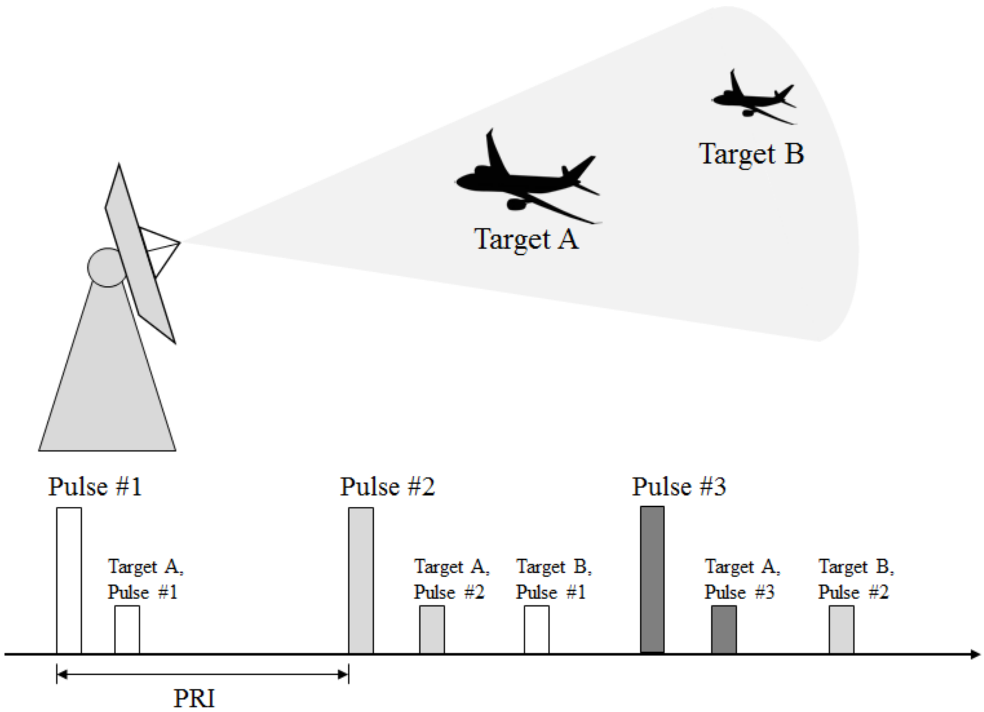

Fig. 2.3 Pulsed radar waveform and radar range ambiguity.

is proportional to the pulse duration, τ, as

$$R_{\Delta} = \frac{c\tau}{2} \tag{2.3}$$

The duty cycle represents the ratio between the pulse duration and the PRI, as follows

$$d_t = \frac{\tau}{T_p} = \tau\, f_p \tag{2.4}$$

with f_p the Pulse Repetition Frequency (PRF), which is the reciprocal of PRI.

2.3 Radar Range Equation

The principal functions of radar systems are three, namely search, track, and recognition (Tait, 2005). The radar performance is influenced by the power of the received signal from the target of interest and by the power of interference factors. The interference factors can be represented by noise, clutter, or jamming. Specifically, clutter is contributions to the radar received signal from undesired targets and other surfaces on the ground and in the atmosphere, while jamming is the intentional emission of RF signals to interfere with the operation of a radar by saturating its receiver with noise or false information. The ratio between the target return and the noise power is called Signal-to-Noise Ratio (SNR), while in the case of clutter signal as interfering signal, the ratio is called Signal-to-Clutter Ratio (SCR). The ratio between the target echo power and the power of total interfering signals is known as the Signal-to-Noise Ratio (SNR) (Richards et al., 2010).

The *Radar Range Equation* (RRE) is mathematical tool used for designing the system with the aim of guaranteeing the required SNR to perform the radar function satisfactorily.

Considering a system transmitting a waveform using an antenna with an isotropic or omnidirectional radiation pattern, the incident power density at the range R would be the total power divided by the surface area of a sphere whose radius is equal to R, as follows

$$Q_i = \frac{P_t}{4\pi R^2} \tag{2.5}$$

where P_t is the peek power of the transmitted EM wave. Generally, radars transmit the EM wave into a finite angular sector using antennas with a directional beam pattern. The power gain obtained using directional antennas is called *antenna gain*. Considering the antenna gain in transmission, G_t, the product $P_t G_t$, known as Effective Isotropic Radiated Power (EIRP), represents the power of an equivalent isotropic radiator which generates the same transmitted flux in all directions. A portion of the incident power on a target is reflected towards the radar. The Radar Cross Section (RCS), σ, represents the target area which produces energy scattered in the direction of the receiver, and it is measured in m^2 (Skolnik, 2001). The received power from a target in free space conditions is given by

$$P_r = \left(\frac{P_t G_t}{4\pi R^2}\right)\left(\frac{\sigma}{4\pi R^2}\right)\frac{A_{eff}}{L_s} \tag{2.6}$$

where A_{eff} is the receiver antenna effective area and L_s (≥ 1) is a loss factor (which includes transmitter losses, propagation losses, receiver or plumbing losses, beam-shape losses and signal processing losses) (Richards et al., 2010). The antenna effective area can be written in terms of the receiver antenna gain, G_r, as follows

$$A_{eff} = G_r \frac{\lambda^2}{4\pi} \tag{2.7}$$

where λ is the transmitted signal wavelength. Hence, by substituting (2.7) into (2.6), it follows

$$P_r = \frac{P_t G_t G_r \sigma \lambda^2}{(4\pi)^3 R^4 L_s} \tag{2.8}$$

The power spectral density of thermal noise is essentially constant over all radar frequencies. However, only the noise signals within the receiver bandwidth, B_r, affects the radar performance. Then, the receiver thermal noise power, P_n, is given by

$$P_n = k\mathtt{T_r}B_r \tag{2.9}$$

where k is the Boltzmann's constant, and $\mathtt{T_r}$ is the receiver noise temperature. The latter is obtained by the sum of the antenna noise temperature, $\mathtt{T_A}$, and the composite temperature of other components, $\mathtt{T_{comp}}$:

$$\mathtt{T_r} = \mathtt{T_A} + \mathtt{T_{comp}} \tag{2.10}$$

It is possible to express the receiver noise power through the reference temperature, $\mathtt{T_0}$, (generally equal to 290 K) and the receiver noise figure, F (Skolnik, 2001). The receiver noise figure of a receiver represents the ratio between the noise output of the receiver and the noise output of an ideal receiver, which is due to external sources only (Tait, 2005). It follows

$$P_n = k\mathtt{T_0}B_r F = k\mathtt{T_0}B_r\left(1 + \frac{\mathtt{T_n}}{\mathtt{T_0}}\right) \tag{2.11}$$

with $\mathtt{T_n}$ the effective noise temperature. Finally, the SNR for a single radar pulse is given by

$$\text{SNR} = \frac{P_r}{P_n} = \frac{P_t G_t G_r \sigma \lambda^2}{(4\pi)^3 R^4 k\mathtt{T_0} B_r F L_s} \tag{2.12}$$

In the case of bistatic radar systems, the RRE is given by (Willis, 2005)

$$\text{SNR} = \frac{P_t G_t G_r \sigma \lambda^2}{(4\pi)^3 R_t^2 R_r^2 k\mathtt{T_0} B_r F L_s} \tag{2.13}$$

where R_t and R_r are the target distances from the transmitter and receiver.

2.3.1 Processing Gain

In many radar applications, very high values of SNR may be required, in order to improve the ability to detect a target in the presence of noise. For this purpose, different processing approaches can be used.

Pulse Compression: *Pulse compression* represents one of most common techniques used to achieve a higher SNR. For an simple unmodulated pulse, the bandwidth is inversely proportional to the pulse length, T. For this reason, it is worth noting from (2.3) and (2.12) that the choice of pulse duration affects a trade-off among the range resolution and the achievable SNR. The pulse compression is an intra-pulse modulation (phase or frequency) which allows to maintain the average transmission power by incorporating a wider bandwidth within the pulse without affecting its duration. In order to take advantage of pulse compression, a appropriate filter is applied to the target echo. Considering the transmission of an arbitrary waveform, $s_{tx}(t)$, defined over the time interval $[0, \tau]$, the received echo, $s_{tx}(t)$, from the target is a scaled and delayed replica of $s_{tx}(t)$ embedded in additive white noise, as follows

$$s_{rx}(t) = \mathrm{a}\, e^{j\phi} s_{tx}(t - t_o) + w(t) \tag{2.14}$$

where 'a' is the amplitude of received signal, and ϕ the phase rotation due to relative motion between the radar and the target. The filter which maximizes the SNR depends on the transmitted waveform, and it is known as matched filter. Its impulse response is a time-reversed and complex conjugated copy of the transmitted waveform

$$h_{\mathrm{MF}}(t) = \mathrm{b}\, s^*_{tx}(-t) \tag{2.15}$$

where b is an arbitrary scale factor, commonly set to 1. The range resolution for a pulse compressed radar signal is expressed in terms of transmitted bandwidth as follows

$$R_\Delta = \frac{c}{2B} \tag{2.16}$$

The maximum signal processing gain, G_{sp}, guaranteed by the matched filter at the instant t_0 is given by the product between the pulse duration and modulated bandwidth, B_m. Therefore, the output SNR from the matched filter is

$$\mathrm{SNR}_{out} = \frac{P_t G_t G_r \sigma \lambda^2}{(4\pi)^3 R^4 k \mathtt{T}_0 B_r F L_s} G_{sp} = \frac{P_t G_t G_r \sigma \lambda^2}{(4\pi)^3 R^4 k \mathtt{T}_0 B_r F L_s} B_m \tau \tag{2.17}$$

For a pulse compression system the matched filter condition is valid for a moving target only compensating the phase rotation in the processing, otherwise a Doppler mismatch loss is usually experienced (Richards et al., 2010).

Pulse Integration: Another common signal processing technique for achieving higher SNR is the integration of the received target echoes from the transmission of a finite number of pulses (known as burst). The received signals can be integrated coherently or non-coherently.
The coherent processing employs both the amplitude and the phase information of received signals in order to sum up in phase all the target contributions from each transmitted pulses. When both the radar system and the target are stationary, all the target returns would be in phase. Otherwise, the relative motion between the radar and the target leads to a phase rotation (or frequency shift), well known as Doppler effect (Chen et al., 2006). Specifically, the Doppler frequency shift represents the difference between the frequencies of the transmitted and the received wave. The latter is approximately given by:

$$f_D = \frac{2v_r}{\lambda} \tag{2.18}$$

with v_r the velocity component along the radial or LOS between the radar and the target. In the case of relative moving target, it is necessary to compensate the phase rotation before summing up all the target returns from each pulses, in order to ensure an improved SNR. One of the most used technique for computing the coherent sum of the radar returns in presence of moving target is the Fast Fourier transform (FFT) processing (or *Doppler processing*). The SNR resulting from the coherent integration is

$$\mathrm{SNR}_c(n_p) = n_p \, \mathrm{SNR}(1) \tag{2.19}$$

with SNR(1) the SNR obtained with a single transmitted pulse. The non-coherent integration averages only the amplitude information of the echoes from the transmitted pulses. The gain obtained by non-coherent integration of n_p pulses $\mathrm{SNR}_{nc}(n_p)$ is not defined unequivocally, but in most of the cases is within the interval $\left[\sqrt{n_p}\,\mathrm{SNR}(1), n_p\,\mathrm{SNR}(1)\right]$ (Richards et al., 2010).

2.3.2 Target RCS

The RCS of a target represents its ability to reflect the incident transmitted power towards the receiver. It is defined as the ratio between the power density intercepted by the target and the power density scattered towards the radar. Three different scattering regions from the target are defined according to the radar wavelength and target dimensions. The *Rayleigh region* occurs when the wavelength is greater than the target dimension, the *resonance region* when they are comparable and the *optical region* when the wavelength is very small with respect to target sizes (Skolnik, 2001). Fig. 2.4 from (Richards et al., 2010) shows the RCS of a sphere normalized with respect to the sphere area, on varying the ratio between the sphere radius and the EM wavelength. In the Rayleigh region the RCS is proportional to the waveform carrier frequency, f_0. In the resonance region the RCS oscillates as a function of the carrier frequency, with a maximum value obtained for sphere radius equal to the wavelength. Finally, in the optical region the RCS tend to the physical area of the sphere as the carrier frequency increases (Skolnik, 2001).

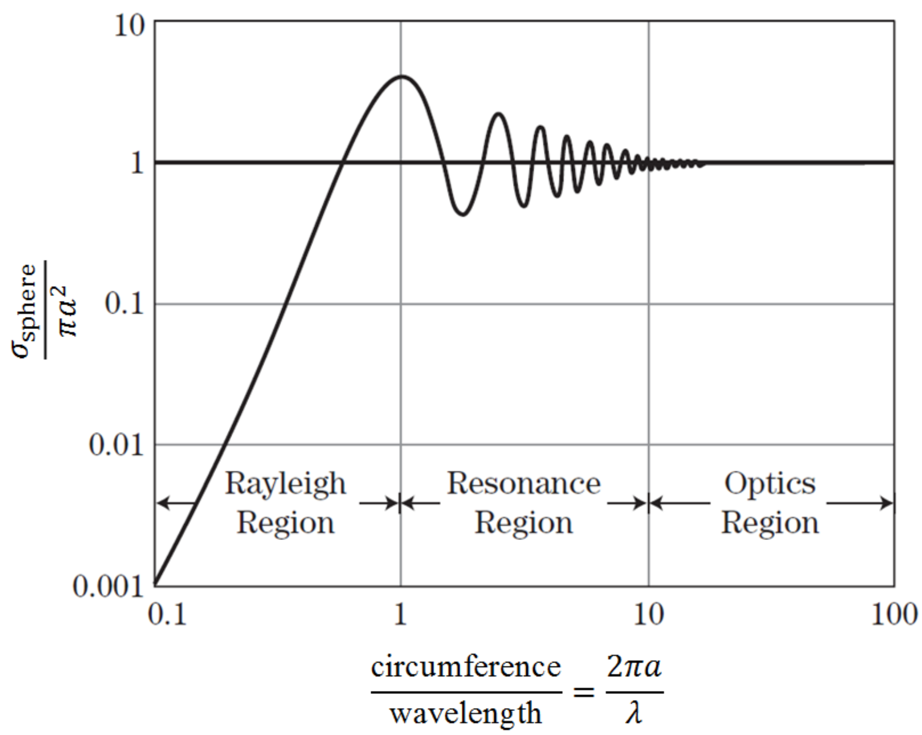

Fig. 2.4 RCS of a sphere with radius a on varying the wavelength λ, from (Richards et al., 2010).

According to the theory of diffraction at high frequency (short wavelength), the signal scattered by a target may be approximated by the sum of localized sources, represented by the principal scattering points on the object. Specifically, the RCS of a target can be written as (Ross and DIV., 1969)

$$\sigma(f_0, \alpha) = \left| \sum_{i=1}^{N_p} \sqrt{\sigma_i}(f_0, \alpha) e^{j\phi_i(f_0,\alpha)} \right|^2 \tag{2.20}$$

where $\sqrt{\sigma_i}(\cdot)e^{j\phi_i(\cdot)}$ is the complex scattering coefficient of the i-th local source, with $i = 1, \cdots, N_p$, where N_p is the total number of scatterers, f_0 is the signal carrier frequency, and α is the aspect angle defined by target orientation vector and the direction of incident EM wave. The phase of scattered field is

$$\phi(f_0, \alpha) = \tan^{-1} \left(\frac{\sum_{i=1}^{N_p} \sqrt{\sigma_i}(f_0, \alpha) \sin(\phi_i(f_0, \alpha))}{\sum_{i=1}^{N_p} \sqrt{\sigma_i}(f_0, \alpha) \cos(\phi_i(f_0, \alpha))} \right) \tag{2.21}$$

Real targets do not reflect the incident power uniformly in all directions, indeed the scattered EM field depends on its particular shape and sizes, hence on the disposition in the space of target scatterers (Ross and DIV., 1969).

RCS fluctuation: Although many techniques for predicting the RCS of several targets are present in the literature, e.g. geometrical theory of diffraction, individual scattering center method, and caustic correction method (Singh, 2004), the scattering phenomenon depends on a large number of factors e.g. the target geometry, the aspect angle, the altitude with respect to radar antenna and atmosphere factors, which lead to uncontrolled scintillation of the RCS. Therefore, the target RCS is usually expressed as a random variable in order to take into account these fluctuation for signal modelling.

The mathematician Peter Swerling introduced the Swerling models in 1954 in order to describe the statistical properties of the RCS of a complex target. Specifically, there are four different Swerling models, which represent the RCS through the chi-square probability density function with $2m$ degrees of freedom (Swerling, 1997)

$$\mathcal{P}(\sigma) = \frac{m}{(m-1)!\sigma_{avg}} \left(\frac{m\sigma}{\sigma_{avg}} \right)^{m-1} e^{-\frac{m\sigma}{\sigma_{avg}}} \tag{2.22}$$

where σ_{avg} is the average over all target RCS values. In Case 1, known as *slow fluctuation*, the RCS for each received pulse during an entire radar scan is constant, but independent from scan-to-scan. The RCS is modelled by an exponential function, obtained from (2.22) for $m = 1$. In the Case 2, known as *fast fluctuation*, the RCS is modelled by the exponential function as in Case 1, but the value of the fluctuations are independent from pulse to pulse. In Case 3 the RCS is assumed constant during a scan and independent from scan-to-scan, as for Case 1. Moreover, the probability function for the RCS is Chi-square of degree 4, obtained from (2.22) for $m = 2$. In Case 4, the probability function is the same as in Case 3, but the fluctuation is pulse to pulse. It is worth noting that other probability density functions can be generally used in specific cases. Through some experimental analysis it has been shown in (Swerling, 1997) that the RCS of missiles shows fluctuation which can be well represented by a log-normal random variable (Liu et al., 2011). For all this cases, the RCS parameter in the RRE is substituted by σ_{avg}, and a *fluctuation loss* parameter is taken into account (Skolnik, 2001).

FSRCS: In the specific case of target with RCS very small, the use of the Forward Scattering (FS) radar may provide higher values of SNR with respect to the other configurations (Abdullah and Ismail, 2006; Willis, 2005). For this reason, FS radars are very attractive for the detection of small objects. This configuration guarantees a relative RCS enhancement since the FS depends only on the area and shape of the target's silhouette. The reason for this enhancement can be found in Babinet's principle (Willis, 2005), which affirms that, in optics, a perfect absorbing target diffracts the same electromagnetic wave as an aperture of the same shape and area A of the target (see Fig. 2.5). Two diffraction types

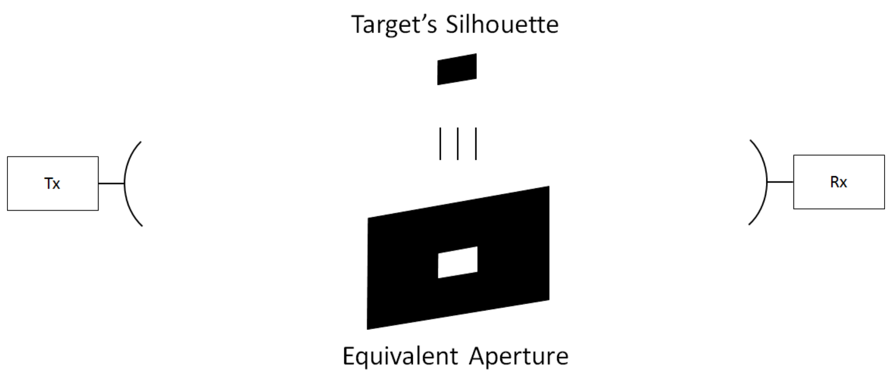

Fig. 2.5 Babinet's model for the forward-scatter case with $\beta = 180°$.

are possible: Fraunhofer diffraction and Fresnel diffraction. In the former case, the target is electromagnetically far from both transmitter and receiver, while in the latter case, the target is close to one of the two. Considering the following coefficients

$$F_t = \frac{d^2}{R_t \lambda} \qquad\qquad F_r = \frac{d^2}{R_r \lambda}, \tag{2.23}$$

where d is the greater dimension of the object, the Fraunhofer diffraction occurs when

$$F_t << 1 \qquad\qquad F_r << 1. \tag{2.24}$$

When these conditions are verified, and the object dimensions are greater than the wavelength (thus optics conditions occur) the FSRCS can be written as

$$\sigma_{FS} = \frac{4\pi A^2}{\lambda^2} = G_{FS} A, \tag{2.25}$$

where G_{FS} represents the peak antenna gain of uniformly illuminated aperture whose area is equal to A. Then within the Fraunhofer zone, the RCS, in the FS case, increases with the target section. When the bistatic angle is smaller than 180°, the forward-scatter RCS rolls off from σ_{FS}. The roll-off is approximated by treating the shadow area, A, as a uniformly illuminated antenna aperture (Willis, 2005).

FS radars usually require reasonably simple hardware and lower power consumption, but they have a limited operational area, such that they work properly for bistatic angle within a narrow interval around 180°. FS radar represents a valid solution for detecting stealth targets since the FSRCS is practically independent from the radar absorbing material (Gao and Yan, 2006). One of the critical drawbacks of FS radar is that this system does not allow one to estimate directly the target range. Nevertheless the absence of range resolution is compensated by the advantage of absence of signal fluctuation because of the target's natural swinging, which represents a limit for coherent signal processing time in conventional radar. Furthermore, the FS radar allows one to improve the power budget by employing a long coherent integration interval.

2.4 Target Classification Basics

Introduced for detecting enemy aircraft during World War II, radar technology has progressed trough the years providing a level of target recognition in addition to the simple detection. In the initial stages of target recognition, a human operator was trained for recognizing an audible representation of received signal from the target illuminated by the radar. Nowadays, the modern technologies and sensors provide high resolution data encouraging the development of automated recognition methods in order to improve the recognition capabilities and reduce the operator workload.

Radar target classification process comprises four fundamental steps, represented in the block scheme in Fig. 2.6. The initial step comprises the radar measurement,

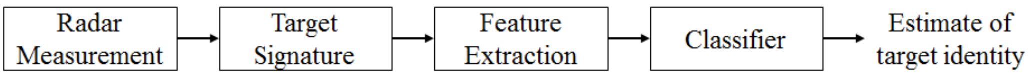

Fig. 2.6 Classification processing block scheme.

by acquiring the signal reflections from the target. The received target echo is then processed for extracting the target signature, which contains the information used for its identification. Following, a set of features is extracted from the target signature by a mathematical process, and given as input to a classifier in order to estimate the target class. Classifiers are mathematical techniques designed to compare the extracted features within a database, which contains the information of all the targets of interest.

In order to perform target recognition, it is important to have a prior knowledge of which are the target to be recognized and, eventually, the possible objects in the scene which are not of interest. The database can be assembled by using a mathematical model of the signatures (hence features) of targets of interest, or by measurements from scaled models of these or, whereas it is possible, by measurements from real targets. In some cases it is possible to assembly the database by a combination of these three methods. A database has to contain reference signatures of all targets of potential interest at all possible radar aspect angles and under different conditions of the scenario. The complexity and the dimension of the database depends on the classification processing and the required features.

The classification performance can be characterized by the probabilities of correct and wrong assignment. The effectiveness of the classification algorithm in terms of these probabilities is affected by the quality of radar measurement, as well as the quality of the mathematical model and the targets similarities (Tait, 2005).

2.4.1 Target Signature Extraction

The aim of target signature extraction process is to obtain an arrays of values for the extraction of target features trough mathematical operations. Target signature may be a distribution function of the radar measurement, e.g. time, frequency or space distribution, which emphasizes target characteristics used then for the recognition process. The transmitted radar waveform has to be designed in order to get high quality target signature compatible with the classification algorithm and reference signature database, guaranteeing satisfactory performance. The radar acquisition is usually pre-processed to get noise reduction and clutter mitigation, which may affects the measurement. Once that the target is detected (and tracked in case of moving target) from the "cleaned" data, the processing continues with the signature extraction. The signature data are usually normalised in order to provide robustness level required for measurements performed under different conditions of sensitivity. Several approaches have been developed for target signature extraction for wide range of applications. The most suitable approach for each application is chosen according to the designed radar, the transmitted waveform and the target characteristics e.g. motions or material composition (Tait, 2005).

2.4.2 Target Feature Extraction

Any classification challenge requires an accurate analysis on the possible targets and which signature can emphasize their difference. Another critical step is the selection of a feature set which can be used to discriminate different targets. Feature extraction processes are mathematical tools used for reducing the dimensionality of target signature and increasing robustness. The features can be either physical parameters, e.g. target dimension, RCS and velocity, or a set of values which synthesize the extracted signature data, e.g. image moments. One of the most important aspect which affects the selection process is the sensitivity of the features with respect to the variations of target parameters e.g. dimension or the aspect angle. In particular, the features have to be chosen in order to minimize the feature space of each class, and maximize the distances between the spaces of different classes. In particular, the main aim is to reduce the feature spaces overlap, in order to achieve better performance. The feature selection affects the complexity of the classifier. In case the feature space of each class are not significant separated, it is necessary to use probabilistic methods and lager number of features in order to perform the target classification properly (Richards et al., 2013; Tait, 2005).

2.5 Micro-Doppler Effect in Radar

In many classification challenges, objects with similar shapes and sizes may be distinguished observing their motions with respect the radar system. As described in Section 2.3.1, when a target is moving the Doppler effect occurs such as the radar return is shifted in the frequency domain with respect to the transmitted signal. A secondary motion of the target, or of any its structural component, in addition to the bulk motion introduces an additional frequency modulation which generates side bands around the main Doppler shift. This secondary modulation is known in literature as *micro-Doppler* (mD) effect (Chen et al., 2006, 2014), and the term *micro-motion* is used to refer to the additional target motions, e.g. rotation or vibration.

The concept of mD effect was originally presented in a coherent laser system, with the specific aim of measuring the kinematic properties of a target, e.g. the rate and the displacement of a vibration. Laser Detection and Ranging (LADAR) systems transmit EWs at optical frequencies being very sensitive to phase variations of received signal, such that even vibration with very small rate and micro displacement can be easily observed. Although even in coherent radar the variations in range cause a phase change in the returned signal from a target, the mD effect is harder to observe in radar systems due to longer wavelengths. However, in case the target micro-motion has rate and displacement high enough, the mD effect may be still observable. The mD modulation may represent a distinctive signature for a target containing information on its operational mode and structural components e.g. helicopter rotor blades or missile wings.

Generally, the motion of a rigid body is given by a combination of translations and rotations. In order to describe the effect of target motion with respect the radar three coordinates systems are considered: the radar coordinates system ($\hat{U}$, $\hat{V}$, $\hat{W}$), centred on the radar; the reference coordinates system ($\hat{X}$, $\hat{Y}$, $\hat{Z}$), which is parallel to the previous one and whose origin is the Mass Centre (MC) of the target; the local coordinates system ($\hat{x}$, $\hat{y}$, $\hat{z}$) such that the axis $\hat{\boldsymbol{z}}$ corresponds with the symmetry axis of target (Hongwei et al., 2010). Fig. 2.7 illustrates the three reference systems, where $\angle \mathrm{El}_{\mathrm{MC}}$ and $\angle \mathrm{Az}_{\mathrm{MC}}$ are the elevation and azimuth angles of the LOS between the radar and the MC of the target with respect the

radar coordinates system.
Without loss of generality and neglecting the envelope of the transmitted signal, it is assumed that the radar transmits a sinusoidal signal as follows

$$s_{tx}(t) = \exp(j2\pi f_0 t) \tag{2.26}$$

where f_0 is the radar carrier frequency. The generic received signal from a target can be written as

$$s_{rx}(t) = \sum_{i=0}^{N_p-1} \sqrt{\sigma}_i(t) \exp\left(j2\pi f_0 \left[t - \frac{2t_i(t)}{c}\right]\right) \tag{2.27}$$

where N_p is the number of scattering points, $t_i(t)$ and $\sigma_i(t)$ are the delay of propagation and the scattering coefficient of the i-th scatterer, respectively. An expression of the propagation delay for the i-th generic point is given by

$$t_i(t) = \frac{2\mathrm{r}_i(t)}{c} \tag{2.28}$$

where $\mathrm{r}_i(t)$ is the distance between the radar and the considered point. The distance $\mathrm{r}_i(t)$ is the norm of the position vector $\boldsymbol{r}_i^{radar}$, i.e.

$$\mathrm{r}_i(t) = \|\boldsymbol{r}_i^{radar}\| = \|\boldsymbol{r}_{MC}^{radar} + \boldsymbol{v}t + \boldsymbol{r}_i(t)\| \tag{2.29}$$

where $\boldsymbol{r}_{MC}^{radar}$ is the initial position vector of the MC with respect to the system ($\hat{U}$, $\hat{V}$, $\hat{W}$), $\boldsymbol{v}$ is the bulk motion velocity of the target and $\boldsymbol{r}_i(t)$ is the position vector of i-th scattering point with respect to the ($\hat{X}$, $\hat{Y}$, $\hat{Z}$) system. Neglecting

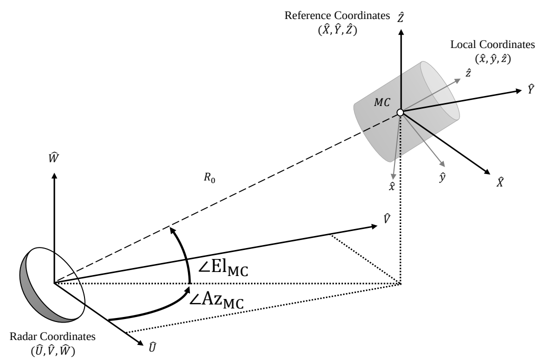

Fig. 2.7 Geometry for radar and target with micro-motions.

the time dependence for conciseness, $\boldsymbol{r}_i$ can be written as the following column vector

$$\boldsymbol{r}_i = \boldsymbol{T}_m \boldsymbol{R}_0 \left(\boldsymbol{r}_i^{local} - \boldsymbol{r}_{MC}^{local}\right) \tag{2.30}$$

where $\boldsymbol{R}_0$ is the Euler matrix that sets the position of the target with respect to the second system $(\hat{X}, \hat{Y}, \hat{Z})$ at the initial time instant, $\boldsymbol{T}_m = \boldsymbol{T}_m(t)$ is the matrix depending on the micro-motions made by the object, while $\boldsymbol{r}_i^{local}$ and $\boldsymbol{r}_{MC}^{local}$ are respectively the positions in the local system of the i-th scattering point and the object MC (Chen et al., 2014; Hongwei et al., 2010; Zakeri et al., 2004). It is worth noting that in case the centre of the local coordinates system $(\hat{x}, \hat{y}, \hat{z})$ is centred in the target MC, the $\boldsymbol{r}_{MC}^{local}$ coincides with the origin of the local coordinates system (as shown in Fig. 2.7).

The Doppler shift of the signal contribution of the i-th scatterer is given by

$$\begin{aligned} f_{D_i} &= \frac{2}{\lambda}\frac{d}{dt}\mathrm{r}_i = \frac{2}{\lambda}\frac{1}{2\mathrm{r}_i}\frac{d}{dt}\left[\boldsymbol{r}_{MC}^{radar} + \boldsymbol{v}t + \boldsymbol{r}_i\right]\left[\boldsymbol{r}_{MC}^{radar} + \boldsymbol{v}t + \boldsymbol{r}_i\right]^T \\ &= \frac{2}{\lambda}\left[\boldsymbol{v} + \frac{d}{dt}\boldsymbol{r}_i\right]^T \boldsymbol{n} \end{aligned} \tag{2.31}$$

where $(\cdot)^T$ is the transpose operator, and $\boldsymbol{n}$ is the unit direction of the vector $\boldsymbol{r}_i$, given by

$$\boldsymbol{n} = \frac{\boldsymbol{r}_{MC}^{radar} + \boldsymbol{v}t + \boldsymbol{r}_i}{\|\boldsymbol{r}_{MC}^{radar} + \boldsymbol{v}t + \boldsymbol{r}_i\|} \tag{2.32}$$

When the target is at relative long distance, such that

$$\|\boldsymbol{r}_{MC}^{radar}\| >> \|\boldsymbol{v}t + \boldsymbol{r}_i\| \tag{2.33}$$

then, $\boldsymbol{n}$ can be approximated as follow

$$\boldsymbol{n} \approx \frac{\boldsymbol{r}_{MC}^{radar}}{\|\boldsymbol{r}_{MC}^{radar}\|} \tag{2.34}$$

which is the direction of radar LOS. Hence, from (2.31) the Doppler shift can be expressed as the sum of two contributions: the first given by the main bulk motion, and the second dependent on target micro motion, as follows

$$f_{D_i} \approx \frac{2}{\lambda}\left[\boldsymbol{v}\right]_{radial} + \frac{2}{\lambda}\left[\frac{d}{dt}\boldsymbol{r}_i\right]_{radial} = f_{bD} + f_{mD_i} \tag{2.35}$$

where

$$f_{mD_i} = \frac{2}{\lambda}\left[\frac{d}{dt}\boldsymbol{r}_i\right]_{radial} \tag{2.36}$$

The knowledge of the micro-motion matrix $\boldsymbol{T}_m$, and of the positions and the coefficients of the principal scattering points allows to evaluate the mD profile of a target, useful for modelling the expected radar return. In this way, the database for a classification algorithm may be preliminary created on simulated data, or a model-based classification algorithm may be designed.

2.6 High Resolution Range Profile

High-Resolution Range Profile (HRRP) is a 1-Dimensional (1D) signature of an object which can be used for target recognition of airborne, ground, sea and even ballistic missile targets, reducing the complexity of classification algorithm with respect to using a 2D ISAR image (Hu and Zhu, 1997; Tait, 2005). It represents a time domain response of the target to a HRR radar pulse, which contains information on the target shape and dimensions (Tait, 2005). HRRPs can be either used as feature vectors input to a classifier, or processed to extract compressed feature vectors, according to the specific classification challenge. It is possible to extract features for the classification process directly from the HRRP analysis, such as the length of target, the amplitude of maximum scatterer and geometrical moments, or though transforms for getting robustness with respect to some parameters, such as by Mellin transforming utilized to circumvent scale-variance in HRRP caused by changes of target aspect angle (Hu and Zhu, 1997). In radar surveillance applications, Stepped Frequency Waveforms (SFWs) are generally used in order to achieve HRRP of a target increasing the system bandwidth. Specifically, SFWs comprise a sequence of N narrowband sub-pulses, known as bursts, which are integrated coherently into a single wideband signal. The carrier frequency of each sub-pulse increases pulse by pulse. The whole sequence transmitted with a fixed PRF can be written as

$$s_{tx}(t) = \sum_{n=0}^{N-1} p_s(t - nT) \exp\left(j2\pi f_n(t - nT_p) + \Phi_n\right) \tag{2.37}$$

where T_p is the PRI, $p_s(t)$ is the sub-pulse envelope, $f_n = f_0 + n\Delta f$ is the carrier frequency of the n-th sub-pulse, with f_0 the fundamental carrier frequency and Δf the bandwidth of sub-pulse, and Φ_n is the initial phase. For a full-band SFW, Δf is equal to the frequency step of the sub-carrier. In this analysis a LFM sub-pulse given by

$$p_s(t) = rect\left(\frac{t}{\tau}\right) \exp(j\pi\mu t^2) \tag{2.38}$$

where μ is the chirp rate given by the ratio between the sub-pulse bandwidth Δf and duration τ, and where

$$rect\left(\frac{t}{\tau}\right) = \begin{cases} 1 & 0 < t \leq \tau \\ 0 & t \geq \tau \end{cases} \tag{2.39}$$

The range resolution achieved by using a SFW radar is given by the entire synthesized bandwidth, as follows

$$R_\Delta = \frac{c}{2N\Delta f} \tag{2.40}$$

The received signal scattered by a target at range R from each transmitted sub-pulse can be written as

$$s_{rx}(t,n) = \Lambda_n p_s\left(t - nT - \frac{2R}{c}\right)\exp\left(j2\pi f_n\left[t - nT - \frac{2R}{c}\right] + \Phi_n\right) \tag{2.41}$$

where Λ_n is the amplitude of received n-th sub-pulse. Considering a reference signal at the range R_0, given by

$$s_0(t,n) = rect\left(\frac{t - nT - \frac{2R_0}{c}}{\tau_0}\right)\exp\left(j2\pi f_n\left[t - nT - \frac{2R_0}{c}\right] + \Phi_n\right) \tag{2.42}$$

where τ_0 is the reference signal sub-pulse duration, the dechirp process for each sub-pulse is computed as follows (Qun Zhang, 2016)

$$\begin{aligned} s_d(t,n) = s_{rx}(t,n)s_0^*(t,n) =& \Lambda_n rect\left(\frac{t - nT - \frac{2R}{c}}{\tau}\right) \times \\ & \exp\left(-j\frac{4\pi[f_0 + n\Delta f]\Delta R}{c}\right) \times \\ & \exp\left(j\frac{4\pi\mu\Delta R}{c}\left[t - nT - \frac{2R_0}{c}\right]\right) \times \\ & \exp\left(-j\frac{4\pi\mu\Delta R^2}{c^2}\right) \end{aligned} \tag{2.43}$$

with $\Delta R = R - R_0$. It is highlighted that the duration of reference sub-pulse τ_0 is chosen slightly longer than τ to avoid the width of the rectangle window not changing after the conjugate multiplication (Qun Zhang, 2016). Let us consider the reference instant of time $t' = t - nT - \frac{2R_0}{c}$, the Fourier Transform of (2.43) with respect t' is

$$\begin{aligned} S_d(\nu, n) =& \Lambda_n \tau \ \mathrm{sinc}\left(\tau\left[\nu + \frac{4\pi\mu}{c}\Delta R\right]\right) \\ & \exp\left(-j\frac{4\pi[f_0 + n\Delta f]\Delta R}{c}\right) \times \\ & \exp\left(-j\frac{4\pi\mu\Delta R^2}{c^2}\right) \\ & \exp\left(j\frac{4\pi\nu\Delta R}{c}\right) \end{aligned} \tag{2.44}$$

where $\mathrm{sinc}(x) = \sin(\pi x)/(\pi x)$, which has a peak in 0 delay. It follows that $S_d(\nu, n)$ has a peak for

$$\nu_0 = -\frac{4\pi\mu}{c}\Delta R \tag{2.45}$$

that is the approximation range profile of the point target. The dechirp process converts a LFM signal of large bandwidth into a narrow bandwidth signal, reducing the sampling requirement with respect to the matched filter. The main disadvantage is represented by the introduction of some phase terms not expected, which has to be compensated in order to obtain the HRRP. Specifically, the third phase term in (2.43) is known as Residual Video Phase (RVP) and the fourth as the sideling term of echo envelope. The RVP and sideling term of echo envelope are compensated for $\nu = \nu_0$ by multiplying $S_d(\nu_0, n)$ with the function (Qun Zhang, 2016)

$$S_{\mathrm{RVP}} = \exp\left(-j\frac{3\pi\nu_0^2}{\mu}\right) \tag{2.46}$$

obtaining a final signal vector whose components are

$$\underline{s}_{rx}(n) = \Lambda_n \tau e^{-j\frac{4\pi}{c}f_n\Delta R} \tag{2.47}$$

with $n = 1, \cdots, N$. The vector $\underline{s}_{rx}$ contains information about the target range in the phase, hence in the frequency domain, which can be converted into space domain information through the Inverse Discrete Fourier Transform (IDFT) (Mahafza and Elsherbeni, 2003). In particular, the HRRP can be extracted as follows

$$\mathcal{H}(\varepsilon) = \left|\frac{1}{N}\sum_{n=0}^{N-1} \Lambda_n \tau e^{j2\pi\frac{n}{N}\left(\varepsilon - \frac{2N\Delta f\Delta R}{c}\right)} e^{-j\frac{4\pi f_0 \Delta R}{c}}\right| \tag{2.48}$$

where $|\cdot|$ is the magnitude operator, and with $\varepsilon = 1, \cdots, N$. In the simpler case of stationary target and with $\Lambda_n = 1$, for $n = 0, \cdots, N-1$, the HRRP of target is

$$\mathcal{H}(\varepsilon) = \left| \frac{\tau}{N} \sum_{n=0}^{N-1} e^{j2\pi \frac{n}{N}\left(\varepsilon - \frac{2N\Delta f \Delta R}{c}\right)} \right| = \left| \frac{\tau}{N} \frac{\sin \pi \left(\varepsilon - \frac{2N\Delta f \Delta R}{c}\right)}{\sin \frac{\pi}{N} \left(\varepsilon - \frac{2N\Delta f \Delta R}{c}\right)} \right| \tag{2.49}$$

which is a discrete function with a peak at zero delay, theoretically

$$\varepsilon_0 = \frac{2N\Delta f}{c} \Delta R \tag{2.50}$$

Since the HRRP is generated through an induced phase shift, the unambiguous maximum range for the HRRP depends on the periodicity of the phase information over 2π, and it can be written as

$$R_u = \frac{c}{2\Delta f} \tag{2.51}$$

Hence, Δf has to be designed based on the expected maximum target extension with respect the reference range.

In case of a moving target with a radial velocity v_r, the target range varies during a set of sub-pulses, such that

$$\Delta R(n) = \Delta R(0) + nTv_r \tag{2.52}$$

with $\Delta R(0)$ the initial target range with respect the transmission and reception of the first sub-pulse. Sampling $S(\nu, n)$ into $4\pi\mu\Delta R(n)/c$ for $n = 0, \cdots, N-1$, thus (2.49) becomes

$$\mathcal{H}(\varepsilon) = \left| \frac{1}{N} \sum_{n=0}^{N-1} \Lambda_n \tau e^{j2\pi \frac{n}{N}\left(\varepsilon - \frac{2N\Delta f \Delta R(0)}{c} - \frac{2Nf_0 T v_r}{c} - \frac{2Nn\Delta f T v_r}{c}\right)} e^{-j\frac{4\pi f_0 \Delta R(0)}{c}} \right| \tag{2.53}$$

The additional phase term due to the target radial velocity leads to a distortion of the synthesized range profile. The phase term depending on target frequency Doppler ($f_0 v_r/c$) leads to a shift of the space response of the target along the synthesized range profile. The phase term depending on the couple velocity v_r with n produces an extension of the peak value over the fine range profile, leading to a wider target space response. It is obvious that this effect becomes worse for higher target velocities and longer burst durations. When the velocity compensation is not computed, the moving target appears at a range different from the actual, approximately given by

$$\widehat{R} \approx R(0) + \frac{f_0 T}{\Delta f} v_r + 2N v_r T \tag{2.54}$$

Fig. 2.8 shows the normalized range profiles from a target with three scattering points for different target velocities. Specifically, Fig. 2.8a shows the HRRP when the target is stationary, while Fig. 2.8b shows the HRRP when the target moves with a radial velocity of 100 m/s. The HRRP is obtained by transmitting a S-band SFW (at 3 GHz), composed by 128 sub-pulses whose each bandwidth is 6 MHz, with a PRF of 20 kHz. The range profiles start at 500 km and the relative distances of three scatterers is 10, 12 and 20 m, respectively. Moreover, a discrete Hamming window w(n) is applied, as follows

$$\mathcal{H}(\varepsilon) = \left| \frac{1}{N} \sum_{n=0}^{N-1} \mathrm{w}(n) \underline{s}_{rx}(n) e^{j2\pi \frac{n}{N}\varepsilon} \right| \tag{2.55}$$

Comparing the two HRRPs in Fig. 2.8 it is worth noting when the target velocity is not compensated, the responses of the three scatterers are wider and shifted (of 3.4 m approximately in the example).

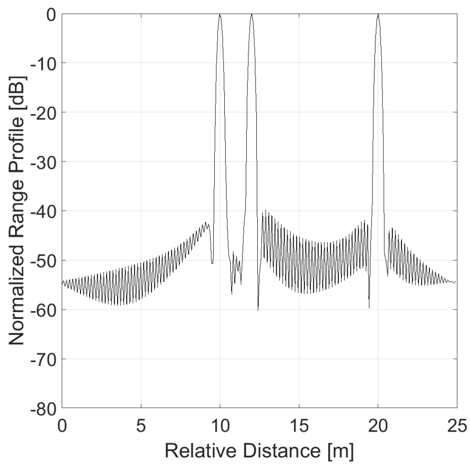

(a) $v_r = 0$ m/s

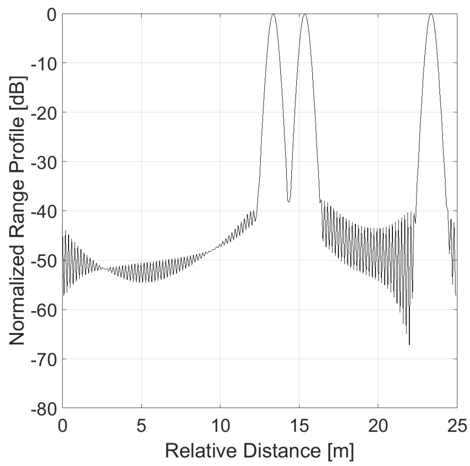

(b) $v_r = 100$ m/s

Fig. 2.8 Range profile of three target points (obtained with Hamming window)

The velocity compensation represents a complex problem in the BMD scenario, since the bulk motion of the cloud of warhead and decoys accelerates and decelerates irregularly. In addition, the BTs flying in the exo-atmosphere have different micro-motions, some of which may be significant even if smaller than the bulk motion of orders of magnitude. Hence, the target velocity is not constant during the burst due to micro-motions as the warhead precession and the decoy tumbling, leading to target spreading along the range profile. Furthermore, the number of pulses composing the entire burst and the PRF have to be designed in order to reduce the range of velocities observed during the dwell time (Clark, 1999). By contrast, the BTs micro-motions affects the positions of scatters in the HRRP, leading to periodic tracks into a frame of sequential HRRPs, which may be useful for target recognition. The authors in (Lei et al., 2012) proposed a graphical analysis for distinguishing between the precessing warhead, and wobbling or tumbling decoys, by taking into account both HRRP frame and time-frequency characteristics of radar return from the target. Firstly, the classification between the micro-motions is computed by analysis the presence of intersections between the tracks of different scatterers, which correspond to specular reflection peaks from the target, occurred only when the target is tumbling. In case the object is tumbling, a discrimination between target shapes (cylinder or cone) is computed by analysis if the peaks occur separated by an equal time interval or not. If the target is not tumbling, then the precession is discriminated from wobbling by observing a sinusoidal behaviour of the mD shifts within the radar echo. In (Da-qing et al., 2013) the HRRP frame is used as an 2D image used as input of an improved Viterbi algorithm used for tracking and isolating the range histories of each scatterer. Secondly, the time-frequency analysis is performed for each isolated scatterers.

2.7 Summary

In this Chapter, the fundamentals of radar systems were discussed, introducing the main configurations and operational modes. Additionally, since the radar performance are generally dependent on the received echo power and the level of system noise, different approaches for increasing the SNR at receiver are discussed in Section 2.3.

The principal steps for performing the target recognition from radar return are analysed in details in Section 2.4. In this context, particular focus was on target classification by exploiting the information about peculiar micro-motions exhibited by an object, e.g. rotation or vibration. For this purpose, the concepts of mD effect in radar return was reviewed. Additionally, the basic principle of the signal processing for obtaining the HRRP of a target with a wideband radar system was described, representing an useful tool for target recognition. Finally, a detailed analysis of the effect of target micro-motions in a HRRP was provided.

Chapter 3

Automatic Target Recognition

3.1 Introduction

Automatic Target Recognition (ATR) uses signal processing tools for the problem of target identification. The ATR processing can be applied to data from different type of sensors, comprising imaging sensors, such as Synthetic Aperture Radar (SAR) and Inverse Synthetic Aperture Radar (ISAR), as well as non-imaging sensors, such as High Range Resolution (HRR) radar and Raman spectrometers (Blacknell and Griffiths, 2013; Richards et al., 2013). In the modern defence system, ATR has a fundamental role since it increases the system efficiency for the interception of certain tactical targets with reduced risk. Nevertheless, ATR systems may be employed even in many civilian and commercial applications, e.g. for landmarks recognition for a visual navigation system or a robotic system, as well as for recognition of particular objects and faces in photographs or video sequences. In any application, the main issue for ATR systems is represented by the clutter and the noise introduced in the received signal by an imperfect sensor (Dudgeon and Lacoss, 1993).

In this Chapter, the ATR in radar is discussed, with particular focus on micro-Doppler (mD) based applications. In Section 3.2 an overview of the main time-frequency analysis tools in the context of radar signal processing is presented, providing a brief review of the principal mD based signatures used for target classification. The Radon Transform (RD) and its inverse function are presented in Section 3.3 as tools used for extracting mD parameters from radar image of a moving target. Following, a discussion on some of the widely used methods in the general context of image recognition is provided. Particularly, the pseudo-Zernike (pZ) and the Krawtchouk (Kr) image moments based approaches and the Gabor

Filter based approach are described, focusing on their application for mD based classification challenges present in literature.

3.2 Time-Frequency Distributions

The conventional Fourier Transform (FT) of a generic signal provides a description of all its spectral components. However, since it does not allow for the extraction of the time-dependent spectral components, the analysis of mD components into a radar return is generally conducted using more sophisticated tools. Specifically, Time-Frequency Distributions (TFD) generates a 2-Dimensional (2D) representation in both time and frequency domains simultaneously, emphasizing the time-varying behaviour of the signal.
One of the most used tool for displaying the time-varying spectral density of time-varying signal is the Short-Time Fourier Transform (STFT) (Chen et al., 2006). The STFT of a generic non-stationary signal $s(t)$ is a linear transform given by

$$S_{\mathrm{STFT}}(t, f) = \int_{-\infty}^{\infty} s(t')w^*(t'-t)e^{-j2\pi f t'}\mathrm{d}t' \tag{3.1}$$

where $w(\cdot)$ is a window function centred at zero delay (Heinzel et al., 2002). Differently from the conventional analysis in the Fourier domain obtained by applying the FT on the entire signal duration, the basic principle of STFT is the computation of FT onto shorter signal segments obtained by moving the window centre t' along the signal time duration, as illustrated in Fig. 3.1 from (Hiatt et al., 1960). In this way, the spectral analysis of the signal for different instants of time is provided. The window duration affects a trade-off between time and frequency resolutions: increasing the window duration a higher frequency resolution is obtained but with a poorer time resolution, and vice-versa (Allen and Mills, 2003). A higher product of time and frequency resolutions may be obtained by the window overlapping, which reduces the effects of the gaps at the edges that are produced when using windows. However, the overlap is limited since signal segments strongly correlated would not provide more information on the time variant spectral components (Heinzel et al., 2002). Different types of window, e.g. Hann or Hamming, can be used in order to achieve the required resolutions. Specifically, the STFT computed using Gaussian windows, known in literature as Gabor Transform, provides the minimal product between the time resolution and the frequency resolution. The selection of the optimal window depends on the specific characteristic of the time-variant signal. In (Jones and Parks, 1990) a

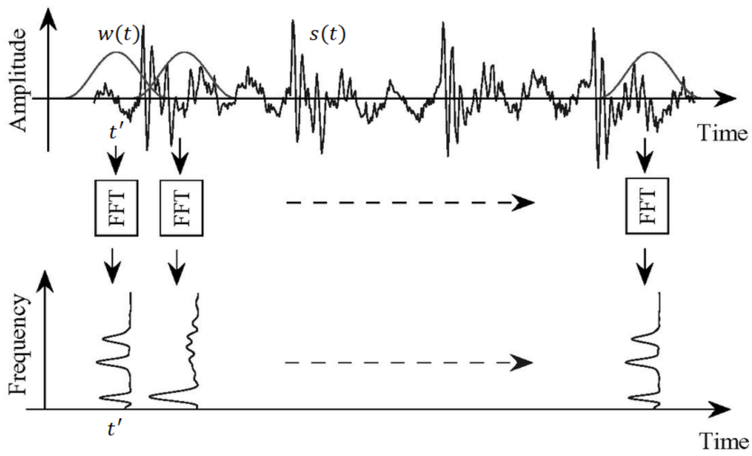

Fig. 3.1 Illustration of STFT processing on the signal $s(t)$ from (Hiatt et al., 1960).

method for selecting the optimal window width of the STFT, without any prior spectral information about the signal, is described. The adaptive STFT uses Gaussian basis functions with different time and frequency parameters to achieve high signal concentration everywhere.

The Wigner-Ville Distribution (WVD) is another common TFD used for extracting information on the time variance spectral components of a signal (Allen and Mills, 2003). The WVD of a generic signal $s(t)$ is a quadratic transform defined as the FT of the time dependent auto-correlation function, as follows

$$S_{\mathrm{WVD}}(t,f) = \int_{-\infty}^{\infty} s\left(t + \frac{t'}{2}\right) s^*\left(t - \frac{t'}{2}\right) e^{-j2\pi f t'} \mathrm{d}t' \tag{3.2}$$

The main advantage of the WVD with respect to the more intuitive STFT is the absence of the trade-off among the time and frequency resolutions, since it generates the TFD by the correlations of time and frequency shifted versions of $s(t)$ with each other (Boashash and Boualem, 2015). However, the WVD suffers from cross-terms between correlated components, which may represents a significant interference factor affecting considerably the interpretation of the time-frequency plane (Hlawatsch and Boudreaux-Bartels, 1992). In practice, it is possible to reduce these interference terms by smoothing in both time and frequency domains. Specifically, the *Pseudo Wigner Distribution* (PWD) is obtained by inserting a window function with respect to the time domain, and it is given by (Goncalves and Baraniuk, 1998)

$$S_{\mathrm{PWD}}(t,f) = \int_{-\infty}^{\infty} \mathfrak{w}(t') s\left(t + \frac{t'}{2}\right) s^*\left(t - \frac{t'}{2}\right) e^{-j2\pi f t'} \mathrm{d}t' \tag{3.3}$$

It is worth noting that the PWD results from a self-correlation of the STFT across frequency, as follows

$$S_{\mathrm{PWD}}(t,f) = \frac{1}{2\pi} \int_{-\infty}^{\infty} S_{\mathrm{STFT}}\left(t, f - \frac{f'}{2}\right) S^*_{\mathrm{STFT}}\left(t, f + \frac{f'}{2}\right) \mathrm{d}f' \tag{3.4}$$

when $w(t) = \sqrt{\mathfrak{w}(2t)}$. The PWD produces better resolution with respect to the STFT, but the cross-terms occurs as well as for the WVD. The *S-method* TFD limits the range of the integral of the PWD with a low-pass windowing function (Stankovic, 1994). It is given by

$$S_{\mathrm{SM}}(t,f) = \frac{1}{\pi} \int_{-\infty}^{\infty} \mathcal{W}(f') S_{\mathrm{STFT}}\left(t, f - \frac{f'}{2}\right) S^*_{\mathrm{STFT}}\left(t, f + \frac{f'}{2}\right) \mathrm{d}f' \tag{3.5}$$

where $\mathcal{W}(f')$ is a finite frequency domain window. The S-method achieves high concentration for auto-term along the frequency axis, removing the cross-terms. It is worth noting that the S-method behaves as the PWD when $\mathcal{W}(f) = 1$, and as the STFT when $\mathcal{W}(f) = \pi\delta(f)$, with $\delta(\cdot)$ the delta function, being different from 0 and equal to 1 into zero delay (Tivive et al., 2015).
The STFT and the PWD are very attractive in real-time classification applications for their low computational complexity. In particular, the STFT is one of the most used TFDs since it can be efficiently implemented using the Fast Fourier Transform (FFT) (Bouchikhi et al., 2011). For this reason, the STFT is taken into consideration as tool for the time-frequency analysis of the signal in the next chapters of the Thesis.

3.2.1 Micro-Doppler based Target Signature

Defined as the square magnitude of the STFT of the signal, the *spectrogram* is often used as a 2D target signature for classification algorithms based on mD information due to target micro-motion. In (Fioranelli et al., 2015b,c), the spectrogram is used to distinguish between unarmed and potential armed personnel in the context of security and surveillance applications. A multistatic radar system is proposed for improving the classification capabilities by taking advantages of diversity of mD effect with respect to the aspect angle variation. Specifically, in (Fioranelli

et al., 2015c) four features are empirically estimated from the spectrogram, which are: mD bandwidth, as the total range of frequencies between the highest and the lowest Doppler frequency in the spectrogram; Doppler offset, given by the difference between the highest and the lowest Doppler frequency; mean period of the swinging of the limbs; the ratio in dB between the value of the spectrogram at the peaks related to the swinging arms and at the line related to the body. In (Fioranelli et al., 2015b), a set of features is evaluated by using the Singular Value Decomposition (SVD) on the spectrograms and estimating the standard deviation of the first right singular vector. In (Fioranelli et al., 2015a) the authors analyse the effect of polarimetry on the same classification scenario, investigating how the classification performance changes by using co-polarized or cross-polarized data, or a combination of both. In (Liu et al., 2012) the is used as a 2D target signature for BM target recognition. The authors propose an data-adaptive window selection approach to get the maximum concentration of the signal components in the spectrogram. Then, the mD modulation frequency is estimated analysing the periodic structures in the image by applying the 2D FFT.
The Cadence Velocity Diagram (CVD) is a 2D target signature obtained by Fourier transforming the spectrogram along the time dimension, as follows

$$\mathcal{S}_{\mathrm{CVD}}(f_c, f) = \left| \int_{-\infty}^{\infty} \left| S_{\mathrm{STFT}}(t, f) \right|^2 e^{-j2\pi f_c t} \mathrm{d}t \right|^2 \tag{3.6}$$

The CVD is a 2D image which shows the repetition rate (or *cadence*) of different velocities which produce the mD modulation on the observed signal. A mD classification method which uses the strongest parts of the CVD for the feature vector construction is described in (Bjorklund et al., 2012). The algorithm was tested successfully in the case of the discrimination of human motion. However it requires high storage capabilities as long as the feature vector is composed by the highest cadence frequencies and sampled velocity profiles corresponding to each of them. In (Clemente et al., 2015a) the evaluation of the CVD as target signature was proposed for the recognition of targets which exhibit micro motions, testing the framework on three different classification challenges, namely helicopters, human motions and animal gaits classification. The CVD is more robust than the spectrogram as mD target signature since it does not depends on the initial phase of moving object, avoiding synchronization problems or the use or more complex classification process (Clemente et al., 2015a).
Another 2D target signature used for mD based classification algorithms is the *cepstrogram*. Starting from the TFD of the radar return, the cepstrogram is defined

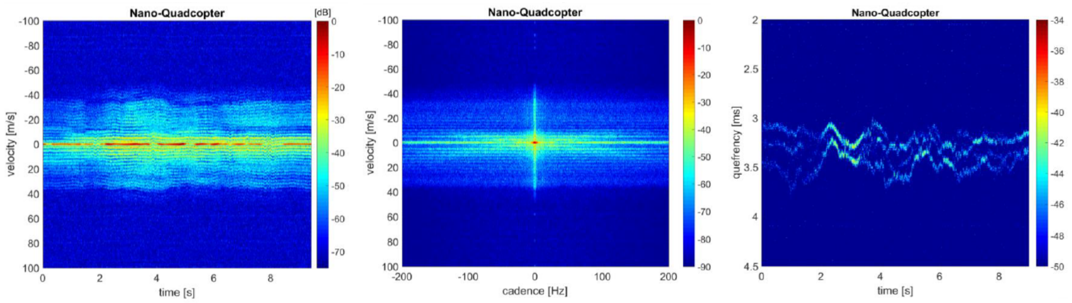

(a) (b) (c)

Fig. 3.2 Examples of TF target signature for a nano-sized quadcopter from (Fuhrmann et al., 2017): (a) spectrogram, (b) CVD and (c) cepstrogram.

as the Inverse Fourier Transform (IFT) of the logarithm of the spectrogram along the frequency domain, as follows

$$\mathcal{S}_{\text{CEP}}(t', t_q) = \left| \frac{1}{2\pi} \int_{-\infty}^{\infty} \log_{10} \left[|S_{\text{STFT}}(t, f)|^2 \right] e^{j2\pi f t_q} \text{d}t \right|^2 \tag{3.7}$$

where t_q variable has the dimension of time, and it is known as *quefrency* (Noll, 1964). The cepstrogram is particularly useful when the integration interval of radar measurements is very long with respect to periodicity of the observed target motion. In (Harmanny et al., 2014) the cepstogram is proposed as 2D target signature for mD based classification of small air-target, as drones and birds. Specifically, the angular velocity of a rotor, or propeller, is directly estimated from cepstrogram which shows the spectrogram periodicity, allowing to discriminate between single rotor or multicopter target types. Fig. 3.2 from (Fuhrmann et al., 2017) shows an example of a mD based target signature from radar measurement of a nano-sized quadcopter by a CW system at Ka band, namely the spectrogram, the CVD and the cepstogram. From Fig. 3.2a and Fig. 3.2b, it is observed that the mD components are not clearly visible in both the Spectrogram and the CVD due to the high rotation velocities of the blades, while from the cepstogram in Fig. 3.2c it is possible to distinguish the mD contribution from different rotors.

3.3 Radon Transform Based ATR

Introduced by Johann Radon in 1917, the Radon Transform (RT) computes the projection of a 2D function onto a specific direction (Deans, 2007). Considering a generic 2D function $f(x, y)$ and a line $\mathcal{L}$ defined in $\mathbb{R}^2$, the RT of $f(x, y)$ is

$$\mathcal{R}_f = \int_{\mathcal{L}} f(x, y)\mathrm{d}l \tag{3.8}$$

where x, y are coordinates of points on the plane, and, $\mathrm{d}l$ is the increment of length along $\mathcal{L}$. In order to define more precisely the integral in (3.8), let us consider the definition of an arbitrary line in the normal form with respect to the coordinate system (x, y), given by

$$\breve{x} = x\cos(\theta) + y\sin(\theta) \tag{3.9}$$

with θ the inclination angle with respect to the x-axis (see Fig. 3.3). Considering the coordinate system $(\breve{x}, \breve{y})$ obtained rotating the system (x, y) by the angle θ such that

$$\begin{aligned} x &= \breve{x}\cos(\theta) + \breve{y}\sin(\theta) \\ y &= \breve{x}\sin(\theta) + \breve{y}\cos(\theta) \end{aligned}$$

the RT of $f(x, y)$ can be written as

$$\mathcal{R}_f = \mathcal{R}_f(\breve{x}, \theta) = \int_{-\infty}^{\infty} f(\breve{x}\cos(\theta) + \breve{y}\sin(\theta), \breve{x}\sin(\theta) + \breve{y}\cos(\theta))\mathrm{d}\breve{y} \tag{3.10}$$

where the limits may be finite if the function $f(x, y)$ is zero outside its domain $\mathcal{D}$. Let us consider the easier case in which the 2D function is given by a delta function located at the point (x_0, y_0) as follows

$$f(x, y) = \delta(x - x_0)\delta(y - y_0) \tag{3.11}$$

Then its RT onto the line in (3.9) is

$$\begin{aligned} \mathcal{R}_f(\breve{x}, \theta) = \int_{\mathcal{L}} \delta(x - x_0)\delta(y - y_0)\mathrm{d}l &= \int_{-\infty}^{\infty} \delta(\breve{x} - \breve{x}_0)\delta(\breve{y} - \breve{y}_0)\mathrm{d}\breve{y} \\ &= \delta(\breve{x} - x_0\cos(\theta) - y_0\sin(\theta)) \end{aligned} \tag{3.12}$$

where

$$\begin{aligned} \breve{x}_0 &= x_0\cos(\theta) + y_0\sin(\theta) \\ \breve{y}_0 &= x_0\sin(\theta) + y_0\cos(\theta) \end{aligned}$$

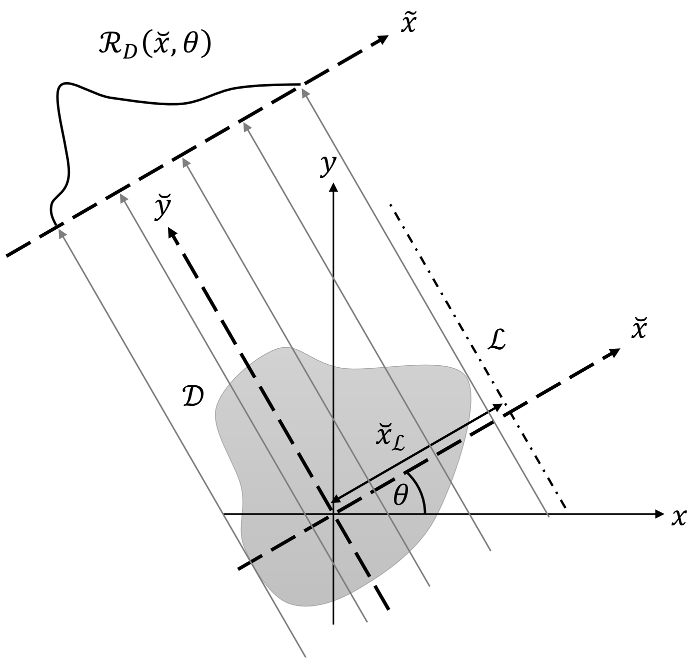

Fig. 3.3 Representation of RT of a generic function $f(x, y)$, whose domain $\mathcal{D}$ and a generic line $\mathcal{L}$ are shown in the original (continuous line) and rotated (dashed line) reference coordinate system.

It is noted that the RT of a delta function in $\mathbb{R}^2$ generates a sinusoidal pattern in the 2D domain $(\breve{x}, \theta)$ as follows

$$\breve{x} = A\, sin(\theta + \theta_0) \tag{3.13}$$

with

$$A = \sqrt{x_0^2 + y_0^2}$$
$$\theta_0 = \tan^{-1}\left(\frac{x_0}{y_0}\right)$$

For this reason the data obtained by the RT is known as *sinogram* (Kertész et al., 2017). By contrast the Inverse Radon Transform (IRT) allows to reconstruct a 2D function from its projections converting any sinusoidal pattern into a point. The IRT can be computed in two ways: the computation in the Fourier domain and the so-called filtered back-projection method (Bai et al., 2011). The first is based on the relation between the RT and the Fourier transform. Specifically the 2D Fourier transform of the generic function f along a line at the inclination angle θ is the one dimension Fourier transform of the RT of that function onto the same line (Deans, 2007). This means that it is possible to calculate the 2D

Fourier transform of $f(x, y)$ by knowing all the projections for $\theta \in [0, \pi[$. The filtered back projection method is widely used in the literature and it is obtained as follows

$$f(x, y) = \int_0^{\pi} \widehat{\mathcal{R}}_f(x\cos(\theta) + y\sin(\theta), \theta)\mathrm{d}\theta \tag{3.14}$$

where $\widehat{\mathcal{R}_f}$ is obtained by filtering the RT of $f(x, y)$ by one dimensional filtered with respect to the $\breve{x}$ domain. Commonly the ramp filter is considered (Bai et al., 2011).

Both the RT and its inverse function are widely used in computer vision applications e.g. for image reconstruction from data acquired by CT, PET or MR scanners or for image classification (Kertész et al., 2017). Many authors propose the use of the RT for extracting Doppler information starting from TFD of radar echoes. In (Wood and Barry, 1994) and (Stankovic et al., 2001) the RT is used for in order to detect linear FM signals. Since a line structure in the TF plane is projected onto a point in the Radon transform the chirp rate value of a linear FM signal can be estimated evaluating the concentration of the WVD along different directions (hence, angles).

Each point of the HRRP of a target obtained by wideband radar represents the integral of the target distribution function along the corresponding equal-phase line. Hence, the HRRP can be seen as the projection of the target distribution along the radar LOS. Since the effect of a rotating scatterer in the range-slow time domain is equivalent to the RT of its space distribution function, the IRT is proposed in the literature as a back-projection approach to reconstruct a 2D image of the target.

In (Bai et al., 2011) two IRT based methods are presented for image reconstruction of rotating parts of a target e.g. airplane or helicopter rotor. The first method consists into the real-valued IRT applied directly on the echoes modulus, while the second one applies the complex-valued IRT on the complex echoes guaranteeing higher image resolution by performing a coherent integration. Fig. 3.4 from (Bai et al., 2011) shows the imaging process of the An-26 plane, with a turbo on each side of the airframe. The ISAR images of each turbo is obtained by applying the real-valued IRT. Specifically, in Fig. 3.4(a) the image obtained from the mixed echoes from the airframe and the turbines is shown, where two strips due to mD signal components can be observed. The focused image of the main body is shown in Fig. 3.4(b), where the mD components are filtered out. The four points around the diagram centre shown in Fig. 3.4(c) and Figs. 3.4(d) represent the four blades of the two turbines, whose diameter is approximately 3.9 m.

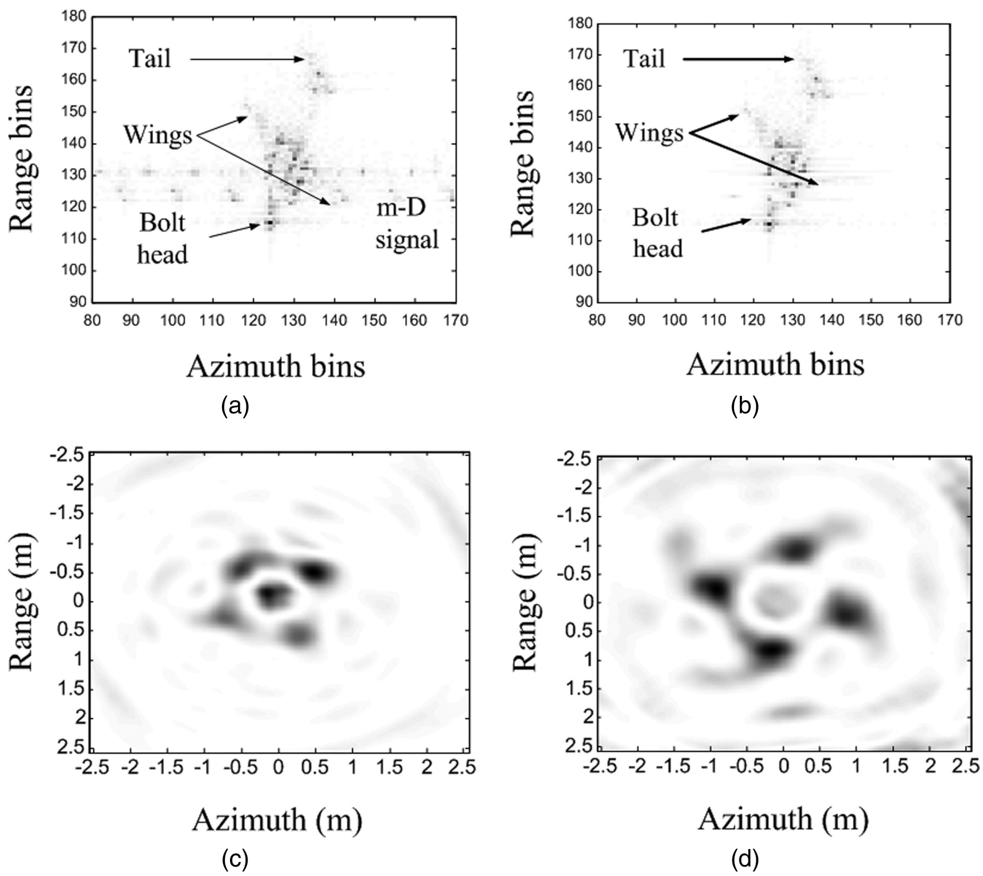

Fig. 3.4 Imaging process of An-26 plane rotors from (Bai et al., 2011): (a) image using target echoes; (b) image of main body; (c) image of first turbo; (d) image of second turbo.

By contrast, the IRT is also proposed in the ISAR/SAR processing for separating the echoes from target rigid body and the contribution from its rotating parts. In the case in which the frequency modulations due to the moving parts of targets are not filtered out, the mD effect introduces a distortion in the SAR/ISAR images. For this reason in (Thayaparan, 2006) two techniques are proposed. The first technique is based on the TFD analysis of radar returns. Specifically, the spectrogram of the echo is evaluated for various window sizes, since the contribution of rotating parts leads to a high concentration in the narrow-window spectrogram, while the rigid body contribution produces a high concentration into wide-window spectrogram. The second approach is based on the IRT computation of the TFD of the received echo. The authors in (Hua et al., 2014) describe a new approach for cleaning the ISAR image of a target from its rotating parts applying the IRT on a frame of target range-profiles. In particular, the rotation period is firstly estimated by autocorrelation method on echo, then the contribution of rotating parts is

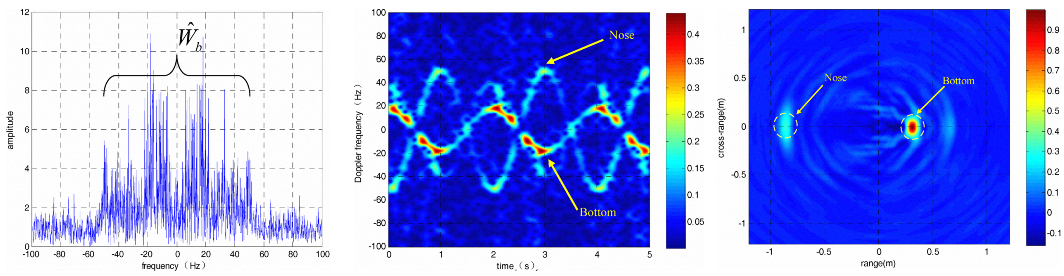

(a) (b) (c)

Fig. 3.5 Imaging process of precessing cone from (Kangle et al., 2009): (a) echo spectrum ; (b) TFD; (c) 2D reconstruction result using inverse Radon transform on Time-Frequency distribution.

detected from the IRT of the range profile frame and filtered out. In (Kangle et al., 2009) a novel technique for the extraction of precession parameters of a conical target is presented. The proposed algorithm is based on the Doppler analysis of the radar echo: the precession parameter (angle and rate) are estimated analysing the spread of echo spectrum. Finally a 2D image of target is reconstructed by applying the IRT on the echo TFD. Fig 3.5 from (Kangle et al., 2009) shows an example of imaging process obtained from a precessing cone. Specifically, Fig. 3.5a and Fig. 3.5b show the spectrum and the spectrogram from a precessing cone, where the two mD frequency components observed correspond to the nose and bottom of the warhead model. From these two figures, it is observed that the estimated spread width of the echo spectrum is equal to the amplitude of the maximum mD frequency component. Finally, Fig. 3.5c shows the reconstructed 2D image of the cone obtained by applying IRT on the spectrogram in Fig. 3.5c, where two peaks are observed as contributions of the cone nose and bottom.

3.4 Pseudo-Zernike Moments Based ATR

Introduced in (Bhatia and Wolf, 1954), the pZ moments of an image $I(x, y)$ are geometric moments computed as the projection of the image on a basis of 2D polynomials which are defined on the unit circle. Specifically, the pZ moments of order r and repetition l are calculated as follows

$$\zeta_{r,l} = \frac{r+1}{\pi} \int_0^{2\pi} \int_0^1 W^*_{r,l}(\rho, \theta)\, I(\rho\cos\theta, \rho\sin\theta)\, \rho \mathrm{d}\rho \mathrm{d}\theta \tag{3.15}$$

with $r \geq |l|$, and where the polynomial $W_{l,r}$ can be written as

$$W_{l,r}(x,y,\rho) = W_{r,l}(\rho,\theta) = \sum_{h=0}^{r-|l|} \frac{\rho^{r-h}(-1)^h(2r+1-h)!}{h!(r+|l|+1-h)!(r-|l|-h)!} e^{jl\theta} \tag{3.16}$$

where $x = \rho\cos\theta$ and $y = \rho\sin\theta$, with $\rho \leq 1$. Fig. 3.6 from (Clemente et al., 2015a) shows the magnitude of pZ polynomials $W_{r,l}(\rho,\theta)$ with order from $r = 0$ to $r = 3$. It is worth noting that the polynomials for positive values of l are rotated version of the ones corresponding to negative values. Moreover, the magnitude of all the shown polynomials for repetition $l = 0$ presents a pattern with concentric circles. The orthogonality relation of the pZ polynomials is satisfied on the unit circle, and it is expressed as follows

$$\iint\limits_{x^2+y^2\leq 1} W^*_{r,l}(x,y) W_{m,k}(x,y) \mathrm{d}x\mathrm{d}y = \frac{\pi}{r+1}\delta_{rm}\delta_{lk} \tag{3.17}$$

where δ_{rm} is the Kronecker delta function, i.e

$$\delta_{rm} = \begin{cases} 1 & r = m \\ 0 & r \neq m \end{cases} \tag{3.18}$$

PZ moments increases the number of moments available for a given order of the polynomial compared to Zernike moments reducing the noise sensitivity. Specifically, the number of linearly independent pZ polynomials of degree $\leq r$ is $(r+1)^2$, whereas for the Zernike polynomials it is $\frac{1}{2}(r+1)(r+2)$. Hence, pZ moments provide more information about the image with respect to Zernike moment at parity of order. The moments have several properties, among which are that they are independent, since the pZ polynomials are orthogonal on the unit circle, and their modulus is rotational invariant. The pZ moments are widely used in image processing for pattern recognition (Nassery and Faez, 1996) and face recognition (Sultana et al., 2014) due to their useful properties, such as scale, translation and rotation invariance. The authors in (Clemente et al., 2015a) propose the pZ moments based feature vector extracted by projecting the CVD from the target observation, considered as a 2D image signature, over a pZ polynomial basis. The algorithm has been compared with two classification techniques based on mD features vectors presented in (Zabalza et al., 2014) and (Molchanov et al., 2012), underlining its better performance. Moreover, the scale invariant property is important for mD based feature due to their more robustness with respect to the angle of view which affects strictly the maximum frequency

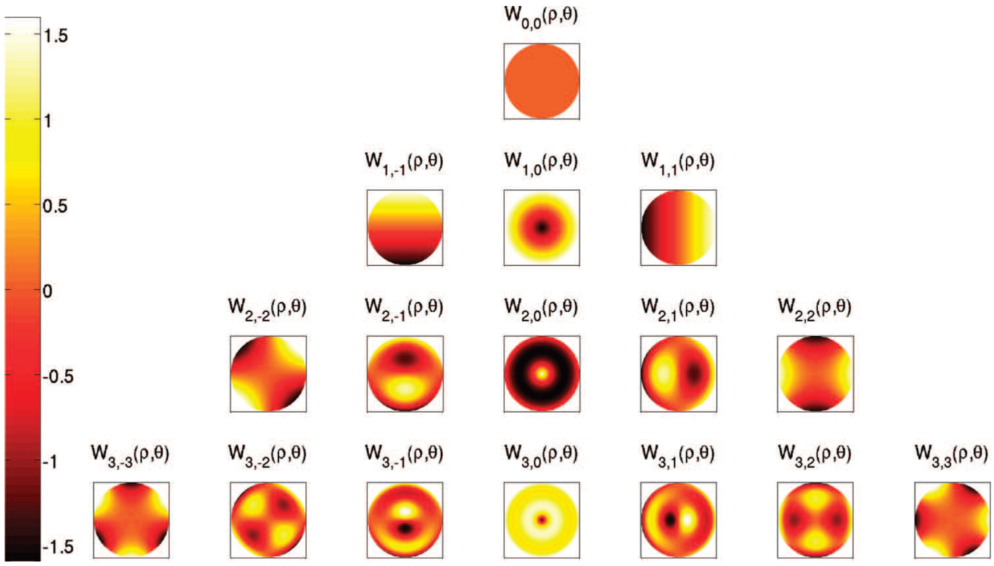

Fig. 3.6 PZ polynomials for orders 0 to 3 (Clemente et al., 2015a).

shift. Specifically, scale invariance allows to apply the algorithm in a multistatic scenario without the requirement of a multistatic training dataset or for an ATR system which works with a carrier frequency slightly different than the one used for the database creation.

3.5 Krawtchouk Moments Based ATR

The Kr moments of order r of an image $I(x, y)$, introduced in (Yap et al., 2003), are computed as the projection of the image on a basis of orthogonal polynomials which are associated with the binomial distribution. These are calculated as the product of the classical Kr polynomials, K_r, and a weight factor to overcome the numerical stability problem as follows (Kaur et al., 2015; Yap et al., 2003)

$$\begin{aligned}\overline{K}_r(x,p,\mathcal{N}) &= K_r(x,p,\mathcal{N})\sqrt{\frac{w(x;p,\mathcal{N})}{\rho(n;p,\mathcal{N})}} = \\ &=_2 F_1\left(-n,-x;-\mathcal{N};\frac{1}{p}\right)\sqrt{\frac{w'(x;p,\mathcal{N})}{w''(n;p,\mathcal{N})}}\end{aligned} \tag{3.19}$$

with

$$\begin{aligned}w'(x;p,\mathcal{N}) &= \binom{\mathcal{N}}{x}p^x(1-p)^{\mathcal{N}-x} \\ w''(x;p,\mathcal{N}) &= (-1)^{\mathcal{N}}\left(\frac{1-p}{p}\right)^n\frac{n!}{(-\mathcal{N})_n}\end{aligned} \tag{3.20}$$

where x and n belonging to $(0, 1, 2, \ldots, \mathcal{N})$, $\mathcal{N} \in \mathbb{N}$, with $\mathbb{N}$ the set of natural numbers, p a real number belonging to the set $(0, 1)$. The classical Kr polynomials are defined trough the Gauss hypergeometric function ${}_2F_1$, given by

$$ {}_2F_1(a, b; c; z) = \sum_{k=0}^{\infty} \frac{(a)_k (b)_k}{(c)_k} \frac{z^k}{k!} \tag{3.21} $$

with $(a)_k$ the Pochhammer symbol, given by

$$ (a)_k = a(a+1)\ldots(a+k-1) = \frac{\Gamma(a+k)}{\Gamma(a)}. \tag{3.22} $$

Fig. 3.7 shows the weighted Kr polynomials with $\mathcal{N} = 100$ for orders from 0 to 3, and p equal to $0.25, 0.50, 0.75$. It is worth noting that p represents a shift

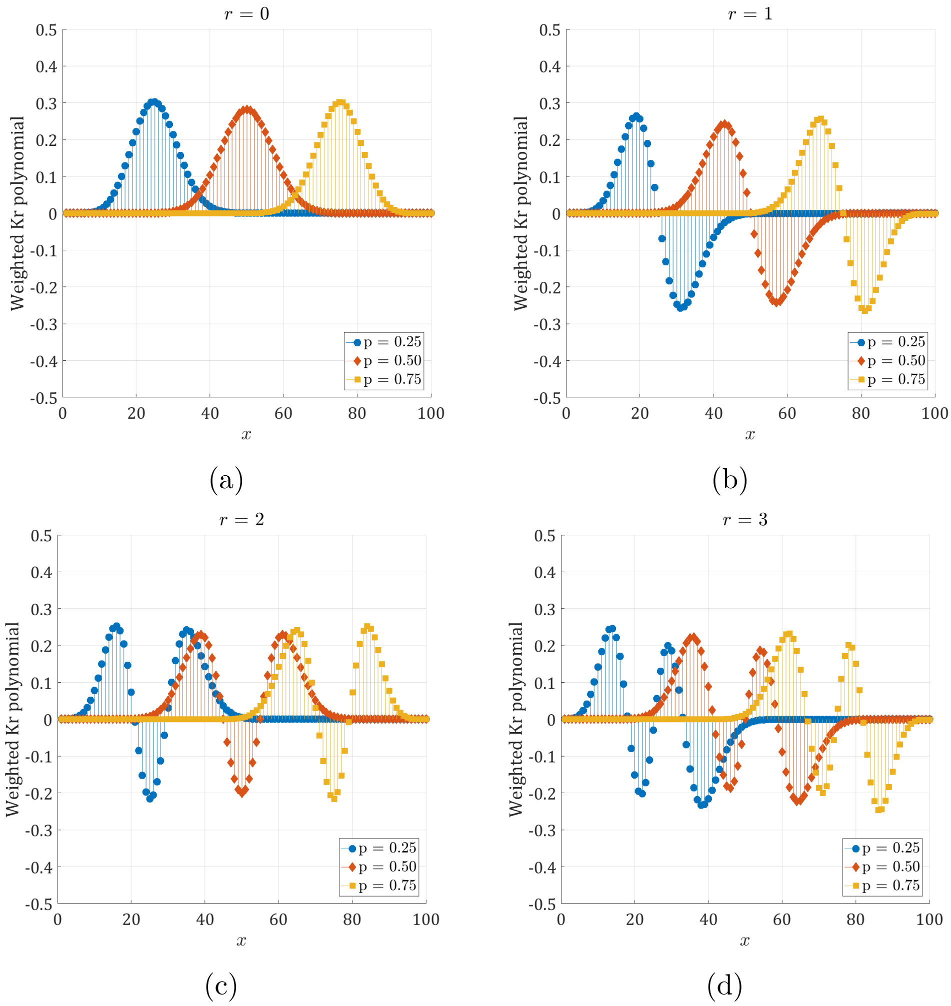

Fig. 3.7 Representation of the weighted Kr polynomials of order (a) $r = 0$, (b) $r = 1$, (c) $r = 2$, (d) $r = 3$, with the parameter $p = 0.25, 0.50, 0.75$ and $\mathcal{N} = 100$.

parameter, such that when p varies of Δp with respect to 0.50, the polynomial is shifted of $\Delta p\mathcal{N}$, approximately (Yap et al., 2003).
Considering a 2D image $I(x, y)$, the Kr moments of order (n, m) are defined as (Kaur et al., 2015)

$$K_{nm} = \sum_{x=0}^{\mathcal{N}_x-1}\sum_{y=0}^{\mathcal{N}_y-1} \overline{K}_n(x, p_1, \mathcal{N}_x - 1) \times \overline{K}_m(y, p_2, \mathcal{N}_y - 1) I(x, y) \tag{3.23}$$

where $\mathcal{N}_x$ and $\mathcal{N}_y$ are the image dimensions along both the axes. Since it is possible to write the image as a series of weighted Kr polynomials scaled by the Kr-moments (Yap et al., 2003), such that

$$I(x, y) = \sum_{x=0}^{\mathcal{N}_x-1}\sum_{y=0}^{\mathcal{N}_y-1} K_{nm}\overline{K}_n(x, p_1, \mathcal{N}_x - 1) \times \overline{K}_m(y, p_2, \mathcal{N}_y - 1) \tag{3.24}$$

hence the Kr moments are a synthetic way to represent the image intensity function $I(x, y)$.
The Kr moments are widely used for image processing in various applications like image reconstruction (Yap et al., 2003), shape recognition (Kaur et al., 2015) and face recognition (Nor'aini and Raveendran, 2009) for their some peculiar characteristics. In (Clemente et al., 2017) the Kr moment based feature vector is proposed for the classification and characterization of military target images. Since they are discretely defined, they do not involve numerical approximation as in the case of continuous orthogonal moments. In this way discretization error does not exist and the amount of resource required to store the polynomials is reduced thanks to the recurrence relations and the symmetry properties of Kr moments (Yap et al., 2003). Moreover, the moments derived from Kr polynomials benefit of scale, rotation and translation invariant properties (Yap et al., 2003). These characteristics, together with the capability to pre-compute the polynomials, make this image moments reliable for real time target recognition.

3.6 2D Gabor Filter Based ATR

The 2D Gabor function is the product of a complex exponential representing a sinusoidal plane wave and an elliptical Gaussian in any rotation. The filter response in the continuous domain can be normalized to have a compact closed form (Ilonen et al., 2007; Kamarainen et al., 2006)

$$g(x,y) = \frac{f_{cs}^2}{\pi\eta_x\eta_y} e^{-\left(\frac{f_{cs}^2}{\eta_x^2}x'^2 + \frac{f_{cs}^2}{\eta_y^2}y'^2\right)} e^{j2\pi f_{cs}x'} \tag{3.25}$$

with

$$x' = x\cos(\vartheta) + y\sin(\vartheta), \quad y' = -x\sin(\vartheta) + y\cos(\vartheta) \tag{3.26}$$

where f_{cs} is the central spatial frequency of the filter, ϑ is the anti-clockwise rotation of the Gaussian envelope and the sinusoidal plane wave, η_x is the spatial width of the filter along the plane wave, and η_y is the spatial width perpendicular to the wave. The sharpness of the filter is controlled on the major and the minor axes by η_x and η_y.The normalized filter harmonic response is (Kamarainen et al., 2006)

$$\mathcal{G}(u,v) = e^{-\frac{\pi^2}{f_{cs}^2}\left(\eta_x^2(u'-f_{cs})^2 + \eta_y^2 v'^2\right)} \tag{3.27}$$

where

$$u' = u\cos(\vartheta) + v\sin(\vartheta), \quad v' = -u\sin(\vartheta) + v\cos(\vartheta). \tag{3.28}$$

Fig. 3.8 represents the real part of a Gabor filter response in the XY plane, with $\eta_x = \eta_y = 2\pi$, $f_{cs} = 4$ and for different orientation angles. Fig. 3.8a and Fig. 3.8b shows that the variation of the orientation angle leads to a rotation of the filter response. Specifically, it is possible observing that the magnitude of 2D response in Fig. 3.8b presents a pattern with parallel lines which are oblique with respect to the x-axis of ϑ.

Fig. 3.9, instead, represents the magnitude of the Gabor filter harmonic response in the UV plane, obtained from the responses in Fig. 3.8. The harmonic response is a pulse whose position depends on both f_{cs} and ϑ. Particularly, the pulse moves on a circumference centred in the origin and whose radius is defined by f_{cs}, while ϑ is the rotation angle in the anti-clockwise direction with respect to the $\hat{u}$ axis, as shown in Fig. 3.9a and Fig. 3.9b. Hence, it is possible to extract local feature in the Fourier domain by varying the filter parameters. Gabor filters have been successfully employed to extract reliable features in several challenges, such as the texture and symbol classification (Kamarainen et al., 2006; Mittal et al., 1999) and in the context of face recognition (Ilonen et al., 2007), especially due to their scale, translation, rotation and illumination invariant properties.

In (Lei and Lu, 2005) authors propose a Gabor filtering approach to extract a feature vector from the mD based signatures for the classification of different

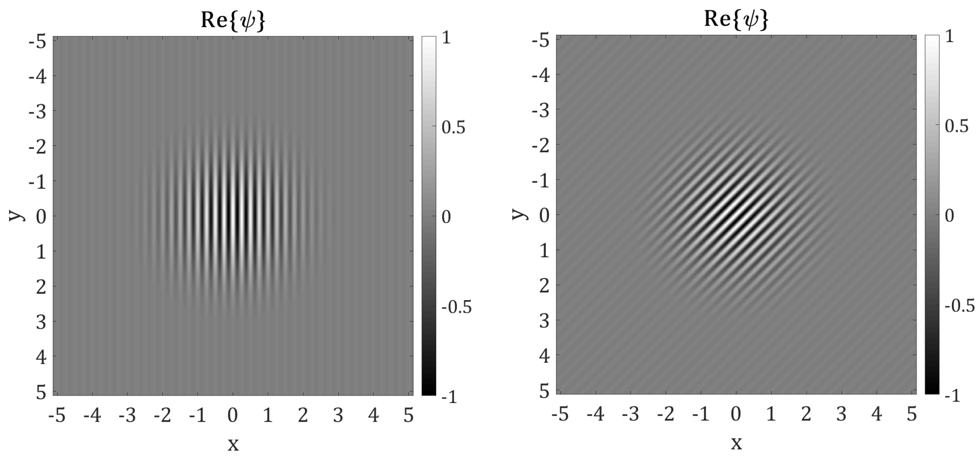

(a) $\vartheta = 0°$ (b) $\vartheta = 45°$

Fig. 3.8 Real part of a Gabor filter response in the xy plane, with $\eta_x = \eta_y = 2\pi$ and $f_{cs} = 4$.

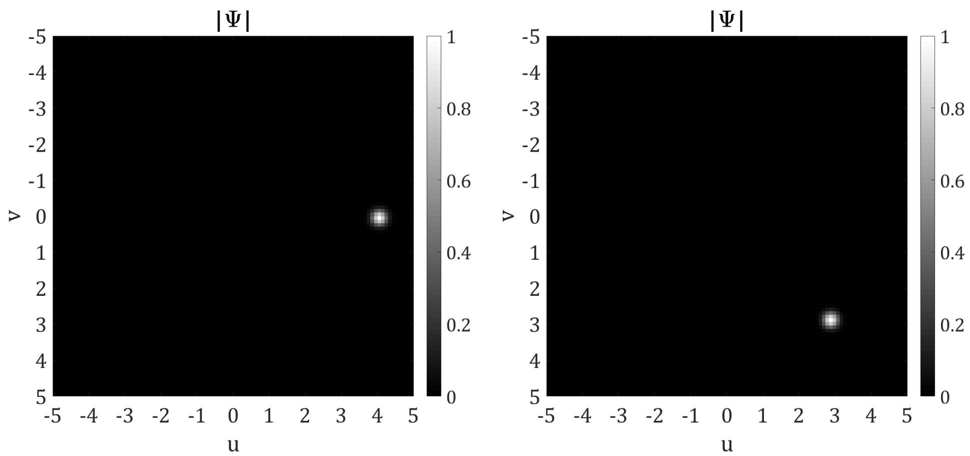

(a) $\vartheta = 0°$ (b) $\vartheta = 45°$

Fig. 3.9 Magnitude of the Gabor filter harmonic response in the uv plane, with $\eta_x = \eta_y = 2\pi$ and $f_{cs} = 4$.

target motions, such as vibration, rotation or tumbling. The proposed method consist of three steps. The first is filtering of the 2D signature (based on TFD of radar return) with a bank of Gabor filters, created by selecting a set of orientation angles. Following, a set of feature vectors is obtained by concatenating the pixel for each output images. Finally, the output images are firstly down-sampled, and then the principal component analysis (PCA) method is used in order to reduce the number of features. In particular, the eigen-decomposition of the matrix containing the down-sampled images from the bank of filters is evaluated, and the eigenvector corresponding to the highest eigenvalues are selected as final features. Authors in (Tivive et al., 2015) proposes a feature extraction method based on a logarithmic version of Gabor filter for human motions classification. Specifically, the log-Gabor filter has similar shape to a Gabor filter on the logarithmic frequency scale with an extended tail in the high-frequency region. The proposed classification method evaluate the 2D mD based signature as the S-method TFD of radar return. Then, a small patch centred on the torso frequency is automatically extracted to guaranteeing robustness with respect to the target speed. The final 2D signature is filtered by a bank of Log-Gabor filters at multiple scales and orientations, and each output image is then normalized with respect to its maximum value and divided in non-overlapping sub-regions. A feature vector for each output image is extracted, whose components are the mean value of each sub-regions. Finally, the dimensionality of features is reduced by applying the 2-Directional 2-Dimensional $(2D)^2$ PCA is applied for obtaining the features dimensionality reduction. The experimental performance based on real radar shown in (Tivive et al., 2015) demonstrates the effectiveness of the method, and the improvement that the use of log-Gabor filter introduced with respect the normal Gabor filter for the specific classification challenge.

3.7 Summary

In this Chapter, an overview of the recent signal processing tools for target signature and features extraction for ATR was presented. A particular focus was on mD based classification approaches and on feature extraction techniques for image classification.

In Section 3.2 the principal tools for the time-frequency analysis of radar return were discussed. Specifically, the most used TFD for obtaining mD profile of a target which exhibits micro-motions were presented in details, highlighting the several trade-offs that each distribution poses. The STFT takes advantage of the implementation through FFT; however, there is a trade off between the time and frequency resolution. The WVD is a quadratic distribution which computes the FT of the signal autocorrelation; it guarantees finer resolutions in both time and frequency with respect the STFT, but it introduces into time-frequency plane cross-terms between correlated components, which may represent interference for a classification algorithm. The PWD and S-method distribution allow to mitigate cross terms with respect to the WVD, by windowing the autocorrelation in the time domain, the first, and both in time and frequency domains the second. Moreover, the basic principles of spectrogram, CVD and cepstogram as mD based target signature were introduced, emphasizing on their advantages in being used for ATR. The spectrogram is used to extract information on the instantaneous mD components within the signal. The CVD shows the the mD shifts and their repetition rates which are present within the analysed signal, being independent on the initial phase of the micro-motion with respect to the spectrogram. The cepstogram is used in presence of targets moving very fast, e.g. drones with very fast rotor blades, such that the spectrogram and CVD have not enough resolution for showing all the mD components distinctly.

The theory of the RT and its inverse function was introduced in Section 3.3, focusing on their application for RI. Specifically, the use of IRT as tool for focusing the radar image of a target with rotational parts has been demonstrated. However, the capability of IRT to extract the mD components from a TFD of radar return or from a sequence of HRRPs has been also used for the extraction of micro-motion parameters (e.g. angular velocity) and for the imaging of rotating target.

Following, the concepts of pZ moments and Kr moments were introduced in the context of image classification. Computed by projecting an image onto two bases of orthogonal polynomials differently defined, both the two mentioned types of image moments have been employed satisfactorily for the identification of target from SAR images thanks their proprieties of scale, translation and rotation invariance. Additionally, the evaluation of pZ moments have been proposed for the extraction of a feature vector in a mD based classification framework. The framework, based on the projection of the CVD obtained from radar return onto a base of pZ polynomials, have been tested in contexts of helicopter and human gaits recognition with success. Finally, the use of 2D Gabor Filter for targets recognition from mD profiles is discussed. In Chapter 4 the described mD based classification framework is tested in the specific challenge of Ballistic Targets (BTs) classification, for discriminating between missile warheads and decoys. In addition, the framework is improving by considering different feature extraction approaches, based on Kr moments and 2D Gabor Filters, which can be singularly used according to the allocated resources for the classification. A novel technique for the same classification challenge is presented in Chapter 5, based on the computation of IRT on a sequence of HRRPs, in combination with of pZ moments evaluation for the features extraction.

Chapter 4

Micro-Doppler based Recognition of BTs

4.1 Introduction

The capability to recognize ballistic targets is an important challenge which has attracted increasing interest in the past few years. During the mid-course phase missiles release both warheads and some other objects (decoys) with the aim to confuse the exo-atmospheric interceptors. Therefore, it is important to distinguish between warheads and decoys in order to maximize the ammunition capabilities. Warheads and decoys exhibit different micro-motions that, if appropriately exploited, may be used to distinguish them (Weiner and Rocklin, 1994). Specifically, the warheads are typically spin-stabilized to ensure that they do not deviate from the intended ballistic trajectories (Bankman et al., 2001). However, warheads exhibit precession and nutation motion due to the effect of the Earth's gravity. By contrast, decoys tumble when released by the missiles due to the atmospheric resistance, the gravity and the absence of a spinning motion (Sessler et al., 2000; Weiner and Rocklin, 1994). Therefore, micro-Doppler (mD) analysis can be used for the purpose of information extraction for target classification, because different behaviours (motions) produce different signatures.
The anti-ballistic missile interceptors are usually equipped with an OnBoard Computer (OBC) to perform control, guidance, target data estimation, mission sequencing and various other critical operations during all the flight, from prelaunch to till impact (Rathore et al., 2014). However, all these operations are made harder due to the high velocities of the moving target and the interceptor which demands higher data update rates from sensors, high frequent commands

to control system. For these reasons fast and low computational classification algorithms are required to optimally exploit the available resources.
In this Chapter, in order to understand the micro-Doppler (mD) shifts, a high frequency based signal model for the targets of interest is developed that incorporates the effects of occlusion for all the scattering points. Then, a laboratory experiment is conducted for the validation of mathematical model. Furthermore, a framework based on the processing of the Cadence Velocity Diagram (CVD) presented in (Clemente et al., 2015b) for radar mD classification is proposed for performing the classification of BTs, in combination with different information extraction techniques. In particular, the classification framework is updated, proposing four different techniques for features extraction from the CVD which require different computational complexity, making the algorithm adaptable to defence system available resources. The first approach is based on the statistical characteristics of the unit area function obtained by averaging and normalizing the CVD. The second method is from (Clemente et al., 2015b) based on the use of pZ moments, while the third one consists of the Kr moments computation of the CVD. The last method is based on the use of the 2D Gabor filters. All approaches are tested on both simulated and experimental data.

4.2 Radar Return from Ballistic Target

In this Section, the mathematical model for the radar return from a BT with micro-motions is described in detail. Specifically, from (2.30) and (2.31) in Section 2.5, it is clear that the mD components due to motion of each scattering point is evaluated defining the micro-motion matrix, $\boldsymbol{T}_m$, according to the target micro-motions.

Warheads

The missile warheads exhibit precession and nutation during the flight onto the exo-atmospheric part of their sub-orbits. In particular, the precession is composed by two micro-motions: the spinning of the target around its symmetry axis, and the conical movement, such that the symmetry axis rotates conically around the precession axis. The nutation is an oscillation of the symmetry axis perpendicular with respect the precession axis. Therefore, in the case of warheads, the matrix $\boldsymbol{T}_m$ is given by the product of three terms, namely

$$\boldsymbol{T}_m = \boldsymbol{R}_c \boldsymbol{R}_s \boldsymbol{R}_n \tag{4.1}$$

where the matrices $\boldsymbol{R}_c$ and $\boldsymbol{R}_s$ depend on conical movement and spinning, respectively, while $\boldsymbol{R}_n$ depends on nutation. Since the matrices $\boldsymbol{R}_c$ and $\boldsymbol{R}_s$ are related to rotation movements, they can be obtained by the Rodrigues formula (Hongwei et al., 2010; Murray et al., 1994)

$$\begin{aligned}\boldsymbol{R}_c &= \hat{\boldsymbol{I}} + \hat{\boldsymbol{E}}(\widehat{\boldsymbol{w}_c})\sin(\Omega_c\, t) + \hat{\boldsymbol{E}}^2(\widehat{\boldsymbol{w}_c})\,(1-\cos(\Omega_c\, t))\\ \boldsymbol{R}_s &= \hat{\boldsymbol{I}} + \hat{\boldsymbol{E}}(\widehat{\boldsymbol{w}_s})\sin(\Omega_s\, t) + \hat{\boldsymbol{E}}^2(\widehat{\boldsymbol{w}_s})\,(1-\cos(\Omega_s\, t))\end{aligned} \tag{4.2}$$

where $\hat{\boldsymbol{I}}$ is the identity matrix of dimension 3×3, Ω_c and $\widehat{\boldsymbol{w}_c}$ are the norm and the direction of the angular velocity vector $\boldsymbol{w}_c$ of conical rotation, Ω_s and $\widehat{\boldsymbol{w}_s}$ are the norm and the direction of the angular velocity vector $\boldsymbol{w}_s$ of spinning, and with $\hat{\boldsymbol{E}}(\cdot)$ the *skew symmetric matrix* defined as (Hongwei et al., 2010)

$$\hat{\boldsymbol{E}}(\boldsymbol{u}) = \begin{bmatrix} 0 & -u_z & u_y \\ u_z & 0 & -u_x \\ -u_y & u_x & 0 \end{bmatrix} \tag{4.3}$$

with $\boldsymbol{u} = [u_x, u_y, u_z]^T$ a generic vector.

In order to evaluate the matrix $\boldsymbol{R}_n$, a new coordinate system $(\widehat{x_n}, \widehat{y_n}, \widehat{z_n})$ has to be considered. The unit directional vector that identifies the symmetry axis of the conical warhead with respect to the principal system $(\hat{X}, \hat{Y}, \hat{Z})$ is defined as follows

$$\hat{\boldsymbol{z}}_0 = \boldsymbol{R}_0\, \boldsymbol{a}_0 \tag{4.4}$$

where $\boldsymbol{a}_0 = [0, 0, 1]^T$, and $\boldsymbol{R}_n$ the Euler matrix which defines the initial position of the symmetry axis into the initial instant of time t_0. Due to the precession, the coordinates of target axis depend on time for its rotation during the conical motion, namely

$$\hat{\boldsymbol{z}}_t = \boldsymbol{R}_c \boldsymbol{R}_0\, \boldsymbol{a}_0 \tag{4.5}$$

where $\hat{\boldsymbol{z}}_t$ represents the unit directional vector at time instant t. Considering the cone axis oscillating in the plane given by the vectors $\hat{\boldsymbol{z}}_t$ and $\widehat{\boldsymbol{w}_c}$, the new reference system $(\widehat{x_n}, \widehat{y_n}, \widehat{z_n})$ is chosen so that $\widehat{\boldsymbol{x}_n}$ coincides with the precession axis (hence, with $\widehat{\boldsymbol{w}_c}$) while the $\widehat{\boldsymbol{z}_n}$ axis is perpendicular to the oscillation plane, as shown in Fig. 4.1. The expressions of the three unit directional vectors of the new reference system are

$$\widehat{\boldsymbol{x}_n} = \widehat{\boldsymbol{w}_c},, \qquad \widehat{\boldsymbol{z}_n} = \widehat{\boldsymbol{w}_c} \times \hat{\boldsymbol{z}}_t, \qquad \widehat{\boldsymbol{y}_n} = \widehat{\boldsymbol{x}_n} \times \widehat{\boldsymbol{z}_n}. \tag{4.6}$$

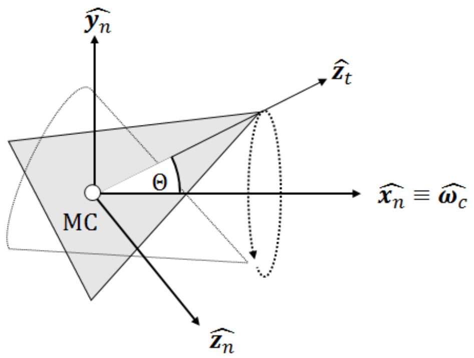

Fig. 4.1 The reference system $(\widehat{x_n},\ \widehat{y_n},\ \widehat{z_n})$.

with $\|\widehat{\boldsymbol{w}_c}\| = \|\widehat{\boldsymbol{z}_t}\| = 1$. Considering the three unit directional vectors $(\widehat{\boldsymbol{x}}, \widehat{\boldsymbol{y}}, \widehat{\boldsymbol{z}})$ of the system $(\hat{X},\ \hat{Y},\ \hat{Z})$, the transition matrix $\boldsymbol{A}_n$, which represents the relationship between the previous and the new system, is given by

$$(\widehat{\boldsymbol{x}_n}, \widehat{\boldsymbol{y}_n}, \widehat{\boldsymbol{z}_n}) = (\widehat{\boldsymbol{x}}, \widehat{\boldsymbol{y}}, \widehat{\boldsymbol{z}})\, \boldsymbol{A}_n. \tag{4.7}$$

Since the reference coordinates $(\hat{X},\ \hat{Y},\ \hat{Z})$ are the natural coordinates, which means that $(\widehat{\boldsymbol{x}}, \widehat{\boldsymbol{y}}, \widehat{\boldsymbol{z}})$ form a 3×3 identity matrix, then matrix $\boldsymbol{A}_n$ is obtained as follows

$$\boldsymbol{A}_n = (\widehat{\boldsymbol{x}_n}, \widehat{\boldsymbol{y}_n}, \widehat{\boldsymbol{z}_n}) \tag{4.8}$$

from which it is clear that the transition matrix is orthonormal. The position vector of a generic point in the new reference system at initial time instant t_0 is

$$\boldsymbol{r}_{n_p}(t_0) = [x_{n_p}(t_0),\ y_{n_p}(t_0),\ z_{n_p}(t_0)]^T\ = \boldsymbol{A}_n^{-1}\, \boldsymbol{r}_p(t_0). \tag{4.9}$$

Considering the case of a sinusoidal oscillation of the precession angle Θ, given by the angle between the directions of conical rotation and spinning angular velocity vectors, it follows

$$\Delta\Theta = \Delta\Theta(t) = \Theta_n \sin(\Omega_n t + \Omega_{n_0}) \tag{4.10}$$

where Ω_n and Θ_n represent the pulsation and the maximum amplitude of the oscillation, respectively, and Ω_{n_0} is the nutation initial phase. Since in the new reference system the oscillation of the cone axis is a rotation around the $\widehat{\boldsymbol{z}_n}$ axis, the position vector $\boldsymbol{r}_{n_p}(t)$ at the instant t is

$$\boldsymbol{r}_{n_p}(t) = \boldsymbol{B}_n \boldsymbol{r}_{n_p}(t_0) = \boldsymbol{B}_n\, \boldsymbol{A}_n^{-1}\, \boldsymbol{r}_p(t_0) \tag{4.11}$$

where $\boldsymbol{B}_n$ is the Euler rotation matrix around $\widehat{\boldsymbol{z}_n}$ axis given by

$$\boldsymbol{B}_n = \begin{bmatrix} \cos(\Delta\Theta) & -\sin(\Delta\Theta) & 0 \\ \sin(\Delta\Theta) & \cos(\Delta\Theta) & 0 \\ 0 & 0 & 1 \end{bmatrix}. \tag{4.12}$$

The position vector in the natural coordinates system is given by

$$\boldsymbol{r}_t = \boldsymbol{A}_n \, \boldsymbol{r}_{n_t} = \boldsymbol{A}_n \, \boldsymbol{B}_n \, \boldsymbol{A}_n^{-1} \, \boldsymbol{r}_{t_0}. \tag{4.13}$$

Finally, the nutation matrix $\boldsymbol{R}_n$ can be written as

$$\boldsymbol{R}_n = \boldsymbol{A}_n \, \boldsymbol{B}_n \, \boldsymbol{A}_n^{-1}. \tag{4.14}$$

Decoys

When the missile releases lightweight decoys, they starts to tumble due to the Earth gravity. The tumbling is defined as the rotation of a decoy such that the angular velocity vector is perpendicular to the symmetry axis of the object. The matrix $\boldsymbol{T}_m$ for the tumbling decoys is given by Rodrigues formula

$$\boldsymbol{T}_m = \boldsymbol{T}_r = \hat{\boldsymbol{I}} + \hat{\boldsymbol{E}}(\widehat{\boldsymbol{w}_r}) \sin(\Omega_r \, t) + \hat{\boldsymbol{E}}^2(\widehat{\boldsymbol{w}_r}) \, (1 - \cos(\Omega_r \, t)) \tag{4.15}$$

with Ω_r and $\widehat{\boldsymbol{w}_r}$ the norm and the direction of the angular velocity vector $\boldsymbol{w}_r$ of decoy rotation.

4.2.1 Approximation at relative EM far field

When the target is at relatively long distance, according to the relation in (2.33), the relative distance between the radar and the i-th scatterer can be approximated as follows

$$\mathrm{r}_i \approx \|\boldsymbol{r}_{\mathrm{MC}}^{radar}\| + < \boldsymbol{v}, \boldsymbol{n} > t + < \boldsymbol{r}_i, \boldsymbol{n} > \tag{4.16}$$

with $\boldsymbol{r}_{\mathrm{MC}}^{radar}$ and $\boldsymbol{r}_i$ the position vectors of the MC and the i-th scatterer with respect the radar system, respectively, $\boldsymbol{v}$ the target bulk velocity vector and $\boldsymbol{n}$ the direction of LOS, and where the operator $< \cdot, \cdot >$ defines the scalar product between the two vectors. Considering the coordinate system ($\tilde{x}$,$\tilde{y}$,$\tilde{z}$) shown in Fig. 4.2, which is centred into MC, and such that $\tilde{x} \equiv \hat{\boldsymbol{z}}_t$ and the vector $\boldsymbol{r}_{\mathrm{MC}}^{radar}$ belongs to the plane $\tilde{x}\tilde{y}$, the projection along the LOS of the distance between the i-th scatterer and the MC is given by

$$< \boldsymbol{r}_i, \boldsymbol{n} >= -\tilde{x}_i \cos(\alpha) - \tilde{y}_i \sin(\alpha) \tag{4.17}$$

where $\tilde{x}_i$ and $\tilde{y}_i$ are the $(\tilde{x}, \tilde{y})$-coordinates of the i-th scatterer, and the aspect angle α is the angle between the target symmetry axis and the LOS direction. The latter is evaluated as

$$\alpha = \alpha(t) = \cos^{-1}\left(< \hat{\boldsymbol{z}}_t, \boldsymbol{n} >\right) \tag{4.18}$$

with $\|\hat{\boldsymbol{z}}_t\| = \|\boldsymbol{n}\| = 1$. The received complex signal can be written as

$$s_{rx}(t) = e^{j\frac{4\pi}{\lambda}t} e^{j\phi_{\mathrm{MC}}} e^{j\phi_{bD}(t)} \sum_{i=1}^{N_p} \sqrt{\sigma_i}(t) e^{j\phi_i} \tag{4.19}$$

with ϕ_{MC} and $\phi_{bD}(t)$ the phase rotations due to the initial MC range and bulk motion, given by

$$\phi_{\mathrm{MC}} = -j\frac{4\pi}{\lambda}\|\boldsymbol{r}_{\mathrm{MC}}^{radar}\| \tag{4.20}$$

$$\phi_{bD}(t) = -j\frac{4\pi}{\lambda} < \boldsymbol{v}, \boldsymbol{n} > t \tag{4.21}$$

and where ϕ_i is the phase of the complex coefficient of the i-th scatterer, given by

$$\phi_i = j\frac{4\pi}{\lambda}\left(\check{x}_i \cos(\alpha) + \check{y}_i \sin(\alpha)\right) \tag{4.22}$$

The direction of LOS can be expressed in terms of elevation and azimuth angle with respect to the angular velocity vector of warhead conical rotation or decoy tumbling. Let us consider the coordinate system $(\hat{u}, \hat{v}, \hat{w})$ shown in Fig. 4.3 such that the axis $\hat{u}$ corresponds with the unit angular velocity vector of conical rotation $\widehat{\omega_c}$, and the plane $\hat{u}\hat{v}$ contains the symmetry axis of the object in the initial observation time instant $\hat{\boldsymbol{z}}_0$. The vectors $\hat{\boldsymbol{z}}_t$ and $\boldsymbol{n}$ in the new coordinate system can be written as

$$\boldsymbol{n} = [\cos(\angle \mathrm{El})\cos(\angle \mathrm{Az}),\ \cos(\angle \mathrm{El})\sin(\angle \mathrm{Az}), \sin(\angle \mathrm{El})]^T \tag{4.23}$$

$$\hat{\boldsymbol{z}}_t = [\cos(\Theta + \Delta\Theta),\ \sin(\Theta + \Delta\Theta)\sin(\Omega_c t), \sin(\Theta + \Delta\Theta)\cos(\Omega_c t)]^T \tag{4.24}$$

with $\angle$El and $\angle$Az the elevation and azimuth angle of radar position, respectively. Substituting (4.23) and (4.24) into (4.18), the aspect angle can be written as

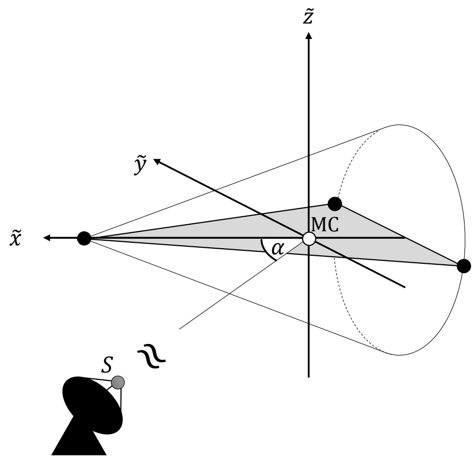

Fig. 4.2 Representations of the reference system ($\tilde{x}$,$\tilde{y}$,$\tilde{z}$).

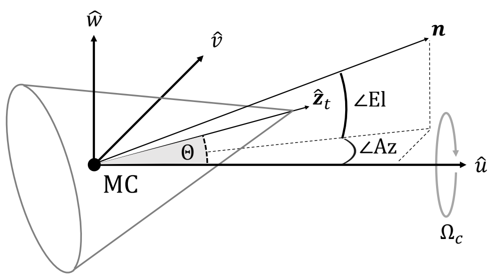

Fig. 4.3 Representations of the reference system ($\hat{u}$, $\hat{v}$, $\hat{w}$).

$$\begin{aligned}\alpha(t) = \cos^{-1}(& \cos(\angle\mathrm{El})\cos(\angle\mathrm{Az})\cos(\Theta+\Delta\Theta)+ \\ & \cos(\angle\mathrm{El})\sin(\angle\mathrm{Az})\sin(\Theta+\Delta\Theta)\sin(\Omega_c t)+ \\ & \sin(\angle\mathrm{El})\sin(\Theta+\Delta\Theta)\cos(\Omega_c t))\end{aligned} \tag{4.25}$$

It is worth noting that in the case of tumbling decoy, since the angular velocity vector is perpendicular to the symmetry axis of the target, the aspect angle can be calculated by (4.25) by applying the following equivalences

$$\Theta = \frac{\pi}{2} \tag{4.26}$$

$$\Delta\Theta = 0 \tag{4.27}$$

$$\Omega_c = \Omega_r = \|\omega_r\| \tag{4.28}$$

In this analysis two possible shapes are considered for the warhead, which are namely cone and cone with triangular fins, while three shapes for decoy, namely cone, cylinder and sphere. The number of scattering points located on the target depends on the considered shape. In particular, they are generally located in proximity of the edges of the target section obtained by the intersection between the target volume and the incident plane, defined as the plane containing both the symmetry axis and the LOS.
For simplicity, in this analysis it is assumed that the phase rotations due to target range and bulk motion are compensated, and the singular scattering proprieties of each scatterer are not taken into account, considering the modulus of scattering coefficients as a binary function whose possible values are $\{0, 1\}$. Specifically, this function depends on the aspect angle $\alpha(t)$, and its value is 1 when there is a LOS for the scattering points, and 0 otherwise. Finally, it is assumed that the radar resolution allows to distinguish different targets in range-azimuth such that the return from different target can be processed distinctly. These simplifier approximations allow us to focus the analysis on the mD components that characterized the return from a target.

Cone

For the conical targets three principal scattering points are considered: the first is in correspondence of the cone tip; the other two points are located on the intersection between the circumference at cone bottom and the incident plane $(\tilde{x}\tilde{y})$, as shown in Fig. 4.6a. The coordinates of the three points into system $(\tilde{x}, \tilde{y}, \tilde{z})$ are

$$\begin{aligned} P_1(\tilde{x}, \tilde{y}, \tilde{z}) = &\ (\ \ h_1, \quad\ \ 0, \ \ 0) \\ P_2(\tilde{x}, \tilde{y}, \tilde{z}) = &\ (-h_2, \quad R_b, \ \ 0) \\ P_3(\tilde{x}, \tilde{y}, \tilde{z}) = &\ (-h_2, \ -R_b, \ \ 0) \end{aligned} \tag{4.29}$$

where h_1 and h_2 are the distance of the cone tip and centre of the cone base with respect to the MC, and R_b is the base radius.
Let us consider the possible variation of $\alpha(t)$ in the interval $[0, \pi]$. For the cone, $\sqrt{\sigma_i}$ is 0 for P_1 when $\alpha(t) \in [\pi - \gamma, \pi]$ and for P_3 when $\alpha(t) \in [\gamma, \pi/2]$, with γ the semi-angle of the cone; while for P_2 the occlusion never occurs for $\alpha(t) \in [0, \pi]$. Then $\sqrt{\sigma_2} = 1$ with $\alpha(t) \in [0, \pi]$. The values of the coefficients modulus on varying the aspect angle for the cone scatterers are synthesized in Table 4.1.

Table 4.1 Modulus of the scattering coefficients for the three principal scattering points P_1, P_2, and P_3 of the cone, with respect to the aspect angles α.

	$\sqrt{\sigma_1}(\alpha)$	$\sqrt{\sigma_2}(\alpha)$	$\sqrt{\sigma_3}(\alpha)$
$\alpha < \gamma$	1	1	1
$\gamma \leq \alpha < \frac{\pi}{2} - \gamma$	1	1	0
$\frac{\pi}{2} - \gamma \leq \alpha < \frac{\pi}{2}$	1	1	0
$\frac{\pi}{2} \leq \alpha < \pi - \gamma$	1	1	1
$\pi - \gamma \leq \alpha \leq \pi$	0	1	1

Cone plus fins

For the the cone with fins, a scattering point in correspondence of the tip of each triangular fin is considered in addition to the main three scatterers described above. In case all the fins tips move on the plane containing the cone base, the coordinates into $(\tilde{x}, \tilde{y}, \tilde{z})$ system are given by

$$P_{fin_i}(\tilde{x}, \tilde{y}, \tilde{z}) = (-h_2, \quad R_b + H_{fin} \cos(\varpi_i), \quad R_b + H_{fin} \sin(\varpi_i)) \tag{4.30}$$

with $i = 1, \cdots, N_{fin}$, N_{fin} is the number of fins, H_{fin} the fin height and ϖ_i is the angle between the i-th fin and $\tilde{y}$ axis, given by

$$\varpi_i = \Omega_s t + \Omega_{s_0} + \frac{2\pi i}{N_{fin}} \tag{4.31}$$

with Ω_{s_0} the initial phase of warhead spinning.
The occlusion function for the fins tips does not only depend on the aspect angle α, but also on the spinning of the cone as it can cause the fins to be occluded behind the warhead body. In order to evaluate the occlusion function for the fins, the physical optics approximation is considered. This is a valid approximation given the high frequency at which the radar system operates. Since the targets of interest are within the Fraunhofer zone (Hongwei et al., 2010), the rays that strike the targets can be considered as parallel. The occlusion of fins occur for $\alpha(t) \in [\gamma_{fin}, \pi/2]$, where γ_{fin} is the semi-angle of an isosceles triangle whose height is equal to the height of the cone, and the base is equal to the diameter of circumference drawn by rotating fins. Therefore, the coefficient $\sqrt{\sigma_{fin_i}}$ is 1 when $\alpha(t) \in [0, \gamma_{fin}]$ and for $\alpha(t) > \pi/2$. The value of scattering coefficient for $\alpha(t) \in [\gamma_{fin}, \pi/2]$ is calculated by comparing the $\tilde{z}$-coordinate of P_{fin_i} with a

suitable threshold as follows

$$\sqrt{\sigma_{fin_i}}(t) = \begin{cases} 1 & \text{if } \tilde{z}_{fin_i}(t) < \mathcal{X} \\ 0 & \text{if } \tilde{z}_{fin_i}(t) \geq \mathcal{X} \end{cases} . \tag{4.32}$$

where $\mathcal{X} = \mathcal{X}(\alpha)$ is the threshold, which depends on the aspect angle, hence on the time. In order to evaluate $\mathcal{X}$, it is necessary to calculate when the straight line joining the radar and tip of the fin becomes tangential to the cone surface, as represented in Fig. 4.4. Considering the reference system ($\tilde{x}_0$,$\tilde{y}_0$,$\tilde{z}_0$), obtained

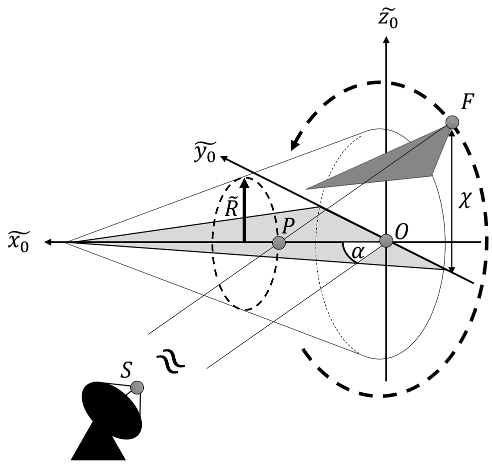

Fig. 4.4 Representations of the reference system ($\tilde{x}_0$,$\tilde{y}_0$,$\tilde{z}_0$).

moving the origin of system ($\tilde{x}$,$\tilde{y}$,$\tilde{z}$) into centre of cone bottom as shown in Fig. 4.4, the position vectors of the generic fin tip $\overline{OF}$, and of the radar $\overline{OS}$ are

$$\begin{aligned} \overline{OF} &= [0, (R_b + H_{fin})\cos(\varpi_i), (R_b + H_{fin})\sin(\varpi)]^T \\ \overline{OS} &= [D'\cos(\alpha), -D'\sin(\alpha), 0]^T \end{aligned} \tag{4.33}$$

with ϖ the angle of the fin tip with respect to the axis $\tilde{y}_0$, and where

$$D' \simeq D + h_2 \cos(\alpha) \tag{4.34}$$

with $D = \|\boldsymbol{r}_{cm}^{radar}\|$ the distance between the radar and the mass centre.
The conical surface is represented by the function:

$$f(\tilde{x}_0, \tilde{y}_0, \tilde{z}_0) = \tilde{R}^2 - \left(\tilde{y}_0^2 + \tilde{z}_0^2\right) = R_b^2 \left(1 - \frac{\tilde{x}_0}{H}\right)^2 - \left(\tilde{y}_0^2 + \tilde{z}_0^2\right) \tag{4.35}$$

where $\tilde{R} = \tilde{R}(\tilde{x}_0)$ is the radius of the generic cone section given by

$$\tilde{R}(\tilde{x}_0) = R_b \left(1 - \frac{\tilde{x}_0}{H}\right) \tag{4.36}$$

where $H = h_1 + h_2$ is the cone height. Considering the generic point of the cone, P, whose position vector is

$$\overline{OP} = \left[H\left(1 - \frac{\tilde{R}}{R_b}, \tilde{R}\cos(\xi), \tilde{R}\sin(\xi)\right)\right]^T \tag{4.37}$$

where ξ is the position angle with respect to $\tilde{y}_0$ axis, the lines from P to F and S are

$$\overline{PF} = \overline{OP} - \overline{OF} = \begin{bmatrix} H\left(1 - \dfrac{\tilde{R}}{R_b}\right) \\ \tilde{R}\cos(\xi) - (R_b + H_{fin})\cos(\varpi) \\ \tilde{R}\sin(\xi) - (R_b + H_{fin})\sin(\varpi) \end{bmatrix} \tag{4.38}$$

$$\overline{PS} = \overline{OP} - \overline{OS} = \begin{bmatrix} H\left(1 - \dfrac{\tilde{R}}{R_b}\right) - D'\cos(\alpha) \\ \tilde{R}\cos(\xi) + D'\sin(\alpha) \\ \tilde{R}\sin(\xi) \end{bmatrix} \tag{4.39}$$

respectively. In order to evaluate the occlusion threshold, it is necessary to evaluate the angle ϖ and ξ such that $\overline{PF}$ and $\overline{PS}$ are both tangent to the conical surface as follows

$$\begin{cases} \left[\frac{\partial f}{\partial \tilde{x}_0}, \frac{\partial f}{\partial \tilde{y}_0}, \frac{\partial f}{\partial \tilde{z}_0}\right]^T \cdot \overline{PF} = 0 \\[2ex] \left[\frac{\partial f}{\partial \tilde{x}_0}, \frac{\partial f}{\partial \tilde{y}_0}, \frac{\partial f}{\partial \tilde{z}_0}\right]^T \cdot \overline{PS} = 0 \end{cases} \tag{4.40}$$

where the components of gradient vector for a generic cone point are evaluated from (4.35) as

$$\begin{aligned} \frac{\partial f}{\partial \tilde{x}_0} &= \frac{-2R_b^2}{H}\left(1 - \frac{\tilde{x}_0}{H}\right) = \frac{-2R_b\tilde{R}}{H}; \\ \frac{\partial f}{\partial \tilde{y}_0} &= -2y_{f_0} = -2\tilde{R}\cos(\xi); \\ \frac{\partial f}{\partial \tilde{z}_0} &= -2z_{f_0} = -2\tilde{R}\sin(\xi); \end{aligned} \tag{4.41}$$

with

$$\tilde{x}_0 = H\left(1 - \frac{\tilde{R}}{R_b}\right). \qquad \tilde{y}_0 = \tilde{R}\cos(\xi); \qquad \tilde{z}_0 = \tilde{R}\sin(\xi); \tag{4.42}$$

From (4.40) and (4.41) follows

$$\begin{cases} (-2\tilde{R}) \quad [R_b - (R_b + H_{fin}) \cos(\xi - \varpi)] = 0 \\ (-2\tilde{R}) \quad \left[D' \sin(\alpha) \cos(\xi) + R_b - \dfrac{R_b D' \cos(\alpha)}{H} \right] = 0 \end{cases} \tag{4.43}$$

which leads to

$$\begin{cases} \cos(\xi - \varpi) = \frac{R_b}{R_b + H_{fin}} \\ \cos(\xi) = \left[\frac{D \cos(\alpha) R_b}{H} - R_b \right] \frac{1}{D \sin(\alpha)} = \left[\frac{\tan(\gamma)}{\tan(\alpha)} - \frac{R_b}{D \sin(\alpha)} \right] \end{cases} \quad \forall \tilde{R} > 0 \tag{4.44}$$

Finally, the threshold is given by

$$\mathcal{X} = (H_{fin} + R_b) \cos(\varpi^*) \tag{4.45}$$

where

$$\varpi^* = \cos^{-1} \left[\frac{\tan(\gamma)}{\tan(\alpha)} - \frac{R_b}{D \sin(\alpha)} \right] - \cos^{-1} \left[\frac{R_b}{R_b + H_{fin}} \right] \tag{4.46}$$

When the radar LOS is perpendicular to the target symmetry axis, a particular assumption for the threshold is taken into consideration when the height of the fin is such that

$$\varpi^*(\alpha, H_{fin}) > \frac{\pi}{N_{fin}}, \qquad \text{with } \alpha = \frac{\pi}{2} \tag{4.47}$$

In this case, the $\mathcal{X}$ for $\alpha = \pi/2$ is given by

$$\mathcal{X} = (H_{fin} + R_b) \cos\left(\frac{\pi}{N_{fin}}\right) \tag{4.48}$$

Fig. 4.5 shows how the threshold values varies as a function of aspect angle for the cone dimensions H and R_b of 1 m and 0.375 m, respectively, fin height $H_{fin} = 0.200$ m and at a distance of 150 km. It is worth noting, that in the evaluation of the occlusion of fins tips, the effect of the fin area is not taken into account for simplicity.

Cylinder

The cylindrical target is represented by four principal scattering points shown in Fig. 4.6b, specifically two for each base, taken by intersecting the circumferences

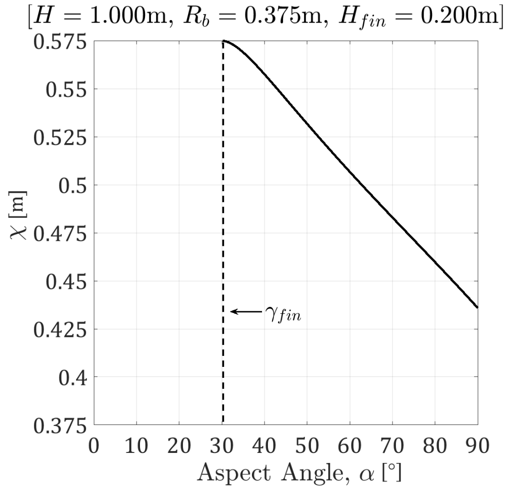

Fig. 4.5 Example of threshold values $\tilde{x}$ as a function of aspect angle (α).

at the bases and the incident plane, such that

$$\begin{aligned} P_1(\tilde{x},\tilde{y},\tilde{z}) &= (\ \tfrac{H}{2}, \quad R_b, \quad 0) \\ P_2(\tilde{x},\tilde{y},\tilde{z}) &= (-\tfrac{H}{2}, \quad R_b, \quad 0) \\ P_3(\tilde{x},\tilde{y},\tilde{z}) &= (-\tfrac{H}{2}, \quad -R_b, \quad 0) \\ P_4(\tilde{x},\tilde{y},\tilde{z}) &= (\ \tfrac{H}{2}, \quad -R_b, \quad 0) \end{aligned} \tag{4.49}$$

In Table 4.2 the coefficients modulus for the cylinder scatterers on varying the aspect angle are shown. In particular, $\sqrt{\sigma_i} = 0$ for P_1 when $\alpha(t) = \pi$; for P_2 when $\alpha(t) = 0$; for P_3 when $\alpha(t) \in [0, \pi/2]$ and for P_4 when $\alpha(t) \in]0, \pi]$.

Table 4.2 Modulus of the scattering coefficients for the four principal scattering points P_1, P_2, P_3 and P_4 of the cylinder, with respect to the aspect angles α.

	$\sqrt{\sigma_1}(\alpha)$	$\sqrt{\sigma_2}(\alpha)$	$\sqrt{\sigma_3}(\alpha)$	$\sqrt{\sigma_4}(\alpha)$
$\alpha = 0$	1	0	0	1
$0 < \alpha < \frac{\pi}{2}$	1	1	0	1
$\alpha = \frac{\pi}{2}$	1	1	0	0
$\frac{\pi}{2} < \alpha < \pi$	1	0	1	0
$\alpha = \pi$	0	1	1	0

Sphere

Due to its symmetry among all directions, a tumbling sphere, with rotation centre coinciding with sphere centre, does not lead to variation of relative radar view of its shape, hence no mD information can be extracted. In this analysis, it is considered for the spherical decoy a displacement d between the tumbling rotation centre and the sphere centre. Three scattering point are considered, as shown in Fig. 4.6c: two on the spherical surface along the symmetry axis, and one corresponding to the sphere centre. The coordinates of the three points in the coordinate system $(\tilde{x}, \tilde{y}, \tilde{z})$ are

$$\begin{aligned} P_1(\tilde{x}, \tilde{y}, \tilde{z}) = &\quad (d \qquad 0, \quad 0) \\ P_2(\tilde{x}, \tilde{y}, \tilde{z}) = &\quad (d + R_b, \quad 0, \quad 0) \\ P_3(\tilde{x}, \tilde{y}, \tilde{z}) = &\quad (d - R_b, \quad 0, \quad 0) \end{aligned} \tag{4.50}$$

with R_b the sphere radius.
For the sphere, the occlusion never occurs for P_1, such that $\sqrt{\sigma_1} = 1$, $\forall \alpha$. For the scatterer P_2, $\sqrt{\sigma_2} = 0$ when $\alpha(t) \in]\pi/2, \pi]$, and for P_3 $\sqrt{\sigma_3} = 0$ when $\alpha(t) \in]0, \pi/2[$. In Table 4.3 the values of coefficient modulus for the sphere scatterers on varying the aspect angle are summarized.

Table 4.3 Modulus of the scattering coefficients for the three principal scattering points P_1, P_2 and P_3 of the sphere, with respect to the aspect angles α.

	$\sqrt{\sigma_1}(\alpha)$	$\sqrt{\sigma_2}(\alpha)$	$\sqrt{\sigma_3}(\alpha)$
$\alpha = 0$	1	1	0
$0 < \alpha < \frac{\pi}{2}$	1	1	0
$\alpha = \frac{\pi}{2}$	1	1	1
$\frac{\pi}{2} < \alpha < \pi$	1	0	1
$\alpha = \pi$	0	0	1

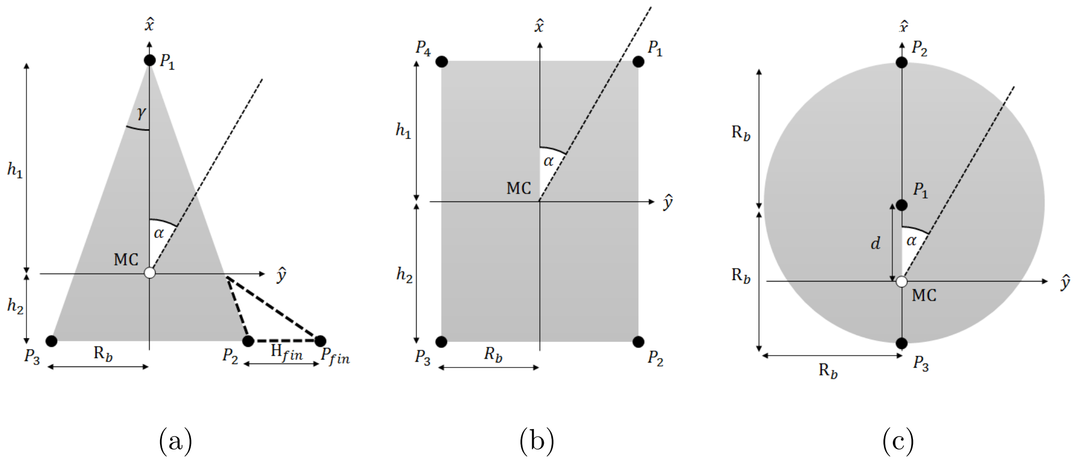

Fig. 4.6 Target shape model: (a) conical target; (b) cylindrical target; (c) spherical target.

4.3 Laboratory Experiment

In this Section the experiment conducted for the evaluation of mD effect due to BT micro-motions is described. The radar measurements containing the target motion information are acquired from scaled replicas of potential BTs with a 24 GHz CW coherent radar, which transmits in vertical polarization. The different target micro-motions are emulated by using a robotic manipulator and an additional rotational motor. A representation of configuration for the mD experiment is shown in Fig. 4.7. The robotic arm is used for introducing the conical rotation

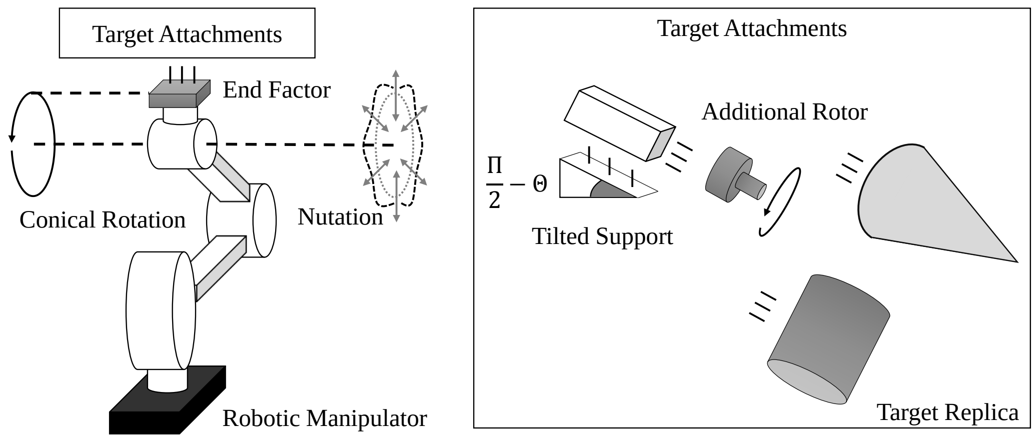

Fig. 4.7 Experiment configuration.

and the nutation for the warhead target, while the additional rotor is used for simulating the warheads spinning and the decoy tumbling. Specifically, the conical rotation is simulated with revolutions of the end factor of robotic arm, while the nutation is introduced by an sinusoidal oscillation of the radius of circumference where the end factor moves, by varying the angles of the robotic arm joints. The additional rotor is attached to the end factor of the robotic arm by a support which depends on the movement. Specifically, the rotor support is tilted of an angle equal to $\pi/2 - \Theta$ in case of precessing warhead, and the length of the support is set such that the target MC results stationary with respect the conical rotation. The decoy tumbling is simulated by using only the rotor. As it can be noted from pictures in Fig. 4.8, which shows the experiment set up, the robotic arm and the additional rotor are wrapped with an anechoic material, avoiding that the radar measurements contain mD information from moving objects different from the target. It has to be underlined that the trajectory of ballistic targets is not

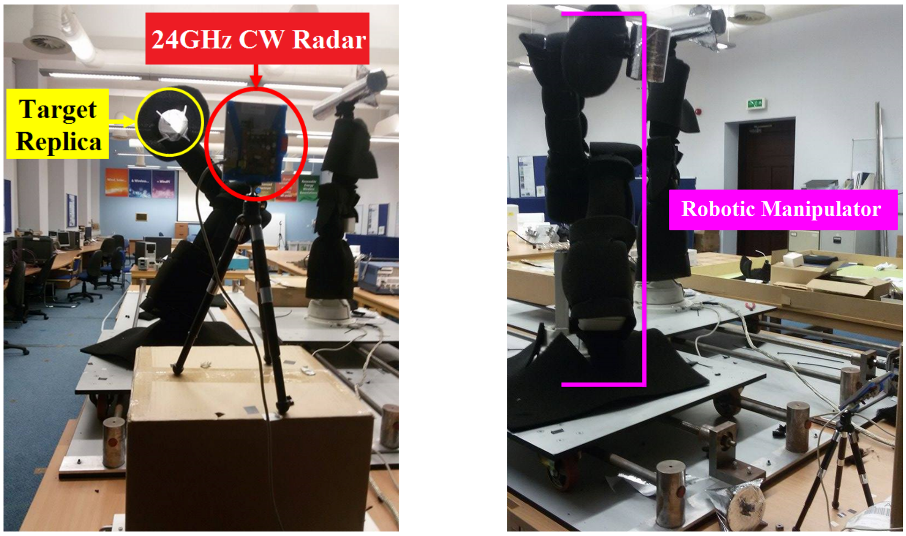

Fig. 4.8 Experiment set up.

taken into account in the experiment considering that the principal movement of the object is compensated. In this way, the classification is based only on the micro-motions of targets of interest.

The database for experimental data contains 5 acquisitions of 20 seconds for each target and for each of the possible 9 pair of azimuth and elevation angles formed using 3 values for both of them, namely $[0°; 45°; 90°]$.

Fig. 4.9 represents examples of spectrograms (in the dB scale) from a conical warhead and a warhead with fins, obtained by using both simulated and real data for different pairs of $(\angle\text{El}, \angle\text{Az})$. Differently from the definition given in Section 3.2.1, in this analysis the spectrogram is defined as the magnitude of the STFT of received signal, in order to reduce the differences between the weights of mD components within the target echo due to different scattering proprieties of each target scatterer. As observed in Fig. 4.9a, the spectrogram from simulated data allows the observations of echo modulations due to the conical rotation and nutation, but not from the spinning, due to the assumption of perfect symmetric conical target. In Fig. 4.9c, instead, it is also possible to observe some flashes due to the target spinning into spectrogram from the acquired data due to the fact that the target replica is not perfectly symmetric. Moreover, since the replicas are wrapped with aluminium foil, the surfaces are not completely smooth, introducing unexpected mD components into received signals. From Fig. 4.9b and Fig. 4.9d, it is possible to note that the two spectrograms show the same trend, where the precession leads to a modulation of the maximum Doppler which is due to the fins rotation. It is pointed out that the main differences between the simulated

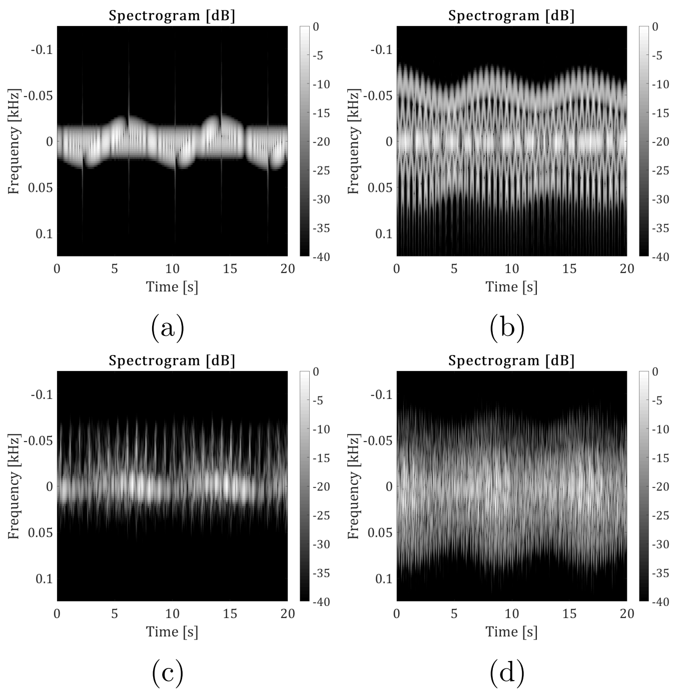

Fig. 4.9 Example of spectrogram obtained by a received signal from a warhead for different pairs of $(\angle\text{El}, \angle\text{Az})$: (a) simulated echo from conical warhead for $(90°, 0°)$; (b) simulated echo from conical warhead with fins for $(0°, 45°)$; (c) laboratory acquisition from from conical warhead $(90°, 0°)$; (d) laboratory acquisition from from conical warhead with fins for $(0°, 45°)$.

and the real cases for the analysed cases are due to the fact that in the presented signal model the RCS of each scatterer is not taken into account (hence, even the dependence on signal polarization), and the initial phase of different micro-motions exhibited by warheads is random in the both simulated and acquired signal.
Fig. 4.10 represents examples of spectrogram (in the dB scale) from the three different shapes considered for the decoys, from both simulated echo and laboratory acquisitions. Even in these cases, it is worth noting that the spectrograms from both simulated and acquired data show the same trends, in term of spectrogram periodicity and maximum Doppler shifts from main scatterers of tumbling objects. However, the absence of a RCS and overall EM model in the simulated data leads to some differences, as mentioned above.

4.4 Classification Framework

In this Section the algorithm proposed in (Clemente et al., 2015b) to extract mD based features for the target classification is reviewed, introducing the different

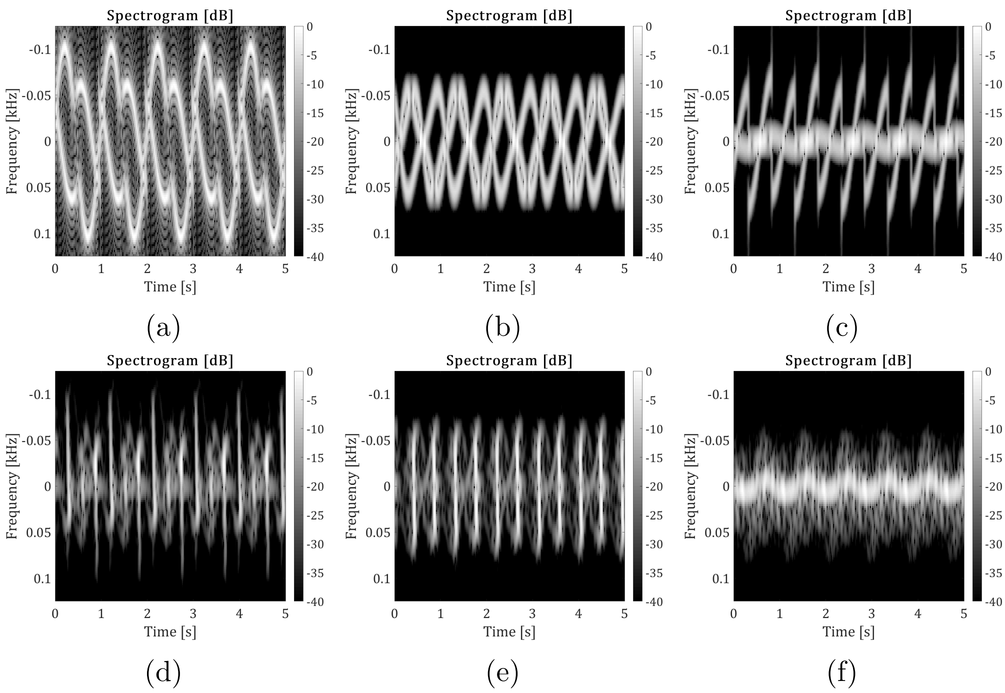

Fig. 4.10 Example of spectrogram obtained by a received signal from a decoy for different pairs of $(\angle\text{El}, \angle\text{Az})$: (a) simulated echo from conical decoy for $(90°, 0°)$; (b) simulated echo from cylindrical decoy for $(45°, 0°)$; (c) simulated echo from spherical decoy for $(0°, 90°)$; (d) laboratory acquisition from conical decoy for $(90°, 0°)$; (e) laboratory acquisition from cylindrical decoy for $(45°, 0°)$; (f) laboratory acquisition from spherical decoy for $(0°, 90°)$.

feature extraction approaches proposed in this chapter. Fig. 4.11 shows a block diagram of the classification method, outlining the common steps used for the four different approaches. The starting point of the proposed algorithm is the received

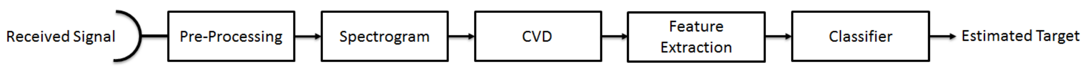

Fig. 4.11 Block diagram of the proposed algorithm.

signal $s_{rx}(n)$, with $n = 0, ..., N_s$, containing mD components and comprising of N_s signal samples. The received signal has to be pre-processed before the evaluation of the mD signature. The first block includes a notch filtering, down-sampling and normalization. The second step is the spectrogram computation of the pre-processed signal $\tilde{s}_{rx}(n)$

$$S_{\text{STFT}}(\nu, m) = \left| \sum_{n=0}^{N_s - 1} \tilde{s}_{rx}(n) w(n-m) \exp\left(-j2\pi\nu \frac{n}{N_s}\right) \right| \tag{4.51}$$

with $m = 0, \cdots, N_c - 1$, where ν is the normalized frequency and $w(\cdot)$ is the smoothing window. The spectrogram is a time-frequency distribution that allows the signal frequency time variations to be evaluated and it is chosen for its robustness with respect to the production of artefacts.

Observing Fig. 4.11, the next step consists in the extraction of the CVD, that is defined as the Fourier Transform of the spectrogram along each frequency bin

$$S_{\mathrm{CVD}}(\nu, \varepsilon) = \left| \sum_{m=0}^{N_c-1} S_{\mathrm{STFT}}(\nu, m) \exp\left(-j2\pi\varepsilon \frac{m}{N_c}\right) \right| \tag{4.52}$$

where ε is known as the cadence frequency. The CVD is chosen because it offers the possibility of using, as discriminants, the cadence of each frequency component within the signal and the maximum Doppler shift, and because the CVD is more robust than the spectrogram since it does not depends on the initial phase of moving objects. In Fig. 4.12a and Fig. 4.12b the CVDs obtained processing the spectrograms shown in Fig. 4.9c and Fig. 4.10d, obtained from the laboratory acquisitions of signal scattered by the conical warhead and decoy, respectively. It is worth noting that the zero cadence component in the CVDs is filtered out. Finally, the CVD has to be processed to extract a Q-dimensional feature vector

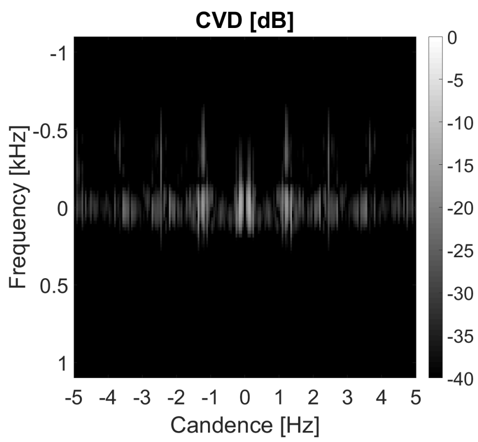

(a) warhead

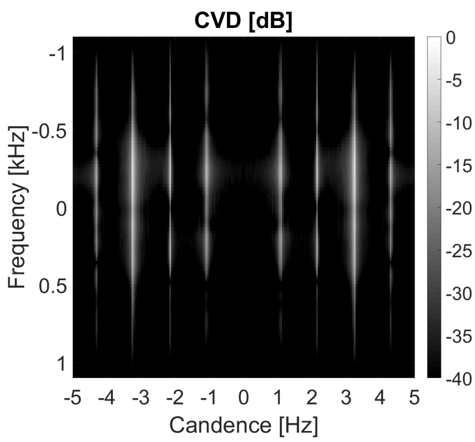

(b) decoy

Fig. 4.12 CVDs obtained processing the spectrograms from the conical warhead in Fig. 4.9c (a) and from the conical decoy in Fig. 4.10d.

$\boldsymbol{F} = [F_0, F_1, \cdots, F_{Q-1}]$, which can identify each class. Before classification, the vector $\boldsymbol{F}$ is normalized as follows

$$\tilde{\boldsymbol{F}} = \frac{\boldsymbol{F} - \varsigma_{\boldsymbol{F}}}{\zeta_{\boldsymbol{F}}} \tag{4.53}$$

where $\varsigma_{\boldsymbol{F}}$ and $\zeta_{\boldsymbol{F}}$ are the statistical mean and standard deviation of the vector $\boldsymbol{F}$, respectively.
The Feature Extraction block of Fig. 4.11 for the four different approaches will be described in the following subsections.

4.4.1 Features Vector Extraction

In this analysis 4 different feature vectors are considered for performing the target classification.

Averaged-CVD Based Feature Vector Approach

In the Averaged-CVD (ACVD) based approach, six features are computed from the ACVD. The starting point is the meaning of the CVD along each cadence bin; the resulting 1D function is then normalised to have a unit area. From the obtained 1D signature $\Lambda_{\text{avg}}(\varepsilon), \varepsilon = 0, \ldots, N_c - 1$, where N_c is the number of cadence bins, four statistical indices are extracted :

- Standard Deviation:

$$F_0 = \sqrt{\frac{1}{N_c - 1} \sum_{\varepsilon=0}^{N_c-1} \left[\Lambda_{\text{avg}}(\varepsilon) - \frac{1}{N_c} \sum_{\varepsilon=0}^{N_c-1} \Lambda_{\text{avg}}(\varepsilon) \right]^2} \tag{4.54}$$

- Kurtosis:

$$F_1 = \frac{\frac{1}{N_c} \sum_{\varepsilon=0}^{N_c-1} \left[\Lambda_{\text{avg}}(\varepsilon) - \frac{1}{N_c} \sum_{\varepsilon=0}^{N_c-1} \Lambda_{\text{avg}}(\varepsilon) \right]^4}{\left(\sqrt{\frac{1}{N_c-1} \sum_{\varepsilon=0}^{N_c-1} \left[\Lambda_{\text{avg}}(\varepsilon) - \frac{1}{N_c} \sum_{\varepsilon=0}^{N_c-1} \Lambda_{\text{avg}}(\varepsilon) \right]^2} \right)^4} - 3 \tag{4.55}$$

- Skewness:

$$F_2 = \frac{\frac{1}{N_c} \sum_{\varepsilon=0}^{N_c-1} \left[\Lambda_{\text{avg}}(\varepsilon) - \frac{1}{N_c} \sum_{\varepsilon=0}^{N_c-1} \Lambda_{\text{avg}}(\varepsilon) \right]^3}{\left(\sqrt{\frac{1}{N_c-1} \sum_{\varepsilon=0}^{N_c-1} \left[\Lambda_{\text{avg}}(\varepsilon) - \frac{1}{N_c} \sum_{\varepsilon=0}^{N_c-1} \Lambda_{\text{avg}}(\varepsilon) \right]^2} \right)^3}. \tag{4.56}$$

Three other indices, specifically the Peak Sidelobe Level (PSL) ratio and two different definitions of the Integrated Sidelobe Level (ISL) ratio, are computed from the normalized autocorrelation of the sequence $\Lambda_{\text{avg}}(\varepsilon)$, $C_{\Lambda_{\text{avg}}}(m), m = 0, \ldots, M-1$.

Specifically

$$F_3 = \text{PSL} = \max_m \frac{\left|C_{\Lambda_{\text{avg}}}(m)\right|}{\left|C_{\Lambda_{\text{avg}}}(0)\right|} \tag{4.57}$$

while the latter are

$$F_4 = \text{ISL}_1 = \frac{\sum_{m=1}^{M-1}\left|C_{\Lambda_{\text{avg}}}(m)\right|}{\left|C_{\Lambda_{\text{avg}}}(0)\right|} \tag{4.58}$$

and

$$F_5 = \text{ISL}_2 = \frac{\sum_{m=1}^{M-1}\left|C_{\Lambda_{\text{avg}}}(m)\right|^2}{\left|C_{\Lambda_{\text{avg}}}(0)\right|} \tag{4.59}$$

respectively. Hence, the final feature vector extracted is $\boldsymbol{F}^{\text{avg}} = [F_0, \cdots, F_5]$.

2D Signature Based Feature Vectors

For the other three feature extraction methods, the CVD is considered as a 2D image representing the target signature. Firstly, the magnitude of the CVD is normalized to obtain a matrix whose values belongs to the set $[0, 1]$ as follows

$$\Lambda_{\text{CVD}}(\nu, \varepsilon) = \frac{S_{\text{CVD}}(\nu, \varepsilon) - \min\limits_{\nu,\varepsilon} S_{\text{CVD}}(\nu, \varepsilon)}{\max\limits_{\nu,\varepsilon}\left[S_{\text{CVD}}(\nu, \varepsilon) - \min\limits_{\nu,\varepsilon} S_{\text{CVD}}(\nu, \varepsilon)\right]}. \tag{4.60}$$

The different feature vectors extracted are based and pZ moments, Kr moments and Gabor filtering, respectively.

pZ moment Based Feature Vector Approach In order to compute the pZ moments, the support of the spectrogram, hence that of the CVD, has to be chosen to be a unit square so that it can be inscribed in the unit circle (Clemente et al., 2015b). A feature vector $\boldsymbol{F}^{\text{pZ}}$ is then extracted, whose q-th element $\boldsymbol{F}_q^{\text{pZ}}$ is the pZ moment $\zeta_{r,l}$ of order r and repetition l calculated from the magnitude of the CVD by (3.15), with $r = l = 0, \cdots, \mathcal{K}_1 - 1$ and $q = 0, \cdots, (\mathcal{K}_1 + 1)^2 - 1$, where $\mathcal{K}_1$ is the maximum value considered for both the moments order and the repetition.

Kr moment Based Feature Vector Approach In the Kr moment based approach, a feature vector $\boldsymbol{F}^{\text{Kr}}$ is extracted, whose q-th element F_q^{Kr} is the Kr moment K_{rl} of order (r, l) calculated from the magnitude of the CVD by (3.23), with $r = l = 0, \cdots, \mathcal{K}_2 - 1$ and $q = 0, \cdots, (\mathcal{K}_2 + 1)^2 - 1$, where $\mathcal{K}_2$ is the maximum value considered for the moments orders.

2D Gabor Filter Based Feature Vector Approach In the 2D Gabor filter based approach, the resulting matrix $\Lambda_{\mathrm{CVD}}(\nu, \varepsilon)$ is filtered with a bank of Gabor filters whose impulse responses $\varrho_{m,l}$ are obtained for various f_l and ϑ_m, with $l = 0, \ldots, L-1$ and $m = 0, \ldots, M-1$, where L and M are the numbers of selected spatial central frequencies and orientation angles, respectively. The choice of the f_l and ϑ_m depends on the specific application and on the worst case image to represent with the moments. The selection of these parameters has to be conducted in order to get an accurate representation of the image under test. In fact, since by varying ϑ_m the harmonic response of the filter moves on a circumference, whose radius is f_l, it is possible to extract local characteristics in the Fourier domain by choosing a set of values for the two parameters. The value of each pixel of the output image is given by the convolution product of the 2D Gabor function and the input image, $\Lambda_{\mathrm{CVD}}(\nu, \varepsilon)$, as

$$\begin{aligned}\Xi_{l,m}(\nu, \varepsilon; f_{cs_l}, \vartheta_m) &= \varrho_{l,m}(\nu, \varepsilon; f_l, \vartheta_m) * \Lambda_{\mathrm{CVD}}(\nu, \varepsilon) = \\ &= \int_{-\infty}^{\infty}\int_{-\infty}^{\infty} \varrho_{l,m}(\nu-\nu_\tau, \varepsilon-\varepsilon_\tau; f_l, \vartheta_m)\Lambda_{\mathrm{CVD}}(\nu_\tau, \varepsilon_\tau)d\nu_\tau d\varepsilon_\tau\end{aligned} \tag{4.61}$$

with $l = 0, \ldots, L-1$ and $m = 0, \ldots, M-1$, where L and M are the numbers of central frequency and orientation angles, respectively. Finally, the outputs of the filters are processed to extract the feature vector used to classify the targets. In particular, a feature is extracted from the output image of each filter by adding up the values of all pixels, as

$$\boldsymbol{F}_q^{\mathrm{GF}} = \sum_{\nu}^{N_\nu - 1}\sum_{\varepsilon}^{N_\varepsilon - 1} |\Xi_{l,m}(\nu, \varepsilon; f_l, \vartheta_m)| \tag{4.62}$$

where $q = mL + l$, with $l = 0, \ldots, L-1$ and $m = 0, \ldots, M-1$, N_ν and N_ε are the dimensions of the image Λ_{CVD} along both axis.

4.4.2 Classifier

The classification performances of the extracted feature vectors are evaluated using the k-Nearest Neighbour (kNN) classifier, modified in order to account for *unknown* class. In particular, let $\mathcal{T}$ is the training vectors set, for each class v an hypersphere $\mathcal{S}_{\mathbf{CM}_v}(\varrho_v)$ is considered, with centre $\mathbf{CM}_v$ and radius ϱ_v. In the case in which the tested vector does not belong to any hypersphere, it is declared as unknown. The operation mode of this classifier is composed by three phases.

In the first phase, the set $\mathcal{N}$ of nearest neighbour training vectors to the tested vector $\mathbf{F}$ is selected from $\mathcal{T}$ as follows

$$\mathcal{N} = \left\{ \tilde{\mathbf{F}}_1, \ldots, \tilde{\mathbf{F}}_k : \forall i = 1, \cdots, k, \ \left\| \tilde{\mathbf{F}}_i - \mathbf{F} \right\| < \min_{\tilde{\mathbf{F}} \in \{\mathcal{T} - \tilde{\mathbf{F}}_1, \cdots, \tilde{\mathbf{F}}_{i-1}\}} \left\| \tilde{\mathbf{F}} - \mathbf{F} \right\| \right\} \quad (4.63)$$

The second phase consists into definition of vector $\boldsymbol{\iota}$ whose elements represent a label for each vector in $\mathcal{N}$. Each label can assume an integer value in the range $[0, V]$, where V is the number of possible classes. The value 0 is assigned when the tested vector does not belong to any hypersphere of the vectors in $\mathcal{N}$, while the values $[1, V]$ correspond to a specific class. Specifically, $\forall i = 1, \ldots, k$, the i-label ι_i is updated as follows

$$\iota_i = \begin{cases} 0 & \left\| \tilde{\mathbf{F}}_i - \mathbf{F} \right\| > \zeta_v \\ v & \text{otherwise} \end{cases} \quad (4.64)$$

where v is the value corresponding to the belonging class of $\tilde{\mathbf{F}}_i$. Finally, the $(V + 1)$-dimensional score vector $\mathbf{s}$ is evaluated, whose elements are the occurrences, normalised to k, of the integers $[0, \ldots, V]$ in the vector $\boldsymbol{\iota}$. The estimation rule then may be implemented as follows:

$$\hat{v} = \begin{cases} \arg\max_v \mathbf{s} & \text{if} \quad \max(\mathbf{s}) > \frac{1}{2} \\ 0 & \text{otherwise} \end{cases} \quad (4.65)$$

where 0 is the unknown class.

Assuming that the feature vectors of each class are distributed uniformly around their mean vector, for all the Monte Carlo runs, the hypersphere radius ϱ_v was chosen equal to $\Upsilon_v \sqrt{12}/2$, where $\Upsilon_v = \mathrm{tr}\left(\mathbf{C}_v\right)$ and $\mathbf{C}_v$ is the covariance matrix of the training vectors which belong to the class v. The choice is made according to the statistical proprieties of Uniform distributions. In fact, for one-dimensional uniform variables the sum of mean and the product between the standard deviation and the factor $\sqrt{12}/2$ gives the maximum possible value of the distribution.

The choice of a kNN classifier is because it is based on the evaluation of the Euclidean distances between the vector under test and the vectors composing the training set of each class in order to estimate the target class. Hence, the classification performance evaluated with kNN classifier are not polarized by the proprieties of the classifier, and it depends only on the characteristic of features to occupy multidimensional spaces for each class sufficiently separated. However, in general other classifiers with similar characteristics could be also selected. The selection of the best classifier is outside the scope of this Thesis.

4.5 Performance Analysis

In this Section the proposed model is tested with both simulated data and laboratory data acquired from replicas of the targets of interest. The targets are divided in two classes which are *warhead* and *decoy*. Moreover, both of them are divided in sub-classes, which are associated to a particular type of target. Specifically, the *warhead* class is composed by two sub-classes: cone and cone with triangular fins at the base, which are replicas of warhead without and with fins, respectively. *Decoy* class, in contrast, is divided in three sub-classes: sphere, cone and cylinder.

In order to analyse the performance of the proposed algorithm, three figures of merit are considered, which are the *Probability of correct Classification* ($\mathcal{P}_C$), the *Probability of correct Recognition* ($\mathcal{P}_R$), and the *Probability of Unknown* ($\mathcal{P}_U$). The meaning of classification is the ability to distinguish between the warhead class and the object class, while recognition means the capability to identify the actual shape of the target within the warhead and the object class. Finally, $\mathcal{P}_U$ is computed as the ratio of the number of analysed objects for which the classifier does not make a decision and the total number of analysed objects.

The analysis of performance is conducted by using both simulated and real data, considering the same the target shapes, dimensions and motion parameters. The conical warhead has a radius, R_b, of 0.375 m and a height, H, of 1 m, while the fin's height, H_{fin}, is 0.20 m. The sizes of the decoys are usually comparable with the dimensions of the warheads in order to confuse the anti-missile radar system. Therefore, both the cylindrical and conical objects are chosen to have a radius and a height equal to 0.375 m and 1 m, respectively, while the sphere diameter is 1 m. As described in Section 4.3, the database of laboratory acquisition have been realized using scaled replicas of the target of interest. In order to simulate an S-Band anti-missile radar system, whose carrier frequency is 3.3 GHz, by using a 24 GHz CW radar the actual dimension of the replicas of the targets used to acquire the real data are scaled by a factor of 0.1375. The precession angle chosen for both the types of warhead is 10° while the precession frequency is 0.25 Hz. The angular velocity of the spinning is 1 Hz, while the nutation frequency is 5 Hz.

For the decoys, the tumbling velocity is 1 Hz.
The performance is shown for varying the Signal to Noise power Ratio (SNR) and observation time, which is either 10 seconds, 5 seconds or 2 seconds. Moreover, for the 2D signature based approaches, the dimension of the feature vector is also varied. The spectrogram is computed using a Hamming window with 75% overlap. The number of points for the DFT computation, N_{bin}, is fixed for the ACVD approach, whereas is adaptively evaluated for the pZ and the Gabor filter methods, in order to obtain a square representation of the spectrogram. Specifically, in these cases N_{bin} is given by

$$N_{bin} = \left\lceil \frac{N_s - W\, overlap}{W\,(1 - overlap)} \right\rceil \tag{4.66}$$

where N_s is the number of signal samples, $\lceil \cdot \rceil$ represents the smaller integer greater than or equal to the argument, and *overlap* is the percentage of overlap expressed in the interval $[0, 1]$. Finally, it is assumed that the effect of the principal translation motion of the targets is compensated before the signals are processed. In this way, the classification is based only on the micro-motions of targets of interest.

4.5.1 Simulated data

The database for simulated data is composed of 3240 realizations of the radar return for each target of interest, obtained by considering 10 signals for each of the possible 18^2 pair of azimuth and elevation angles formed using 18 values for both of them, between 5° and 90° with a step size of 5°. The initial phase of the micro-motions is taken randomly in uniform distribution $[0, 2\pi]$ and an additive white Gaussian noise is added to each simulation.
A Monte Carlo approach is used in order to calculate the mean of the three figures of merit over several cases. Specifically, the means are evaluated over 50 different Monte Carlo runs in which all the available simulated signals are divided randomly into training or testing sets with 70% used for training and 30% for testing. The k value of classifier has to be chosen greater than 1 in order to consider the *unknown* class; specifically, it is set to 3.

ACVD approach

The performance in terms of $\mathcal{P}_C$ and $\mathcal{P}_R$ obtained by using the ACVD based feature vector approach for simulated data is shown in Fig. 4.13a. It is observed that

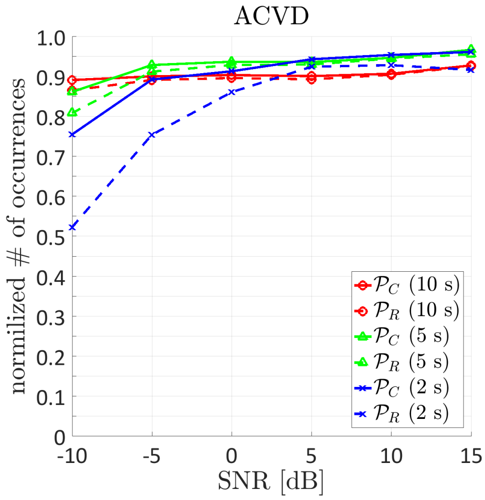

(a) $\mathcal{P}_C$ and $\mathcal{P}_R$

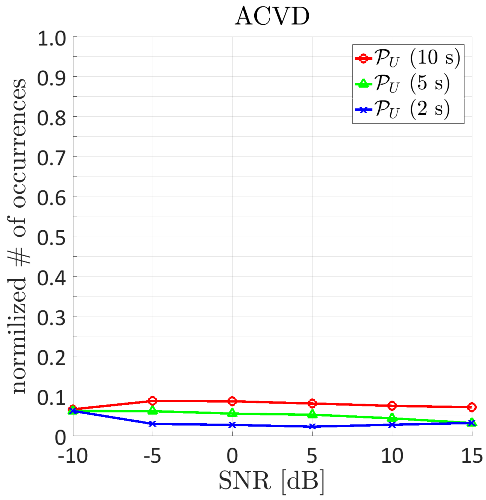

(b) $\mathcal{P}_U$

Fig. 4.13 Performance of the ACVD based feature vector approach for simulated data on varying the signal's duration and the SNR.

the performance generally improves as the SNR increases, such that both of the figures of merits increase, showing a slight difference as the signal duration varies. In particular, the gap between the two probabilities increases as the observation time decreases for the lower SNR scenarios considered in the analysis; however, the gap decreases as the SNR increases. Moreover, it is worth pointing out that the highest values are obtained for observation times of 2 and 5 seconds and SNR greater than 5 dB, with both $\mathcal{P}_C$ and $\mathcal{P}_R$ close to 0.95. For a signal's duration of 10 seconds $\mathcal{P}_C$ and $\mathcal{P}_R$ are independent on the SNR, being approximatively 0.90. Observing Fig. 4.13b, which shows $\mathcal{P}_U$, it is noted that it is almost constant at about 0.1, for all the values of SNR and signal's duration of 10 seconds, while smaller than 0.5 for 2 and 5 seconds observation times. Defining the probability of misclassification, $\mathcal{P}_M$, as

$$\mathcal{P}_M = 1 - \mathcal{P}_C - \mathcal{P}_U \tag{4.67}$$

and since $\mathcal{P}_C$ is slightly greater than 0.9 for SNR greater than 0 dB, it is clear that $\mathcal{P}_M$ decreases as the SNR increases, becoming smaller than 10^{-2} for all the considered observation times.

pZ moments approach

The performance obtained by using the pZ based approach for simulated data is shown Fig. 4.14. In this case the dimension of the feature vector, Q, depends on

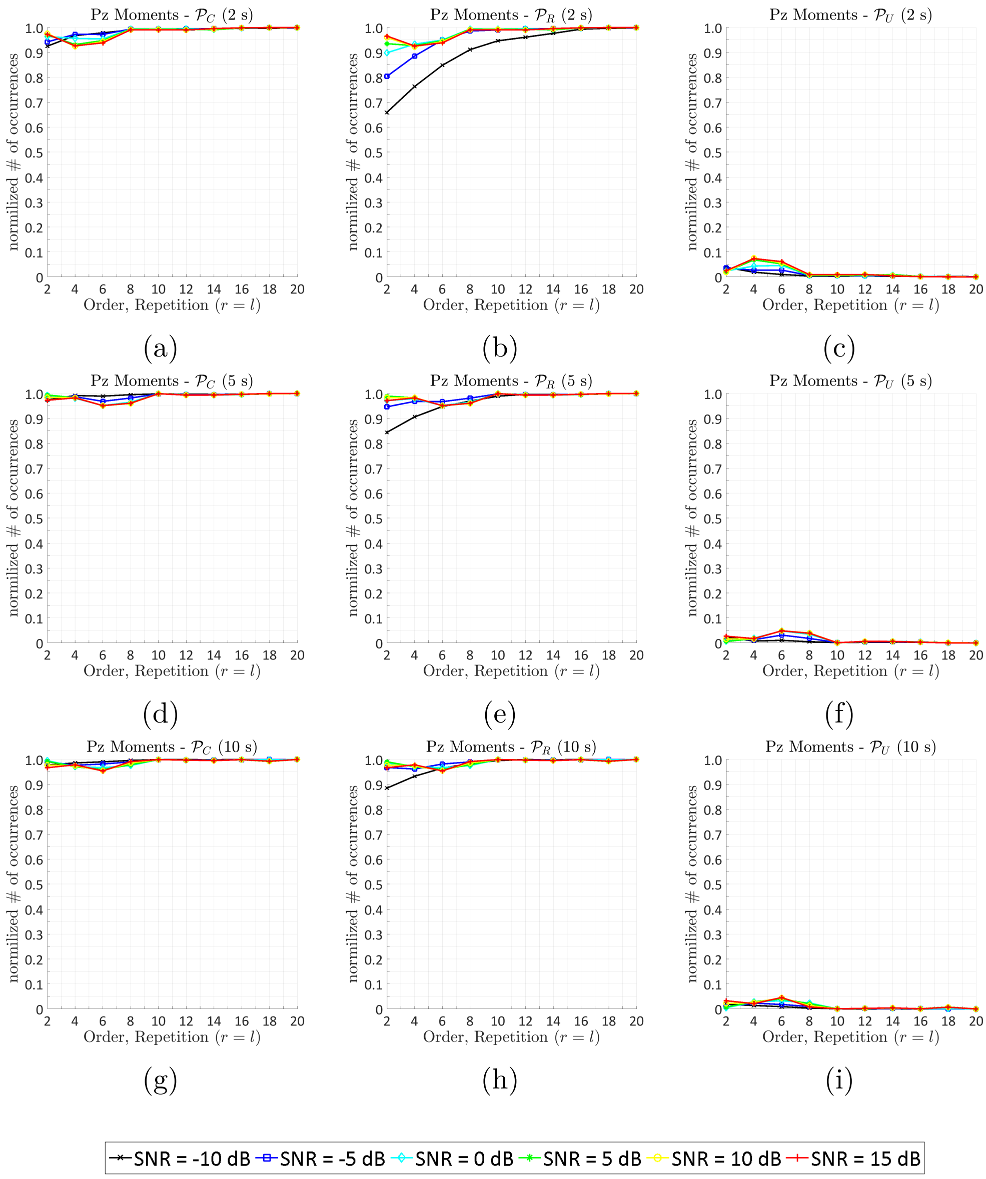

Fig. 4.14 Performance of the pZ moments based feature vector approach for simulated data; the analysis is conducted on varying the order, the signal's duration and the SNR.

the polynomial order and repetition, which determine the number of pZ moments. Observing Fig. 4.14a, Fig. 4.14d and Fig. 4.14g it is noted that $\mathcal{P}_C$ is greater than 0.99 independently on the value of SNR and observation time for moments order grater than 10. For smaller values of the order, there is a drop in the performance which is more significant as the SNR increases, such that the minimum value of $\mathcal{P}_C$ is about 0.95 for SNR equal to 15 dB. On the other hand, it is worth noting that $\mathcal{P}_U$ increases in correspondence of the mentioned drops of $\mathcal{P}_C$. This trend seems likely to be due to two factors. Firstly, for small values of the SNR, the feature vectors of a given class occupy a wider region in the multidimensional space: then, it is easier for the regions to intersect each other. On the other hand, for high values of SNR, smaller regions are occupied by feature vectors for each class, such that it is more likely that a feature vector under test is not close enough to be classified as belonging to the correct class. Then, it is clear that this trend strictly depends on the choice of a $k$nn classifier. A different classifier, less dependent on distances in the multidimensional space might produce different results. Nevertheless, from (4.67) it is clear that even in these cases the $\mathcal{P}_M$ is smaller than 10^{-2}. From Fig. 4.14b, Fig. 4.14e and Fig. 4.14h, it is clear that the capability to recognize a target improves significantly for negative values of the SNR by increasing the moments order. For positive value of the SNR, $\mathcal{P}_C$ and $\mathcal{P}_R$ are approximatively equal. Therefore, for moments order greater than 10 and SNR greater than $-10\,d$B, $\mathcal{P}_R$ is greater than 0.98 for all the considered observation time.

Kr moments approach

The results obtained by using the Kr moments based approach for simulated data are shown in Fig. 4.15. As well as for pZ moments, even in this case Q, hence the number of Kr moments, depends on the polynomials order. Fig. 4.15a shows that for observation time of 2 seconds, $\mathcal{P}_C$ increases quickly as the moments order increases, while the performance decreases slightly as the SNR increases. One more time, the main reason of this trend is the choice of the particular classifier, as described above. Observing Fig. 4.15d and Fig. 4.15g it is noted that $\mathcal{P}_C$ is greater than 0.90 for all the considered values of moments order and SNR, reaching values greater than 0.99 for order greater than 8 independently on the SNR. From Fig. 4.15a, Fig. 4.15d and Fig. 4.15g it is noted that $\mathcal{P}_R$ increases as the moments order increases, and that the gap between $\mathcal{P}_C$ and $\mathcal{P}_R$ becomes negligible for moments order and SNR greater than 8 and $-10\,d$B, respectively. Consequently, $\mathcal{P}_U$ decreases as the moments order increases, as observed in Fig. 4.15a, Fig. 4.15d and Fig. 4.15g. Specifically $\mathcal{P}_U$ is smaller than 0.05 for all the value of SNR and moments order, when the signal's duration is 2 seconds, while for 5 and 10 seconds long observations it is smaller than $10^{-}2$ for all the considered value of SNR when the order is greater than 8.

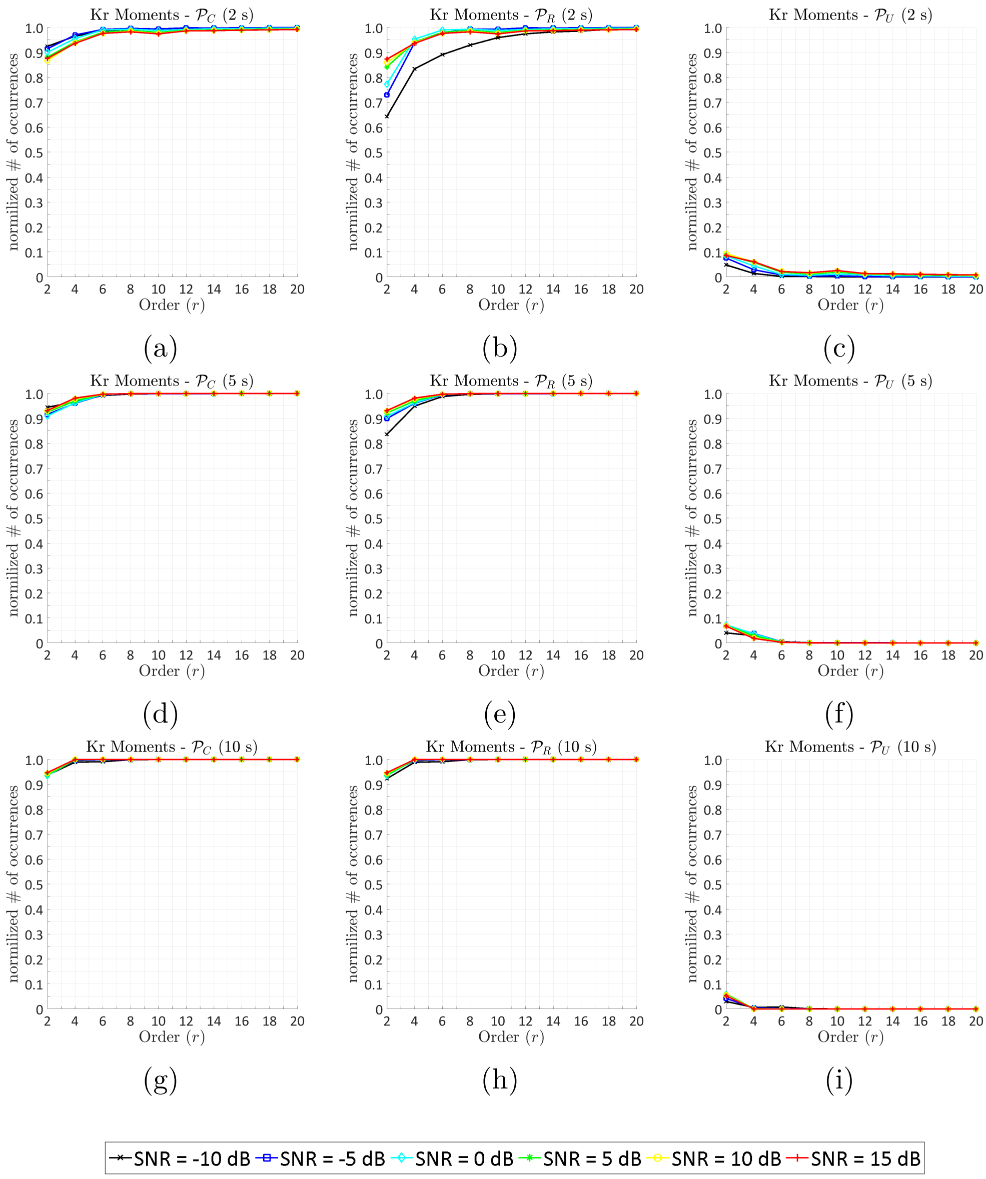

Fig. 4.15 Performance of the Kr moments based feature vector approach for simulated data; the analysis is conducted on varying the moments order, the signal duration and the SNR.

2D Gabor filter approach

The mean values of $\mathcal{P}_C$, $\mathcal{P}_R$ and $\mathcal{P}_U$ for the Gabor filter approach are shown in Fig. 4.16 shows. For this approach, the dimension of feature vector corresponds to the number of filters, which depends on the orientation angular step θ_{step}. Recall that Q is given by

$$Q = L\left(\left\lceil \frac{\pi/2}{\vartheta_{step}} \right\rceil + 1\right) \tag{4.68}$$

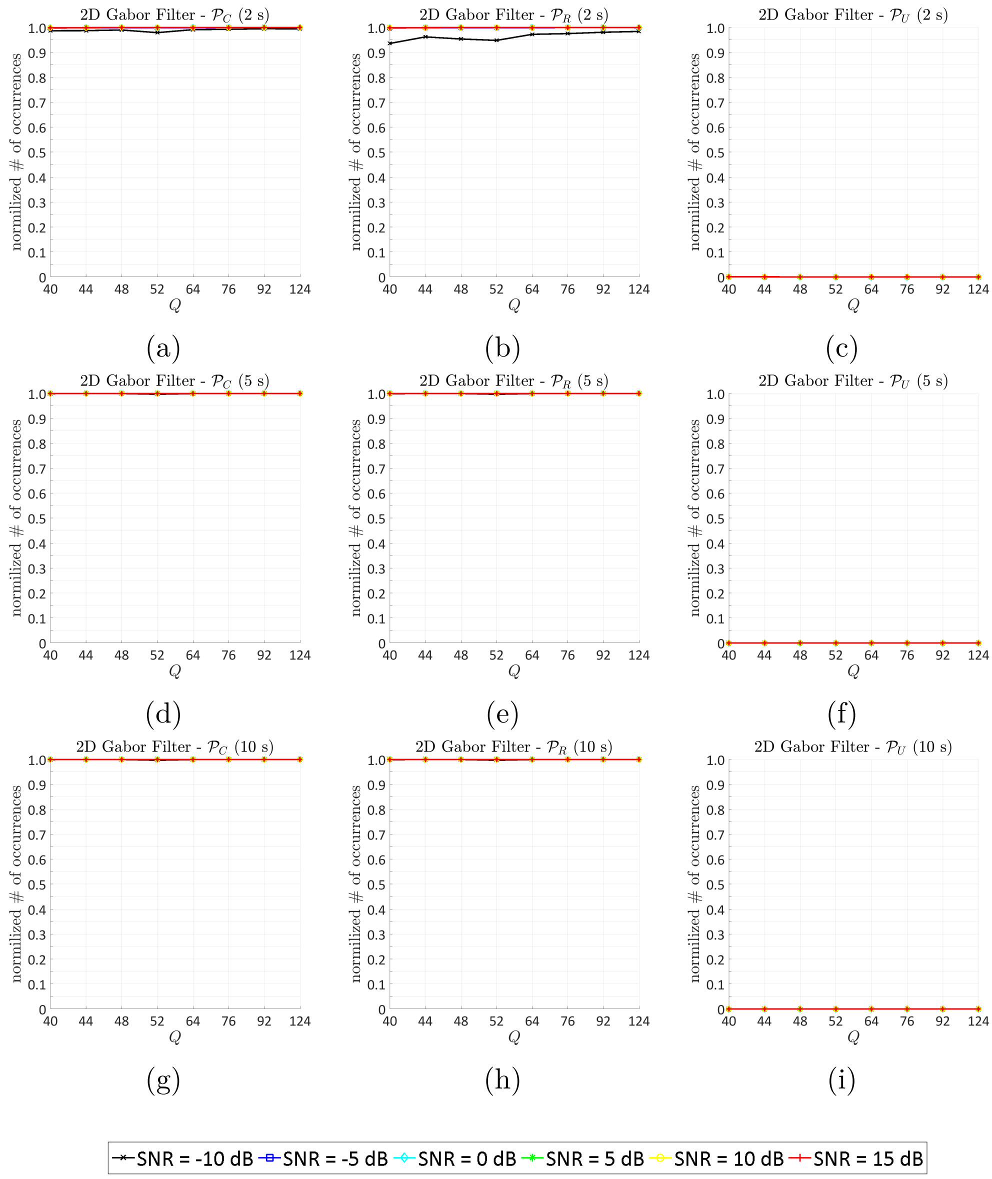

Fig. 4.16 Performance of the 2D Gabor Filter based feature vector approach for simulated data; the analysis is conducted on varying the number of features, Q, the signal's duration and the SNR.

where ϑ_{step} is the orientation angular step and L in the number of central frequencies. The latter was fixed at 4 values; 0.5, 1, 1.5 and 2. The value of ϑ_{step} was set to be an integer in the interval $[3°, 10°]$. In this way, an analysis on varying the density of the considered positions of the harmonic response on each circumference with radius equal to fcs_l is conducted. The values of the orientation angle, ϑ_m, is given by

$$\vartheta_m = m\,\vartheta_{step} \tag{4.69}$$

with $m = 0, \ldots, M-1$ and where

$$M = \left\lceil \frac{\pi/2}{\vartheta_{step}} \right\rceil . \tag{4.70}$$

From (4.69) and (4.70), it is important outlining that the features are extracted moving the harmonic response of the filter considering only the first quadrant, due to the symmetry of the expected image for this application.
Fig. 4.16a, Fig. 4.16d and Fig. 4.16g show that $\mathcal{P}_C$ is greater than 0.99 for all the considered values of SNR, observation time and Q. Fig. 4.16b, Fig. 4.16e and Fig. 4.16h shows that in the worst case $\mathcal{P}_R$ varies within 0.95 and 0.97 for SNR equal to $-10\,d$B, on varying the filter bank dimension. For all the other considered cases, instead, $\mathcal{P}_R$ is approximately equal to $\mathcal{P}_C$, being greater than 0.99. Consequently, $\mathcal{P}_U$ is always smaller than 10^{-2}, as shown in Fig. 4.16c, Fig. 4.16f and Fig. 4.16i. Therefore, it is worth noting that the performance does not change significantly when varying the feature vector dimension.

4.5.2 Experimental data

The analysis of performance for real data is evaluated on varying the observation time and the SNR, as done for the simulated data. It is worth noting that, since the total number of acquisition is not enough for assessing the performance of the algorithm, the laboratory acquisition acquisitions of 20 seconds have been split into segments of 10, 5 and 2 seconds, conducting an analysis on the signal time duration. In addition, assuming that the noise for the acquired signals in a controlled environment is negligible, the analysis on the SNR was conducted by adding white Gaussian noise to the real data. Finally, before processing, the received signals are down-sampled by a factor of 10. It is worth noting that the trajectory of ballistic targets is not taken into account in the experiment as well as for the simulated data, considering that the principal movement of the object is compensated.
Differently from the previous analysis, the mean of the three figures of merit for real data are evaluated over 500 different Monte Carlo runs, since the database dimension is smaller than the one for simulated data. Even in this case, in each Monte Carlo run all the available experimental measurements are divided randomly into training or testing sets with 70% used for training and 30% for testing. The k value of classifier is set to 3 as for the analysis on simulated data.

ACVD approach

The performance on the experimental data for the ACVD based method in terms of $\mathcal{P}_C$ and $\mathcal{P}_R$ is shown in Fig. 4.17a, while Fig. 4.17b shows the $\mathcal{P}_U$. The

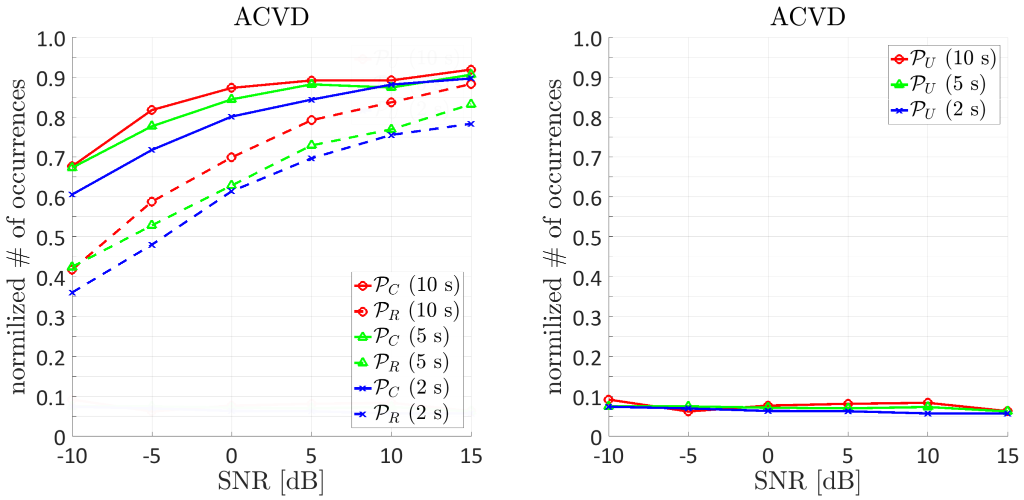

(a) $\mathcal{P}_C$ and $\mathcal{P}_R$ (b) $\mathcal{P}_U$

Fig. 4.17 Performance of the ACVD based feature vector approach for real data on varying the signal duration and the SNR.

performance trend obtained in the previous subsection for the simulated data is confirmed by the real data. In fact, both $\mathcal{P}_C$ and $\mathcal{P}_U$ increase as the SNR increases; however, the effect of changing the observation time is more evident in this case. Moreover, the gap between the two figures of merit decreases as both the observation time and the SNR increase. Observing Fig. 4.17b, it is pointed out $\mathcal{P}_U$ is almost constant for all analysed cases and it is smaller than 0.1.

pZ moments approach

The results obtained by using the pZ moments based approach by using the database with experimental acquisitions are shown in Fig. 4.18. Observing Fig. 4.18a, Fig. 4.18b, Fig. 4.18d, Fig. 4.18e, Fig. 4.18g and Fig. 4.18h it is worth noting that the performance in terms of correct classification and recognition are very sensitive to high level of noise, with unsatisfactory results for the lower values of moments order and negative value of SNR. However, both $\mathcal{P}_C$ and $\mathcal{P}_R$ generally improves as the moments order, the observation time and the SNR increase, leading to decrement of $\mathcal{P}_U$, as observed in Fig. 4.18c, Fig. 4.18f and Fig. 4.18i, it is clear that as the SNR, the observation time and the moments order increase. The gap between $\mathcal{P}_C$ and $\mathcal{P}_R$ becomes smaller as the moments

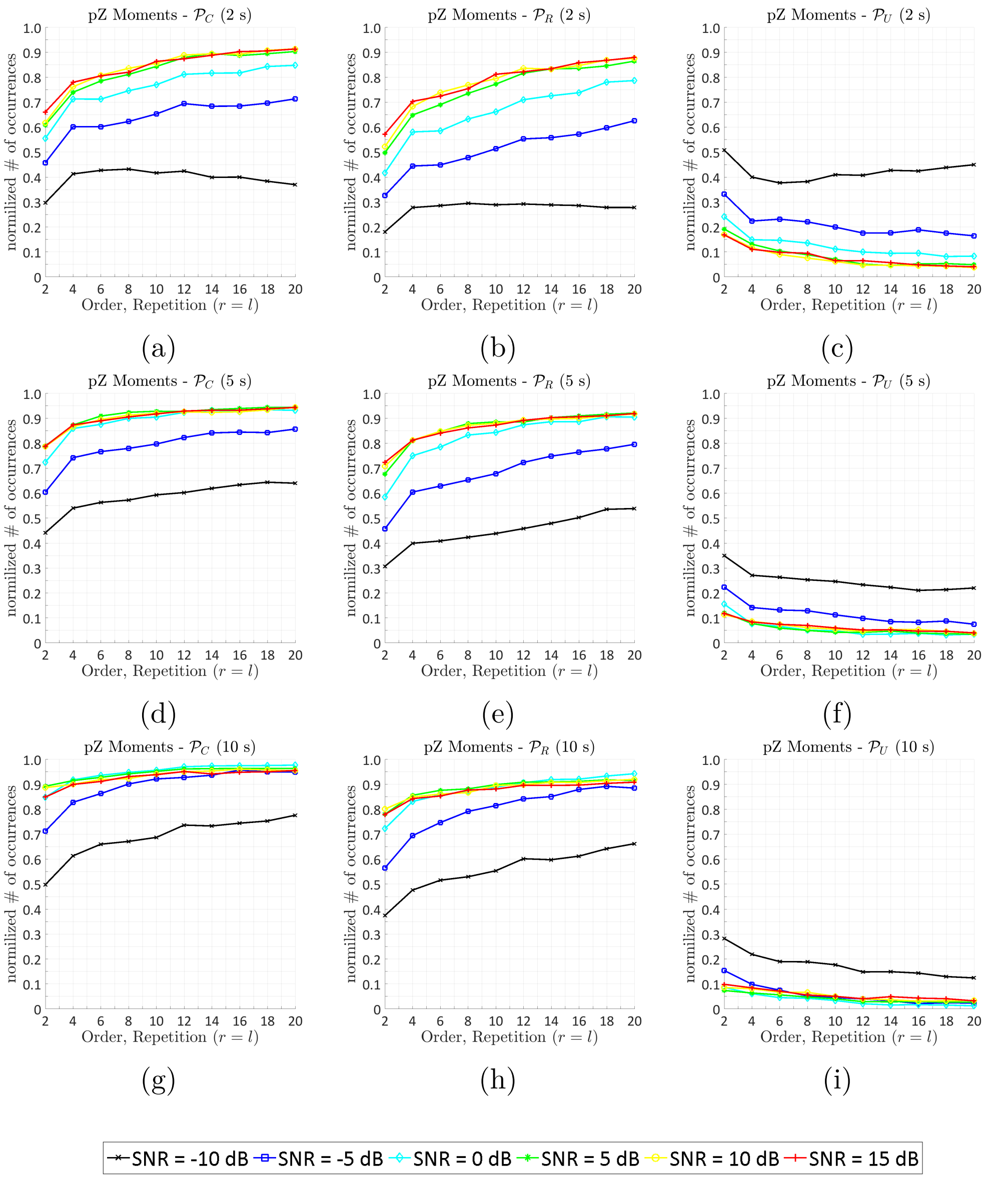

Fig. 4.18 Performance of the pZ moments based feature vector approach for real data; the analysis is conducted on varying the moments order, the signal duration and the SNR.

order increases. However, unlike the performance obtained on simulated data, the maximum value reached by the two probabilities is around 0.90.

Kr moments approach

The graphs in Fig. 4.19 shows the results obtained by using the Kr moments based approach. From the figure it is worth noting that the trend observed by using the simulated data is confirmed even with real data. Fig. 4.19a and Fig. 4.19b show that for 2 seconds long radar observations $\mathcal{P}_C$ and $\mathcal{P}_R$ increases significantly as

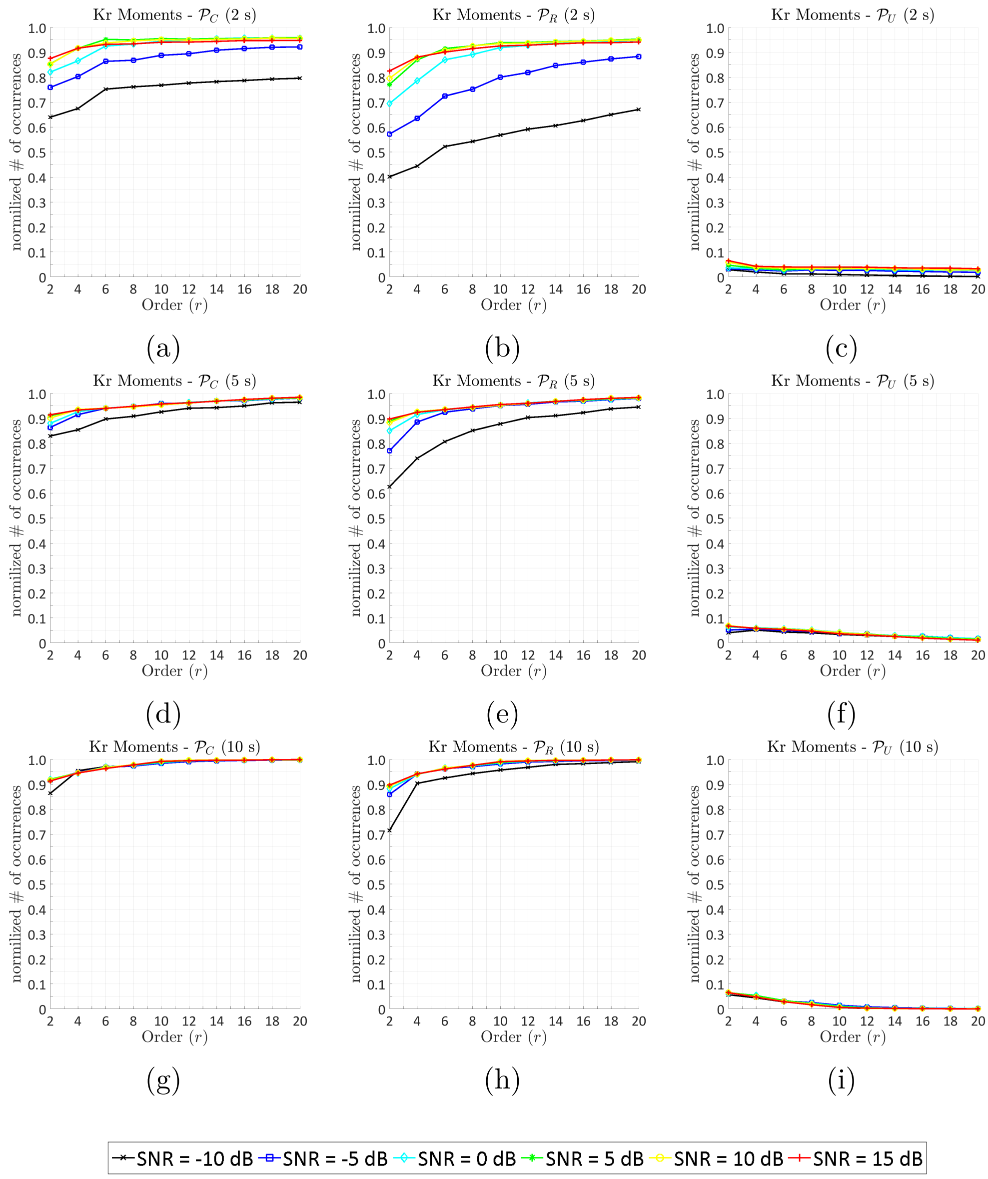

Fig. 4.19 Performance of the Kr moments based feature vector approach for real data; the analysis is conducted on varying the moments order, the signal duration and the SNR.

the SNR increases, while from Fig. 4.19a, Fig. 4.19b, Fig. 4.19d and Fig. 4.19e it is pointed out that they are almost constant for 5 and 10 seconds, when the SNR is greater than $-10\,d$B. Moreover, the gap between the two probabilities becomes negligible for SNR greater than $-5\,d$B and moments order greater than 10. Finally, from Fig. 4.18c, Fig. 4.18f and Fig. 4.18i it is worth noting that $\mathcal{P}_U$ decreases as the moments order increases. Nevertheless, the latter is smaller than 0.1 in all the analysed cases.

2D Gabor Filter approach

The performance of the 2D Gabor filter based method are shown in Fig. 4.20. Observing Fig. 4.20a, Fig. 4.20b, Fig. 4.20d, Fig. 4.20e, Fig. 4.20g and Fig. 4.20h,

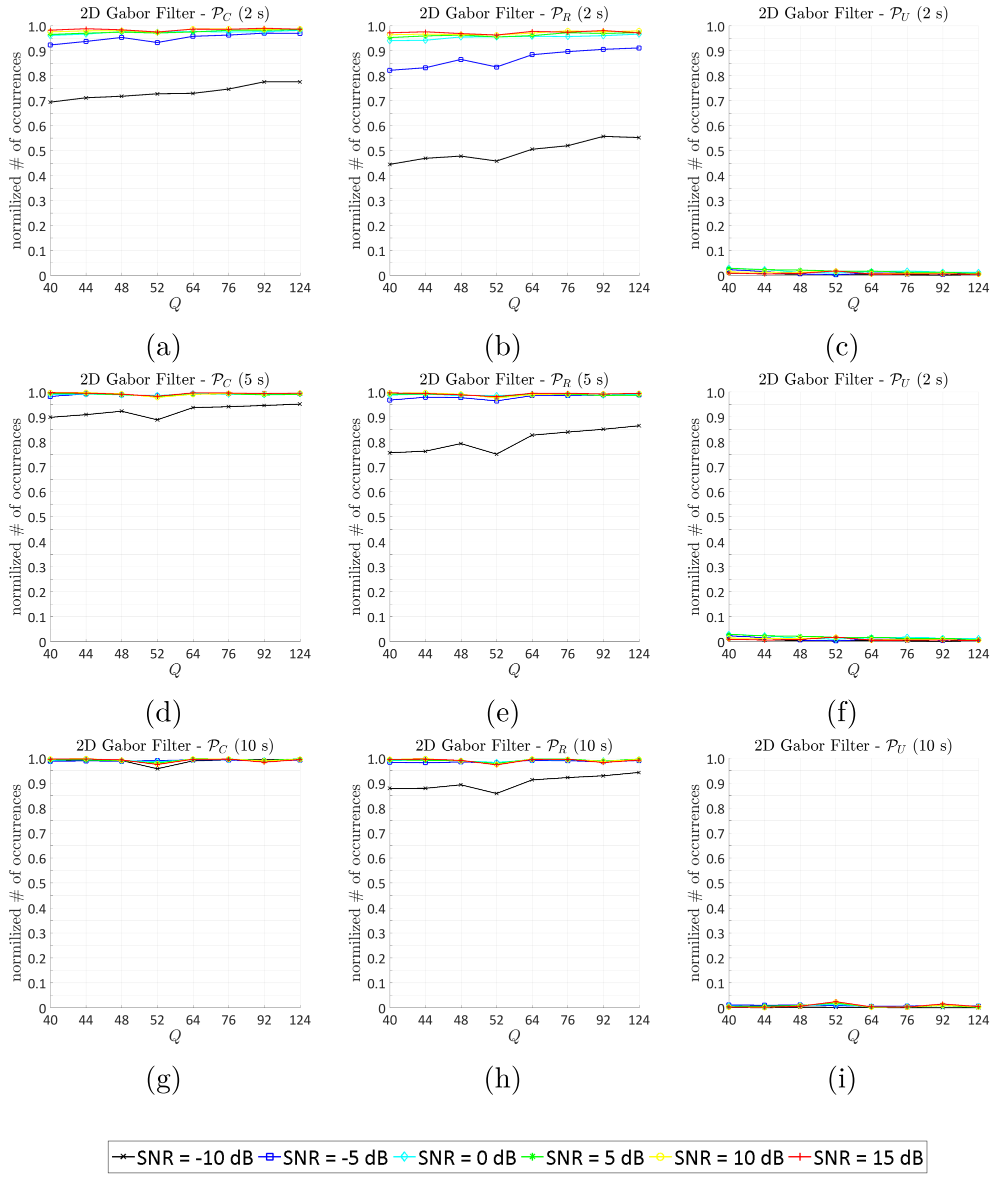

Fig. 4.20 Performance of the Gabor Filter based feature vector approach for real data; the analysis is conducted on varying the number of features Q, the signal duration and the SNR.

it is clear that both $\mathcal{P}_C$ and $\mathcal{P}_R$ increase as the SNR and observation time increase. In particular, for signal duration of 5 seconds, both $\mathcal{P}_C$ and $\mathcal{P}_R$ are greater than 0.98 for SNR grater than $-10\,d$B; for observation time of 10 seconds, instead, $\mathcal{P}_C$ is greater than 0.99 for the all analysed cases. Finally, the gap between the two probabilities decreases as the SNR increases, being equal for high values of the SNR. Fig. 4.20c, Fig. 4.20f and Fig. 4.20i show $\mathcal{P}_U$ versus Q, which is clearly smaller than 0.05 in all the analysed case.

Performance in presence of the Booster

The performance with real data was evaluated also in the case in which the received signal was scattered from an additional object different from warheads and decoys. This analysis is of interest since, during the flight, the missile releases some debris in addition to the decoys, such as the booster used in the boost phase. As in the case of decoys, when the booster has been released by the missile, it starts tumbling as shown in Fig. 4.21, where the model used for the booster is shown. However, the booster rotation velocity is smaller than the decoys', while its dimensions are bigger. It is assumed that the booster has a cylindrical shape, whose diameter and height are 0.75 m and 5 m, respectively, with triangular fins, whose base is 0.50 m and height is 1 m; the tumbling velocity is one fifteenth of the decoy's.

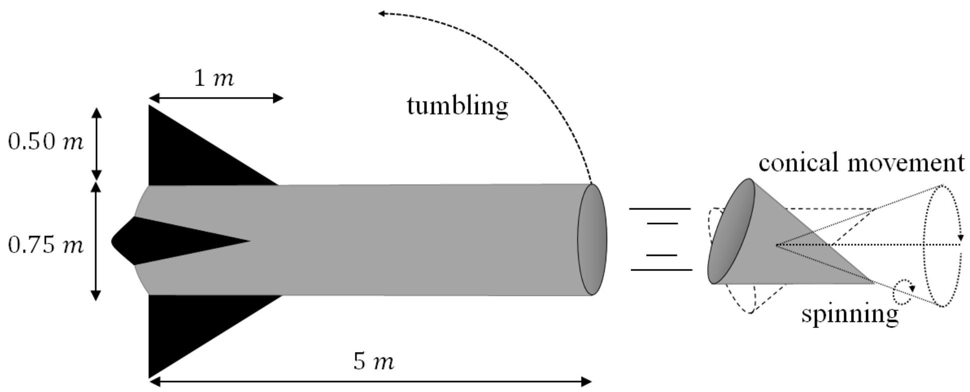

Fig. 4.21 Representation of booster: model dimensions and difference of movement respect with warhead.

This analysis is conducted by training the classifier with feature vectors belonging to either warhead class or decoy class, and then by testing it on the booster feature vector. Moreover, the performance is evaluated in terms of $\mathcal{P}_U$, as defined above, and *probability of misclassification (Error) as a Warhead* ($\mathcal{P}_{eW}$), determined by the ratio of the number of times in which the booster is classified as a warhead and the total number of tests. Note, in this specific case, classifying the booster as unknown represents the correct classification as there is no specific *booster* class.

Fig. 4.22 shows $\mathcal{P}_U$ and $\mathcal{P}_{eW}$ obtained by the ACVD based algorithm as

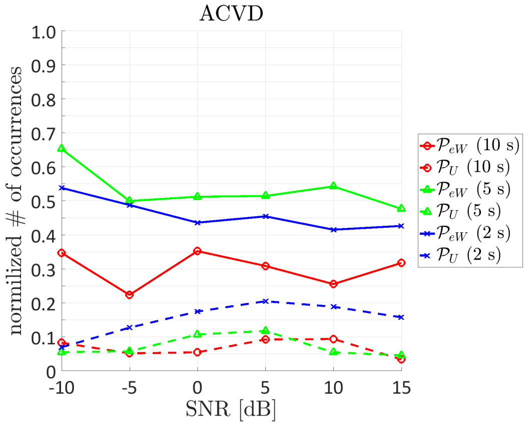

Fig. 4.22 Performance of the ACVD based feature vector approach for real unknown data (booster); the analysis is conducted on varying the signal duration and the SNR.

the signal duration and the SNR are varied. From Fig. 4.22 it is observed that even if $\mathcal{P}_U$ increases and, consequently, $\mathcal{P}_{eW}$ decreases as the signal duration increases, $\mathcal{P}_{eW}$ remains greater than $\mathcal{P}_U$. Moreover, the performance does not change significantly on varying the SNR.

Results obtained by using the pZ moments based approach are shown in Fig. 4.23. Observing the figure it is clear that the probability of classifying the booster as unknown increases as the order grows up to 4, independently of the observation length, where the maximum value is reached, and it is above 0.80 for SNR equal to 0 and 5 dB. Considering orders greater than 4, $\mathcal{P}_U$ remains constant for positive values of SNR, while it significantly decreases for SNR smaller than 0 dB. However, for moments order of about 20, $\mathcal{P}_U$ grows as the SNR increases. It is noticed that $\mathcal{P}_{eW}$ decreases as the observation time increases for negative value of SNR, while it increases for SNR greater than 0 dB. However, the best results are obtained for positive values of the SNR and for signal duration of 2 and 5 seconds, reaching probabilities of error smaller than 0.20.

Results obtained by using the Kr moments based approach are shown in Fig. 4.24. From Fig. 4.24a it is noted that for 2 seconds long observations $\mathcal{P}_U$ increases as the SNR increases, but reaching a maximum value around 0.50 for the lower values of the moments order. Indeed, $\mathcal{P}_U$ decreases as the order, hence, the feature vector dimension increases. This trend is because vectors composed by greater number of Kr moments occupy wider spaces for each class such that iit is more probable for a test vector being closer ot one of them. On the other hand, Fig. 4.24d shows that $\mathcal{P}_{eW}$ increases as the moments order increases for observation time of 2 seconds, being greater than $\mathcal{P}_U$ for each value of SNR when r is greater

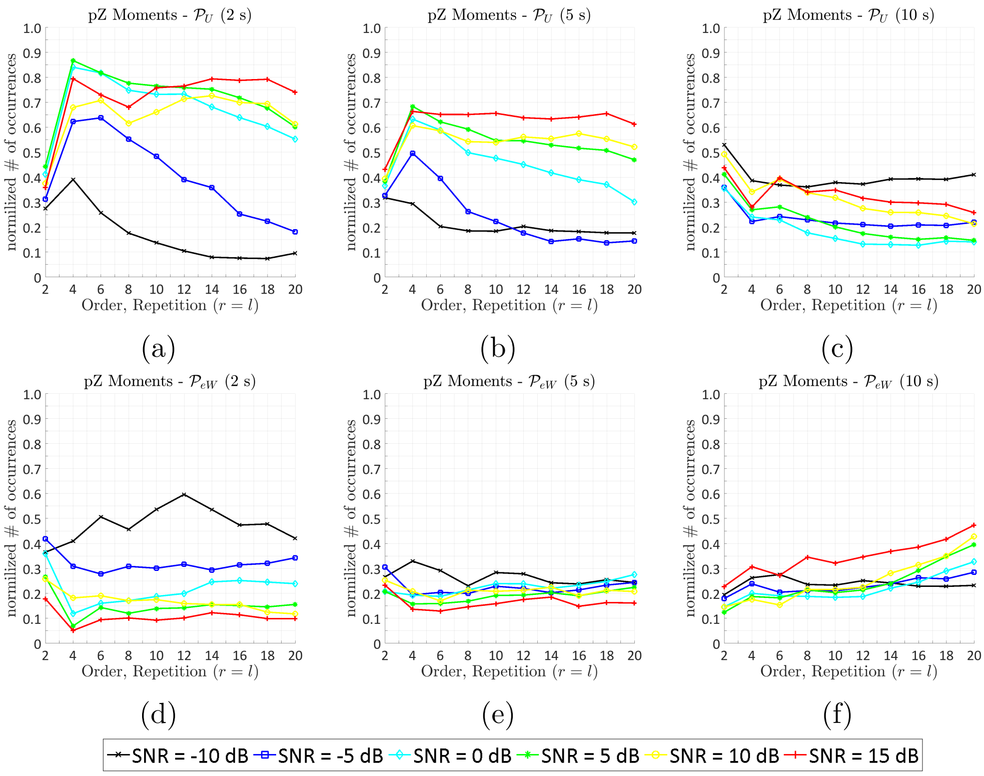

Fig. 4.23 Performance of the pZ based feature vector approach for real unknown data (booster); the analysis is conducted on varying the moments order, the signal duration and the SNR.

than 8. Observing Fig. 4.24b, Fig. 4.24c, Fig. 4.24e and Fig. 4.24f, it is worth noting that the performance improves as the observation time increases. From the figures, the values of $\mathcal{P}_U$ and $\mathcal{P}_{eW}$ appear almost constant as the order increases. The best performance in terms of $\mathcal{P}_U$ is obtained for the lowest values of the order, equal to 2, and for the lowest considered SNR, which is $-10\,d$B. Moreover, it is noted that $\mathcal{P}_{eW}$ decreases as the observation time increases, being lower than 0.30 for 10 seconds long signals and for all the values of moments order and SNR.

Finally, $\mathcal{P}_U$ and $\mathcal{P}_{eW}$ obtained for 2D Gabor filter based feature vector are shown in Fig. 4.25. From the graphs, one can deduce that the performance improves as the signal duration and the SNR increase. In particular, the performance for the signal duration of 2 seconds is not satisfactory since $\mathcal{P}_{eW}$ is always greater than $\mathcal{P}_U$. However, for observation time of 5 seconds $\mathcal{P}_U$ becomes greater than $\mathcal{P}_{eW}$ from SNR greater than $-10\,d$B reaching about 0.90 for highest values of SNR. Finally, for signal duration equal to 10 seconds, $\mathcal{P}_U$ is constantly greater than 0.90 independently of the values of the SNR and Q; on the other hand, $\mathcal{P}_{eW}$ is smaller than 10^{-2} for values of the SNR greater than $0\,d$B.

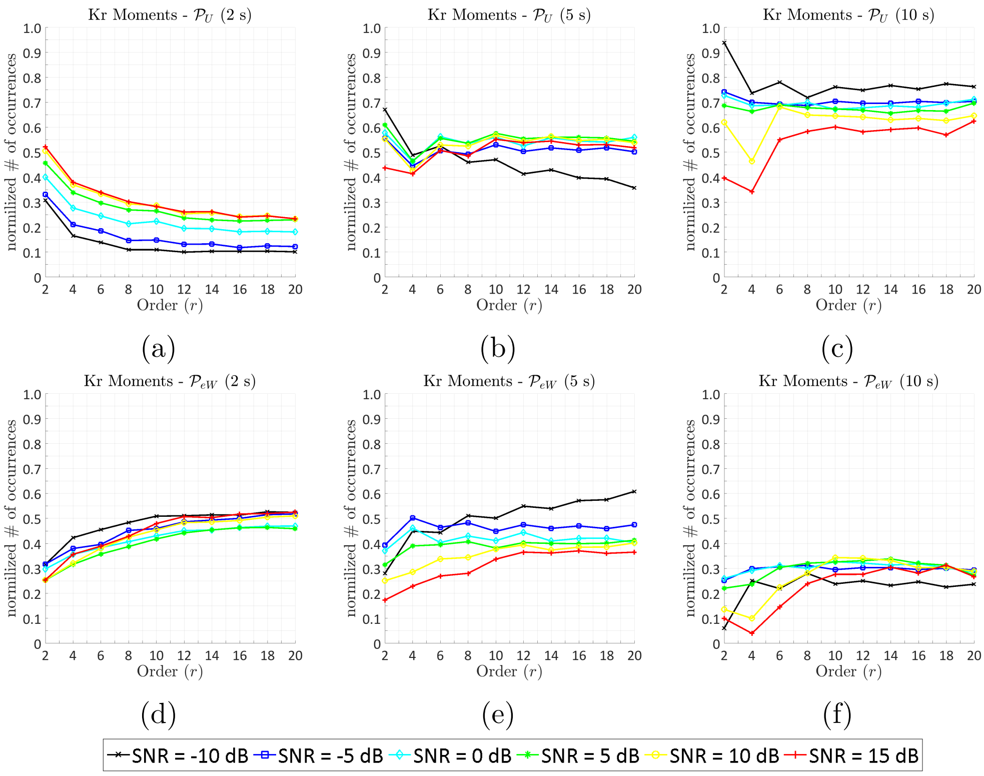

Fig. 4.24 Performance of the pZ based feature vector approach for real unknown data (booster); the analysis is conducted on varying the moments order, the signal duration and the SNR.

Consequently it is clear that in the case of classification of unknown objects which are not used to train the classifier, such as the booster, the ACVD based approach does not guarantee satisfactory performance. The pZ moments based approach is able to give good performance for small signal duration and for high SNR, while the Kr moments approach for longer signal duration and for low SNR. Alternatively the Gabor filter approach provided the optimum results for an observation time of 5 seconds, for SNR greater than $-10\,d$B, and of 10 seconds, independently of the noise levels.

4.5.3 Average Running Time

One of the most common requirements for ATR algorithms in defence applications are the feasibility and reliability in real time implementation. The four feature extraction methods presented in this Chapter have different computational load. In this subsection, the methods are compared in terms of average running time needed to extract the feature vectors. The algorithms are implemented on Matlab

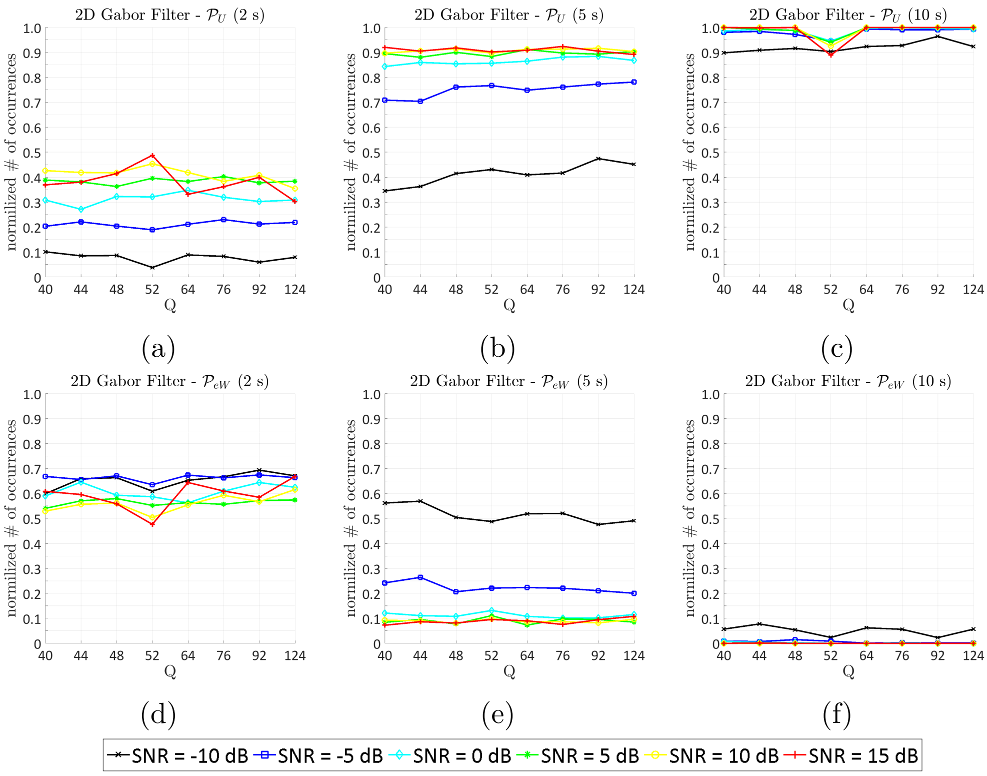

Fig. 4.25 Performance of the Gabor Filter based feature vector approach for real unknown data (booster); the analysis is conducted on varying the number of features Q, the signal duration and the SNR.

environment, and the average running time is evaluated with a Monte Carlo approach over 1000 runs. It is worth noting that in the common steps are not taken into account, in the analysis, starting the of the running time after the elaboration of the CVD. Moreover, the pZ and Kr polynomials for the evaluation of the corresponding moments are precomputed and loaded on memory, as well as the 2D Gabor filter bank.

The ACVD based approach is a very fast method since it requires to average the CVD along the frequency dimension, for extracting six features from a 1D signature. Specifically, the average running time is smaller than 10^{-3} seconds for all the observation time considered. Fig. 4.26 represents the average running time for the extraction of the feature vectors for pZ moments, Kr moments and 2D Gabor filter based approaches, on varying the the signal's duration, hence the CVD dimensions, and the vector dimension. It is observed from Fig. 4.26a that the computation of pZ moments requires more time increasing the duration of radar observation and the moments order. The highest elaboration time is about 4 seconds, required for order equal to 20 and for 10 seconds long signals. Fig.

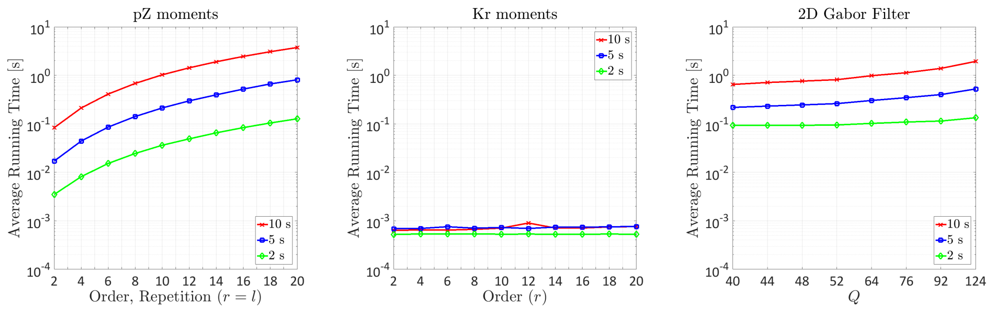

(a) (b) (c)

Fig. 4.26 Performance of the pZ moments, Kr moments and 2D Gabor filter based approaches in terms of average running time for the feature vector extraction.

4.26b shows that the computation time of Kr moments is almost independent on the considered orders, with a slightly gap between the evaluation for 2 seconds long signals and 5 and 10 seconds, for which the difference is negligible. This trend is because the Kr moments are computed by a matrix product, and the matrix dimensions considered into the analysis do not affect the computational time guaranteed by the hardware used for the evaluation. Finally, for all the analysed cases the average running time is smaller than 10^{-3} seconds, such as for the ACVD method. The main reason of the faster implementation of the Kr moments with respect the pZ ones is that they are discretely defined, and they not requires the inscription of the 2D signature within the unit circle, as the pZ moments do. For the same reason, discretization error does not exist for Kr moments and the amount of resource required to store the polynomials is reduced thanks to the recurrence relations and the symmetry properties of Kr moments. Fig. 4.26c shows that the average running time for the 2D Gabor filter based features vector increases significantly as the signal duration increases, while it slightly increases by increasing the filter bank dimension within the set of considering values. Comparing Fig. 4.26a and Fig. 4.26c it is observed that, by fixing the signal duration, for moments order greater than 10 pZ moments require longer running time than the 2D Gabor filtering does for all the considered filter bank dimension. The highest computational time for 2D Gabor filter approach is about 2 seconds, obtained by using 124 filters in case of 10 seconds long signals.

4.6 Summary

In this Chapter the capability of mD based recognition in the specific challenge of distinguishing between warheads and decoys has been evaluated. The signal

model described in Section 4.2 has been used to simulate the received signal from the different targets, with different shapes and dimensions, on varying the elevation and azimuth angles. By using a robotic manipulator for simulating the target motions and a CW radar, instead, a real database has been obtained by acquiring in laboratory the signals scattered by scaled replicas of the targets of interest. Subsequently, a framework presented in (Clemente et al., 2015b) has been used for performing the classification, introducing four different techniques for the extraction of mD based feature vectors from the CVD.
The reliability of these techniques has been demonstrated by testing them both on simulated and real mD data. The results have shown that, for both simulated and laboratory data, all the proposed approaches generally ensure a sufficient degree of correct classification. Moreover, an analysis on real unknown data has been conducted in order to test the presented methods also in the case in which the feature vector under test does not belong to one of the classes of interest, such as the booster separated from warhead. In this case, the results have shown that the 2D Gabor based approach guarantees better performance with respect the other approaches for a sufficient observation time, recognizing the unknown target properly. Finally, an analysis on the average running time to evaluate the features, as figure of merit of computational complexity of the methods, has been conducting. The latter has showed that Kr moments based approach is the faster method, being very suitable for real time applications, such as for the OBC of interceptor.
In conclusion, from the analysis of the performance, one can deduce that the framework is reliable for the classification of BTs, and it can be adapted by choosing the best feature vector extraction approach suitability with respect to the radar scenario and the available resources.

Chapter 5

Classification Algorithm for Ballistic Targets based on High Resolution Range Profile frame

5.1 Introduction

The information regarding target micro-motions can be extracted from both Doppler and range analysis of radar returns. In the previous Chapter, an adaptive framework for BM classification is presented, demonstrating the capability to discriminate between warheads and decoys using the micro-Doppler (mD) information. In particular, the framework is based on the evaluation of the spectrogram and of the Cadence Velocity Diagram (CVD), which allows to observe the cadence of the mD frequencies within the received echo. In order to perform the target classification, the CVD is used as target signature from which a feature vector is extracted by using several approaches, which are different in terms of computational cost and feature vector dimension.

On the other hand, the micro-motions exhibited by the target lead to range migrations of its principal scattering points observable through a High Resolution Range Profile (HRRP) frame obtained by a wideband radar. The use of SFWs for achieving a HRRP in a BMD scenario is thoroughly analysed in (Clark, 1999). Since in this specific scenario the profile may contain a number of objects with different velocities, a technique for velocities compensation is presented based on the use of Wavelets and of a velocity extraction method.

Over the past few years Frequency Stepped Chirp Radars (FSCR) have been widely used also in missile terminal guidance (Liu and Chang, 2013). The authors in (Liu and Chang, 2013) proposed a novel velocity estimation algorithm for missile-borne FSCR with the aim to compensate the distortion in the HRRP due to relative motion between the radar and the target. Specifically, the algorithm is based on the evaluation of the waveform entropy in the Doppler amplitude spectrum.

The authors in (Lei et al., 2012) investigated the effect of target micro-motions on the distribution characteristic of the HRRP over the time. In particular an analysis on the capability to discriminate between different target shapes and micro-motions (such as precession, wobbling and tumbling) is conducted by a graphical analysis which combines information extracted from the HRRP frame and a Time-Frequency Distribution (TFD).

In this Chapter a novel ATR algorithm based on IRT is presented with the aim to classify targets in a BMD scenario from a sequence of HRRPs. Specifically the IRT of the HRRP frame, obtained by a SFW radar, leads to a 2D target signature containing information on target motions and the spatial distribution of its principal scattering points. Then from the target signature a feature vector is extracted, whose elements are the pZ moments extracted from the 2D target signature. The pZ moments are very attractive for image classification for their useful properties, such as scale, translation and rotation invariance. For this specific classification approach the rotation and scale invariance are fundamental to ensure robustness with respect to the velocity and initial phase of the target micro-motions.

5.2 HRRP frame from BTs

Let us consider the transmission of a sequence of bursts with a fixed PRF, according to (2.49). The transmitted signal can be written as

$$s_{tx}(t) = \sum_{m=0}^{M-1} \sum_{n=0}^{N-1} p_s(t - nT - mNT) e^{j2\pi f_n t} \tag{5.1}$$

with M the number of bursts. The received echo from a target at RF is expressed as the superimposition of the signals from each principal scattering point. After de-chirping operation, by mixing the received signal with the reference signal, as described in Section 2.6, the compensation of the Residual Video Phase (RVP) and of the envelope sideling phase (Qun Zhang, 2016), the received sample corresponding to n-th sub-pulse of m-th burst is

$$s(n,m) = \sum_{i=0}^{N_P-1} \sqrt{\sigma_i}(n,m) e^{j\phi_i(n,m)} e^{-j\frac{4\pi}{c} f_n \Delta R} \tag{5.2}$$

with $m = 0, \cdots, M-1$ and $n = 0, \cdots, N-1$, $\sqrt{\sigma_i}$ and ϕ_i are the modulus and the phase of the electromagnetic contribution of i-th scattering point, and $\Delta R = \Delta R(t) = R_{\mathcal{MC}}(t) - R_0(t)$, with $R_{\mathcal{MC}}(t)$ the distance between the radar and the mass centre of the target and $R_0(t)$ the reference range. As described in Section 4.2.1, the phase of each coefficient depends on the relative distance between the target MC and the scattering point projected onto the LOS, according to (4.25). Specifically, it is a function of the carrier frequency of each sub-pulse and of the aspect angle, as follows

$$\phi_i(n,m) = \phi_i(f_n, \alpha(t)) \simeq \frac{4\pi f_n}{c} \left[\tilde{x}_i \sin\alpha(t) + \tilde{z}_i \cos\alpha(t)\right] \tag{5.3}$$

where $(\tilde{x}_i, \tilde{z}_i)$ are the coordinates of the i-th scattering points onto incident plane $\tilde{x}\tilde{z}$, and where $\alpha(t)$ is given by (4.18). For simplicity, in the following analysis two different motion models are taken into account: the precession, as warhead motion, and the tumbling, as decoy motion. The effect of nutation on the HRRP frame for precessing target is neglected, so that $\Delta\Theta = 0$. Moreover, for simplicity and without loss of generality thanks to the symmetric geometry, the radar azimuth angle $\angle\mathrm{Az}$ is set equal 0, such that

$$\alpha(t) = \cos^{-1}(\cos(\angle\mathrm{El})\cos(\Theta) + \sin(\angle\mathrm{El})\sin(\Theta)\cos(\Omega_c t)) \tag{5.4}$$

The conventional method for extracting the HRRPs from the echoes from each transmitted bursts is the computation of the IDFT along the stepped frequencies, as described in Section 2.6. Specifically the (ε, m)-th element of the HRRP frame is

$$\mathcal{H}(\varepsilon,m) = \left| \frac{1}{N} \sum_{n=0}^{N-1} w(n) \sum_{i=0}^{N_P-1} \sqrt{\sigma_i}(n,m) e^{j\phi_i(n,m)} e^{-j\frac{4\pi}{c} f_n \Delta R} e^{j\frac{2\pi n}{N}\varepsilon} \right|^2 \tag{5.5}$$

with $\varepsilon = 1, ..., N$ and $m = 1, ..., M$, and $w(\cdot)$ is the smoothing window. Three target shapes are considered, namely cone, cylinder and cone plus cylinder. The number of scattering points depends on the target shape. As in the previous Chapter, for a conical target three principal scattering points are considered: the first is in correspondence of the cone tip; the other two points are located on the intersection between the circumference at cone bottom and the incident plane. The cylindrical target is represented by four principal scattering points, specifically two for each base, taken by intersecting the circumferences at the bases and the incident plane. Finally, for a target composed by a cone and a cylinder which share the base, five scattering points are considered. One represents the tip of the cone, while the other four are taken on the circumferences in correspondence of the cylinder bases on the incident plane, as shown in Fig. A.1c in Appendix A.

Complex Scattering Coefficient Models

Three different mathematical approaches are considered for the complex coefficients of the target scattering points. For simplicity, the first approach consists of approximation according to which the modulus of coefficients is equal to 1 when there is LOS between radar and the scattering points, while it is 0 when occlusion occurs , as considered in Chapter 4. The values of the coefficients modulus on varying the aspect angle for the cone and cylinder scatterers are synthesized in Table 4.1 and Table 4.2, respectively, for $\alpha(t) \in [0, \pi]$. For the target composed by a cone plus a cylinder, $\sqrt{\sigma_i} = 0$ for P_1 when $\alpha(t) \in [\pi - \gamma, \pi]$; for P_3 when $\alpha(t) = 0$; for P_4 when $\alpha(t) \in [0, \pi/2]$; for P_5 when $\alpha(t) \in]0, \pi]$; even for the cone plus cylinder, the occlusion never occurs for P_2 with $\alpha(t) \in [0, \pi]$. Table 5.1 synthesizes how the coefficients modulus for the cone plus cylinder vary on the aspect angle. The values of complex coefficients modulus for $\alpha(t) \in [\pi, 2\pi]$ can be

Table 5.1 Modulus of the scattering coefficients for the four principal scattering points P_1, P_2, P_3, P_4 and P_5 of the cone plus cylinder, with respect to the aspect angles α.

	$\sqrt{\sigma_1}(\alpha)$	$\sqrt{\sigma_2}(\alpha)$	$\sqrt{\sigma_3}(\alpha)$	$\sqrt{\sigma_4}(\alpha)$	$\sqrt{\sigma_5}(\alpha)$
$\alpha = 0$	1	1	0	0	1
$0 < \alpha < \gamma$	1	1	1	0	1
$\gamma < \alpha < \frac{\pi}{2}$	1	1	1	0	0
$\alpha = \frac{\pi}{2}$	1	1	1	0	0
$\frac{\pi}{2} < \alpha < \pi - \gamma$	1	1	1	1	0
$\pi - \gamma < \alpha < \pi$	0	1	1	1	0
$\alpha = \pi$	0	0	1	1	0

easily obtained thanks to the symmetry of the targets considered in this analysis. The other two mathematical models for the scatterer complex coefficients refer to two different polarizations: vertical and horizontal polarization. The mathematical expressions of the coefficients are shown in Appendix A. The phase of the complex coefficients for this two models is evaluated with respect to a reference phase centre, RP, which can be different from the mass centre. Since the mass centre is stationary with respect to the micro motions, the electromagnetic field scattered by the target is generally calculated by considering the mass centre as the phase reference centre. For this reason (5.2) is modified in the case of RCS model for vertical and horizontal polarization taking into account a corrective term for the phase as follows

$$s(n,m) = \sum_{i=0}^{N_P-1} \sqrt{\sigma_i}(n,m) e^{j\phi_i(n,m)} e^{-j\frac{4\pi}{c}f_n \Delta R} e^{-j\frac{2\pi}{c}d_{MP}\cos(\alpha_{n,m})} \tag{5.6}$$

where $\alpha_{m,n} = \alpha(mT+nTr)$, $d_{MR} = MC - RP$ is the distance along the symmetric axis between the mass centre MC and the phase reference centre RP, shown in Fig. A.1a, Fig. A.1b and Fig. A.1c in Appendix A.

Fig. 5.1 shows the normalized HRRPs (in dB) obtained for a conical target varying the aspect angle over 360°, with $\Delta R = 0$, for the three models for scattering coefficients. The cone height and diameter are 1 m and 0.7 m, respectively. It is highlighted that The HRRPs are simulated in the hypothesis that the object is stopped during the acquisition of each burst and in absence of noise, in order to analyse only the variation of HRRP of the target over the aspect angle. This means that the aspect angle is considered constant during the burst, such that $\alpha_{n,m} = \alpha_m = \alpha(mT)$. A SFWs radar with a total bandwidth of 800 MHz between 2.6 and 3.4 GHz is considered, transmitting 128 square sub-pulses with a PRF of 20 kHz. The range resolution guaranteed by the considered radar is 18.75 cm. For each value of aspect angle the received signal vector is zero-padded along the stepped frequency computing the IDFT over 512 bins to obtain the HRRP. Moreover, a Hann window is used in order to emphasize the scatterers with lower coefficient modulus in the vertical and the horizontal polarization. Observing Fig. 5.1b and Fig. 5.1c it is noted that the contribution of the cone tip in the scattered field is generally lower than the contribution of the scatterers on the bottom, in both polarizations. However in a small interval of values of aspect angle, the tip of the cone is more visible in the vertical polarization than in the horizontal.

Fig. 5.2 shows the normalized HRRPs over 360°, with $\Delta R = 0$, from a cylinder whose height and diameter are 1 m and 0.7 m, respectively. From Fig. 5.2a it is noted that for each value of the aspect angle three scatterers are simultaneously visible at most. Moreover, while for the vertical polarization the scattering coefficients of some scatterers are higher then the others, with horizontal polarization

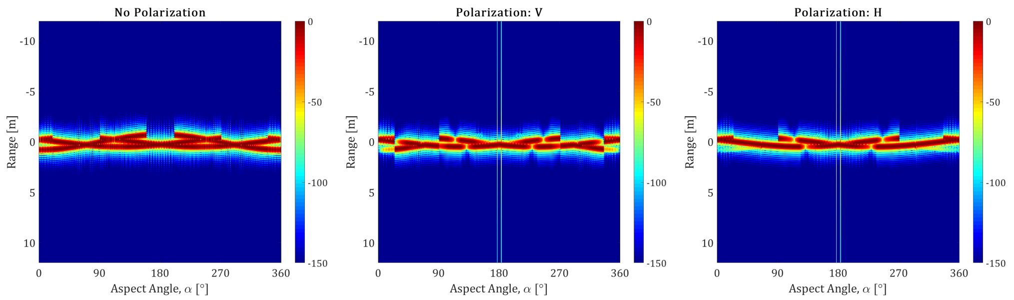

(a) (b) (c)

Fig. 5.1 Normalized HRRP from the cone for $\alpha \in [0, 2\pi]$: (a) no-Polarization; (b) Vertical Polarization; (c) Horizontal Polarization.

the scattering contributions of visible scatterers are similar between each other, as shown in Fig. 5.2b and Fig. 5.2c.

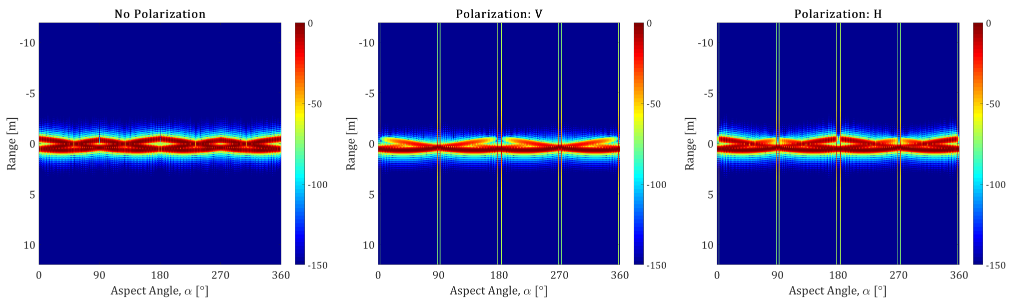

(a) (b) (c)

Fig. 5.2 Normalized HRRP from the cylinder for $\alpha \in [0, 2\pi]$: (a) no-Polarization; (b) Vertical Polarization; (c) Horizontal Polarization.

Fig. 5.3 shows the normalized HRRPs over 360°, with $\Delta R = 0$, from target composed by a cone plus a cylinder. The cone and cylinder heights are 1.4 m and 0.7 m, respectively, while the diameter is 0.4 m. Fig. 5.3b and 5.3c show that the contribution from the cone tip is generally lower than the ones from the other scatterers. However, even in this case the tip of the cone is more visible in the vertical polarization than in the horizontal one.
Finally it is pointed out that even for the RCS model of cylinder and cone plus cylinder for both the analysed polarizations, some approximations are considered leading to errors in the HRRP evaluation for some values of the aspect angle, as described for the cone.
As described in Section 2.3.2, the RCS of missiles shows fluctuation represented by a log-normal random variable. For this reason, the modulus of the each received signal sample $s(n, m)$ is multiplied by the square-root of a coefficient $\boldsymbol{L}_n(n, m)$,

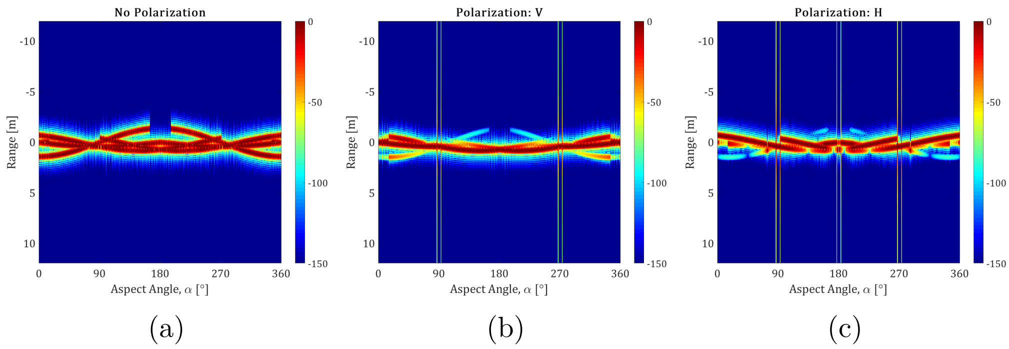

Fig. 5.3 Normalized HRRP from the cone plus cylinder for $\alpha \in [0, 2\pi]$: (a) no-Polarization; (b) Vertical Polarization; (c) Horizontal Polarization.

which is a statistical sample from log-normal distribution. Finally, the expression of the HRRP frame in presence of Additive White Gaussian Noise (AWGN) can be written as

$$\mathcal{H}(\varepsilon, m) = \left| \frac{1}{N} \sum_{n=0}^{N-1} w(n) \left[\sqrt{\boldsymbol{L}_n}(n, m) s(n, m) + \boldsymbol{N}_0(n, m) \right] e^{j \frac{2\pi n}{N} \varepsilon} \right|^2 \tag{5.7}$$

with $\varepsilon = 1, ..., N$ and $m = 1, ..., M$, and where $\boldsymbol{N}_0(n, m)$ is the AWGN sample. It is worth noting that for this analysis the fast fluctuation of target RCS is considered, such that the fluctuations are independent from sub-pulse to sub-pulse of the entire sequence of HRRPs.

5.3 Classification Algorithm

In this Section a novel classification algorithm which is able to extract reliable feature from the HRRP frame based on the micro-motions exhibited by BTs is presented. Specifically the algorithm is based on the IRT and the evaluation of pZ moments of a 2D target signature. Fig. 5.4 represents a block scheme of the presented algorithm.

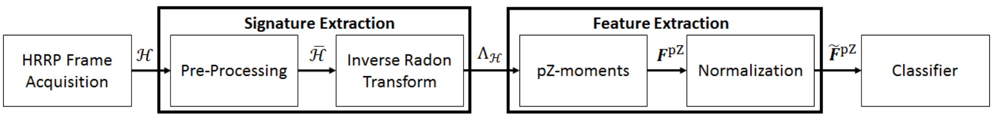

Fig. 5.4 Algorithm block scheme.

HRRP Frame Acquisition

The aim of the first block is to acquire a HRRP frame whose time duration is approximately long as the period of rotational motion exhibited by the target. Therefore an accurate estimation of main rotation period exhibited by the target is needed. In the literature there are presented several method for the estimation of rotation rate $\widehat{\Omega_c}$ of a target (Bai and Bao, 2014; Kangle et al., 2009; Liu et al., 2010; Yan et al., 2011). However, the rate estimation processing is out of the scope of this work. The number $\widehat{M}$ of bursts needed for computing the target classification depends on the estimated rotation rate value $\widehat{\Omega_c}$ and the SFWs radar parameters. Specifically it follows

$$\widehat{M} = \left\lceil \frac{\widehat{\Omega_c}}{2\pi \mathrm{BRF}} \right\rceil \tag{5.8}$$

where BRF is the Burst Repetition Frequency, which is the number of the entire sub-pulse sequences transmitted in a second. It is worth noting that an approximation error may occur due to the fact that the number of bursts to cover an entire rotation period is not an integer.

Fig. 5.5 represents the HRRP frame acquisition scheme, where two possible configuration are illustrated. In the first configuration (**case 1** in Fig. 5.5) the estimation of the rotation rate, and consequently of the number $\widehat{M}$ of bursts making up the HRRP frame, is computed by using primary observations of the target by cooperative system. Then the SFWs radar will transmit $\widehat{M}$ bursts for generating the frame for the classification algorithm. In the second configuration (**case 2** in Fig. 5.5), data acquired directly by the SFWs radar are used for the estimation of $\widehat{M}$. Then the selection data block will extract the sequence of bursts for the classification directly from the available data.

The received signals from each burst are processed as described in Section 2.6 in order to obtain a HRRP frame from the target. The output of the first block is the matrix, $\mathcal{H}$, whose each column contains the HRRP from a single burst.

Signature Extraction

The signature extraction block is composed by two steps (see Fig. 5.4). The Pre-processing block consists into two steps. The first is the normalization of each

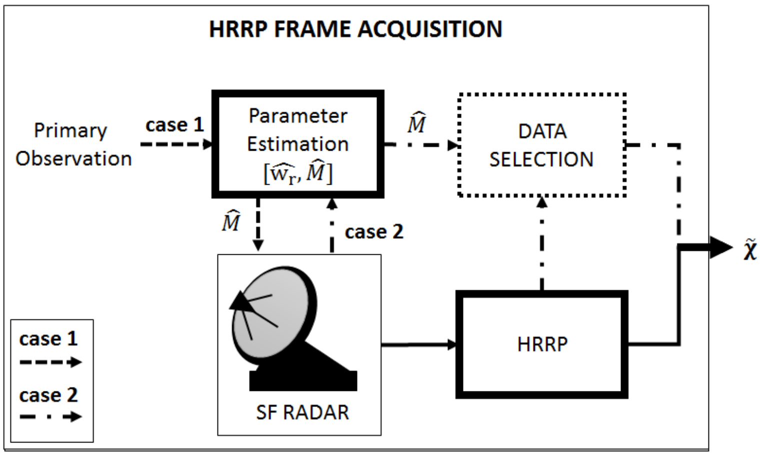

Fig. 5.5 HRRP frame generation block scheme.

HRRP which makes up the frame with respect to its own maximum value

$$\bar{\mathcal{H}}(\varepsilon, m) = \frac{\mathcal{H}(\varepsilon, m)}{\max_{\varepsilon} \mathcal{H}(\varepsilon, m)} \tag{5.9}$$

The second step of pre-processing block consists into resizing the normalized frame $\bar{\mathcal{H}}$ around the range of mass centre, $R_{\mathcal{MC}}$, such that the interval of considered ranges is greater than the maximum dimension of the targets of interest. Following the target signature for the classification algorithm is extracted by applying IRT of the pre-processed HRRP frame. Specifically, the filtered back-projection method with ramp filter is considered, as commonly used in the literature (Bai et al., 2011).

The space distribution function of principal target scatterers is a 2D function defined on the plane $\tilde{x}\tilde{z}$ given by the superimposition of delta functions as follows

$$\mathcal{F}(\tilde{x}, \tilde{z}) = \sum_{i=1}^{N_p} \delta(\tilde{x} - \tilde{x}_i)\delta(\tilde{z} - \tilde{z}_i) \tag{5.10}$$

where $(\tilde{x}_i, \tilde{z}_i)$ are the coordinates of the i-th scattering point onto plane $\tilde{x}\tilde{z}$. In the hypothesis that the principal motion of the target is compensated, the range of each scatterer R_i in the HRRP frame depends on the aspect angle as follows

$$R_i(t) = \Delta R - \tilde{x}_i \cos\alpha(t) - \tilde{z}_i \sin\alpha(t) \tag{5.11}$$

Fig. 5.6 shows the range maps and their IRT for the three scatterers of a cone considering an entire rotation period, T_r, for different couple of values of $(\angle\mathrm{El}, \Theta)$. The micro-motions exhibited by target leads to a periodic tracks in the range-slow time domain. Specifically each scattering point generates a sinusoidal path centred into ΔR in the HRRP frame when $\alpha(t)$ varies into $[0, \pi]$. Then, applying the IRT, all the energy recovered from the path of a single scatterer is concentrated into a point obtaining an image which represents the profile of the object with the exact relative distances between scatterers onto plane $\tilde{x}\tilde{z}$ (ISAR image of the object). However, from (4.25) it is clear that $\alpha(t)$ generally varies periodically into $[|\Theta - \angle \mathrm{El}|, |\Theta + \angle \mathrm{El}|]$, hence each scatterer moves on a different periodic path. In this specific case, by applying the IRT, the energy from each path is dispersed into the final 2D image, such that each of them generates a close line, e.g. circumference or ellipse. For example, Fig. 5.6e shows the IRT of the range map from a precessing cone with $(\angle \mathrm{El}, \Theta) = (60°, 10°)$, in which each scatterer leads to a different circumference, while Fig. 5.6f shows the IRT of the range map from a wobbling cone with $(\angle \mathrm{El}, \Theta) = (60°, 90°)$, where the contribution from the cone tip is concentrated in a point, while the points on the base generate an ellipse. Therefore, the IRT of HRRP frame can represent the target signature since the close lines are strictly related to the coordinates of scattering points onto plane $\tilde{x}\tilde{z}$.

The 2D target signature Λ is obtained normalizing by $\hat{M}$ the IRT of the output of the pre-processing block, $\tilde{\mathcal{H}}$, as follows

$$\Lambda_{\mathcal{H}} = \frac{\mathrm{IRT}\{\bar{\mathcal{H}}\}}{\hat{M}} \tag{5.12}$$

One of the principal property of the RT is that any rotation of the input function $f(x, y)$ inducts a linear shifting to the sinogram $\mathcal{R}_f(p, \phi)$. As a result, considering the HRRP frame of a target as the RT of its scatterers space distribution function, then the initial phase of the micro-motion leads to a rotation of the target signature. For this reason the choice of features which are invariant for rotation are of interest in this classification problem.

Feature Extraction

The pZ moments are geometrical moments with several properties, among which is that their modulus is rotational invariant, as described in Section 3.4. Specifically, the $(O + 1)^2$ pZ moments of the target signature $\Lambda_{\mathcal{H}}$ are computed in order to extract the feature vector, where O is the maximum order according to (3.15) A

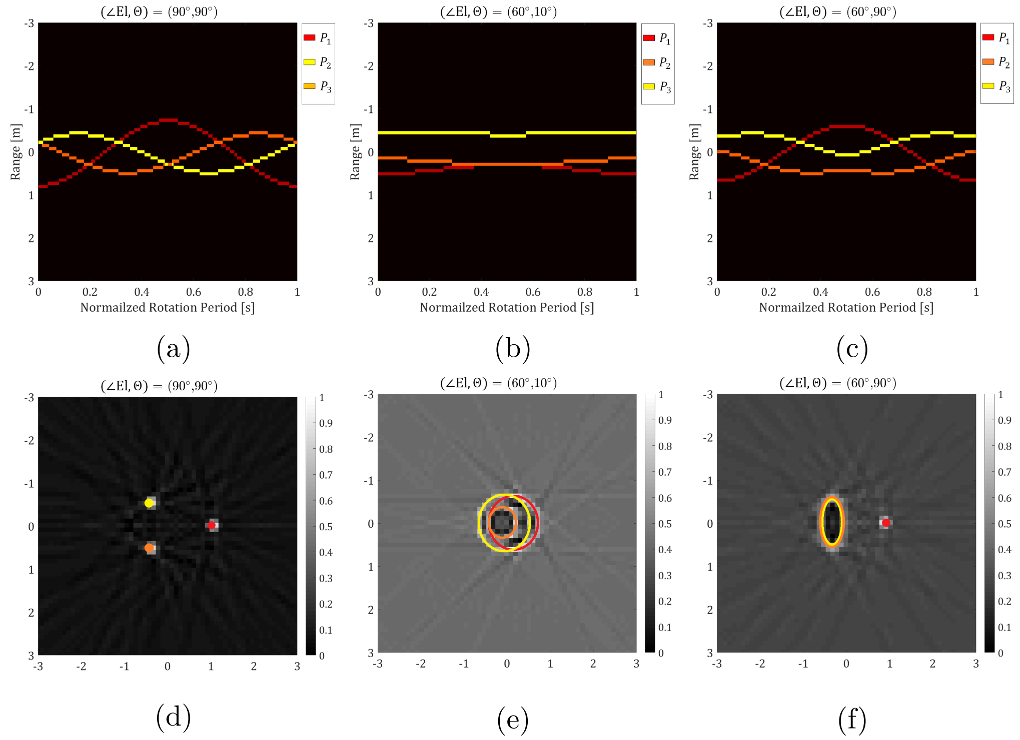

Fig. 5.6 Range map and its IRT for the three points of cone considering a whole rotation period, T_r, for different couple of values of $(\angle \mathrm{El}, \Theta)$: (a) range map for a complete rotation of cone with $(\angle \mathrm{El}, \Theta) = (90°, 90°)$, (b) range map for precessing cone with $(\angle \mathrm{El}, \Theta) = (60°, 10°)$, (c) range map wobbling cone with $(\angle \mathrm{El}, \Theta) = (60°, 90°)$; (d),(e) and (f) are the IRT of the range maps (a),(b) and (c), respectively.

$(O+1)^2$-dimensional feature vector is obtained, whose z-th element is

$$F_z^{\mathrm{pZ}} = |\zeta_{o,l}| \tag{5.13}$$

where $o = l = 0, \cdots, O-1$ and $z = 0, \cdots, (O+1)^2 - 1$. Since the pZ moments are defined on the unit circle, the signature $\Lambda_{\mathcal{H}}$ is inscribed in the unit circle. Finally, in order to avoid that polarized vector may affect the classification process, the final feature vector as input of classifier is statistically normalized according to (4.53). The classification performances of the extracted feature vectors are evaluated using a the k-Nearest Neighbour (kNN) classifier for its capability to give as output the scores for each class and for its low computational load. Additionally, as described in Section 4.4.2, by using the kNN classifier the performance of the classification features are not polarized by the specific proprieties of the classifier.

5.4 Micro-motion Velocity Effect

In presence of a target which moves with a radial velocity v along the LOS, the target range varies during the burst acquisition about $2Nv_rT$. Let us assume that the target is tracked and the main Doppler shift due to the bulk motion is compensated perfectly, such that $\Delta R(t) = R_{\mathcal{MC}}(t) - R_0(t) = 0$. From these assumption follows that the HRRP frame shows how the distance between the radar and each principal scattering point of the target changes with time due to the micro-motions. The position of the peak value of the fine range profile for each scatterer of the target locates at (Qun Zhang, 2016)

$$\frac{4\pi}{c}\Delta f \hat{R}_i \approx -\frac{4\pi}{c}\Delta f R_i - \frac{4\pi}{c} f_0 v_i T \tag{5.14}$$

where $\hat{R}_i$ is the estimated range of the i-th scatterer, R_i is the projection of the distance between the i-th scatterer and the mass centre along the LOS, and v_i is the velocity of the i-th scatterer due to the micro-motion. It is worth noting that the micro-motion of a target leads to a multi-targets (scatterers) scenario, in which each of them has a different velocity profile, given by

$$v_i = v_i(t) = (\tilde{x}_i \sin\alpha(t) - \tilde{z}_i \cos\alpha(t)) \frac{\mathrm{d}\alpha(t)}{\mathrm{d}t} \tag{5.15}$$

with

$$\frac{\mathrm{d}\alpha(t)}{\mathrm{d}t} = \frac{\Omega_c \sin(\angle\mathrm{El}) \sin(\Theta) \sin(\Omega_c t + \phi)}{\sqrt{1 - (\sin(\angle\mathrm{El}) \sin(\Theta) \cos(\Omega_c t + \phi) + \cos(\angle\mathrm{El}) \cos(\Theta))^2}} \tag{5.16}$$

Hence, the displacement from the effective range for each scatterer is different according to its position on target surface, the target motion and the radar position. Fig. 5.7 shows an example of how HRRP frame from the three considered shapes varies considering the stop-and-go hypothesis (dash line) and the continuous motion during the burst acquisition (continuous line). In the example shown, $(\angle\mathrm{El}, \Theta) = (90°, 90°)$ and $\Omega_c = 6\pi$. Moreover, the occlusion and the polarization scattering proprieties of the scatterers are not taken into consideration for making clear the micro-motion effect on the HRRPs. It is worth noting that a rotational motion leads to a circular shift of the tracks of each scatterer in the frame. This shift leads to a rotation of the 2D image recovered by using the IRT. Additionally, the maximum range of each scatterer is greater with respect the real value, such that the object appears greater in the target signature. However, since the velocity

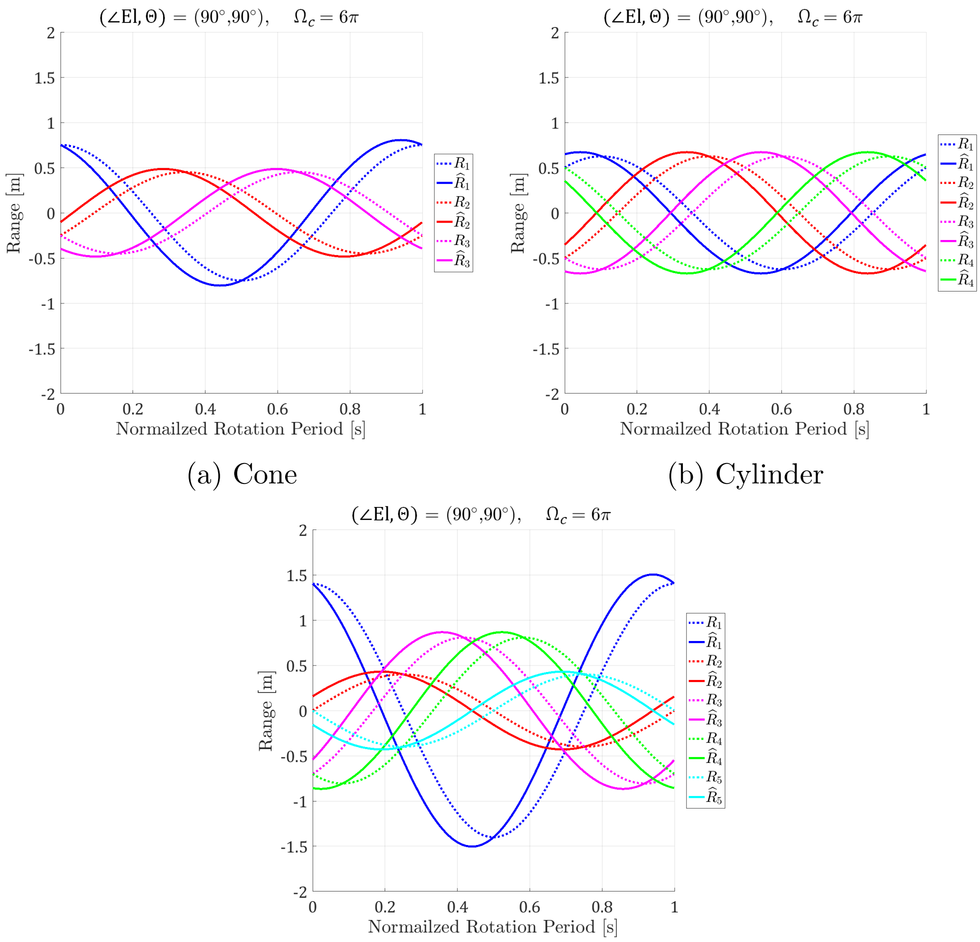

(a) Cone (b) Cylinder

(c) Cone plus Cylinder

Fig. 5.7 Example of HRRP frame from the three considered shapes considering the stop-and-go hypothesis (dashed line) and continuous motion during the burst acquisition (continuous line), for $(\angle \mathrm{El}, \Theta) = (90°, 90°)$ and $\Omega_c = 6\pi$.

of each scatterer depends on the geometry of the target and their distances from target MC, the signature shape (hence, the target shape) may appear distorted, e.g. the conical shapes appear with a greater hight and base ratio. Finally, since a rotation leads to an harmonic radial velocity, the velocity in even not constant during the burst. Specifically, acceleration affects the HRRP reducing the SNR on the 2D target signature.

The pZ moments based features guarantee robustness against rotational and scale effects on the target signature. However, in order to reduce the deformation effect due to the micro-motion and to improve the classification capabilities, the radar SFW may be adaptive to the estimated rotation rate.

5.5 Performance Analysis

In this Section the performance of the proposed classification algorithm is evaluated with simulated data. The algorithm is tested considering three possible shapes for the BTs which are the cone, the cylinder and the cone plus cylinder. The cone and the cylinder have the same height and radius which are 1 m and 0.375 m, respectively. The third shape is obtained by joining a cone whose height and radius are 1.4 m and 0.2 m, respectively, and a cylinder with a height of 0.7 m and radius 0.2 m. Table 5.2 synthesizes the dimensions of target of interest.

Table 5.2 Target Dimensions.

	h_1 [m]	h_2 [m]	r [m]
Cone	0.750	0.250	0.375
Cylinder	0.500	0.500	0.375
Cone plus Cylinder	1.400	0.700	0.200

Hence, six classes are considered, each of them corresponding to a particular shape and motion:

1. *precessing cone*;
2. *wobbling cone*;
3. *precessing cylinder*;
4. *wobbling cylinder*;
5. *precessing cone plus cylinder*;
6. *wobbling cone plus cylinder*;

Generally the precession angle of warheads with a conical shape is relatively small compared to the half cone angle (Bankman et al., 2001) and its value is generally within $[4°, 12°]$ (Sisan et al., 2008). In this work the precessing classes for each shape are obtained by fixing the precession angle Θ equal to $10°$, while for the wobbling classes $\Theta = 90°$.

Both the training and testing sets are simulated considering a SFWs radar transmitting bursts composed by 128 square sub-pulses with a total bandwidth of 800 MHz and a PRF of 20 kHz. All the SFWs radar parameters are synthesized in Table 5.3.

Table 5.3 SFWs radar system parameters.

Carrier frequency	[GHz]	2.600
Total bandwidth	[MHz]	800
Number of sub-pulses	N	128
Waveform bandwidth	[MHz]	6.25
Pulse Repetition Frequency	[kHz]	20
Burst Repetition Frequency	[Hz]	156.25

The training set for each class is realized for different values of the radar elevation angle $\angle\mathrm{El}_u$, given by:

$$\angle\mathrm{El}_u = u\,5^\circ \qquad\qquad \text{with } u = 1, 2, \cdots, 18. \tag{5.17}$$

Each sample of training set is obtained considering the target stopped during the acquisition of a single burst and in absence of noise. Specifically, for a each $\angle\mathrm{El}_u$ a 360 long HRRP frame is simulated such that the target has completed a rotation of 1° between two sequential bursts with respect to its motion. Finally the initial phase of rotation is set equal to zero.

The testing set is realized considering noisy observations and continuously moving targets, even during a single burst. In particular, since the warhead spinning and decoy wobbling frequencies are typically smaller than 3 Hz (Li-hua et al., 2006), the dataset for testing each class is realized on varying the rotation rate within $[0.25, 3]$ Hz. Specifically the angular rotation velocities considered are

$$\Omega_{c_v} = 2\pi\left[\frac{1}{4} + \frac{v}{8}\right]\frac{\mathrm{rad}}{\mathrm{s}} \qquad\qquad \text{with } v = 0, \cdots, 22 \tag{5.18}$$

From (5.8) it is pointed out that the HRRP frame length decreases as the rotation rate increases. Fig. 5.8 shows how the number of bursts of the frame varies with the rotation rate for the SFWs radar described above.

The dataset for the test of each class for a fixed noise power and rotation rate is composed by 900 samples, obtained by realizing 20 acquisitions for each value of $\angle\mathrm{El}_\epsilon = \epsilon\,10^\circ$ with $\epsilon = 1, 2, \cdots, 9$. All the acquisition are different for the noise observation and for the initial phase of the micro-motions. The initial phase is drawn randomly from a uniform distribution $[0, 2\pi]$.

The performance of the proposed algorithm are evaluated in terms of: Probability of correct Motion identification ($\mathcal{P}_M$), which represents the capability to distinguish between precessing and wobbling targets; Probability of correct Shape identification ($\mathcal{P}_S$), which represents the capability to distinguish between the

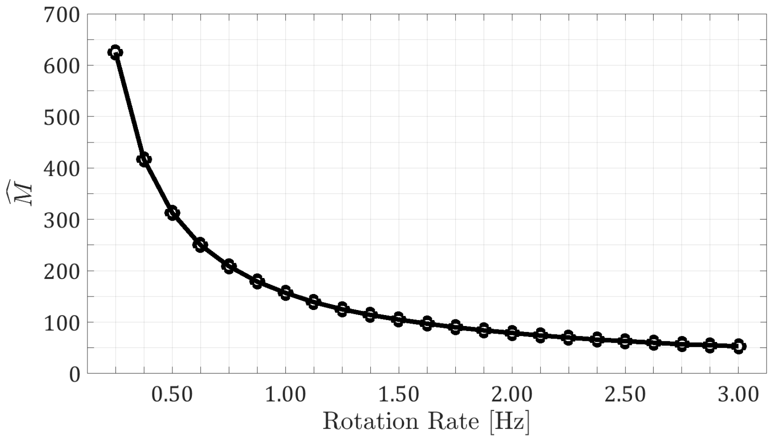

Fig. 5.8 Number of bursts to obtain the HRRP frame on varying the angular rotation velocity and for the SFWs radar described in Table 5.3

shapes of targets; Probability of correct Classification (P_C), the capability to identify the motion and the actual shape of the target.
The analysis is conducted on varying the Signal to Noise power Ratio (SNR), referring to the noise which affects the received signal samples as output of the stretch processing, and considering the RCS oscillation according to the lognormal distribution with zero mean and variance equal to 0.4 (Kangle et al., 2009). The mean of the three probabilities for each couple of values of SNR and rotation rate is evaluated with a Monte Carlo approach over 10^4 different runs in which 100 samples for each class are randomly taken from the testing dataset and classified. The k value of the k-NN classifier is chosen equal to 1.

Fig. 5.9 shows the performance obtained on varying the SNR and the angular rotation rate, considering the no-polarization RCS model. In order to reduce the distortion in the HRRP due to the variation of the aspect angle within the burst interval a Hamming window is used. It is observed that the performance in terms of the three probabilities increases as the SNR increases and decreases as the rotation velocity increases. The main reason is that the IRT integrates incoherently the HRRPs of the frame, increasing the SNR of the final image. This incoherent processing gain depends on the frame dimension: the longer the HRRP frame, the higher the processing gain. However Fig. 5.9a shows that $P_S \geq 0.99$ for SNR greater than $-5dB$ for all the considered rotation rates. P_C and P_M are very similar for SNR greater than $-5dB$ since P_S is close to 1. Specifically, for these SNR values P_C and P_M varies within $[0.93, 0.95]$ for all the rotation rates. It is worth noting that the performance in terms of motion recognition and correct classification are affected by the fact that the aspect angle varies in the same way

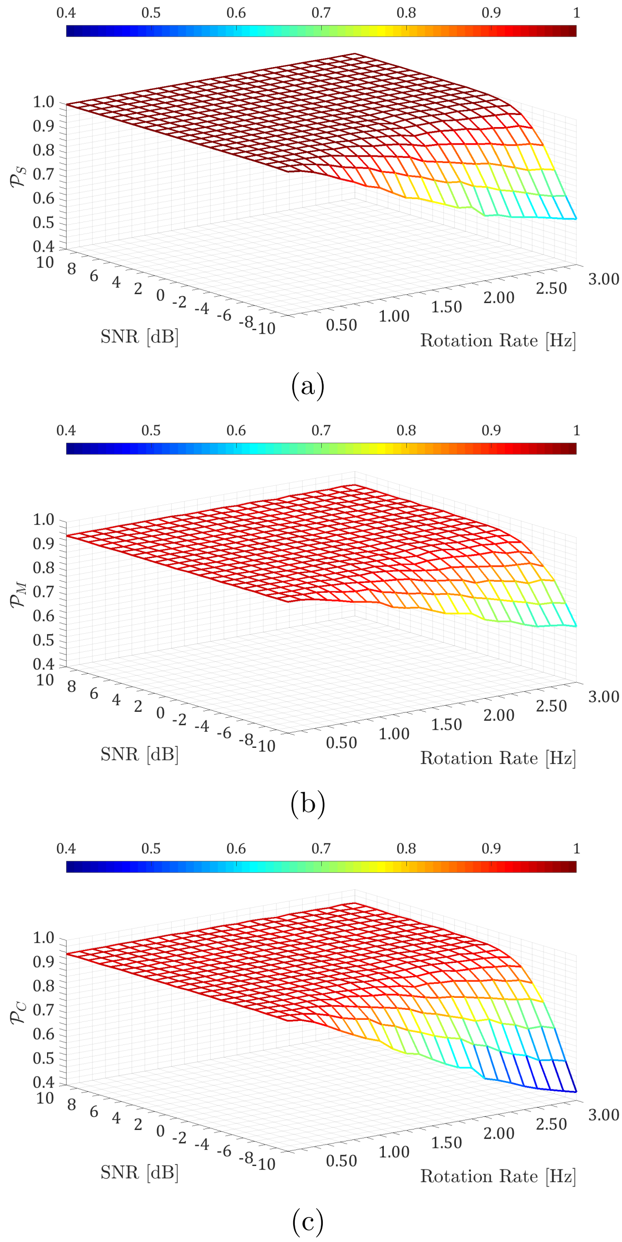

Fig. 5.9 Performance in terms of $\mathcal{P}_S$ (a), $\mathcal{P}_M$ (b) and $\mathcal{P}_C$ (c) by using the no polarization model for the RCS.

when the values of the angles $\angle$El and Θ are switched. In this analysis there is a case in which precession and wobbling lead to the same variation of aspect angle. Specifically, since the training set for each class is composed by 18 feature vectors, the ambiguity in the motion classification is around $1/18 \approx 5.5\%$, which leads to a maximum value for P_M close to 0.95.

Fig. 5.10 shows the performance obtained on varying the SNR and the angular rotation rate, considering the RCS model for the vertical polarization. In this case a Hann window is used with the aim to reduce the distortions in the HRRP due to the variation of the aspect angle within the burst interval and to increase the capability to observe scatterers with lower coefficients. It is observed that

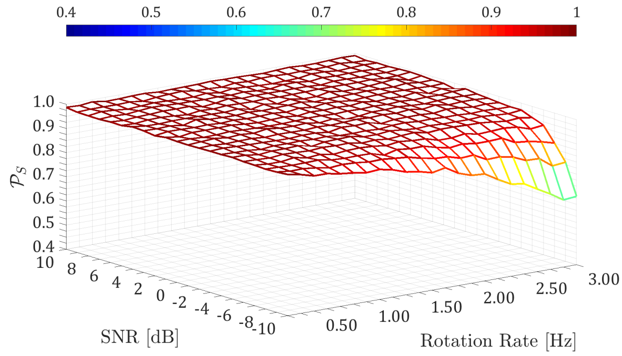

(a)

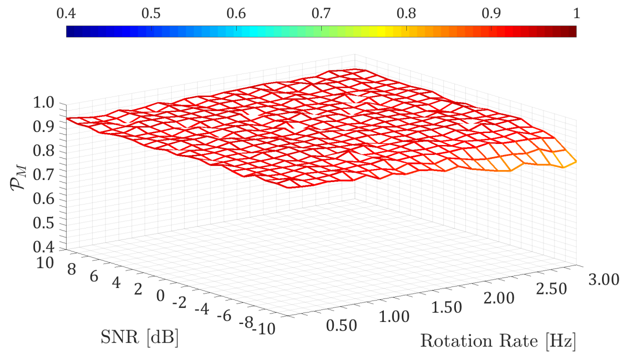

(b)

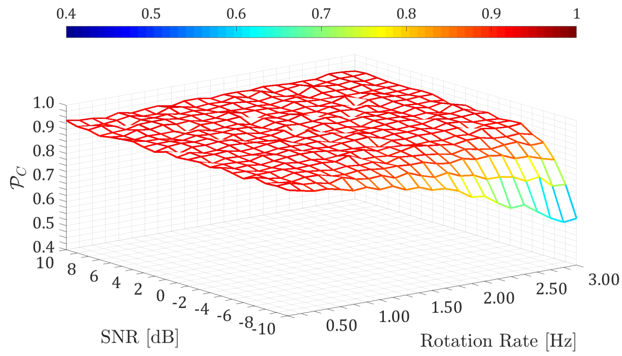

(c)

Fig. 5.10 Performance in terms of $\mathcal{P}_S$ (a), $\mathcal{P}_M$ (b) and $\mathcal{P}_C$ (c) by using the RCS model for vertical polarization.

the performance obtained with the vertical polarization model confirms the trend observed in Fig. 5.9 for the no-polarization model. Specifically Fig. 5.10a shows that $P_S > 0.97$ for all the considered rotation rates when the SNR is greater than $-5dB$, reaching a maximum value of about 0.99. Fig. 5.10b and Fig. 5.10c show that P_M varies within $[0.92, 0.95]$ and P_C varies within $[0.91, 0.94]$ for all the considered rotation rates when the SNR is greater than $-5d$B. Moreover, it is observed that the performance for lower values of SNR and higher rotation rates obtained with the RCS model for vertical polarization are better than the ones for the no-polarization model. The scattering coefficients for the RCS model described in (Ross and DIV., 1969) takes into consideration the target shape not only in terms of distances between the scatterers, but also of its characteristics about shape flatness and sharpness. This information may have particular importance into processing of data with very low SNR values.

Fig. 5.11 shows the performance obtained on varying the SNR and the angular rotation rate, considering the RCS model for the horizontal polarization. Even in this case a Hann window is used to emphasize the scatterers with lower coefficients. From Fig. 5.11a it is observed that the capability to discriminate between the different target shapes decreases lightly by using horizontal polarization rather than the vertical polarization. The main reason is due the scattering proprieties of points in proximity of the sharpest parts of the object. In particular, the tips of the cone and the cone plus cylinder are more visible using the vertical polarization rather than the horizontal, in agreement with the mathematical model in (Ross and DIV., 1969), as described above. However, P_S varies within $[0.94, 0.96]$ when the SNR is greater than $-2d$B, for all the considered values of the rotation rate. The performance in terms of P_M are similar for both the polarization models (observing Fig. 5.10b and Fig. 5.11b), varying within $[0.92, 0.95]$ for all the considered rotation rates when the SNR is greater than $-5d$B. The loss in the performance in terms of P_S using horizontal polarization leads to a loss in P_C, which varied within $[0.875, 0.905]$ for all the considered rotation rate when the SNR is greater than $-3d$B. Finally, it is pointed out that even the performance using the RCS model for horizontal polarization are better than the ones using the no-polarization model for lower values of SNR and higher rotation rates.

The rotation rates of precession and wobbling are generally different. In fact while the warhead spinning and the decoy wobbling frequency may be similar, the precession frequency is typically an order of magnitude smaller with respect to the spinning (Bankman et al., 2001). Therefore, the system capability in terms of motion recognition may be improved considering also the estimated rotation velocity. For this reason the capability to recognize the target shape is considered the most relevant in this analysis. In fact the identification of the shape may be discriminant between warheads and decoys allowing also to understand which kind of warheads the target can be (cone plus cylinder can represent a warheads

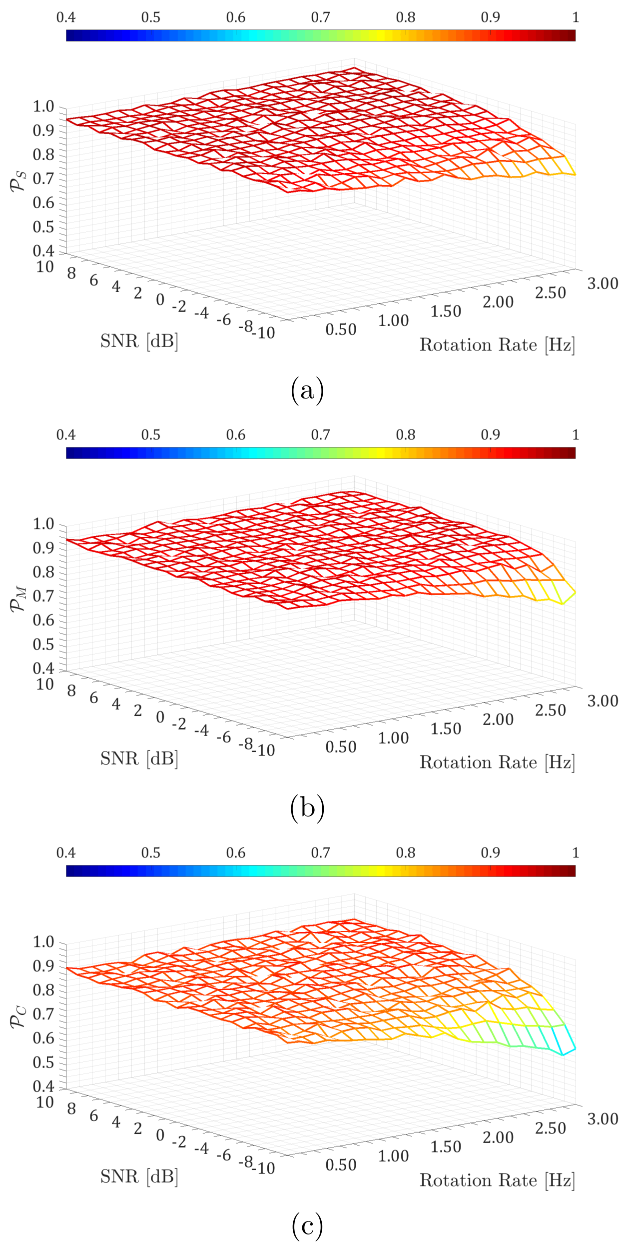

Fig. 5.11 Performance in terms of $\mathcal{P}_S$ (a), $\mathcal{P}_M$ (b) and $\mathcal{P}_C$ (c) by using the RCS model for horizontal polarization.

with an additional booster for manoeuvring).
Finally it is important to point out that the classification algorithm is independent on initial phase of micro-motion and robust with respect to the receiver noise, the RCS scintillation and the approximation error on the HRRP frame dimension.

5.6 Summary

In this Chapter a novel framework for the radar classification of BTs has been presented with the aim to distinguish between warheads and decoys. The presented algorithm employs the information relative to the range migrations of the principal target scatterers due to the micro-motions, which are directly observable from a HRRP frame.

The effect of micro-motions on the SFWs radar return is analysed emphasizing on differences due to the signal polarization and due to the micro-motions exhibited by missile warheads and decoys.

The presented algorithm is based on the use of RT applied on the HRRP frame received from the target in order to extract a 2D target signature. A feature vector for the final classification is evaluated by computing the pZ-moments from the 2D target signature, guaranteeing classification being independent on the initial phase of the target micro-motions (no synchronization required).

The effectiveness of proposed approach is tested on simulated SFW radar data, obtained by considering three model for the RCS of the targets of interest: no polarization model, vertical and horizontal polarization models. The dataset for testing the algorithm has been realized for different values for the micro-motion parameters (e.g rotation velocities and precession angle), radar position angle and noise power.

The results have shown that the framework facilitates the discrimination between the warheads and the decoys with a satisfactory degree of correct shape and motion classification. In particular, the use of vertical polarization guarantees better performance than the horizontal polarization in terms of capability of shape identification and, consequently, of target classification. The reason is due to the higher scattering proprieties of points in proximity of the sharpest parts of the objects (e.g. cone tip) in the vertical polarization. The features are robust with respect to the SNR, the RCS oscillation and the HRRP distortions due to micro-movements. Specifically, this algorithm performs well in noise because the IRT has a high accumulation gain to sinusoidal curves in the target signature. However, it is worth noting that, in order to apply efficiently the proposed algorithm, it is required good estimations of target rotation rate and MC range.

Chapter 6

Space-borne Passive Bistatic Radar for SSA and BMD: a Precursory Study

6.1 Introduction

Recently FS radars have been used in many different scenarios for performing radar tasks e.g. detection, tracking and imaging. In (Cherniakov et al., 2006) an algorithm for the classification of vehicles with different size is proposed based on different frequency Doppler shifts which characterize the target signature. In (Hu and Zhu, 1997) the capability to detect an aircraft by a FS radar using the Global Navigation Satellite System (GNSS) satellites as illuminator of opportunity was demonstrated experimentally. Moreover, target classification was performed by evaluating the Shadow Inverse Synthetic Aperture Radar image from received signals. The authors in (Abdullah et al., 2017) show experimentally the capability of extracting micro-Doppler (mD) information due to target secondary motions e.g. rotation or vibration, which may be used for target classification using FS configuration.

In this Chapter the concept of FS is exploited for Space Situational Awareness (SSA). A novel radar system for the detection of very small space debris, which may allow the development of target tracking and classification capabilities, is presented. Specifically, the precursory study of a new space-borne PBR system for space target detection is investigated, determining its detection capabilities in terms of target dimensions based on the Radar Range Equation (RRE).

The main motivations for a space-borne PBR is that: i) it reduces the distance between transmitter and receiver and ii) allows for a lower relative velocity between illuminator and receiver and iii) bypasses the atmosphere and the sources of error and attenuation that come with it. The long distance has an impact on the required gain of the antenna, while the relative velocity has an impact on the integration time, and thus the ability to detect small objects. Moreover a space-borne receiver in LEO avoids the detection of other flying objects, or bird flock.

6.2 Space-Borne Passive Radar System

In this section a new system for space debris detection and monitoring is described. The idea is to fly a receiver at low-altitude, collect and analyse the radio waves coming from any satellite flying at higher altitudes and broadcasting towards the Earth. One or more nano-satellites, or cubeSats, in LEO would form a low-cost detection system with a sufficient lifetime to collect enough data on the existing debris population but not long enough to increase such a population. As illustrated in Fig. 6.1, a sensing platform comprises essentially three principal components: a Software Defined Radio (SDR) as a passive bistatic radar receiver, a Low Noise Amplifier (LNA), and one or more antennas. The LNA is introduced to enhance the sensing capacity by increasing the receiver gain. Any satellite

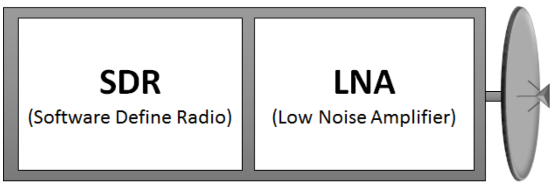

Fig. 6.1 Representation of proposed radar system for space debris detection and tracking.

transmitting radio waves towards the Earth within the frequency band of the antenna on the sensing platform represents a suitable illuminator. The source of RF illumination can be selected statically or dynamically among the available platforms (e.g. existing constellations such as Iridium, GNSS, HY2A). One of the main features considered in this work for the illuminator selection, is the satellite altitude. In fact, the RF source has to fly at higher orbits with respect to the receiver, such that the FS region between transmitter and receiver can be exploited for the detection of space debris. By using the FS configuration, an object can be detected by measuring the variation in received power. When there is no object along the LOS between transmitter and receiver, the received power is almost constant in time. When an object approaches the LOS, the FS field starts to shadow the receiver leading to a loss of received power. The proposed system configuration is described in Fig. 6.2. As described in Section 2.3.2, the

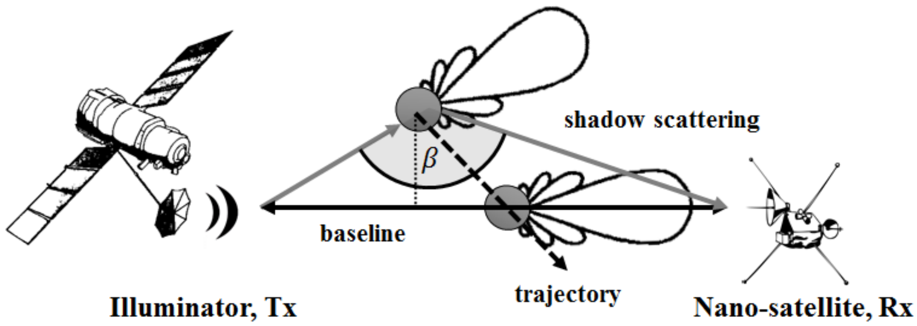

Fig. 6.2 Working principle of the proposed Passive Radar on a nano-satellite.

peak FS RCS is reached when the target crosses the LOS and the wavelength is smaller than the target silhouette's area, such that it is given by (2.25). This peak value can be used as a signature for the detectability of an object. Note, however, that even in the case in which the bistatic angle never reaches 180°, the detection via FS radar can take place considering the sidelobes effect of the diffracted field (Cherniakov et al., 2006).
Nevertheless the absence of range resolution of FS radar is compensated by the advantage of absence of signal fluctuation because of the target's natural swinging, which represents a limit for coherent signal processing time in conventional radar. Notice that in order to obtain the maximum benefit from a long coherent processing interval the received signal must have a zero frequency offset with respect to the matched filter. By using a PBR on a nano-satellite or on a cubeSat, the Doppler offset can be very small in case of transmitter, receiver and target move on similar directions. Moreover, the attenuation and delays introduced into the received signal by the atmosphere (e.g. by troposphere) are avoided.
In case the signal transmitted by the illuminator is known (e.g. GNSS), a way to achieve a good performance from a such passive system is to create a replica of the expected scattered signal from the debris for the receiving system, assuming a preliminary knowledge of system kinematics. However, since the Doppler effect which affects the received signal result from the relative movement of transmitter, receiver and target (which can be about thousands of meters per second in the worst case of opposite fly directions), it is not guaranteed to yield a constant Doppler offset during the acquisition time interval. For this reason, a bank of matched filters could also be used, in case of small deviations from the expected

Doppler, assuming linear variation (Benson, 2014).

An alternative approach is proposed in (Mahmud et al., 2016), where a multi-step processing strategy is described for reducing the computational cost. Firstly, the received signal is correlated with a replica of the expected signal over a relative short integration period. The latter is taken short enough such that the phase error between the received signal and the replica is approximately constant. Through Integrate and Dump (I&D) operations, complex observations of the beat signal between the replica and the actual indirect arrival are obtained. Finally, the full length coherent integration is obtained by adjusting the phase of the samples of I&D operations and summing over the observation period. This second step is robust against phase errors that are inconsistent over the observation period. This approach, which has been demonstrated in case of GNSS signals, can be potentially adapted for decoding other weak signals as well (Mahmud et al., 2016).

Another possible solution is the crystal video detector. The crystal video detector consists into widely used detection scheme, based on the square law detector, followed by mean level cancellation and matched filter. The authors in (Ustalli et al., 2017) present a full characterization of the performance of the crystal video detector for a FS radar in presence of a moving target onto linear trajectory against Additive White Gaussian Noise (AWGN). Specifically, it is shown that the crystal video detector has limited losses with respect to the ideal detector, when the target is in far field. For this reason, this kind of detector can be used for the proposed system for monitoring a specific set of orbits at suitable distance from the space-borne receiver's orbits and the selected illuminator's ones.

6.3 Detection Capability Analysis

In this Section the detection capabilities of the proposed radar system are evaluated. Before extracting the desired radar information, the SNR is generally increased by processing the received signal. Specifically, considering the signal processing gain G_{sp} from the use of matched filter for a modulated pulse in reception, and the incoherent integration of N pulses, the SNR is

$$\overline{\mathrm{SNR}} = \frac{P_t G_t G_r \sigma \lambda^2}{(4\pi)^3 R_t^2 R_r^2 k T_0 B_r F L_s} \sqrt{N} G_{sp}. \tag{6.1}$$

Note that targets orbiting in space exhibit additional motion components on top of the basic Keplerian one. In particular, orbital perturbations, with a frequency higher than the orbital period, and attitude motion lead to a fluctuation of the area of the target's silhouette that is measured by the radar (Qun Zhang, 2016). Therefore, an incoherent integration of radar pulses has to be considered in order to take into account the fluctuations of the target's silhouette.

6.3.1 Figure of merit

The key performance indicator for the proposed passive bistatic radar system is the minimum size of detectable targets. Since in the case of FS the RCS depends only on the target silhouette area, the information on sizes of detectable object can be obtained from the RCS. Rearranging (2.13), the RCS into bistatic configuration can be written as a function of the system parameters and SNR as follows

$$\sigma = \frac{(4\pi)^3 R_t^2 R_r^2 k T_0 B_r F L_s}{P_t G_t G_r \lambda^2} \frac{\overline{\mathrm{SNR}}}{\sqrt{N} G_{sp}}. \tag{6.2}$$

In this way it is possible to define what the minimum RCS of a detectable target is by fixing the SNR at the receiver that is needed to guarantee a given probability of detection.
From (2.25) and (6.2) it follows that the minimum silhouette's area, $\bar{A}$, of a detectable object by a FS system in the Fraunhofer zone is obtained from the minimum required RCS as follows

$$\bar{A} = \sqrt{\frac{\lambda^2 \sigma_{min}}{4\pi}} = \frac{4\pi R_t R_r}{\lambda} \sqrt{\frac{k T_o B_r F L_s \widehat{\mathrm{SNR}}}{P_t G_t G_r G_{sp} \sqrt{N}}}, \tag{6.3}$$

where $\widehat{\mathrm{SNR}}$ is the minimum SNR required to guarantee detection. It is worth noting that $\bar{A}$ is a function of the target's altitude, such as

$$\bar{A} \propto R_t R_r = f(\rho_{st}|\rho_{rx}, \rho_{tx}) = (\rho_{st} - \rho_{rx})(\rho_{tx} - \rho_{st}), \tag{6.4}$$

where ρ_{st}, ρ_{rx} and ρ_{tx} are the altitudes of the target, the receiver and the transmitter, respectively. From this proportion, it is possible evaluating how $\bar{A}$ varies with respect to the distance between target, transmitter and receiver, hence, for a fixed value of $\bar{A}$, the received power is highest when the target is close to the transmitter or the receiver. Specifically, the target's altitude which corresponds to the higher values of minimum silhouette's area of the detectable object, $\overline{\rho_{st}}$, is evaluated imposing the derivative of $f(\rho_{st}|\rho_{rx}, \rho_{tx})$ with respect to ρ_{st} equal to 0 as follows

$$\frac{\partial}{\partial \rho_{st}} f(\rho_{st}|\rho_{rx}, \rho_{tx}) = (\rho_{st} - \rho_{rx}) - (\rho_{tx} - \rho_{st}) = 2\rho_{st} - \rho_{rx} - \rho_{tx} = 0. \tag{6.5}$$

Hence,

$$\overline{\rho_{st}} = \frac{\rho_{rx} + \rho_{tx}}{2} \tag{6.6}$$

Therefore, for a certain system, fixing the transmitter's and receiver's altitude, the greatest value of $\bar{A}$ is achieved when the object is in the middle of the baseline of the FS radar. Since it is possible to detect objects with smaller silhouette's area when they are closer to the receiver or to transmitter, the altitude of the orbits of major interest for the detection of very small debris is a key parameter for setting the receiver's altitude, according to the receiver gain and the characteristics of the available illuminators.

6.3.2 Observation Zone of Interest

From the current distribution of space objects in Fig. 6.3, one can see that the peak density in LEO is at an altitude of around 800 km. Fig. 6.3 represents the spatial density of LEO space debris by the altitude according to NASA report to the United Nations Office for Outer Space Affairs in 2011 (NASA, 2011). This

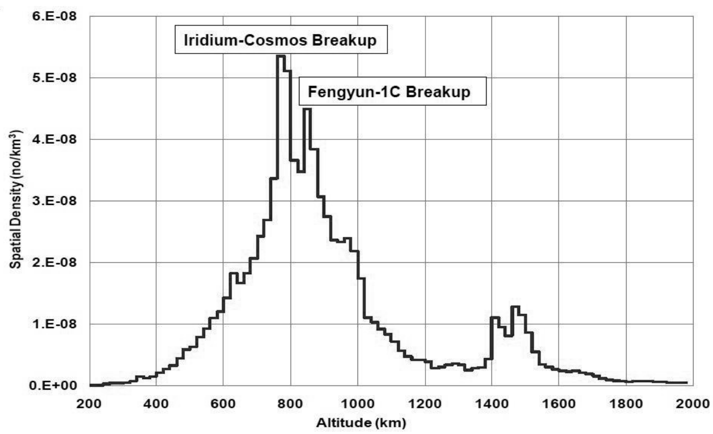

Fig. 6.3 Spatial density of objects in LEO, according to the 2011 NASA report to the United Nations Office for Outer Space Affairs (NASA, 2011).

spatial density was drastically increased by two impact events that generated as many as 6000 trackable objects (Pelton, 2013). The first was the deliberate destruction by a missile of the Chinese Feng-Yun weather satellite. The second impact was between the operational Iridium 33 mobile communications satellite and the defunct Russian Kosmos 2251 weather satellite. Given the high density of objects in this orbit regime, without loss of generality, we will consider targets flying in that region.

6.3.3 Selection of the Illuminators

The choice of the illuminators is driven by a number of parameters that concur to increase the SNR. For the design of the proposed system, the key selection criteria are the EIRP of the RF sources, their distance from the target's zone and receiver, the carrier frequency (or wavelength), the system bandwidth, which determines the power of noise at the receiver, and the modulation scheme used by the source, which determines the signal processing gain and gain of the integration time.

In this Chapter a set of two illuminators is considered for the analysis of performance. The first is the Haiyang-2A (HY2A), which is a second generation satellite series for ocean monitoring approved by the China National Space Administration (CNSA) in Beijing (ESA, 2011). The satellite has been placed at an altitude of 971 km, on a near sun-synchronous frozen orbit, with an inclination of 99.3°. The orbital period is of 104.45 minutes. The HY2A is equipped with an active Radio Altimeter (RA), which works at two different frequencies (Ku-band and C-band). The altimeter uses the LF-chirps (Low Frequency) to perform its task with bandwidths of 320 MHz, 80 MHz and 20 MHz in Ku-band and 160 MHz in C-band. The pulse duration is 102.4 μs, and the altimeter transmits with a PRF between 1 kHz and 4 kHz. For this system, the achievable signal processing gain from the matched filtering is 45.15 dB for a pulse of 102.4 ms covering 320 MHz of bandwidth in Ku-band, and 42.14 dB for the 160 MHz wide pulse in C-band.

The second set of illuminators is the Global Star (GS) constellation. GS is a LEO satellite constellation dedicated to satellite phone and low-speed data communications. Specifically, the system broadcasts with a C-to-S Band transponder and receives with an L-to-C Band transponder, respectively. The GS payloads have been placed at an altitude of about 1400 km, with an orbit inclination of about 52° and an Orbit Period-Nodal is about 114 minutes. Therefore, GS constellation does not cover polar areas, due to the lower orbital inclination (Globalstar, 1997). The GS Canada mobile-satellite network primary modulation and multiplexing method is Code-Division Multiple Access (CDMA). The system operates in four distinct frequency bands (Globalstar, 1997):

1. The forward or down-link service from satellite to user terminal operates in a band of 16.5 MHz between 2483.5 MHz and 2500 MHz where there are 13 frequency-division multiplexed channels, each 1.23 MHz wide;

2. The return or up-link service from user terminal to satellite operates in the band between 1610 MHz and 1626.5 MHz;

3. The forward feeder link from feeder-link earth station to satellite occupies the band from 5091 MHz to 5250 MHz where there are 8 channels 16.5 MHz wide in right-Hand Circular Polarization (RHCP) and another 8 channels 16.5 MHz wide transmitted in LHCP;

4. The return feeder link from satellite to feeder-link earth station occupies the band $6875 - 7055$ MHz with 16 frequency-division multiplexed RF channels, each one 16.5 MHz wide and associated with a separate antenna-pattern beam in the $1610 - 1626.5$ MHz band.

For the system proposed in this work the 16.5 MHz wide downlink, from satellite to user, in $2483.5 - 2500$ MHz bandwidth and the 180 MHz wide return feeder link, from satellite to ground station, in $6875 - 7055$ MHz are employed. Considering a signal segment of 10 ms for computing the radar detection, the two signal processing gain are $52.17\,d$B and $62.55\,d$B for the C-band and S-band downlink, respectively.

6.3.4 Numerical Results

The new technologies allow to satisfy the demand of very small radio receiver devices with high performance in terms of gain and noise figure. The State-of-Art of the available electronic components already available on the market, let us to considered for the numerical simulations in the following, a cubeSAT composed of an SDR with a noise figure of $8\,d$B (Research™, 2017), and a LNA which guarantees a gain in the range of $[40\,,50]\,d$B with a noise figure within $[2\,,4.5]\,d$B (RF-LAMBDA, 2017; RFCCOMP.com, 2017). The receiving antenna could be either a high gain deployable parabolic dish, a foldable patch array or a membrane antenna (Rahmat-Samii et al., 2017). Specifically, in the following analysis a parabolic dish is considered as receiving antenna. In this case, the antenna gain is given by

$$G_r = \frac{4\pi\eta_e A_p}{\lambda^2} = \eta_e \left(\frac{\pi D}{\lambda}\right)^2 \tag{6.7}$$

where η_e is the antenna efficiency, A_p the physical aperture area, λ the wavelength, D the antenna diameter. By fixing the antenna diameter and efficiency, the gain of the receiving antenna is evaluated from (6.7) given the wavelength. For the following performance analysis the efficiency η_e is set equal to 0.5 and the diameter D equal to 0.5 m. The total receiver gain is then given by the sum of the receiver antenna gain and LNA gain in dB domain. The values of all other parameters are reported in Table 6.1. It is worth noting that the proposed system allows one

Table 6.1 Link Budget Parameters.

Parameter	**Description**		**HY2A**		**GSTAR**	
λ	Wavelength.	[mm]	22	57	43	120
G_r	Receiver antenna gain.	[dB]	34.03	25.78	28.15	19.30
$EIRP$	EIRP.	[dB]	52.5	47	19	37
B_R	Radar's Bandwidth.	[MHz]	320	160	180	16.5
G_{sp}	Signal processing gain.	[dB]	45.15	42.14	62.55	52.04
G_{LNA}	LNA gain.	[dB]	40	42	40	50
F	Radar's noise figure.	[dB]	10	10	10	12.5
k	Boltzmann's constant.	[J/K]	1.38×10^{-23}			
T_0	Noise reference temperature.	[K]	290			
SNR	SNR at radar receiver.	[dB]	10			

to solve the problem of atmosphere absorption which represents one of the most relevant loss factors. However, the FS is maximum when the signal wavelength is small with respect the target dimensions, as described in Section 2.3.2. For this reason, in the following analysis two values for the loss factor are taken into consideration: loss factor equal to 0 dB, which represents the best case, and a loss factor of 20 dB.

Fig. 6.4 show the minimum silhouette's area of detectable object as a function of the integration time, for Ku-band and C-band transmitted chirp signals from a HY2A satellite, and for a C-band and S-band transmitted signal from a GS satellite, when the receiver is placed at 300 km of altitude with the target at 800 km. It is worth noting that, since in the HY2A case, pulsed transmission is taken into consideration, the number of non-coherently integrated pulses N is given by the product between the altimeter PRF and the duration of integration time. In the GS case, which involves continuous transmission, sequential segments of 10 ms are incoherently integrated such that N is given by the ratio between the duration of the integration time and the length of the single segment. From Fig. 6.4 it is apparent the HYA2 as illuminator allows the detection of smaller targets with respect to the GS payload, since the latter is at higher altitude and transmits

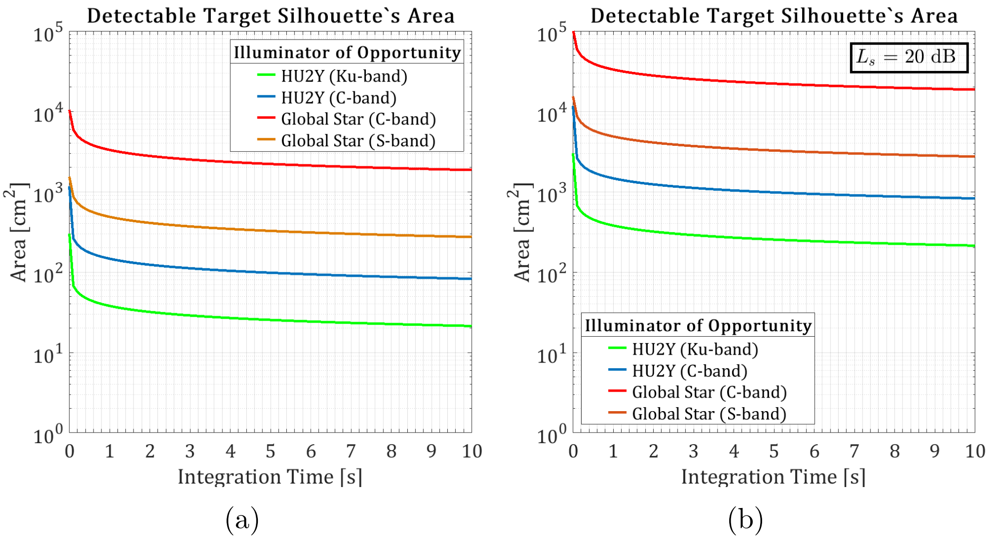

Fig. 6.4 Minimum silhouette's area of detectable target as a function of cubeSAT's altitude and integration time, by using Ku-band and C-band transmitted signal from a HY2A satellite and S-band and C-band signals from a GS satellite: $L_s = 0\,d\mathrm{B}$ (a) $L_s = 20\,d\mathrm{B}$ (b).

with a lower EIRP. Moreover, it is worth noting that higher is the signal carrier frequency, hence smaller wavelength, than higher is the parabolic antenna gain. Moreover, the diffraction phenomenon has a smaller effect for lower wavelength. For this reason the best performance is obtained by using the Ku-band pulses from the HYA2, such that, even for very small integration time, it is possible to detect object with an area smaller than 100 cm^2 (around 50 cm^2 for integration times longer than 0.5 seconds), in the best scenario without losses. The performance obtained by using GS payload decreases of a factor 10, when the S-band signal is used, and of a factor 100 for C-band signal. Specifically, in this analysis the use of the S-band signal outperforms the C-band signal as consequence of higher gain of LNA used in the first bandwidth, while the higher gain in terms of receiver antenna and signal processing obtained with C-band signal is compensated by the higher EIRP for the S-band channel. When a loss factor of 20 dB is considered for all system losses (comprising losses for edge diffraction when target dimensions are comparable with wavelength), the minimum value of detectable target's silhouette area increases of a factor 10 for all the analysed cases.

6.3.5 Integration time

The integration time is defined as the time interval needed to transmit and receive the integrated pulses to perform the radar detection. For a FS PBR the maximum

possible integration time is the interval during which the target is approximately along the LOS between the transmitter and the receiver.
The maximum integration time for the proposed system depends on the orbits of transmitter, receiver and space target and on both transmitter and receiver antenna's pointing and patterns. In this sub-section we analyse the maximum and minimum possible integration times assuming different orbit geometries. For simplicity only circular orbits are considered. Furthermore, the bore-sight of the transmitter is expected to be aligned with the nadir direction and the bore sight of the receiver antenna is aligned with the zenith direction.

Let us consider that at $t = 0$ transmitter, receiver and target are aligned. The coordinate system $(\tilde{U}, \tilde{V}, \tilde{W})$ is defined such that the plane $\tilde{U}\tilde{V}$ contains the orbit flown by the receiver and the $\tilde{U}$-axis is along the line going through the transmitter, receiver and target at $t = 0$.
Considering the three orbit radii d_{rx}, d_{st} and d_{tx}, which represent the distances from the Earth center to receiver, space target and transmitter, then the position vectors of the three objects in the $(\tilde{U}, \tilde{V}, \tilde{W})$ reference frame are defined as

$$\boldsymbol{p}_{rx}(t) = d_{rx}[\cos(\omega_{rx}t), \sin(\omega_{rx}t), 0]^T \tag{6.8}$$

$$\boldsymbol{p}_{st}(t) = d_{st}[\cos(\omega_{st}t), \sin(\omega_{st}t)\cos(\alpha_{st}), \sin(\omega_{st}t)\sin(\alpha_{st})]^T \tag{6.9}$$

$$\boldsymbol{p}_{tx}(t) = d_{tx}[\cos(\omega_{tx}t), \sin(\omega_{tx}t)\cos(\alpha_{tx}), \sin(\omega_{tx}t)\sin(\alpha_{tx})]^T \tag{6.10}$$

where ω_{rx}, ω_{st} and ω_{tx} are the angular velocities of receiver, space target and transmitter, respectively, and α_{st} and α_{tx} represent the squint angle with respect to the plane $\tilde{U}\tilde{V}$ of the orbits of space target and transmitter. Note that the three orbits are coplanar if α_{st} and α_{tx} are 0 or π. However, in the case of squint angle equal to π the orbits of transmitter and target are retrograde with respect to the orbit of the receiver.
The angular velocity ω_{orbit} for an object orbiting circularly around the Earth, hence the orbital period, depends only on the distance from the Earth centre d. In particular, according to Kepler's Third Law it follows that

$$\omega = \omega(d) = \sqrt{\frac{\mu}{d^3}}. \tag{6.11}$$

where μ is the gravity constant of the Earth. According to the Cosine Rule, the bistatic angle can be evaluated considering the relative distance between the three elements of the radar scenario (see Fig. 6.5) which are defined as follows

$$l_1(t) = \|\boldsymbol{p}_{tx}(t) - \boldsymbol{p}_{rx}(t)\| \tag{6.12}$$

$$l_2(t) = \|\boldsymbol{p}_{tx}(t) - \boldsymbol{p}_{st}(t)\| \tag{6.13}$$

$$l_3(t) = \|\boldsymbol{p}_{st}(t) - \boldsymbol{p}_{rx}(t)\| \tag{6.14}$$

Then the bistatic angle is

$$\beta(t) = \cos^{-1}\left(\frac{l_2^2(t) - l_1^2(t) + l_3^2(t)}{2l_2(t)l_3(t)}\right) \tag{6.15}$$

It is highlighted that since the Earth has not a perfect spherical shape, the

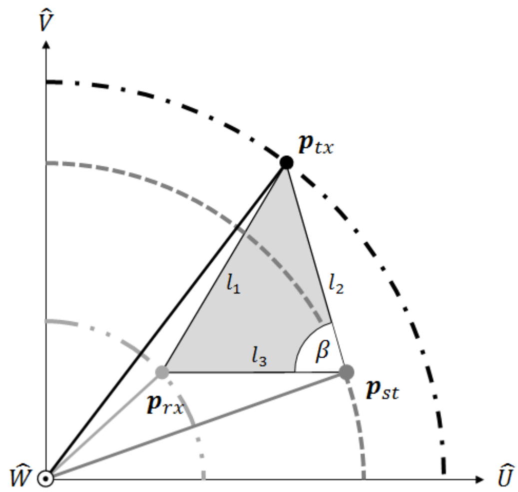

Fig. 6.5 Representation of the bistatic angle β between transmitter, receiver and target moving on different orbits.

transmitter and the receiver at different altitudes experience different precession of the line of the nodes (Vallado, 2007). Therefore the orbits of transmitter, target and receiver cannot remain coplanar, and the illuminator (the transmitter) needs to be selected dynamically to allow higher integration times.

A measure of maximum integration time is obtained evaluating the duration of time interval during which the configuration of radar system is such that the bistatic angle is around 180°. Fig. 6.6 shows how the bistatic angle β varies on time considering the initial instant such that transmitter, receiver and target are aligned. In particular let us consider the general cases of a transmitter at 963 km 1400 km (e.g. HU2Y and GS payload) from the Earth and, as in the analysis described above, the target and receiver at 800 km and 300 km, respectively, different values of the squint angles $(\alpha_{st}, \alpha_{tx})$ are considered. It is easily noted

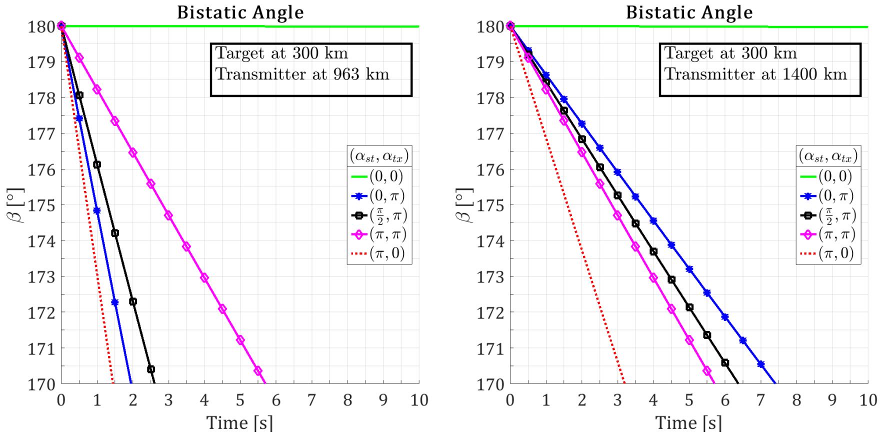

(a) (b)

Fig. 6.6 Example of bistatic angle variation from the instant of alignment of transmitter, receiver and target for different values of couple $(\alpha_{st}, \alpha_{tx})$; the receiver is at 1400 km, target at 800 km, and transmitter at 963 km (a), 1400 km (b).

that the possible integration time is longer when the orbits of three elements are coplanar and covered in the same direction. The worst case is obtained when the orbits are coplanar but the target moves in the opposite direction with respect to transmitter and receiver. The examples in Fig. 6.6 shows that reducing the transmitter's altitude, the variation of bistatic angle becomes more sensitive with respect to squint angles of transmitter's and target's orbits. This trend is due to the greater transmitter angular velocity obtained decreasing the distance from Earth centre. Finally, from Fig. 6.4 it is worth noting that the gain in terms of sizes of detectable object, obtained by the incoherent integration, is more influential for shorter integration time. In fact, by increasing highly the number of integrated pulses the size of detectable object decreases slowly. Hence, it is possible to guarantee satisfactory system detection capability even for target moving in the opposite direction with respect to transmitter and receiver.

6.4 BMD Application

The proposed system may be used as support for military surveillance and BMD. A potential advantage of the proposed solution resides in the capability to fly over sensitive zones, thus being able to support primary detection and tracking systems enhancing their early detection capabilities. A research on the kinematics advantages of using space-based interceptor for Missile defence against the ground-based one during boost phase was reported in (keun Jang et al., 2008). A space-borne receiver at very low orbits may be used to support the early detection of missile during its initial flight phases over 300 km and during the mid-course phase. The maximum altitude of sub-orbital trajectories of the intercontinental ballistic missiles (ICBMs) can be considerably more than for a LEO reaching values greater than 1000 km. The maximum altitudes depends the covered range based on the position of launch point and their target point (Aydin et al., 2005). As described in Section 1.1, during the mid-course phase a ballistic missile releases different objects in addition to the warhead, such as decoys or boosters used to overcome the atmosphere. These targets exhibit different micro-motions during their trajectory. It has been experimentally demonstrated the capability to extract mD profile of a target by employing a FS radar in (Abdullah et al., 2017). Therefore, since it has been demonstrated in Chapter 4 the capability to distinguish between missile warheads and decoys from mD profile of a target, the proposed configuration may be used for detection and classification of ballistic threats by exploiting the Doppler and mD informations.

6.4.1 Target Silhouette's Area

Let us consider the coordinate system $(\hat{u}, \hat{v}, \hat{w})$ presented in Section 4.2 shown in Fig. 4.3. The vector $\hat{\boldsymbol{b}}$ represents the direction of the baseline between the transmitter and receiver in the hypothesis that it goes through the target's MC. It is given by

$$\hat{\boldsymbol{b}} = [cos(\varepsilon_1)cos(\varepsilon_2), cos(\varepsilon_1)sin(\varepsilon_2), sin(\varepsilon_1)]^T \tag{6.16}$$

where ε_1 and ε_2 are the elevation and azimuth angle into the defined coordinate system.

Let us consider the local coordinate system $(\tilde{u}, \tilde{v}, \tilde{w})$ shown in Fig. 6.7 whose origin is MC. The new coordinate system is defined such that the transmitter and receiver are both approximately located on the $\tilde{u}$-axis and the symmetry axis of the target is in the plane $\tilde{u}\tilde{w}$, such that

$$\tilde{u} = \hat{\boldsymbol{b}} \tag{6.17}$$

$$\tilde{v} = \hat{\boldsymbol{z}}_t \times \hat{\boldsymbol{b}} \tag{6.18}$$

$$\tilde{w} = \tilde{u} \times \tilde{v} \tag{6.19}$$

The orientation angle φ is defines as the angle between the $\hat{z}_t$ and $\tilde{w}$-axis. The symmetry axis in the coordinate system $(\tilde{u}, \tilde{v}, \tilde{w})$ is obtained as follows

$$\hat{\boldsymbol{z}}^* = \boldsymbol{M}_T \hat{\boldsymbol{z}}_t \tag{6.20}$$

where

$$\boldsymbol{M}_T = [\tilde{u}, \tilde{v}, \tilde{w}]^T \tag{6.21}$$

is the transition matrix. The orientation angle varies according to the micro-motions exhibited by the target, and it is obtained as

$$\varphi = cos^{-1}\left(< \hat{\boldsymbol{z}}^*, \tilde{w} >\right) \tag{6.22}$$

The target silhouette's area which determines the FSRCS according with (2.25) is evaluated by projecting the target volume on plane $\tilde{v}\tilde{w}$.

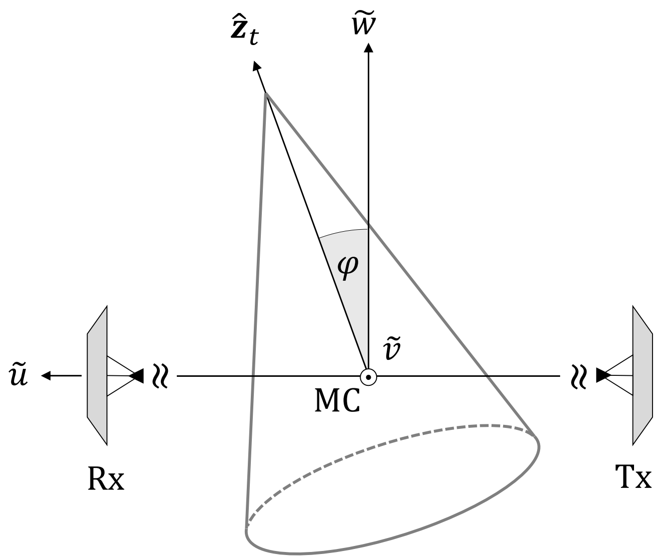

Fig. 6.7 Coordinate system $(\tilde{x}, \tilde{y}, \tilde{z})$.

Let us consider a conical target. The position vectors of the tip and the generic point of the base in the local coordinate system for target the oriented by angle φ are

$$\bar{\boldsymbol{P}}_{tip} = \begin{bmatrix} h_1 \sin(\varphi) \\ 0 \\ h_1 \cos(\varphi) \end{bmatrix} \qquad \bar{\boldsymbol{P}}_b = \begin{bmatrix} R_b \cos(\psi)\cos(\varphi) + h_2 \sin(\varphi) \\ R_b \sin(\psi) \\ R_b \cos(\psi)\sin(\varphi) - h_2 \cos(\varphi) \end{bmatrix} \tag{6.23}$$

where h_1 and h_2 are the distances of tip and centre of the cone base from the mass centre, respectively, R_b is the radius of the cone base, and $\psi \in [0, 2\pi[$. The projection of the tip on the $\tilde{v}\tilde{w}$ is the point $(0, h_1 \cos(\varphi))$, while from the projection of the base the parametric equation of a closed curve is obtained for $\psi \in [0, 2\pi[$, as follows

$$\begin{cases} v = R_b \sin(\psi) \\ w = R_b \cos(\psi)\sin(\varphi) - h_2 \cos(\varphi) \end{cases} \tag{6.24}$$

Specifically (6.24) is the parametric equation of an ellipse whose semi-major axis and semi-minor axis are

$$a_1 = R_b \tag{6.25}$$

$$a_2 = R_b \sin(\varphi) \tag{6.26}$$

respectively, and centre in $(0, -h_2 \cos(\varphi))$. The silhouette's area coincides with the area of the cone base projection for orientation angles such that the projection of the cone tip lies inside the ellipse. Otherwise, it is necessary to evaluate the tangents from the tip projection to the ellipse. In particular, the following system of equations has to be solved

$$\begin{cases} \frac{v^2}{R_b^2} + \frac{(w+h_2\cos(\varphi))^2}{R_b^2\sin^2(\varphi)} = 1 \\ v = m(w - h_1\cos(\varphi)) \end{cases} \tag{6.27}$$

By substituting the second equation into the first, a parametric equation in the variable m is obtained as follows

$$\begin{aligned} & w^2[m^2\sin^2(\varphi) + 1] + w[2\cos(\varphi)(h_2 - h_1 m^2 \sin^2(\varphi))] \\ & + [m^2\sin^2(\varphi)h_1^2\cos^2(\varphi) + h_2^2\cos^2(\varphi) - R_b^2\sin^2(\varphi)] \\ & = 0 \end{aligned} \tag{6.28}$$

In order to determine the tangents from the tip projection to the ellipse the discriminant, Δ, is set equal to 0 e.g.

$$\begin{aligned} & \Delta = \\ & [2\cos(\varphi)(h_2 - h_1 m^2\sin^2(\varphi))]^2 - 4[m^2\sin^2(\varphi) + 1]\times \\ & [m^2\sin^2(\varphi)h_1^2\cos^2(\varphi) + h_2^2\cos^2(\varphi) - R_b^2\sin^2(\varphi)] \\ & = 0 \end{aligned} \tag{6.29}$$

From (6.29) follows that the gradients of two tangents are

$$m_{1,2} = \mp\sqrt{\frac{R_b^2}{H^2\cos^2(\varphi) - R_b^2\sin^2(\varphi)}} \tag{6.30}$$

for

$$H^2\cos^2(\varphi) - R_b^2\sin^2(\varphi) > 0 \tag{6.31}$$

then

$$\varphi \in \left]0, \tan^{-1}\left(\frac{H}{R_b}\right)\right[\bigcup\left]\pi - \tan^{-1}\left(\frac{H}{R_b}\right), \pi\right[\tag{6.32}$$

with $H = h_1 + h_2$. Since the tip projection is along the $\hat{z}$-axis and ellipse in (6.24) is symmetric around $\tilde{w}$-axis itself, the two tangent points have the same $\tilde{w}$-coordinate which is

$$w_{1,2}^*(\varphi) = -\frac{[2\cos(\varphi)(h_2 - h_1 m_{1,2}^2\sin^2(\varphi))]}{2[m_{1,2}^2\sin^2(\varphi) + 1]} \tag{6.33}$$

From (6.24), the angle ψ^* corresponding to the $\tilde{w}$-coordinate of tangent points is

$$\psi^* = \psi^*(\varphi) = \cos^{-1}\left[\frac{w_{1,2}^*(\varphi) + h_2\cos(\varphi)}{R_b\sin(\varphi)}\right] \tag{6.34}$$

such that

$$\psi^* \in \left]0, \frac{\pi}{2}\right[\tag{6.35}$$

and the coordinates on the $\tilde{v}$-axis are

$$v_{1,2}^*(\varphi) = \mp R_b\sin(\psi^*(\varphi)) \tag{6.36}$$

Finally, the silhouette's area as function of the angle φ is

$$A_{cone}(\varphi) = \begin{cases} RH & \varphi = 0 \\ R_b^2\sin(\varphi)(\pi - \psi^*(\varphi)) + H|v_{1,2}^*(\varphi)|cos(\varphi) & 0 < \varphi < \tan^{-1}\left(\frac{H}{R_b}\right) \\ \pi R_b^2\sin(\varphi) & \tan^{-1}\left(\frac{H}{R_b}\right) \leq \varphi \leq \frac{\pi}{2} \end{cases} \tag{6.37}$$

It is possible to calculate the area for the other values of φ due to the object's symmetry. Fig. 6.8 shows how the projection of the cone varies with the orientation angle. From Fig. 6.8c it is observed that when φ is equal or greater than the cone semi-angle, the projection of the cone tip lies on the base projection, hence the silhouette's area is given by the base surface's area

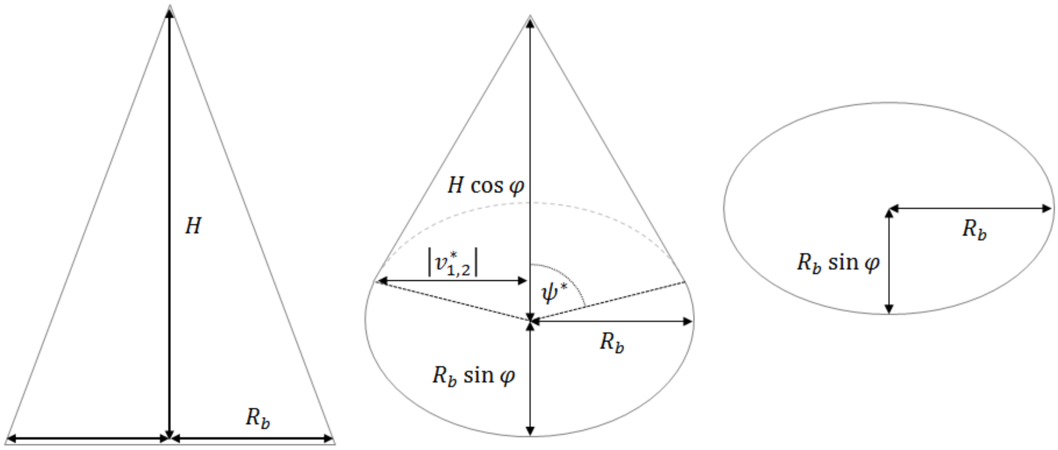

(a) (b) (c)

Fig. 6.8 Conical target silhouette's area: (a) $\varphi = 0$; (b) $0 < \varphi < \tan^{-1}\left(\frac{H}{R_b}\right)$; (c) $\tan^{-1}\left(\frac{H}{R_b}\right) \leq \varphi \leq \frac{\pi}{2}$.

Considering a cylindrical target, the silhouette's area coincides with the area of projection of the surface of the side for $\varphi = 0$. Specifically the latter is given by a rectangular whose height is the cylinder height and the base is its diameter, as shown in Fig. 6.9a. Fig. 6.9b shows that for $\psi = \left]0, \frac{\pi}{2}\right[$ the silhouette's area is given by the sum of the areas of an ellipse and a rectangular as consequence of the projection of the volume on the plane $\tilde{v}\tilde{w}$. Finally, for $\varphi = \frac{\pi}{2}$ the silhouette's area is given by the base surface's area (see Fig. 6.9c). Then, it follows that the area for a cylindrical target as function of orientation angle is

$$A_{cylinder}(\varphi) = \pi R_b^2 \sin(\varphi) + 2R_b H \cos(\varphi) \tag{6.38}$$

Where $\psi = \left]0, \frac{\pi}{2}\right[$. Even for the cylinder the silhouette's area for the other values of the orientation angle are easily obtained thanks to the symmetry of the object.

6.4.2 Numerical Results

In this Section the performance of the novel methods is assessed by evaluating the capability to detect a conical and cylindrical object whose dimension are comparable with the modern missile warhead's dimensions.
Fig. 6.10a shows the silhouette's area on varying the orientation angle of conical

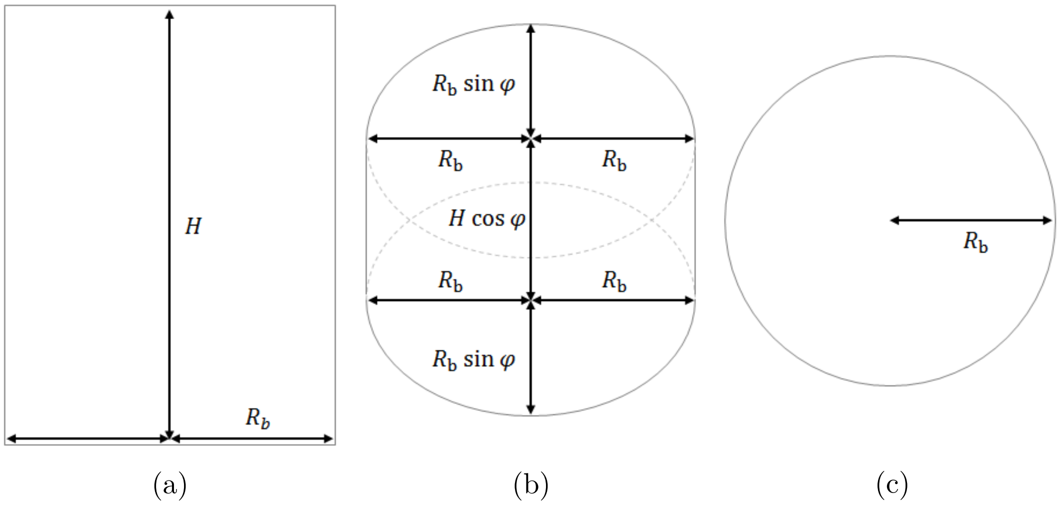

Fig. 6.9 Cylinder silhouette's area: (a) $\varphi = 0$; (b) $0 < \varphi < \frac{\pi}{2}$; (c) $\varphi = \frac{\pi}{2}$.

and cylindrical targets whose radius and height are 0.375 m and 1 m, respectively (as considered in Section 4.5). In the described example, since the cone and the cylinder have the same base, the silhouette's area is the same for $\varphi = 90°$, while for all the other values of aspect angle the silhouette of cylinder is greater than the cone's one. In more detail, the minimum area of cylinder's silhouette coincides with the base area obtained for an aspect angle of 90°. For the cone with mentioned dimensions the minimum silhouette's area is obtained for $\varphi = 0°$ and it is equal to 3750 cm^2.

Fig. 6.10b, in stead, represents the minimum target area that could be detected using a GS payload as illuminator when target is at 1000 km and receiver at 300 km from the Earth, on varying the integration time. It is observed that the described configuration allows to detect a target with an area of 1500 cm^2 by using a single radar pulse in the best case, with $L_s = 0\,d$B. However the minimum silhouette's area of detectable target is smaller than 500 cm^2 after 1 second of integration. From Fig. 6.10b and Fig. 6.10a it is worth noting that it would be possible to detect both the cone and the cylinder for any orientation angles and integration times by using the S-band channel from the GS payload, even in the case of $L_s = 20\,d$B. When the C-band channel is used, the analysed target may be always detected for any integration times in the best scenario with $L_s = 0\,d$B, while when a loss factor of $20\,d$B is considered, for an integration time greater than 4 seconds the cone may be detected for orientation angles smaller than 45° and the cylinder for angles smaller than 75°.

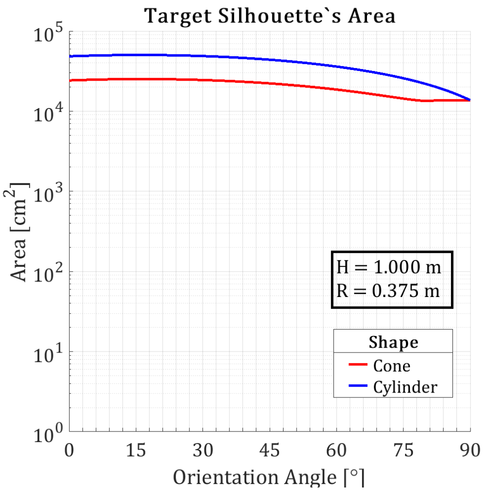

(a)

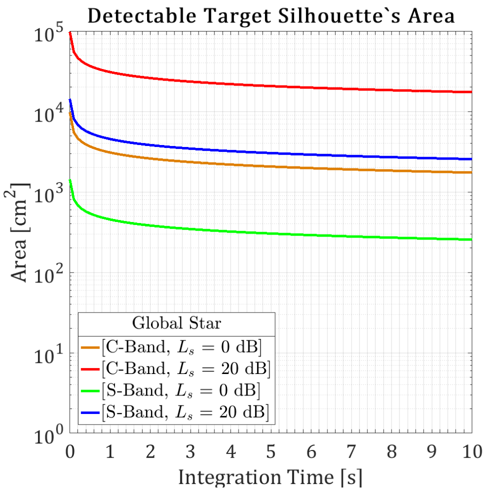

(b)

Fig. 6.10 Performance in terms of minimum silhouette's area of detectable target at 1000 km by using Global Star payload as transmitter for a receiver's altitude of 300 km, on varying the integration time, for $L_s = 0\,d$B and $L_s = 20\,d$B (a); cone and cylinder silhouette's area on varying the orientation angle, whose radius and height are 0.375 m and 1 m, respectively (b).

6.5 Summary

In this Chapter a precursory study of a new space-based passive radar system for SSA was described. The proposed system comprises of a PBR deployed on a small space-borne platform, equipped with an SDR and a passive antenna to perform radar task for space surveillance. The analysis of performance showed that the proposed system may represent a low budget solution for the detection even of very small space objects with sizes of few centimetres. One of the most important aspects is that the relative shorter distances between transmitter, target and space based receiver with respect to a ground based receiver guarantees higher SNR for the radar tasks. Moreover, the performance of the proposed system is less affected by atmospheric absorption due to the system geometry. For the same reason the system functionality is independent of weather conditions and interference factor represented by flying man-made vehicles or bird flock.
It has been showed that, with integration times shorter than 10 seconds and an appropriate choice of the illuminator, the system can detect objects with section areas as small as 50 cm^2 with a receiver positioned at 300 km in the best scenario. It is pointed out that, at the altitudes considered in this analysis, the expected lifetime of the receiver is such to limit the risk to increase the debris population. The proposed system may be used for the space surveillance of sensitive areas for a

primary detection of potential dangerous targets, such BM warheads, guaranteeing potentially additional capability of target identification since FS radars can be used for the acquisitions of mD profile of an object.

Chapter 7

Conclusions and Future Work

The research presented in this Thesis investigates new signal processing solutions for the identification of sensitive targets, such as Ballistic Missile (BM) warheads, and for monitoring the population of space debris orbiting around the Earth.

In Chapter 2 an study on the main aspects of modern radar system was presented. Both the fundamentals and the advanced concepts were introduced, with a particular focus on common approaches for achieving higher Signal-to-Noise Ratio (SNR) at receiver in order to better perform the generic radar tasks. Furthermore, the principal steps of target recognition process were introduced in details, emphasizing the recent approaches proposed for target identification. In this context, the Chapter also provided a description of the micro-Doppler (mD) effect in radar echoes from targets which exhibit secondary motions in addition to the main bulk motion, e.g. rotation or vibration. Additionally, the processing for obtaining the High Resolution Range Profile (HRRP) of target by using a Stepped Frequency Waveform (SFW) was introduced, with an analysis about how the target micro-motions affect the resulting profile.

Chapter 3 presented a research review on the recent tools used for radar classification of moving targets. Specifically, the most used Time-Frequency Distribution (TFD) for observing how the frequencies components of a signal varies on time were exhaustively introduced, describing the trade-offs which each function poses in terms of time-frequency resolution, computational complexity, and production of artefacts which represent interference factors for classification algorithms. Moreover, the principal mD based profiles used as target signature were reviewed, looking with particular attention for their application for BM classification. Therefore, the spectrogram, the Cadence Velocity Diagram (CVD) and cepstogram were described. Following, the theory of Radon Transform (RT) and Inverse Radon

Transform (IRT) was discussed, with particular focus on their use in Radar Imaging (RI) of target with rotational motions. The Chapter also introduced some of the recent feature extraction approaches used in the context of image classification: the pseudo-Zernike (pZ) image moment based approach, the Krawtchouk (Kr) image moment based approach and the 2-Dimensional (2D) Gabor Filter based approach. The three approaches were mathematically analysed, reporting some examples of Automatic Target Recognition (ATR) application based on Synthetic Aperture Radar (SAR) images and mD profiles of the target. Specifically, a mD based classification framework based on the evaluation of the pZ moments projecting the CVD from the target onto a base of pZ polynomials was introduced. The framework was tested with success for the classification of helicopters and for distinguish different human gaits. The described features guarantee high level of robustness against the initial phases of target motions and the aspect angel between radar Line-Of-Sight (LOS) and the principal target axis.
An experimental validation of capability to distinguish between BM warheads and decoys based on mD profile of a target was discussed in Chapter 4. A mathematical model for the radar return from warhead with precession and nutation, and from tumbling decoys, was described in details, considering the approximation at relative far field. In particular, two shapes were considered for the warhead, namely cone and cone with fins, and three as decoys, namely cone, cylinder and sphere. Moreover, a laboratory experiment was conducted for simulating the radar returns from a BMD scenario. By using a robotic manipulator and an additional rotor the different target micro-motions were simulated, and a dataset was created acquiring data from scaled replicas of the target of interest with a Continuous Waveform (CW) radar. In order to performing the target classification, the framework described in Chapter 3 based on the evaluation of the CVD was taken into consideration. The framework was adapted to different feature extraction approaches, which lead to different computational complexity and advantages. In addition to pZ moments, the Kr moments were extracted and the 2D Gabor filter were used considering CVD as 2D image. A simpler approach was also proposed based on the estimation of statistical indices from the 1-Dimensional (1D) Averaged CVD (ACVD). All the described features were tested on both simulated and experimental data with success, guarantee different level of efficiency and robustness against noise level into radar measurements, the duration of target observations, initial phases of target motions and radar aspect angle.
It is worth noting that the performance of the proposed features were evaluated

using the k-Nearest Neighbours (k-NN) classifier, which simply compares the Euclidean distances between the vector under test with the training dataset of each class. Hence, future research could involve a study of the best mD features in combination with a more sophisticated classifier in terms of computational cost and reliability for Ballistic Targets (BTs) classification. Moreover, a new model based classification algorithm can be investigated using the mathematical model for the radar return proposed in this Chapter, and including information on the coefficient of principal scattering points.

In Chapter 5 a novel classification algorithm for BTs was proposed, based on the elaboration of a sequence of target HRRPs, acquired during an entire period of principal target rotational movement. The algorithm is based on the evaluation of the pZ moments from the IRT of the acquired HRRP frame. For the analysis of performance, two possible motions were taken into consideration, namely precession and tumbling, and three possible target shapes, namely con, cylinder and cone plus cylinder. The effectiveness of the features were tested successfully on simulated data, considering different polarization for the radar waveform, demonstrating high degree of robustness against noise level into radar measurements, the initial phase and angular velocity of target motion. Specifically, a Stepped Frequency Waveform (SFW) radar was considered for the simulation of HRRPs of the target.

The characteristics of the designed radar waveform affects the target signature and the performance of the classification algorithm. In particular, the effect on the HRRP due to the target micro-motion velocity, in terms of radar range displacement from the real distance of the scattering point from the radar, depends on the number of sub-pulses used to synthesize the assigned total bandwidth and on the Pulse Repetition Frequency (PRF). These parameters also have a significant impact on the final SNR of the target signature. Therefore, a further research on possible adaptable SFWs based on the estimated target micro-motion velocity could be conducted in the context of cognitive radar, improving the performance in presence of faster rotating object in lower SNR scenarios. Moreover, the design of a suitable model in agreement with to the target of interest (in terms of shape and dimension) and radar system parameters (e.g. polarization and bandwidth) can also lead to a model based classification algorithm guaranteeing high performance.

Chapter 6 provides the precursory study of a new solution in Space Situational Awareness (SSA) context for space target detection. The proposed system consists of a space-borne Passive Bistatic Radar (PBR) system installed on one or more small platforms flying at low altitude and receiving the Radio Frequency (RF)

signals transmitted by non-cooperative illuminators at higher altitudes. This system may represent a low cost alternative solution since the shorter distances and smaller relative velocities between transmitter, receiver and target, allows to achieve suitable SNR with a simpler hardware and lower costs. Specifically, the required gain of the antenna is lower with respect to a ground-based system for the shorter distances, while the relative velocity has an impact on the integration time, improving the capability to detect smaller objects. Furthermore, such a system guarantees all the advantages of PBR, in terms of low power requirement, lighter payload and the absence of dedicated frequency allocation need. Additionally, by exploiting the enhancement in terms of target RCS guaranteed by the Forward Scattering (FS) configuration, the proposed system also represents a suitable solution against the stealth technology for the detection of object with very small RCS (obtained by using radar absorbing material). For this reason, it offers a possible solution for supporting military surveillance of space activities in sensitive areas and for early detection of specific targets, as BMs. Thanks to the modern technologies it is possible to assemble a PBR on a cubeSAT with relative high performance in terms of receiver gain and noise figure. The numerical results, obtained by the Radar Range Equation (RRE), showed that the system, if feasible, may allow to detect very small objects in the order of few centimetres, guaranteeing robustness against atmospheric absorptions and weather conditions, and against interference factor represented by flying man-made vehicles or bird flock. Since the system capabilities depend on the distance between transmitter and receiver, the use of LEO emitters at higher orbits as illuminator of opportunity is most suitable for achieving better detection performance. The expected increase in LEO emitters, such as OneWeb, could represent an important factor for improving the performance of such a system.
The capabilities of the system can be further improved by integrating signals from several illuminators. To this aim, wide-band antennas and suitable receiver filters have to be considered in order to recover all the received channels. It is also possible to use several cubeSAT receivers working together in order to perform target localization and ranging. Moreover, since FS radar has been used with success for target discrimination based on Doppler analysis of echoes, it is possible to identify specific targets by analysing their peculiar micro-motions exhibited while orbiting. The feasibility of the proposed system and all these potential configurations could be subjects of future investigation.

Appendix A

A.1 Complex Coefficients of Target Principal Scattering Point

In this appendix the expression of the complex coefficient for each scatterer is described for the two polarizations, vertical and horizontal, for the three shapes considered as target in Chapter 5, namely cone, cylinder and cone plus cylinder (as shown in Fig. A.1). The details about the model design and validation are

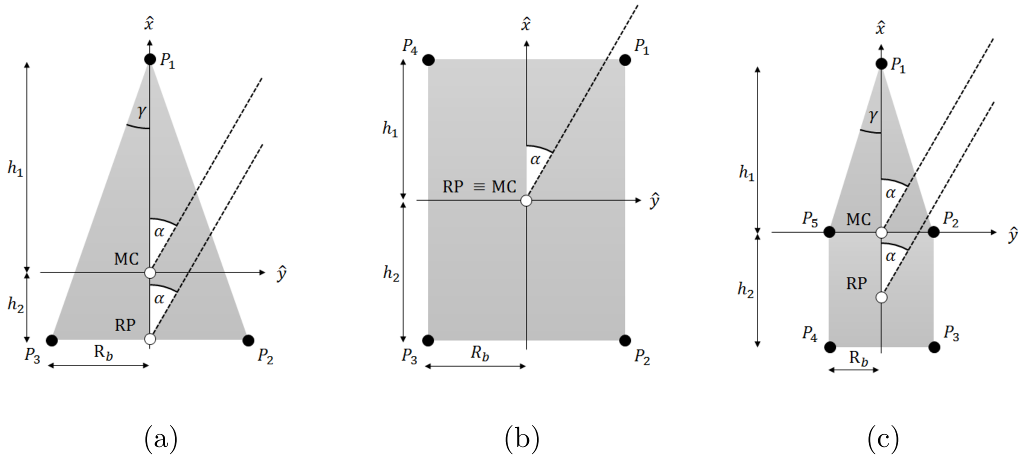

Fig. A.1 Target shape model: (a) cone; (b) cylinder; (c) cone plus cylinder target.

presented in (Ross and DIV., 1969).

Cone

Considering the cone semi-angle, γ, and the base radius, R_b (see Fig. A.1a), the modulus of scattering coefficients of the cone are

$$\sqrt{\sigma_1} = \begin{cases} \frac{\sin(\frac{\pi}{n_1})}{4k\sqrt{2\pi}\, n_1}\sqrt{\frac{R_b \csc(\alpha)}{k}}\left[\left\{\cos\left(\frac{\pi}{n_1}\right) - \cos\left(\frac{2(\pi-\gamma-\alpha)}{n_1}\right)\right\}^{-1}\right] & \alpha \in [0, \pi-\gamma[\\ 0 & \alpha \in [\pi-\gamma, \pi] \end{cases} \tag{A.1}$$

$$\sqrt{\sigma_2} = \mathcal{A}\left[\left\{\cos\left(\frac{\pi}{n_2}\right) - \cos\left(\frac{3\pi-2\alpha}{n_2}\right)\right\}^{-1} \mp \left\{\cos\left(\frac{\pi}{n_2}\right) - 1\right\}^{-1}\right] \qquad \alpha \in [0, \pi] \tag{A.2}$$

$$\sqrt{\sigma_3} = \begin{cases} \mathcal{A}\times \\ \left[\left\{\cos\left(\frac{\pi}{n_3}\right) - \cos\left(\frac{3\pi+2\alpha}{n_3}\right)\right\}^{-1} \mp \left\{\cos\left(\frac{\pi}{n_3}\right) - 1\right\}^{-1}\right] & \alpha \in [0, \gamma[\cup]\frac{\pi}{2}, \pi] \\ 0 & \alpha \in [\gamma, \frac{\pi}{2}] \end{cases} \tag{A.3}$$

where

$$\mathcal{A} = \frac{\sin(\frac{\pi}{n_2})}{n_2}\sqrt{\frac{R_b \csc(\alpha)}{k}} \tag{A.4}$$

with

$$n_1 = 2 - \frac{2\,\gamma}{\pi} \tag{A.5}$$

$$n_2 = n_3 = \frac{3}{2} - \frac{\gamma}{\pi} \tag{A.6}$$

and $k = \frac{2\pi}{\lambda}$ the propagation factor, where λ is the wavelength. The phase of the coefficients are given by

$$\phi_1 = \frac{\pi}{4} - 2k(h_1 + h_2)\cos(\alpha) \tag{A.7}$$

$$\phi_2 = \frac{\pi}{4} - 2kR_b \sin(\alpha) \tag{A.8}$$

$$\phi_3 = -\frac{\pi}{4} + 2kR_b \sin(\alpha) \tag{A.9}$$

where h_1 and h_2 are the distance of the tip and the base centre with respect the centre of mass, respectively. The choice of the sign in (A.2) and (A.3) depends on the polarization, specifically, the upper sign is associated to the vertical polarization for the incident electric field, while the lower to the horizontal polarization.

The expressions of coefficients for α in proximity of values 0 and π have been updated in (Ross and DIV., 1969), since singularities arise in (A.2) and (A.3). Specifically, in order to evaluate magnitude and phase of the total scattered field from a conical target for incidence at near tail-on, by using (2.20) and (2.21) described in Chapter 2, the polarization-independent contribution from (A.2) and (A.3) are substituted by

$$\left(\sqrt{\sigma_2}e^{j\phi_1} + \sqrt{\sigma_3}e^{j\phi_3}\right)_{pol-ind} = 2\sqrt{\pi}kr^2 \frac{J_1(2kR_b\sin(\alpha))}{(2kR_b\sin(\alpha))} e^{-j\frac{\pi}{2}} \tag{A.10}$$

for $\alpha \in [0, \gamma]$, where $J_1(\cdot)$ is the Bessel function of first order.
Defining α_{ca} as the axial crossover angle, such that

$$2kR_b\sin(\alpha_{ca}) = 2.44 \tag{A.11}$$

the total scattered field for $\alpha \in [\pi - \alpha_{ca}, \pi]$, hence from incidence at near perpendicular to the cone base, is

$$\begin{aligned}\sqrt{\sigma}e^{j\phi} = \left(\sqrt{\sigma_2}e^{j\phi_2} + \sqrt{\sigma_3}e^{j\phi_3}\right) =& \frac{2r\sqrt{\pi}\sin\left(\frac{\pi}{n_2}\right)}{n_2}\times \\ &\left[J_0(2kR_b\sin(\alpha))\left\{\cos\left(\frac{\pi}{n_2}\right) - \cos\left(\frac{3\pi}{n_2}\right)\right\}^{-1}\right. \\ &-J_1(2kR_b\sin(\alpha))\frac{\frac{2j\tan(\alpha)}{n_2}\sin\left(\frac{3\pi}{n_2}\right)}{\left(\cos\left(\frac{\pi}{n_2}\right) - \cos\left(\frac{3\pi}{n_2}\right)\right)^2} \\ &\left.\mp J_2(2kR_b\sin(\alpha))\left\{\cos\left(\frac{\pi}{n_2}\right) - 1\right\}^{-1}\right]\end{aligned} \tag{A.12}$$

where $J_i(\cdot)$, with $i = 0, 1, 2$, is the Bessel function of i-th order. It is worth noting that (A.10) is independent on polarization.

Cylinder

Due to the object symmetry along both the two axis of the cylinder, shown in Fig. A.1b, the expressions of the scattering coefficients are written for $\alpha \in \left[0, \frac{\pi}{2}\right]$. In particular, considering the axial crossover angle, α_{ca}, and the broadside crossover angle, α_{cb}, defined such that (Ross and DIV., 1969)

$$2kR_b \sin(\alpha_{ca}) = 2.44 \tag{A.13}$$

$$2kh \cos(\alpha_{cb}) = 2.25 \tag{A.14}$$

with R_b the base radius and $h = h_1 = h_2$ is the distance between the base centre and the phase reference centre, the modulus of the scattering coefficients for $\alpha \in \left]\alpha_{ca}, \frac{\pi}{2} - \alpha_{cb}\right[$ are

$$\sqrt{\sigma_1} = \mathcal{B}\left[\left\{\cos\left(\frac{2\pi}{3}\right) - \cos\left(\frac{\pi + 2\alpha}{3/2}\right)\right\}^{-1} \mp \left\{\cos\left(\frac{2\pi}{3}\right) - 1\right\}^{-1}\right] \tag{A.15}$$

$$\sqrt{\sigma_2} = \mathcal{B}\left[\left\{\cos\left(\frac{2\pi}{3}\right) - \cos\left(\frac{4\alpha}{3}\right)\right\}^{-1} \mp \left\{\cos\left(\frac{2\pi}{3}\right) - 1\right\}^{-1}\right] \tag{A.16}$$

$$\sqrt{\sigma_3} = \mathcal{B}\left[\left\{\cos\left(\frac{2\pi}{3}\right) - \cos\left(\frac{\pi - 2\alpha}{3/2}\right)\right\}^{-1} \mp \left\{\cos\left(\frac{2\pi}{3}\right) - 1\right\}^{-1}\right] \tag{A.17}$$

$$\sqrt{\sigma_4} = 0 \tag{A.18}$$

where

$$\mathcal{B} = \frac{2}{3}\sin(\frac{2\pi}{3})\sqrt{\frac{R_b \csc(\alpha)}{k}} \tag{A.19}$$

and k is the propagation factor. Even for the cylinder coefficients the upper sign is associated to the vertical polarization and the lower to the horizontal polarization. The phase of the coefficients are given by

$$\phi_1 = \frac{\pi}{4} - 2k[R_b \sin(\alpha) + h\cos(\alpha)] \tag{A.20}$$

$$\phi_2 = \frac{\pi}{4} - 2k[R_b \sin(\alpha) - h\cos(\alpha)] \tag{A.21}$$

$$\phi_3 = -\frac{\pi}{4} + 2k[R_b \sin(\alpha) - h\cos(\alpha)] \tag{A.22}$$

$$\phi_4 = -\frac{\pi}{4} + 2k[R_b \sin(\alpha) + h\cos(\alpha)] \tag{A.23}$$

For $\alpha \in]0, \alpha_{ca}]$ the polarization-independent contribution due to diffraction interjection between scatters P_1 and P_3 (see Fig. A.1b) is given by

$$\left(\sqrt{\sigma_1}e^{j\phi_1} + \sqrt{\sigma_3}e^{j\phi_3}\right)_{pol-ind} = 2kR_b^2\sqrt{\pi}\frac{J_1(2kR_b\sin(\alpha))}{2kR_b\sin(\alpha)}e^{-j\frac{\pi}{2}-j2kH\cos(\alpha)} \tag{A.24}$$

For LOS in the axial direction ($\alpha = 0$), the magnitude and phase scattered filed from the target is given by

$$\sigma(\alpha = 0) = \frac{4\pi R_b^4}{\lambda^2} \tag{A.25}$$

$$\phi(\alpha = 0) = -\frac{\pi}{2} - 2kh. \tag{A.26}$$

Considering the interval $\alpha \in \left[\frac{\pi}{2} - \alpha_{cb}, \frac{\pi}{2}\right[$, the polarization-independent contribution from (A.15) and (A.16) is substituted by

$$\left(\sqrt{\sigma_1} e^{j\phi_1} + \sqrt{\sigma_2} e^{j\phi_2}\right)_{pol-ind} = -2h\sqrt{rk}\frac{\sin(2kR_b\sin(\alpha))}{2kR_b\sin(\alpha)} e^{j\frac{\pi}{4} - j2kR_b\sin(\alpha)} \tag{A.27}$$

In the broadside direction ($\alpha = \frac{\pi}{2}$) follows

$$\sigma(\alpha = \frac{\pi}{2}) = kR_b(2h)^2 \tag{A.28}$$

$$\phi(\alpha = \frac{\pi}{2}) = \frac{\pi}{4} - 2kR_b \tag{A.29}$$

The scattered field from the cylinder for the other values of α can be evaluated thanks to the symmetry proprieties of the target.

Cylinder plus Cone

Considering a target composed by a cone and a cylinder which share the base, as shown in Fig. A.1c, the modulus of scattering coefficients are

$$\sqrt{\sigma_1} = \begin{cases} \frac{\sin(\frac{\pi}{n_1})}{4k\sqrt{2\pi}\,n_1}\sqrt{\frac{R_b\csc(\alpha)}{k}}\left[\left\{\cos\left(\frac{\pi}{n_1}\right) - \cos\left(\frac{2(\pi-\gamma-\alpha)}{n_1}\right)\right\}^{-1}\right] & \alpha \in [0, \pi-\gamma[\\ 0 & \alpha \in [\pi-\gamma, \pi] \end{cases} \tag{A.30}$$

$$\sqrt{\sigma_2} = \begin{cases} \mathcal{C}_1 \times \\ \left[\left\{\cos\left(\frac{2\pi}{3}\right) - \cos\left(\frac{\pi+2\alpha}{3/2}\right)\right\}^{-1} \mp \left\{\cos\left(\frac{2\pi}{3}\right) - 1\right\}^{-1}\right] & \alpha \in [0, \pi[\\ 0 & \alpha = \pi \end{cases} \tag{A.31}$$

$$\sqrt{\sigma_3} = \begin{cases} \mathcal{C}_2 \times \\ \left[\left\{ \cos\left(\frac{2\pi}{3}\right) - \cos\left(\frac{4\alpha}{3}\right) \right\}^{-1} \mp \left\{ \cos\left(\frac{2\pi}{3}\right) - 1 \right\}^{-1} \right] & \alpha \in]0, \pi] \\ 0 & \alpha = 0 \end{cases} \tag{A.32}$$

$$\sqrt{\sigma_4} = \begin{cases} \mathcal{C}_1 \times \\ \left[\left\{ \cos\left(\frac{2\pi}{3}\right) - \cos\left(\frac{\pi-2\alpha}{3/2}\right) \right\}^{-1} \mp \left\{ \cos\left(\frac{2\pi}{3}\right) - 1 \right\}^{-1} \right] & \alpha \in [0, \gamma[\\ 0 & \alpha \in [\gamma, \pi] \end{cases} \tag{A.33}$$

$$\sqrt{\sigma_5} = \begin{cases} \mathcal{C}_2 \times \\ \left[\left\{ \cos\left(\frac{2\pi}{3}\right) - \cos\left(\frac{\pi+2\alpha}{3/2}\right) \right\}^{-1} \mp \left\{ \cos\left(\frac{2\pi}{3}\right) - \cos\left(\frac{4\pi}{3}\right) \right\}^{-1} \right] & \alpha \in]\frac{\pi}{2}, \pi] \\ 0 & \alpha \in [0, \frac{\pi}{2}] \end{cases} \tag{A.34}$$

where, coherently to the other target shapes, the upper sign is associated to the vertical polarization and the lower to the horizontal polarization, and where

$$\mathcal{C}_1 = \frac{\sin(\frac{2\pi}{n_2})}{n_2} \sqrt{\frac{R_b \csc(\alpha)}{k}} \tag{A.35}$$

$$\mathcal{C}_2 = \frac{\sin(\frac{2\pi}{n_3})}{n_3} \sqrt{\frac{R_b \csc(\alpha)}{k}} \tag{A.36}$$

with R_b the base radius, and

$$n_1 = 2 - \frac{2\gamma}{\pi} \tag{A.37}$$

$$n_2 = 1 + \frac{\gamma}{\pi} \tag{A.38}$$

$$n_3 = \frac{3}{2} \tag{A.39}$$

The phase of the coefficients are given by

$$\phi_1 = \frac{\pi}{4} - 2k\left[R_b\sin(\alpha) + \left(h_1 + \frac{h_2}{2}\right)\cos(\alpha)\right] \tag{A.40}$$

$$\phi_2 = \frac{\pi}{4} - 2k\left[R_b\sin(\alpha) + \frac{h_2}{2}\cos(\alpha)\right] \tag{A.41}$$

$$\phi_3 = \frac{\pi}{4} - 2k\left[R_b\sin(\alpha) - \frac{h_2}{2}\cos(\alpha)\right] \tag{A.42}$$

$$\phi_4 = -\frac{\pi}{4} + 2k\left[R_b\sin(\alpha) - \frac{h_2}{2}\cos(\alpha)\right] \tag{A.43}$$

$$\phi_5 = -\frac{\pi}{4} + 2k\left[R_b\sin(\alpha) + \frac{h_2}{2}\cos(\alpha)\right] \tag{A.44}$$

considering that the phase reference centre is on the symmetric axis at the same distance from the cylinder bases centres. As done for the conical target when incidence is at and near the nose-on axial aspect, even for target composed by a cone and a cylinder (A.31) and (A.33) for $0 \leq \alpha \leq \gamma$ are substituted by

$$\begin{aligned}\left(\sqrt{\sigma_2}e^{j\phi_2} + \sqrt{\sigma_4}e^{j\phi_4}\right) =& \frac{2R_b\sqrt{\pi}\sin\left(\frac{\pi}{n_2}\right)}{n_2}e^{-j2kh_2\cos(\alpha)}\times \\ &\left[J_0(2kR_b\sin(\alpha))\left\{\cos\left(\frac{\pi}{n_2}\right) - \cos\left(\frac{2\pi}{n_2}\right)\right\}^{-1}\right. \\ &-J_1(2kR_b\sin(\alpha))\frac{\frac{2j\tan(\alpha)}{n_2}\sin\left(\frac{2\pi}{n_2}\right)}{\left(\cos\left(\frac{\pi}{n_2}\right) - \cos\left(\frac{2\pi}{n_2}\right)\right)^2} \\ &\left.\mp J_2(2kR_b\sin(\alpha))\left\{\cos\left(\frac{\pi}{n_2}\right) - 1\right\}^{-1}\right]\end{aligned} \tag{A.45}$$

Defining the cross over aspect angle α_{ca} as

$$2kR_b\sin(\alpha_{ca}) = 2.44 \tag{A.46}$$

for $\pi - \alpha_{ca} \leq \alpha \leq \pi$, the polarization-independent contribution from (A.32) and (A.34) is substituted by

$$\left(\sqrt{\sigma_3}e^{j\phi_3} + \sqrt{\sigma_5}e^{j\phi_5}\right)_{pol-ind} = 2\sqrt{\pi}kr^2\frac{J_1(2kR_b\sin(\alpha))}{(2kR_b\sin(\alpha))}e^{-j\frac{\pi}{2}+j2kh_2\cos(\alpha)} \tag{A.47}$$

Finally, for the evaluation of scattered field in proximity of broadside direction, the polarization-independent contribution from (A.32) and (A.34) is substituted by

$$\left(\sqrt{\sigma_2}e^{j\phi_2} + \sqrt{\sigma_3}e^{j\phi_3}\right)_{pol-ind} = -2h_2\sqrt{rk}\frac{\sin(2kh_2\cos(\alpha))}{2kh_2\cos(\alpha)}e^{j\frac{\pi}{4}-j2kR_b\sin(\alpha)} \quad \text{(A.48)}$$

for $\alpha_{cb} \leq \alpha \leq \pi - \alpha_{cb}$, where the broadside cross over angle α_{cb} verify

$$2kh_2\cos(\alpha_{cb}) = 2.25 \quad \text{(A.49)}$$

All other contributions to the total return from the target are well behaved in this angular region (Ross and DIV., 1969).

References

(2008). IEEE Standard Radar Definitions. *IEEE Std 686-2008 (Revision of IEEE Std 686-1997)*, pages c1–41.

(2017). *National research on space debris, safety of space objects with nuclear power sources on board and problems relating to their collision with space debris.* Committee on the Peaceful Uses of Outer Space Scientific and Technical Subcommittee 54$^{\text{th}}$ session. http://www.unoosa.org/res/oosadoc/data/documents/2017/aac_105c_12017crp/aac_105c_12017crp_12_0_html/AC105_C1_2017_CRP12E.pdf, Accessed at: 2017-01-12.

Abdullah, R. R. and Ismail, A. (2006). Forward Scattering Radar: current and future applications. *International Journal of Engineering and Technology*, 3(1):61–67.

Abdullah, R. S. A. R., Alnaeb, A., Salah, A. A., Rashid, N. E. A., Sali, A., and Pasya, I. (2017). Micro-Doppler Estimation and Analysis of Slow Moving Objects in Forward Scattering Radar System. *Remote Sensing*, 9(7).

Allen, R. L. and Mills, D. (2003). *TimeFrequency Signal Transforms*, pages 712–801. Wiley-IEEE Press.

Aydin, A. T., Pace, P. E., and Tummala, M. (2005). "Orbit selection for space based interception of a select ICBM case". In *2005 IEEE International Conference on Systems, Man and Cybernetics*, volume 2, pages 1882–1888 Vol. 2.

Bai, X. and Bao, Z. (2014). High-Resolution 3D Imaging of Precession Cone-Shaped Targets. *IEEE Transactions on Antennas and Propagation*, 62(8):4209–4219.

Bai, X., Zhou, F., Xing, M., and Bao, Z. (2011). High Resolution ISAR Imaging of Targets with Rotating Parts. *IEEE Transactions on Aerospace and Electronic Systems*, 47(4):2530–2543.

Bankman, I., Rogala, E., and Pavek, R. (2001). Laser Radar in Ballistic Missile Defense. *Johns Hopkins APL Technical Digest*, 22(3):379–393.

Benson, C. R. (2014). Enhancing space situational awareness using passive radar from space based emitters of opportunity. In *2014 Military Communications and Information Systems Conference (MilCIS)*, pages 1–5.

Bhatia, A. B. and Wolf, E. (1954). On the circle polynomials of Zernike and related orthogonal sets. *Mathematical Proceedings of the Cambridge Philosophical Society*, 50:40–48.

Bjorklund, S., Johansson, T., and Petersson, H. (2012). Evaluation of a micro-Doppler classification method on mm-wave data. In *Radar Conference (RADAR), 2012 IEEE*, pages 0934–0939.

Blacknell, D. and Griffiths, H. (2013). *Radar automatic target recognition (ATR) and non-cooperative target recognition (NCTR)*. The Institution of Engineering and Technology.

Boashash and Boualem (2015). *Time-frequency signal analysis and processing: a comprehensive reference*. Academic Press.

Bouchikhi, E. H. E., Choqueuse, V., Benbouzid, M., Charpentier, J.-F., and Barakat, G. (2011). A Comparative Study of Time-Frequency Representations for Fault Detection in Wind Turbine. In *IECON 2011, Melbourne, Australia*, pages pp.3584 – 3589.

Chen, V., Li, F., Ho, S., and Wechsler, H. (2006). Micro-Doppler Effect in Radar: Phenomenon, Model, and Simulation Study. *IEEE Transactions on Aerospace and Electronic Systems*, 42(1):2–21.

Chen, V. C., Tahmoush, D., and Miceli, W. J., editors (2014). *Radar Micro-Doppler Signatures: Processing and Applications*. Radar, Sonar & Navigation. Institution of Engineering and Technology.

Cherniakov, M., Abdullah, R. S. A. R., Jancovic, P., Salous, M., and Chapursky, V. (2006). Automatic ground target classification using forward scattering radar. *IEE Proceedings - Radar, Sonar and Navigation*, 153(5):427–437.

Clark, M. (1999). High range resolution techniques for ballistic missile targets. Technical report, British Aerospace Land and Sea Systems, Newport Road, Cowes, Isle of Wight, PO3 1 8PF, United Kingdom.

Clemente, C., Pallotta, L., De Maio, A., Soraghan, J., and Farina, A. (2015a). A novel algorithm for radar classification based on Doppler characteristics exploiting orthogonal pseudo-Zernike polynomials. *IEEE Transactions on Aerospace and Electronic Systems*, 51(1):417–430.

Clemente, C., Pallotta, L., Gaglione, D., Maio, A. D., and Soraghan, J. J. (2017). Automatic Target Recognition of Military Vehicles With Krawtchouk Moments. *IEEE Transactions on Aerospace and Electronic Systems*, 53(1):493–500.

Clemente, C., Pallotta, L., Proudler, I., De Maio, A., Soraghan, J., and Farina, A. (2015b). Pseudo-Zernike-based multi-pass automatic target recognition from multi-channel synthetic aperture radar. *Radar, Sonar Navigation, IET*, 9(4):457–466.

Da-qing, C., Su-dao, X., Rong-chen, W., and Zhe, Z. (2013). Micro-motion analysis based on HRRP sequence. In *IET International Radar Conference 2013*, pages 1–5.

Deans, S. (2007). *The Radon Transform and Some of Its Applications*. Dover Books on Mathematics Series. Dover Publications.

Dudgeon, D. E. and Lacoss, R. T. (1993). An Overview of Automatic Target Recognition. *Lincoln Laboratory Journal*, 6(1).

Ender, J., Leushacke, L., Brenner, A., and Wilden, H. (2011). Radar techniques for space situational awareness. In *2011 12th International Radar Symposium (IRS)*, pages 21–26.

ESA (2011). eoPortal Directory: HY-2A (Haiyang-2A) / Ocean-2A. https://directory.eoportal.org/web/eoportal/satellite-missions/h/hy-2a, Accessed at: 2017-01-12.

Fioranelli, F., Ritchie, M., and Griffiths, H. (2015a). Analysis of polarimetric multistatic human micro-Doppler classification of armed/unarmed personnel. In *Radar Conference (RadarCon), 2015 IEEE*, pages 0432–0437.

Fioranelli, F., Ritchie, M., and Griffiths, H. (2015b). Classification of Unarmed/Armed Personnel Using the NetRAD Multistatic Radar for Micro-Doppler and Singular Value Decomposition Features. *Geoscience and Remote Sensing Letters, IEEE*, 12(9):1933–1937.

Fioranelli, F., Ritchie, M., and Griffiths, H. (2015c). Multistatic human micro-Doppler classification of armed/unarmed personnel. *Radar, Sonar Navigation, IET*, 9(7):857–865.

Fuhrmann, L., Biallawons, O., Klare, J., Panhuber, R., Klenke, R., and Ender, J. (2017). Micro-Doppler analysis and classification of UAVs at Ka band. In *2017 18th International Radar Symposium (IRS)*, pages 1–9.

Gaglione, D., Clemente, C., Ilioudis, C. V., Persico, A. R., Proudler, I., Soraghan, J. J., and Farina, A. (2018). Waveform Design for Communicating Radar Systems Using Fractional Fourier Transform. *Digital Signal Processing*. (under review).

Gaglione, D., Clemente, C., Ilioudis, C. V., Persico, A. R., Proudler, I. K., and Soraghan, J. J. (2016). Fractional Fourier Transform Based Co-Radar Waveform: Experimental Validation. In *2016 Sensor Signal Processing for Defence (SSPD)*, pages 1–5.

Gao, R. X. and Yan, R. (2006). Non-stationary signal processing for bearing health monitoring. *International Journal of Manufacturing Research*, 1(1):18–40.

Globalstar, L. (1997). Description of Globalstar System.

Goncalves, P. and Baraniuk, R. (1998). Pseudo affine Wigner distributions: definition and kernel formulation. *IEEE Transactions on Signal Processing*, 46(6):1505–1516.

Harmanny, R. I. A., de Wit, J. J. M., and Cabic, G. P. (2014). Radar micro-Doppler feature extraction using the spectrogram and the cepstrogram. In *European Radar Conference (EuRAD), 2014 11th*, pages 165–168.

Heinzel, G., Rüdiger, A., and Schilling, R. (2002). Spectrum and spectral density estimation by the Discrete Fourier transform (DFT), including a comprehensive list of window functions and some new at-top windows.

Hiatt, R. E., Siegel, K. M., and Weil, H. (1960). Forward Scattering by Coated Objects Illuminated by Short Wavelength Radar. *Proceedings of the IRE*, 48(9):1630–1635.

Hlawatsch, F. and Boudreaux-Bartels, G. (1992). Linear and quadratic time-frequency signal representations. *IEEE Signal Processing Magazine*, 9(2):21–67.

Hongwei, G., Lianggui, X., Shuliang, W., and Yong, K. (2010). Micro-Doppler Signature Extraction from Ballistic Target with Micro-Motions. *IEEE Transactions on Aerospace and Electronic Systems*, 46(4):1969–1982.

Hu, R. and Zhu, Z. (1997). Researches on radar target classification based on high resolution range profiles. In *Proceedings of the IEEE 1997 National Aerospace and Electronics Conference. NAECON 1997*, volume 2, pages 951–955 vol.2.

Hua, Y., Guo, J., and Zhao, H. (2014). The usage of inverse-radon transformation in ISAR imaging. In *2014 IEEE International Conference on Control Science and Systems Engineering*, pages 167–170.

Ilonen, J., Kamarainen, J., and Kalviainen, H. (2007). Fast extraction of multi-resolution Gabor features. In *Image Analysis and Processing, 2007. ICIAP 2007. 14th International Conference on*, pages 481–486.

Jayasimha, S. and Jyothendar, P. (2013). Detection of orbital debris using self-interference cancellation residual signal. In *2013 IEEE International Conference on Space Science and Communication (IconSpace)*, pages 124–127.

Jones, D. L. and Parks, T. W. (1990). A high resolution data-adaptive time-frequency representation. *IEEE Transactions on Acoustics, Speech, and Signal Processing*, 38(12):2127–2135.

Kamarainen, J., Kyrki, V., and Kalviainen, H. (2006). Invariance properties of Gabor filter-based features-overview and applications. *Image Processing, IEEE Transactions on*, 15(5):1088–1099.

Kangle, L., Weidong, J., Yongxiang, L., and Xiang, L. (2009). Feature extraction of cone with precession based on micro-Doppler. In *2009 IET International Radar Conference*, pages 1–5.

Kaur, B., Joshi, G., and Vig, R. (2015). Analysis of shape recognition capability of Krawtchouk moments. In *Computing, Communication Automation (ICCCA), 2015 International Conference on*, pages 1085–1090.

Kertész, G., Szénási, S., and Vámossy, Z. (2017). Application and properties of the radon transform for object image matching. In *2017 IEEE 15th International Symposium on Applied Machine Intelligence and Informatics (SAMI)*.

keun Jang, S., Hutchins, R. G., and Pace, P. E. (2008). Boost phase ICBM engagement using space-based interceptors: A comparison of guidance laws. In *2008 IEEE International Conference on System of Systems Engineering*, pages 1–5.

Kirkland, P., Clemente, C., Persico, A. R., Vasile, M., and Soraghan, J. (2016). CubeSAT based passive bistatic radar for space debris detection and tracking. In *Stardust Final Conference on Asteroids and Space Debris*.

Lei, J. and Lu, C. (2005). Target classification based on micro-Doppler signatures. In *IEEE International Radar Conference, 2005.*, pages 179–183.

Lei, P., l. Li, K., and x. Liu, Y. (2012). Feature extraction and target recognition of missile targets based on micro-motion. In *Signal Processing (ICSP), 2012 IEEE 11th International Conference on*, volume 3, pages 1914–1919.

Levanon, N. and Mozeson, E. (2004). Wiley-IEEE Press.

Li-hua, L., Zhuang, W., and Wei-dong, H. (2006). Precession Period Extraction of Ballistic Missile Based on Radar Measurement. In *2006 CIE International Conference on Radar*, pages 1–4.

Liu, B. and Chang, W. (2013). Motion compensation for missile-borne frequency stepped chirp radar. In *IET International Radar Conference 2013*, pages 1–6.

Liu, L., Ghogho, M., McLernon, D., and Hu, W. (2010). Ballistic missile precessing frequency extraction based on maximum likelihood estimation. In *2010 18th European Signal Processing Conference*, pages 1562–1566.

Liu, L., Ghogho, M., McLernon, D., and Hu, W. (2011). Pseudo Maximum Likelihood Estimations of ballistic missile precession frequency. In *2011 IEEE International Conference on Acoustics, Speech and Signal Processing (ICASSP)*, pages 3796–3799.

Liu, L., McLernon, D., Ghogho, M., Hu, W., and Huang, J. (2012). Ballistic Missile Detection via micro-Doppler Frequency Estimation from Radar Return. *Digital Signal Processing*, 22(1):87–95.

Mahafza, B. and Elsherbeni, A. (2003). *MATLAB Simulations for Radar Systems Design*. CRC Press.

Mahmud, M. S., Qaisar, S. U., and Benson, C. (2016). Affordable processing for long coherent integration of weak debris-scattered GNSS signals with inconsistent Doppler. In *2016 Annual IEEE Systems Conference (SysCon)*, pages 1–6.

Melvin, W. L. and Scheer, J. A. (2014). *Principles of Modern Radar Volume III-Radar Applications*. SciTech Publishing.

Mittal, N., Mital, D., and Chan, K. L. (1999). Features for texture segmentation using Gabor filters. In *Image Processing And Its Applications, 1999. Seventh International Conference on (Conf. Publ. No. 465)*, volume 1, pages 353–357 vol.1.

Molchanov, P., Astola, J., Egiazarian, K., and Totsky, A. (2012). Classification of ground moving radar targets by using joint time-frequency analysis. In *2012 IEEE Radar Conference*, pages 0366–0371.

Murray, R. M., Li, Z., Sastry, S., and Sastry, S. (1994). *A Mathematical Introduction to Robotic Manipulation*. CRC press.

NASA (2011). USA Space Debris Environment, Operations, and Policy Updates. http://www.unoosa.org/pdf/pres/stsc2011/tech-31.pdf, Accessed at: 2017-01-12.

Nassery, P. and Faez, K. (1996). Signature pattern recognition using pseudo Zernike moments and a fuzzy logic classifier. In *Proceedings of 3rd IEEE International Conference on Image Processing*, volume 1, pages 197–200 vol.2.

Noll, A. M. (1964). Short-Time Spectrum and Cepstrum Techniques for Vocal-Pitch Detection. *The Journal of the Acoustical Society of America*, 36(2):296–302.

Nor'aini, A. and Raveendran, P. (2009). Improving face recognition using combination of global and local features. In *Mechatronics and its Applications, 2009. ISMA '09. 6th International Symposium on*, pages 1–6.

Pelton, J. (2013). *Space Debris and Other Threats from Outer Space*. SpringerBriefs in Space Development. Springer-Verlag New York.

Persico, A. R., Clemente, C., Gaglione, D., Ilioudis, C. V., Cao, J., Pallotta, L., Maio, A. D., Proudler, I., and Soraghan, J. J. (2017a). On Model, Algorithms, and Experiment for Micro-Doppler-Based Recognition of Ballistic Targets. *IEEE Transactions on Aerospace and Electronic Systems*, 53(3):1088–1108.

Persico, A. R., Clemente, C., Ilioudis, C., Gaglione, D., Cao, J., and Soraghan, J. (2015). Micro-Doppler Based Recognition of Ballistic Targets Using 2D Gabor Filters. In *2015 Sensor Signal Processing for Defence (SSPD)*, pages 1–5.

Persico, A. R., Clemente, C., Pallotta, L., Maio, A. D., and Soraghan, J. (2016a). Micro-Doppler classification of ballistic threats using Krawtchouk moments. In *2016 IEEE Radar Conference (RadarConf)*, pages 1–6.

Persico, A. R., Ilioudis, C., Clemente, C., Brueggenwirth, S., Bieker, T., and Soraghan, J. (2016b). Ballistic Targets Discrimination based on High Resolution Range Profiles. In *11th IMA International Conference on Mathematics in Signal Processing*.

Persico, A. R., Ilioudis, C., Clemente, C., and Soraghan, J. (2017b). Novel Approach for Ballistic Targets Classification from HRRP Frame. In *2017 Sensor Signal Processing for Defence Conference (SSPD)*, pages 1–5.

Persico, A. R., Ilioudis, C. V., Clemente, C., and Soraghan, J. J. (2018a). Novel Classification Algorithm for Ballistic Targets based on High Resolution Range Profile frame. *IEEE Transactions on Aerospace and Electronic Systems*. (under review).

Persico, A. R., Kirkland, P., Clemente, C., Vasile, M., and Soraghan, J. J. (2018b). Cubesat-based Passive Bistatic Radar for Space Situational Awareness: a Feasibility Study. *IEEE Transactions on Aerospace and Electronic Systems*. (accepted for being published).

Qun Zhang, Ying Luo, Y.-a. C. (2016). *Micro-Doppler Characteristics of Radar Targets*. 1st edition.

Rahmat-Samii, Y., Manohar, V., and Kovitz, J. M. (2017). For Satellites, Think Small, Dream Big: A review of recent antenna developments for CubeSats. *IEEE Antennas and Propagation Magazine*, 59(2):22–30.

Rathore, H., Katukuri, M., Rao, D., and Narayana Murthy, B. (2014). Real-time embedded software design for onboard computer of Anti-Ballistic missile system. In *Computer and Communications Technologies (ICCCT), 2014 International Conference on*, pages 1–5.

Research^{TM}, E. (2017). USRP E312. https://www.ettus.com/content/files/USRP_E312_Datasheet.pdf, Accessed at: 2017-01-12.

RF-LAMBDA (2017). http://www.rflambda.com, Accessed at: 2017-01-12.

RFCCOMP.com (2017). Part of the HD Communications Group. = http://www.rfcomp.com, Accessed at: 2017-01-12.

Richards, M., Holm, W., Melvin, W., Scheer, J., and Scheer, J. (2013). *Principles of Modern Radar: Advanced Techniques*. EBSCO ebook academic collection. IET.

Richards, M. A., Scheer, J. A., Holm, W. A., Beckley, B., Mark, P., Richards, A., et al. (2010). *Principles of Modern Radar Volume I-Basic Principles*. Citeseer.

Ross, R. and DIV., G. D. F. W. T. F. W. (1969). *Investigation of Scattering Principles. Volume 3. Analytical Investigation*. Defense Technical Information Center.

Sessler, A., Cornwall, J., Dietz, B., Fetter, S., Frankel, S., Garwin, R., Gottfried, K., Gronlund, L., Lewis, G., Postol, T., and Wright, D. (2000). Countermeasure: A Technical Evaluation of the Operational Effectiveness of the Planned US National Missile Defense System. Technical report, Union of Concerned Scientists MIT Security Studies Program.

Singh, H. (2004). Comparative study of high frequency techniques in radar cross-section (RCS) estimation. In *Proceedings of the 9th International Seminar/Workshop on Direct and Inverse Problems of Electromagnetic and Acoustic Wave Theory, 2004. DIPED 2004.*, pages 29–33.

Sisan, H., Jianxiong, Z., Hongzhong, Z., and Daobin, L. (2008). Estimating the precession angle of ballistic targets in midcourse based on HRRP sequence. In *2008 IEEE Radar Conference*, pages 1–4.

Skolnik, M. I. (2001). *Introduction to Radar Systems*. Electrical engineering series. McGraw-Hill Higher Education.

Smirnov, N. N. and Institute, E. S. (2002). *Space debris : hazard evaluation and mitigation*. London : Taylor & Francis.

Stankovic, L. (1994). A method for time-frequency analysis. *IEEE Transactions on Signal Processing*, 42(1):225–229.

Stankovic, S., Djurovic, I., and Pitas, I. (2001). Watermarking in the space/spatial-frequency domain using two-dimensional Radon-Wigner distribution. *IEEE Transactions on Image Processing*, 10(4):650–658.

Sultana, M., Gavrilova, M., and Yanushkevich, S. (2014). Expression, pose, and illumination invariant face recognition using lower order pseudo Zernike moments. In *2014 International Conference on Computer Vision Theory and Applications (VISAPP)*, volume 1, pages 216–221.

Swerling, P. (1997). Radar probability of detection for some additional fluctuating target cases. *IEEE Transactions on Aerospace and Electronic Systems*, 33(2):698–709.

Tait, P. (2005). *Introduction to Radar Target Recognition*. Radar, Sonar and Navigation Series 18. Institution of Engineering and Technology.

Thayaparan, T. (2006). Separation of target rigid body and micro-doppler effects in SAR/ISAR imaging. Technical memorandum, drdc ottawa tm 2006-187, Defence R&D Canada, Ottawa.

Tivive, F., hung, S., and Bouzerdoum, A. (2015). Classification of micro-Doppler signatures of human motions using log-Gabor filters. *IET Radar, Sonar Navigation*, 9(9):1188–1195.

Ustalli, N., Lombardo, P., and Pastina, D. (2017). Detection Performance of Forward Scatter Radar Using a Crystal Video Detector. *IEEE Transactions on Aerospace and Electronic Systems*, PP(99):1–1.

Vallado, D. (2007). *Fundamentals of Astrodynamics and Applications*, volume 21. Springer-Verlag New York, 3 edition.

Weiner, S. D. and Rocklin, S. M. (1994). Discrimination Performance Requirements for Ballistic Missile Defense. *The Lincoln Laboratory Journal*, 7(1):63–88.

Willis, N. (2005). *Bistatic Radar*. Electromagnetics and Radar. Institution of Engineering and Technology.

Wood, J. C. and Barry, D. T. (1994). Radon transformation of time-frequency distributions for analysis of multicomponent signals. *IEEE Transactions on Signal Processing*, 42(11):3166–3177.

Yan, H., Fu, X., Lei, X., Li, P., and Gao, M. (2011). Parametric estimation of micro-Doppler on spatial precession cone. In *Proceedings of 2011 IEEE CIE International Conference on Radar*, volume 1, pages 613–616.

Yap, P.-T., Paramesran, R., and Ong, S.-H. (2003). Image analysis by Krawtchouk moments. *Image Processing, IEEE Transactions on*, 12(11):1367–1377.

Zabalza, J., Clemente, C., Caterina, G. D., Ren, J., Soraghan, J., and Marshall, S. (2014). Robust PCA micro-doppler classification using SVM on embedded systems. *IEEE Transactions on Aerospace and Electronic Systems*, 50(3):2304–2310.

Zakeri, B., Zahabi, M., and Alighale, S. (2004). Micro-Doppler Feature Extraction of Experimental Helicopter Data using Wavelet and Time-Frequency Analysis. In Proceedings of the International Conference on Radar Systems (RADAR).

Özcan, M. B., Gürbüz, S. Z., Persico, A. R., Clemente, C., and Soraghan, J. (2016). Performance analysis of co-located and distributed MIMO radar for micro-Doppler classification. In *2016 European Radar Conference (EuRAD)*, pages 85–88.